Probing Photoinduced Dynamics Within Dye-Sensitised Solar Cells

Fiona A. Black

A thesis submitted for the degree of

Doctor of Philosophy in Chemistry

School of Natural and Environmental Sciences

Newcastle University

October 2018

Abstract

The low efficiencies of p-type nickel oxide (NiO) dye-sensitised solar cells currently hinder the performance of tandem devices, which combine both dye-sensitised photocathodes and photoanodes to create a multi-junction cell. The maximum potential efficiency of such devices is over 40 %, relative to a limit of 33 % for single-junction devices. Fast charge-recombination has been identified as a major limiting factor of dye-sensitised NiO systems, but there is little correlation between solar cell efficiency and the lifetime of the $dye^{-}|NiO^{+}$ charge-separated state. This suggests that charge-recombination dynamics are complex with multiple intermediates often observed when these systems are illuminated. In this thesis the photoinduced charge transfer dynamics of a selection of light-absorbing compounds are investigated by ultrafast time-resolved spectroscopy, with the aims of further understanding the processes which occur inside a NiO dye-sensitised solar cell and influencing the design of future systems.

Chapter 4 investigates a number of broadly-absorbing push-pull dyes which all form a charge-separated state when adsorbed on NiO. Dyes with boron dipyrromethene (bodipy) acceptor groups perform better in dye-sensitised solar cells when they contain a thiophene bridge and when there is stronger electronic communication between the donor and acceptors. A combination of single-point and global analysis of transient absorption data is used to extract the lifetimes associated with the charge-separated state. Similar techniques are used to investigate dyes with cationic acceptor groups, and it is proposed that interactions between the charged acceptor group and the iodide/triiodide redox couple reduce recombination processes. A key result of this chapter is the characterisation of a bodipy-localised triplet excited state in the infrared region, which is observed for a push-pull dye in dichloromethane but not in acetonitrile or when adsorbed on NiO.

In Chapter 5 a series of bodipy chromophore-polyoxometalate hybrid molecules are presented and the photoinduced dynamics are compared for systems where the metal, linker group, counter cation and bridge length are modified in two solvents. A global analysis method is used to identify the presence of charge-transfer intermediates where the spectra of excited state species overlap. It is found that all structural changes have an effect on the dynamics, suggesting that these systems can be effectively tuned to different applications. Most interestingly, when the solvent is changed from acetonitrile to dichloromethane for a bodipy-polyoxomolybdate, recombination of the charge-transfer excited state occurs via a bodipy-localised triplet excited state, which is again characterised in the infrared region.

The relationship between solar cell performance and structure is investigated in Chapter 6 for an extensive series of ruthenium sensitisers with cyclometalating ligands. Small variations in the structure have a large effect on the photophysical properties of the dyes, but less impact on the performance of ruthenium-sensitised titanium dioxide solar cells.

Finally, Chapter 7 presents a new molecule for the sensitisation of p-type metal oxides. The design of this dye combines properties which were found to be beneficial in the preceding chapters, including a push-pull structure, spectroscopic handles and simple synthesis. In general the properties of the dye are favourable and a promising internal quantum efficiency of 13 % is achieved for initial dye-sensitised solar cell tests.

Acknowledgements

There are many people who I would like to thank for their advice and assistance over the course of this project. Firstly, I would like to thank my supervisor Dr. Elizabeth Gibson for introducing me to the field of dye-sensitised solar cells and providing me with motivation and support throughout my time in her research group. Collaborations with the groups of Dr. Guillaume Izzet and Dr. Valery Kozhevnikov have provided interesting samples and I would like to thank them for their efforts. I would also like to thank the staff responsible for the ULTRA system at the Rutherford Appleton Laboratory, specifically Dr. Ian Clark and Dr. Igor Sazanovich for their patience as I conducted experiments under their supervision. Similarly, Dr. Pavel Chábera, Dr. Karel Zidek and Prof. Tönu Pullerits at Lund University. Finally, I would like to thank all past and present members of the Gibson research team, especially Gareth, Nathan and Nils who have always made time to help me with experiments and discussions. I hope to find the same charisma and team spirit amongst my future colleagues. Lastly, I would like to thank my parents for their constant support and faith.

Publications

The following publications contain work by the author which is included in this thesis.

i) Summers, G. H.; Lefebvre, J. F.; Black, F. A.; Davies, E. S.; Gibson, E. A.; Pullerits, T.; Wood, C. J.; Zidek, K. Design and characterisation of bodipy sensitizers for dye-sensitized NiO solar cells *Phys. Chem. Chem. Phys.* **2015**, *18*, 1059-70.

ii) Black, F. A.; Wood, C. J.; Ngwerume, S.; Summers, G. H.; Clark, I. P.; Towrie, M.; Camp, J. E.; Gibson, E. A. Charge-transfer dynamics at the dye-semiconductor interface of photocathodes for solar energy applications *Faraday Discuss.* **2017**, *198*, 449-461.

iii) Black, F. A.; Clark, C. A.; Summers, G. H.; Clark, I. P.; Towrie, M.; Penfold, T.; George, M. W.; Gibson, E. A. Investigating interfacial electron transfer in dye-sensitized NiO using vibrational spectroscopy *Phys. Chem. Chem. Phys.* **2017**, *19*, 7877-7885.

iv) Black, F. A.; Jacquart, A.; Toupalas, G.; Alves, S.; Proust, A.; Clark, I. P.; Gibson, E. A.; Izzet, G. Rapid photoinduced charge injection into covalent polyoxometalate–bodipy conjugates *Chem. Sci.* **2018**, *9*, 5578-5584.

The following publications contain additional contributions from the author which are not discussed in this thesis.

v) El Moll, H.; Black, F. A.; Wood, C. J.; Al-Yasari, A.; Reddy Marri, A.; Sazanovich, I. V.; Gibson, E. A.; Fielden, J. Increasing p-type dye sensitised solar cell photovoltages using polyoxometalates *Phys. Chem. Chem.Phys* **2017**, *19*, 18831-18835.

vi) Sinopoli, A.; Black, F. A.; Wood, C. J.; Gibson, E. A.; Elliott, P. I. Investigation of a new bis(carboxylate)triazole-based anchoring ligand for dye solar cell chromophore complexes *Dalton Trans.* **2017**, *46*, 1520-1530.

Contents

Abbreviations

AM	Air mass
APCE	Absorbed photon-to-current conversion efficiency
DADS	Decay-associated difference spectra
ΔG_{CS}	Gibbs free energy of charge-separation
ΔG_{inj}	Gibbs free energy of injection
ΔG_{reg}	Gibbs free energy of regeneration
DSC	Dye-sensitised solar cell
ε	Molar absorption coefficient
$E_{0\text{-}0}$	Zero-zero energy
EADS	Evolution-associated difference spectra
$E^{0'}{}_{redox}$	Formal energy of the electrolyte
E_F	Fermi potential of the semiconductor
E_{redox}	Redox potential of the electrolyte
FF	Fill factor
FTO	Fluorine-doped tin oxide
HOMO	Highest occupied molecular orbital
IPCE	Incident photon-to-current conversion efficiency
I_{SC}	Short-circuit current
J_{SC}	Short-circuit current density
λ_{exc}	Wavelength of excitation
λ_{max}	Wavelength of maximum absorption
LHE	Light harvesting efficiency

LUMO	Lowest unoccupied molecular orbital
η	Power conversion efficiency
η_{cc}	Charge collection efficiency
NHE	Normal hydrogen electrode
OTTLE	Optically transparent thin layer electrochemical
Φ_{FL}	Quantum yield of fluorescence
qE_F	*quasi*-Fermi potential of the semiconductor
R_S	Series resistance
R_{SH}	Shunt resistance
τ_e	Electron lifetime
τ_h	Hole lifetime
τ_{inj}	Charge-injection time
τ_{exc}	Excited state lifetime
τ_{FL}	Fluorescence lifetime
τ_{rec}	Charge-recombination time
τ_{reg}	Regeneration time
τ_{tr}	Charge-transport time
V_{OC}	Open-circuit voltage

Chapter 1

Introduction

1.1 Solar energy

The world energy consumption stands at around 4 $\times 10^{20}$ J per year, which equates to an average of 13 Terawatts of power,[1] and The International Energy Outlook 2017 predicts that this will rise by 28 % between 2015 and 2040.[2] Considering that the earth receives 10^4 times what mankind consumes in a year from the sun (3 $\times 10^{24}$ J), solar energy is by far the most abundant energy source available.[3–5] The current technologies which harness this energy are solar thermal and solar electric (photovoltaics), which directly convert sunlight to electricity, though there is also considerable research into solar fuel cells (photoelectrochemical/photobiological).[6]

In the United Kingdom over 12 Gigawatts of photovoltaics are installed, generating 3.4 % of the total electricity.[7] This is a promising figure but to increase our photovoltaic output significantly, innovative solutions are required. This will most likely arise from a combination of solar technologies, for example at Swansea-based company SPECIFIC building-integrated photovoltaics for electricity generation are combined with batteries for storage and solar air collectors for heating.[8]

1.2 Photovoltaics

Photovoltaics are categorised into three generations. The first contains monocrystalline and polycrystalline silicon (c-Si) solar cells, which are made from silicon wafers of high

purity with a thickness of between 0.2 mm to 0.5 mm.[9,10] The wafers are doped with either phosphorus to create n-type silicon or boron to create p-type silicon and a pn-junction is formed at the interface. The working principles of a pn-junction solar cell are shown in Figure 1.1. Photons are absorbed at the pn-junction and an electron-hole pair is generated (1). Thermal relaxation (2,2') and recombination (3) processes can occur. The electric field at the junction helps to separate electrons and holes (4,4') and the charges are collected at front and back contacts (5,5'). Crystalline silicon has an indirect band gap so a large amount of material is required for sufficient light absorption,[11] but the efficiencies are high, generally 15-19 %.[12]

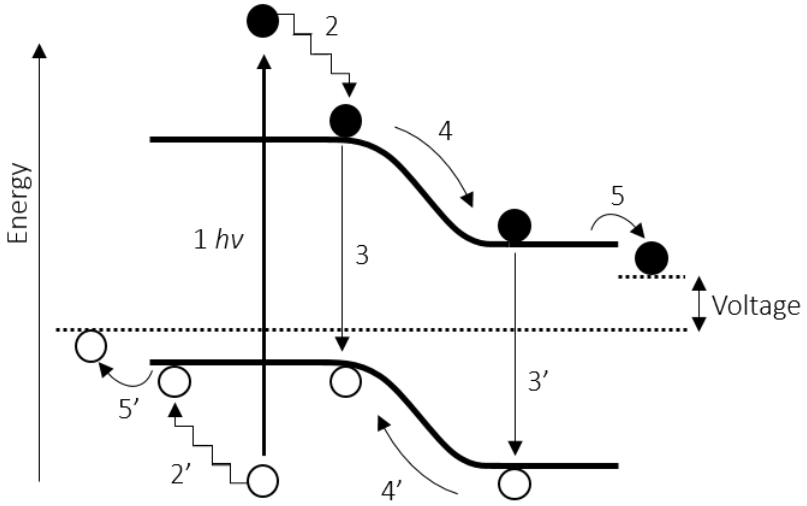

Figure 1.1: Representation of the working and loss mechanisms in a pn-junction solar cell. 1) Light absorption; 2,2') thermal relaxation; 3,3') recombination losses; 4,4') junction loss; 5,5') contact loss.

The second generation contains thin film technologies including amorphous silicon (a-Si), cadmium telluride (CdTe) and copper indium gallium selenide (CIGS), which is an alloy of copper indium selenide ($CuInSe_2$) and copper gallium selenide ($CuGaSe_2$).[13] These are also pn-junction cells and operate in a similar way to crystalline silicon, but the semiconductor is deposited with a thickness of a few micrometers.[13,14] This is possible because these materials have a direct band-gap, and therefore stronger light absorption, so less material is required. Cadmium telluride has a particularly well-suited band gap to the solar spectrum, which is shown in Figure 1.2 together with the band gap energies of some other common semiconductor materials. The benefits of these devices are that they are cheaper to produce, and can be made flexible to a certain degree. These devices

generally achieve around 18 % efficiency,[14] but there are limited known resources of indium and tellurium which could limit the scale-up potential.[9]

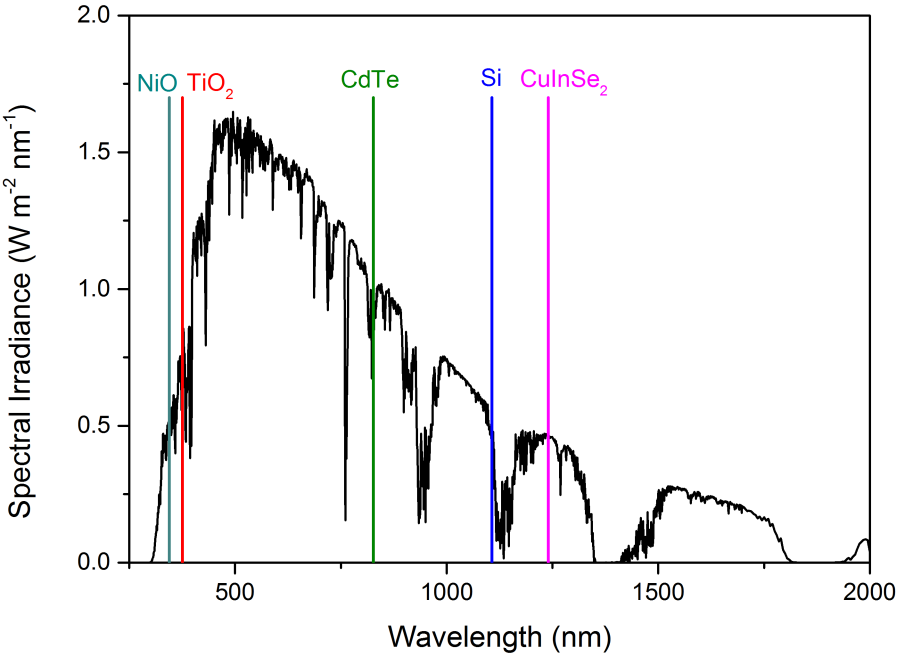

Figure 1.2: The AM (air mass) 1.5 global solar spectrum. The band gap energies of commonly used semiconductor materials are shown: NiO 3.6 eV; TiO_2 3.3 eV; CdTe 1.5 eV; Si 1.1 eV; $CuInSe_2$ 1.0 eV. Spectrum downloaded and adapted from ref [15].

The first two generations contain single junction cells which have a theoretical maximum efficiency of 33 %, as defined by William Shockley and Hans Queisser in 1961.[16] One of the limitations is the thermal relaxation loss which occurs when photons with greater energy than the band gap promote electrons and holes to higher energy than the band edges. This process is labelled (2,2') in Figure 1.1. Similarly, photons with lower energy than the band edge are transmitted and do not create an electron/hole pair which can be extracted. For silicon which has a band gap of 1.1 eV, photons with energies corresponding to wavelengths longer than 1127 nm cannot contribute to the photocurrent. Materials with a wider band gap than silicon give a higher photovoltage but absorb a narrower region of the solar spectrum so generate a smaller photocurrent. Therefore a compromise between photovoltage and photocurrent gives the highest power (current (Amps) × voltage (Volts) = power (Watts)).

Multi-junction cells can split the absorption of high and low energy photons which reduces thermal relaxation losses and increases the theoretical efficiency beyond that of the Shockley-Queisser limit to around 45 % for two junctions.[17–20] This limit increases to *ca.* 65 % for an infinite number of stacked cells,[21] and currently the highest efficiencies for multi-junction cells are 38.8 % for a four-junction cell, 37.9 % for a three-junction cell and 32.8 % for a two-junction cell.[22] Third generation photovoltaics include multi-junction cells and also emerging technologies which achieve high efficiencies with relatively low materials and production costs. These devices tend to be more versatile in their applications, and include dye-sensitised, quantum dot and perovskite solar cells. The efficiencies of these devices have reached 14 %, 22.7 % and 13.4 %, respectively.[22,23]

1.2.1 The role of dye-sensitised solar cells

Dye-sensitised solar cells contain a thin layer of transparent, nanostructured semiconducting material sensitised with dye molecules to absorb light. Different to a pn-junction device, the processes of light absorption and charge transport are separated. The basic structure of a dye-sensitised solar cell is shown in Figure 1.3 along with that of a pn-junction device.

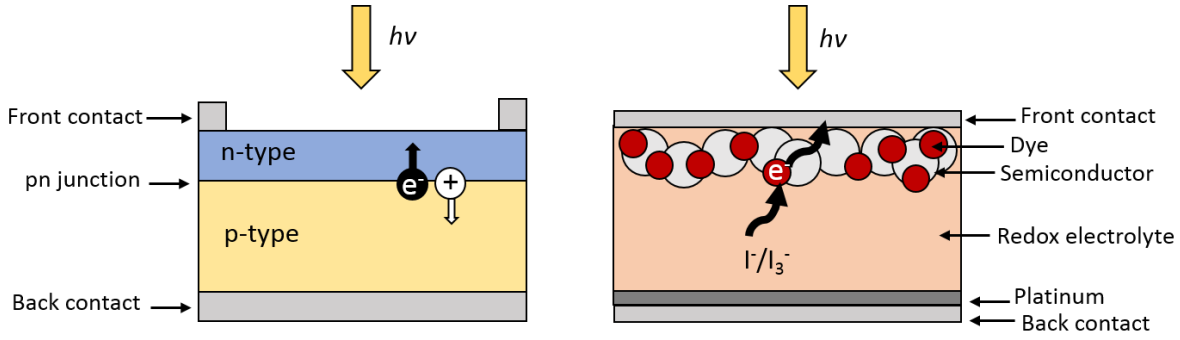

Figure 1.3: Simple representation of the components in a pn-junction solar cell (left) and a dye-sensitised solar cell (right).

Charge separation in a pn-junction device is assisted by the electric field which exists at the junction, whereas the semiconductor is nanostructured in a dye-sensitised solar cell and the electric field does not play a major role in charge separation. Instead, the charges are separated by diffusion through the semiconductor towards the front contact and through a liquid junction containing a redox couple to the back contact due to favourable kinetics.[24]

Commonly n-type titanium dioxide (TiO_2) and p-type nickel oxide (NiO) are used as semiconducting materials in these devices, and their band gap energies are included in Figure 1.2. The light-absorbing compounds presented in this thesis are small organic molecules or metal complexes, though a variety of dyes have been investigated, some of which will be discussed in Section 1.4.

Dye-sensitised solar cells have a number of potential applications for which pn-junction solar cells are less suited. For example, they are semi-transparent so can be incorporated into windows, and the choice of dye allows a range of colours. Their ability to collect diffuse light means they perform well indoors which is also a benefit for areas where there is relatively low solar irradiation, for example in the United Kingdom.[25] In addition to low materials costs, dye-sensitised solar cells are easy to produce and can be printed onto glass or plastic.[26,27] There are a number of companies who have successfully commercialised dye-sensitised solar cells, for example Solaronix (Switzerland), G24 Power Ltd. (Newport, United Kingdom), Dyenamo (Sweden), Exeger (Sweden) and Dyesol (Australia).

The concept of a dye-sensitised solar cell was proposed in the 1970s,[28] but the efficiency of early systems did not exceed 1 %.[29–32] It was not until 1991 when Brian O'Regan and Michael Grätzel developed a device based on a nanostructured titanium dioxide film sensitised with a ruthenium complex which achieved efficiencies over 7 % that research in this area increased.[33] This can be seen in the number of publications into dye-sensitised solar cells, Figure 1.4. In recent years, the numbers of publications on dye-sensitised solar cells has dropped, whilst research into perovskite solar cells has increased rapidly.[34] The efficiencies of perovskite solar cells are competing with commercialised second generation solar cells,[35] however, the presence of lead and the stability of these systems is a concern in terms of commercial viability.[36,37]

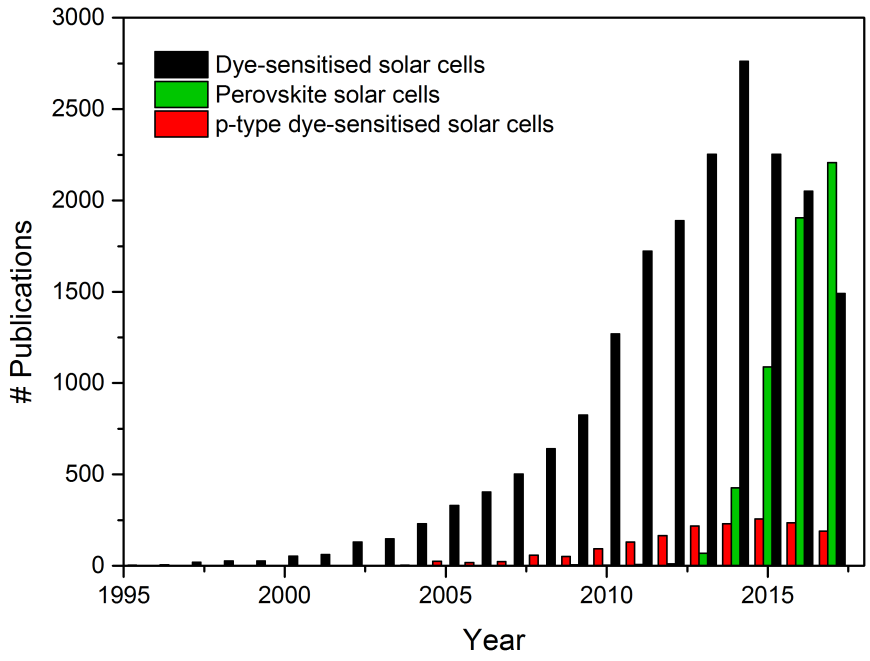

Figure 1.4: Number of publications by year of articles containing "dye-sensitised" or dye-sensitized" and "solar" and "p-type". Also "perovskite" and "solar cell" (Scopus search).

1.3 Working principles

n-Type and p-type dye-sensitised solar cells contain similar components, but electrons flow in opposite directions. The working mechanisms of n-type, p-type and tandem dye-sensitised solar cells are relevant to the studies in this thesis.

1.3.1 n-Type

Figure 1.5 shows a simple representation of the forward processes present in an n-type solar cell containing a dye-sensitised titanium dioxide photoanode, an iodide/triiodide redox couple in solution and a platinised counter electrode. The dye attaches to the semiconductor surface via an anchoring group. Fluorine-doped tin oxide (FTO) coated glass is commonly used as a conductive substrate to fabricate dye-sensitised solar cells. When the dye, D, absorbs a photon of light, an electron is promoted to a higher electronic state, D^* (1). In an organic dye this transition is from the HOMO level (highest occupied molecular orbital) to the LUMO level (lowest unoccupied molecular orbital).

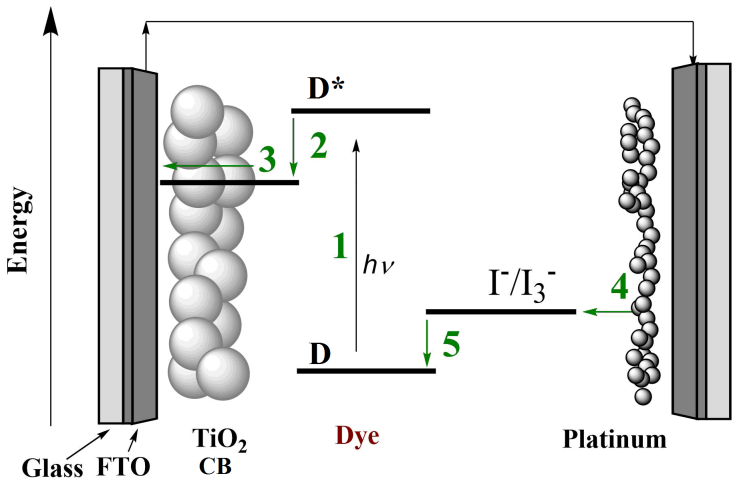

Figure 1.5: Representation of the relative energy levels and forward processes in an n-type titanium dioxide dye-sensitised solar cell. 1) Dye excitation; 2) charge-injection; 3) charge transport; 4) reduction of redox couple; 5) dye-regeneration.

The dye can transfer an electron into the conduction band (CB) of titanium dioxide if there is an exergonic driving force where the Gibbs free energy is sufficiently negative (2). This process is charge-injection and results in an oxidised form of the dye, as shown in Equation 1.1, where D^* is the excited dye, D^+ is the oxidised form of the dye and $e^-(TiO_2)$ is an electron in titanium dioxide. Here, the resulting dye$^+$|TiO$_2^-$ system is referred to as the charge-separated state.

$$D^* \rightarrow D^+ + e^-(TiO_2) \tag{1.1}$$

The negative charge in titanium dioxide passes through the semiconductor via diffusion and is collected at the back contact (3). These processes are referred to as charge transport and charge collection, respectively. The redox couple shuttles the charge from the counter electrode at the other side of the cell (4) to the dye (5), where processes 1) to 4) are repeated. The dye-regeneration process also requires a decrease in Gibbs free energy.

The redox couple used in this work is iodide/triiodide, in an electrolyte containing iodine and a source of iodide (eg. lithium iodide). Many one-electron processes occur for the iodine/iodide system in solution and the dye-regeneration process is believed to proceed through the following mechanism.[38–40] Iodine binds with iodide to form triiodide, Equation 1.2, and the equilibrium of this process is such that very little free iodine is present.[41]

Triiodide diffuses through the electrolyte to the counter electrode where it is reduced to iodide, Equation 1.3, which regenerates the oxidised dye via Equations 1.4 and 1.5. The radical species generated in Equation 1.5 undergoes a disproportionation reaction to reform iodide and triiodide, Equation 1.6.

$$I_2 + I^- \rightarrow I_3^- \tag{1.2}$$

$$I_3^- + 2e^- \rightarrow 3I^- \tag{1.3}$$

$$D^+ + I^- \rightarrow DI \tag{1.4}$$

$$DI + I^- \rightarrow D + I_2^{-\bullet} \tag{1.5}$$

$$2I_2^{-\bullet} \rightarrow I_3^- + I^- \tag{1.6}$$

Overall, for titanium dioxide dye-sensitised solar cells, the key reaction involved in dye-regeneration is described in Equation 1.7.

$$2I^- \rightarrow e^- + I_2^{-\bullet} \tag{1.7}$$

These forward processes compete with loss mechanisms which are shown in Figure 1.5, and are described by Equations 1.8, 1.9 and 1.10. Dye relaxation (1) from the excited state to the ground state occurs via a radiative or non-radiative pathway and depends on the excited state lifetime, τ_{exc}. For an efficient device this process should be slower than the time taken for electrons to diffuse through titanium dioxide, the charge transport time, τ_{tr}.

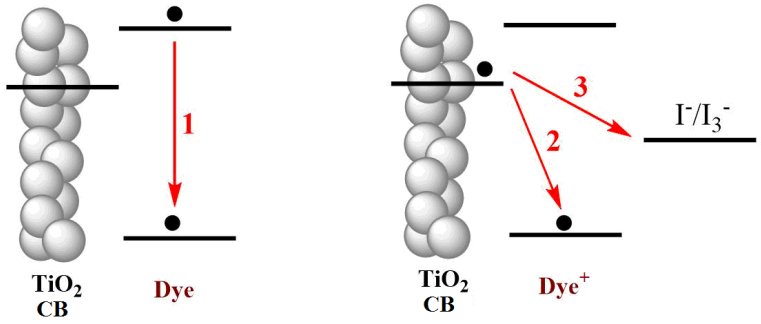

Figure 1.6: Recombination processes in an n-type titanium dioxide dye-sensitised solar cell. 1) Dye relaxation; 2) $dye^{+}|TiO_2^{-}$ recombination; 3) $electrolyte^{+}|TiO_2^{-}$ recombination.

Recombination of the negative charge in titanium dioxide following injection can occur with the electron vacancy in the dye or with species in the electrolyte (2,3). The latter is believed to occur via interactions with free iodine.[42] These processes are shown in Equations 1.9 and 1.10 respectively, and both result in the loss of the charge pair.

$$D^{*} \rightarrow D \tag{1.8}$$

$$D^{+} + e^{-}(TiO_2) \rightarrow D \tag{1.9}$$

$$I_2 + 2e^{-}(TiO_2) \rightarrow 2I^{-} \tag{1.10}$$

1.3.2 p-Type and tandem

Photocathodic systems commonly contain nanostructured nickel oxide as the transparent p-type semiconductor. The forward processes in a nickel oxide dye-sensitised solar cell are shown in Figure 1.7. Following dye excitation (1), electron-injection occurs from the valence band of nickel oxide into the HOMO level of the dye to form the $dye^{-}|NiO^{+}$ charge-separated state (2).

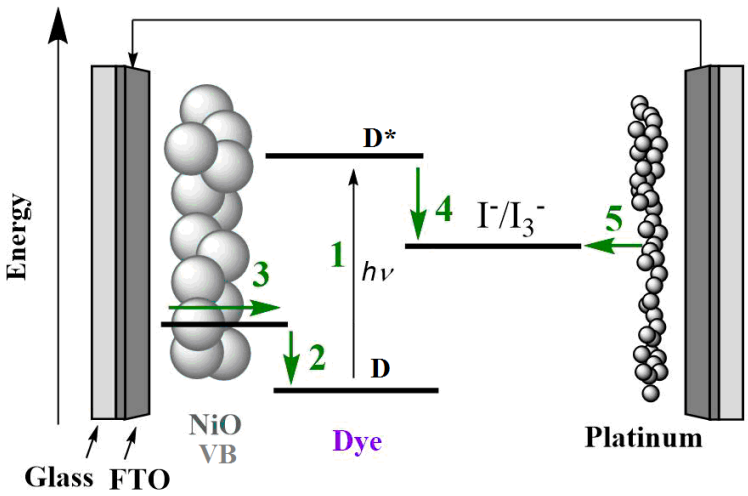

Figure 1.7: Energy level diagram of the forward processes in a p-type nickel oxide dye-sensitised solar cell. 1) Dye excitation; 2) charge-injection; 3) charge transport; 4) dye-regeneration; 5) oxidation of the redox couple.

In this case the charge-separated state consists of a reduced form of the dye and a hole generated in the valence band of nickel oxide, as shown in Equation 1.11.

$$D^{*} \rightarrow D^{-} + h^{+}(NiO) \tag{1.11}$$

The hole diffuses through mesoporous nickel oxide and is collected at the back contact (3). In Figure 1.7, the arrow represents electron movement, as the electrons move towards the dye. Dye-regeneration (4) is thought to occur via an interaction between the reduced dye and triiodide, as shown in Equation 1.12.[43] Equation 1.13 shows the regeneration of triiodide at the counter electrode.

$$D^{-} + I_3^{-} \rightarrow D + I_2^{-\bullet} + I^{-} \tag{1.12}$$

$$3I^{-} \rightarrow I_3^{-} + 2e^{-} \tag{1.13}$$

The important reaction involved in regeneration of the dye for p-type systems is given in Equation 1.14.

$$I_3^{-} + e^{-} \rightarrow I_2^{-\bullet} + I^{-} \tag{1.14}$$

Dye relaxation and recombination processes which occur for p-type systems are shown in Figure 1.8.

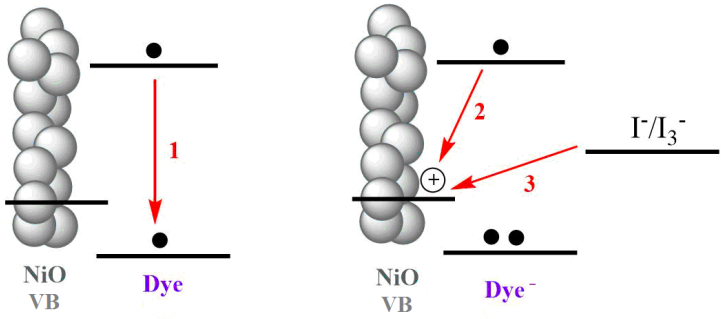

Figure 1.8: Energy level diagram of the backward processes in a p-type nickel oxide dye-sensitised solar cell with an iodide/triiodide redox couple. 1) Dye relaxation; 2) dye$^-$|NiO$^+$ recombination; 3) electrolyte$^-$|NiO$^+$ recombination.

Holes in nickel oxide can recombine with the reduced dye (Equation 1.15) or with species in the electrolyte. It is also possible for nickel oxide to transfer an electron to $I_2^{-\bullet}$, which generates a hole in nickel oxide and can contribute to the photocurrent. This has been observed in the incident photon-to-current conversion efficiency (IPCE) spectrum.[44]

$$D^- + h^+(NiO) \rightarrow D \tag{1.15}$$

By replacing the platinum counter electrode of a titanium dioxide dye-sensitised solar cell with a dye-sensitised nickel oxide photocathode to create a tandem cell, the theoretical maximum efficiency increases to that of a two-junction device.[19,45,46] In this situation, different sensitisers are used at each side of the cell, one absorbing low energy photons and the other absorbing high energy photons. In a tandem device, the forward processes are a combination of the n-type and p-type sides of the cell, and are shown in Figure 1.9. The cell is illuminated so that higher energy photons are absorbed at the front and lower energy photons are collected at the back. Upon illumination both dyes absorb a photon of light (1,1'). At the titanium dioxide side, the dye, D, injects an electron into the conduction band (2).

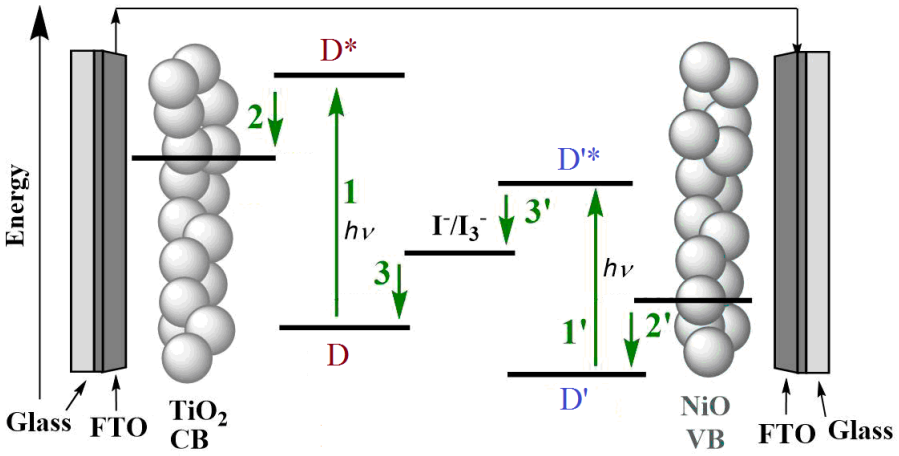

Figure 1.9: Energy level diagram of the forward processes in a tandem dye-sensitised solar cell. 1,1') Dye excitation; 2,2') charge-injection; 3,3') dye-regeneration.

This electron travels around the circuit and regenerates D' at the nickel oxide side of the cell (2'). The redox mediator shuttles charge between the two sides of the cell (3,3').

1.3.3 Energetics

The relative energy levels in a dye-sensitised solar cell determine the open-circuit voltage (V_{OC}) and the Gibbs free energies of charge-injection and regeneration, ΔG_{inj} and ΔG_{reg}. These are labelled for both titanium dioxide and nickel oxide systems in Figure 1.10.

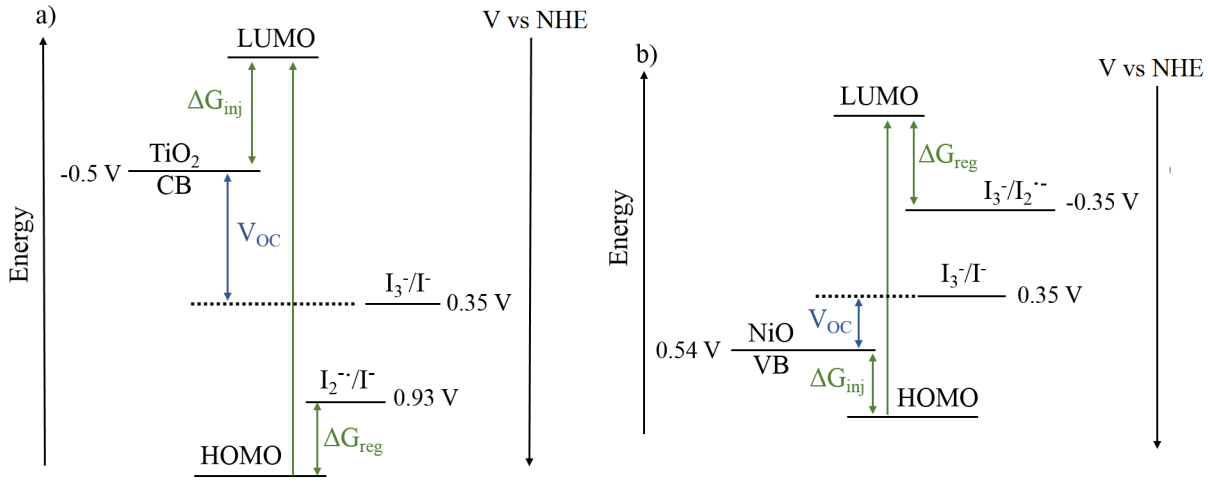

Figure 1.10: Energy level diagram of a dye-sensitised solar cell. a) n-Type TiO_2; b) p-type NiO.

The open-circuit voltage of the cell is the difference between the *quasi*-Fermi potential of

the semiconductor, $qE_{\mathrm{F,n}}$ for n-type or $qE_{\mathrm{F,p}}$ for p-type, and the redox potential of the electrolyte at the counter electrode, E_{redox}, as shown by Equations 1.16 and 1.17.[39]

$$V_{\mathrm{OC}}(n) = E_{\mathrm{redox}} - qE_{\mathrm{F,n}} \tag{1.16}$$

$$V_{\mathrm{OC}}(p) = qE_{\mathrm{F,p}} - E_{\mathrm{redox}} \tag{1.17}$$

In the dark the Fermi level of a semiconductor, $\mathrm{E_{F,dark}}$, lies between the valence band and conduction band, as shown in Figure 1.11. Under illumination the system is not in thermodynamic equilibrium due to injected electrons or holes, and in this case the Fermi level is referred to as the *quasi*-Fermi level, which lies close to the conduction band edge in an n-type system and close to the valence band edge in a p-type system.

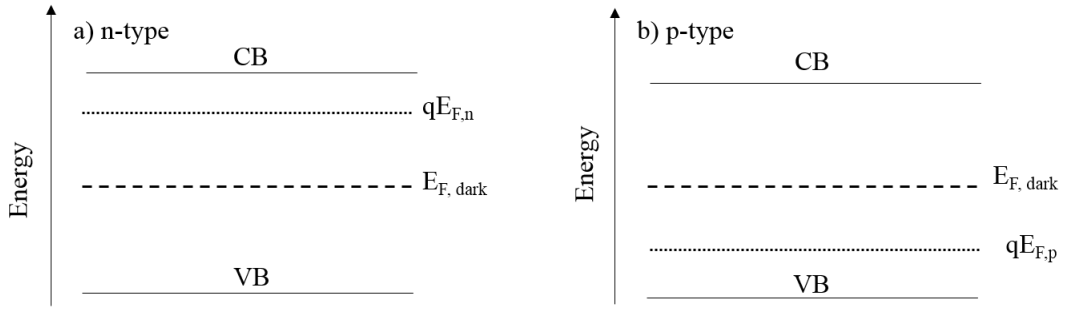

Figure 1.11: Energy level diagram of the Fermi energy in the dark ($\mathrm{E_{F,dark}}$) and the *quasi*-Fermi energy at equilibrium under illumination for an n-type semiconductor ($\mathrm{qE_{F,n}}$) and a p-type semiconductor ($\mathrm{qE_{F,p}}$).

The redox potential of the iodide/triiodide redox couple is given by the Nernst equation:

$$E_{\mathrm{redox}} = {E^{0\prime}}_{\mathrm{redox}} + \frac{RT}{2F} \ln \frac{[I_3^-]}{[I^-]^3} \tag{1.18}$$

Where ${E^{0\prime}}_{\mathrm{redox}}$ is the formal redox energy of the electrolyte, R is the gas constant, T is the temperature and F is the Faraday constant.[40] For the iodide/triiodide couple in acetonitrile solution, E_{redox} is 0.35 V vs NHE.[40,47]

Given that $\mathrm{E_{F,n}}$ for titanium dioxide is approximately -0.50 V vs NHE,[48] and $\mathrm{E_{F,p}}$ for nickel oxide is approximately 0.54 V vs NHE measured in aqueous solution at pH 7,[44,49] the maximum open-circuit voltage ($\mathrm{V_{OC}}$) is much higher for titanium dioxide cells (*ca.*

0.85 V) than for nickel oxide cells (*ca.* 0.19 V). This difference is clearly shown in Figure 1.10. In a tandem dye-sensitised solar cell the V_{OC} is the difference between the *quasi*-Fermi potentials of the n-type and p-type semiconductors, Equation 1.19. This equates to the addition of the photovoltages of the separate cells, so the maximum voltage achievable by a tandem cell using these materials is *ca.* 1.04 V.

$$V_{\mathrm{OC}}(pn) = qE_{\mathrm{F,p}} - qE_{\mathrm{F,n}} \tag{1.19}$$

In an n-type system, the driving force for injection, ΔG_{inj}, is the potential difference between the conduction band edge of the semiconductor and the excited state potential of the dye (D^+/D^*). ΔG_{reg} is the potential difference between $I_2^{-\bullet}/I^-$ (0.93 V vs NHE) and the oxidised dye species, which is estimated using the ground state oxidation potential of the dye (D/D^+). It has been reported that a ΔG_{inj} of -0.1 eV and a ΔG_{reg} of more than -0.2 eV is required for a functioning device.[24,50,51] For a p-type system ΔG_{inj} is the potential difference between the valence band edge of the semiconductor and the excited state potential of the dye (D^*/D^-) and ΔG_{reg} is the potential difference between $I_3^-/I_2^{-\bullet}$ (-0.08 V vs NHE)[52] and the ground state reduction potential of the dye (D/D^-). There is a larger driving force for charge-recombination in n-type dye-sensitised titanium dioxide systems and this process has been reported to occur in the Marcus inverted region when the reorganisation energies have been measured or estimated using density functional theory.[53–55] For dye-sensitised nickel oxide, charge-recombination occurs in the Marcus normal region and the rate of recombination increases with driving force.[56,57]

1.3.4 Kinetics

The fate of an electron in a dye-sensitised solar cell is determined by kinetic competition between productive and recombination processes. The typical lifetimes associated with these processes are given in Figure 1.12. Electron injection time, τ_{inj}, typically occurs in the range of 100 femtoseconds to 100 picoseconds for a dye|TiO_2 system[40,54,58–63] and is generally faster than the decay of the dye excited state, τ_{exc}, which is on a nanosecond to microsecond timescale. The electron transport time, τ_{tr}, is on the order of milliseconds[47,64,65] which is sufficiently fast to compete with semiconductor/electrolyte recombination processes which occur over 1-20 milliseconds for titanium dioxide with an

iodide/triiodide couple.[66–68] This is the most important loss mechanism for titanium dioxide systems as it competes with regeneration of the oxidised dye by triiodide, τ_{reg}, (100 nanoseconds to 10 microseconds).[40]

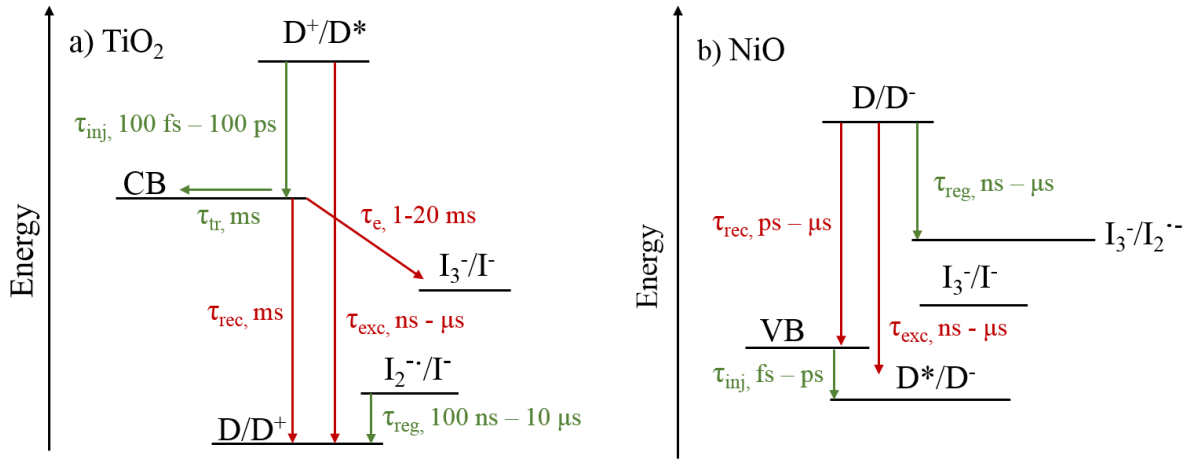

Figure 1.12: Energy level diagram of the components within a dye-sensitised solar cell with the relevant timescales of each process. a) n-Type TiO_2; b) p-type NiO.

For p-type nickel oxide systems charge-injection is a fast process, between 100 femtoseconds to 100 picoseconds.[39] However, $dye^-|NiO^+$ recombination generally occurs on a picosecond to nanosecond timescale, and is often faster than regeneration which has been reported from nanosecond up to microsecond.[69,70] Elaborate donor-acceptor dyes can give charge-separated state lifetimes up to microseconds.[57,71–73] Fast charge-recombination may be a result of the low hole mobility of nickel oxide or the electronic vacancies which exist above the valence band edge.[74] Where charge transport through titanium dioxide is believed to be diffusive, for nickel oxide a hole-hopping mechanism at the nickel oxide/electrolyte interface has been proposed, which may also promote semiconductor/electrolyte recombination.[44,73,75] This hopping mechanism for nickel oxide is believed to originate from 'trap states' caused by the presence of Ni^{3+} and Ni^{4+}.[74,76]

1.4 The field of p-type dye-sensitised solar cells

1.4.1 Nickel oxide

Despite its low hole mobility, nickel oxide is still the most extensively investigated material for p-type dye-sensitised solar cells,[39,77,78] and has been used in other solar en-

ergy applications, for example as a photoactive electrode for hydrogen production with a cobaloxime catalyst,[79] and in a tandem water splitting device with a bismuth(III) vanadate photoanode.[80] The p-type conductivity of nickel oxide is due to non-stoichiometric NiO_x which occurs in oxygen rich environments.[81] Nickel oxide has a pale green colour due to Ni^{2+} cations, which turn dark brown upon oxidation to Ni^{3+}.[82]

1.4.2 Advancements

The first p-type dye-sensitised solar cell (p-DSC) was fabricated with a nickel oxide photocathode by Lindquist and coworkers in 1999.[49] Nickel oxide films sensitised with Erythrosin B gave a modest photocurrent density (J_{SC}) and voltage (V_{OC}) under 1 sun illumination (J_{SC} = 0.23 mA cm^{-2}, V_{OC} = 83 mV). The overall power conversion efficiency (η) was 0.0076 %. This system was incorporated into the first tandem dye-sensitised solar cell with an N3|TiO_2 photoanode to give a power conversion efficiency of 0.39 %.[19] N3 is a ruthenium complex commonly used in n-type dye-sensitised solar cells. There has been extensive research into p-type dye-sensitised systems since these initial results, and a number of review articles documenting this effort have been published.[39,52,77,78] Some of the key developments will be highlighted here.

Modifying the sensitiser is the most popular area of investigation, with many different classes of molecule reported. Early work in this field by groups of Hagfeldt, Hammarström and Odobel included small molecule dyes such as a phosophorus porphyrin[83] and Coumarin 343.[84] Coumarin 343 is still used as a reference dye for p-type systems,[45,85,86] with the highest efficiency achieved by Fujihara in 2008 (η = 0.057 %).[87] However, Coumarin 343 suffers from fast charge-recombination when adsorbed on nickel oxide.[88] There are many examples of small sensitisers which generate photocurrents around 1.0 mA cm^{-2} with power conversion efficiencies around 0.01-0.04 %.[45,85,89]

A new class of p-type dye with push-pull character was introduced by Sun's group,[69,90,91] with dyes based on a triphenylamine donor group, a carboxylic acid anchoring group and a variety of acceptor groups connected to the donor by a conjugated bridge. The most successful dye, P1, contained malononitrile acceptor groups. An initial power conversion efficiency of 0.08 % was achieved for this dye,[92] which rose to 0.15 % when the film thickness was increased (J_{SC} = 5.48 mA cm^{-2}, V_{OC} = 84 mV).[86] The highest efficiency for

P1 has been achieved with an aqueous cobalt(ethylenediamine)$^{2+/3+}$ electrolyte (η = 0.4 %).[93]

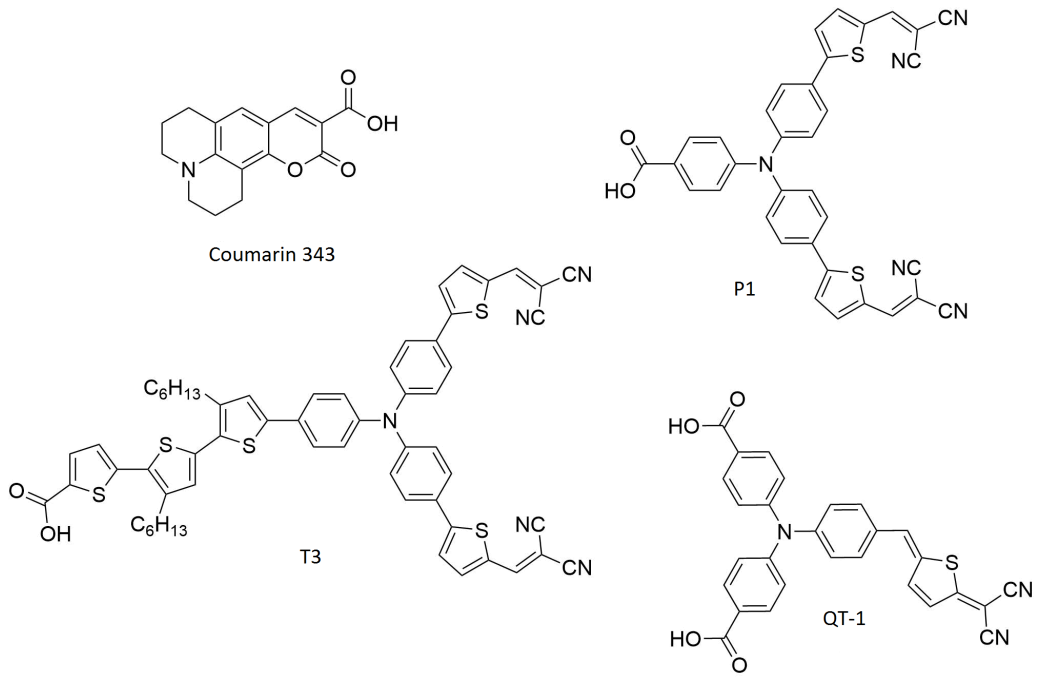

Figure 1.13: The structure of Coumarin 343 and some successful push-pull dyes.

Since the development of P1, push-pull dyes containing a triphenylamine donor group have been popular, with photocurrent densities commonly around 2.0 mA cm^{-2} and efficiencies of 0.1 %.[94–96] A push-pull dye which gives higher performance is T3 which is an analogue of P1 with an extended thiophene linker between the anchor and donor (J_{SC} = 4.01 mA cm^{-2}, V_{OC} = 144 mV, η = 0.19 %).[97] The simple dye QT-1 from the groups of Zhou and Song achieved 8.2 mA cm^{-2} (η = 0.33 %), the success of which was attributed to the small size of the dye allowing high dye-loading, and a high molar absorption coefficient.[98] Our group has reported a push-pull dye with boron dipyrromethene (bodipy) acceptor groups which performed well and had a long-lived charge-separated state on nickel oxide (J_{SC} = 3.15 mA cm^{-2}, V_{OC} = 79 mV, η = 0.08 %).[70]

Elaborate and extended structures have been shown to reduce recombination of the dye^{-}|NiO^{+} charge-separated state. Structures developed by the group of Odobel containing a peryleneimide (PI) donor group and a naphthalenediimide (NDI) acceptor have sufficiently long-lived charge-separated states to allow the use of a slower redox couple, for example cobalt$^{2+/3+}$.[99–101] Cobalt$^{2+/3+}$ redox couples have many advantages over the

iodide/triiodide redox couple, including lower absorption in the visible region, fewer photoinduced side reactions and a more negative redox potential.[22,43,102] The photovoltage of a peryleneimide-naphthalenediimide (PI-NDI) system was 350 mV (J_{SC} = 1.66 mA cm^{-2}, η = 0.20 %), the highest photovoltage reported for a p-DSC at the time.

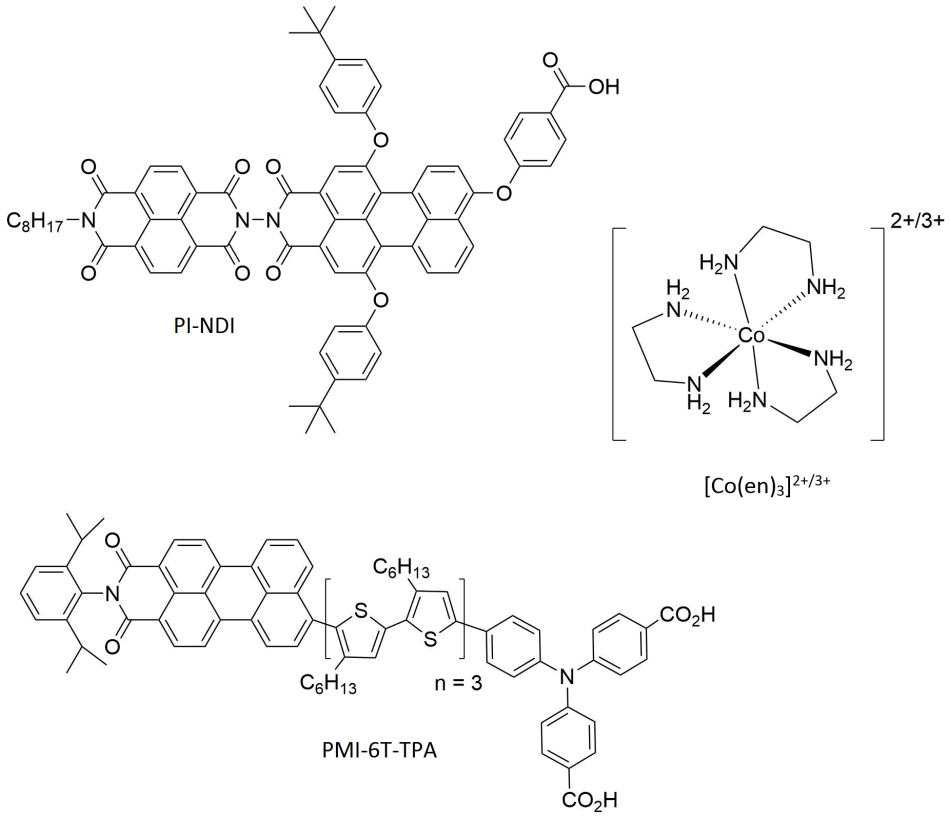

Figure 1.14: The structures of peryleneimide dyes and a cobalt(diaminoethane)$^{2+/3+}$ redox couple.

The group of Bach has developed a peryleneimide dyad (PMI-6T-TPA), which was particularly successful with a cobalt$^{2+/3+}$ diaminoethane complex (J_{SC} = 4.44 mA cm^{-2}, V_{OC} = 709 mV, η = 1.30 %).[103] PMI-6T-TPA|NiO was also used in a tandem device with N719|TiO_2 (η = 1.91 %).[46] Other classes of p-type dye include squaraines,[104–107] porphyrins,[108–110] quantum dots,[111–114] small peryleneimide dyes,[43,57,115,116] and metal complexes.[117–120] For the development of tandem dye-sensitised solar cells, absorption at the photocathode should have minimal overlap with absorption at the photoanode. There have been attempts to develop p-type dyes which absorb further into the red region, for example our group has reported a series of cationic dyes, and incorporated the most successful dye into a tandem cell.[121,122] Squaraine,[107,123] lead sulphide quantum dot[113] and diketopyrrolopyrrole[124] dyes have also shown photocurrent responses above 600 nm.

1.4.3 The charge-separated state

The fast recombination of the dye$^-$|NiO$^+$ charge-separated state is a major limitation of nickel oxide dye-sensitised solar cells. In Table 1.1, dye structures and their corresponding dye$^-$|NiO$^+$ charge-separated state lifetimes are shown for all p-type nickel oxide systems where this information was reported. Where the dyes have been tested for their performance in a solar cell, the efficiency is also given. Charge-recombination is generally believed to occur over a range of timescales due to holes present in different states in nickel oxide, so in some cases multiple lifetimes are attributed to this process.

Dye structure	τ(dye$^-$|NiO$^+$)	η (%)	ref (year)
Coumarin 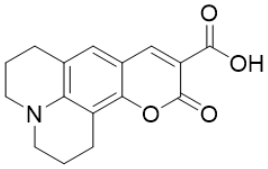	20 ps	0.057	[87, 88] (2005)
Porphyrin 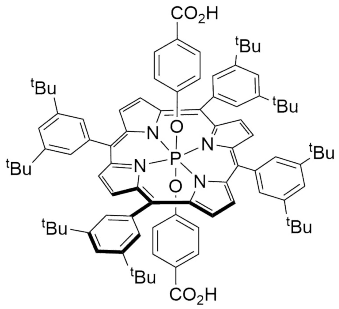	2.5 ns	-	[83] (2005)
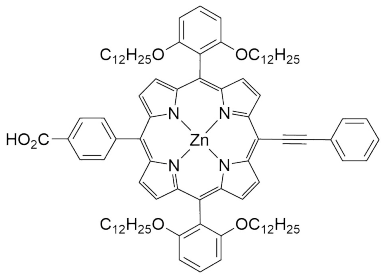	51.7 ps	0.06	[110] (2016)
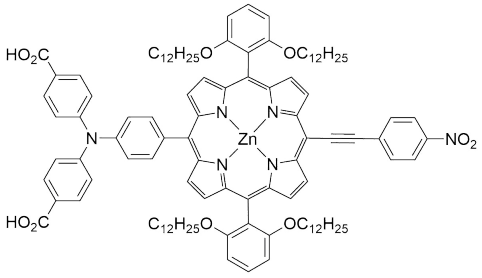	50-100 ps	0.056	[110] (2016)

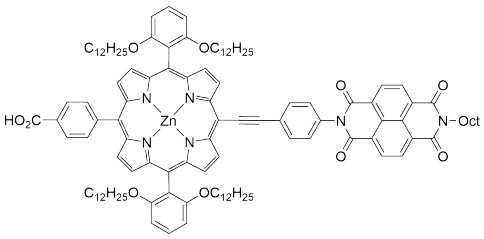	219 ps	0.012	[110] (2016)
Coordination compounds			
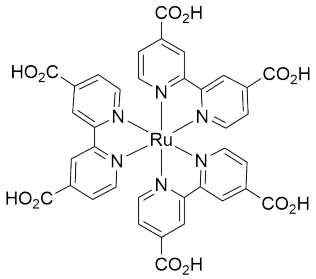	5.1 μs	0.004	[118] (2012)
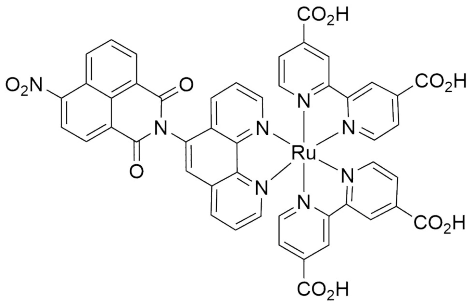	14 μs	0.006	[118] (2012)
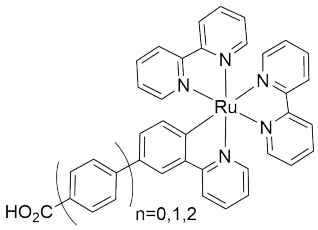	n = 0, 250 ps n = 1, 600 ps n = 2, 1.1 ns	0.009 0.033 0.051	[119] (2012)
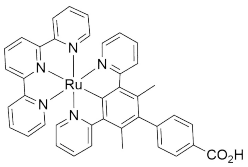	371 ps	-	[125] (2013)
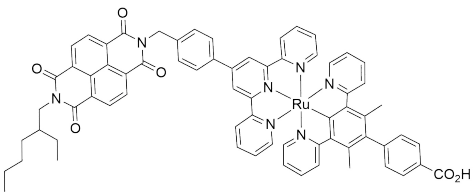	426 ps	-	[125] (2013)
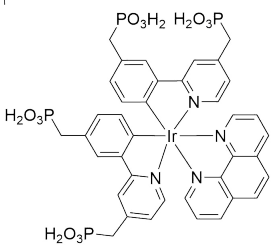	50-70 ns, 1 μs, 5-30 μs	0.021	[120] (2014)

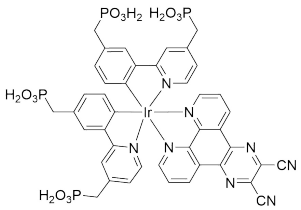	50-70 ns, 1 μs, 5-30 μs	0.068	[120] (2014)
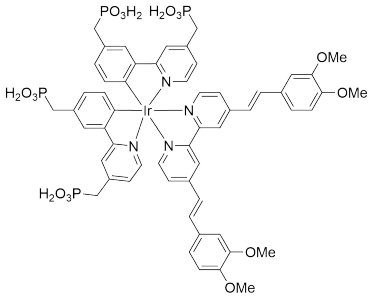	50-70 ns, 1 μs, 5-30 μs	0.061	[120] (2014)
Peryleneimide			
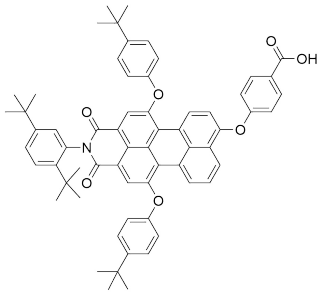	100 ps, 6.8 ns	0.046	[99–101] (2011)
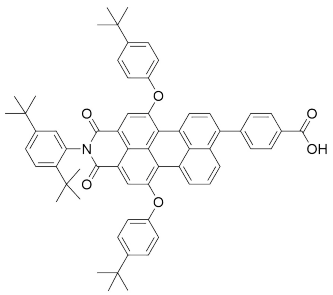	190 ps, 9.2 ns	0.043	[101] (2011)
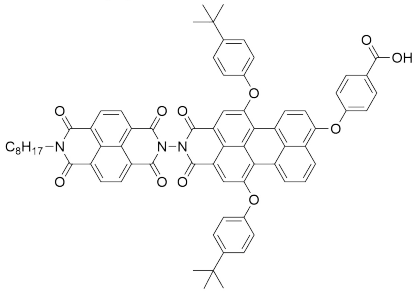	5 μs, 50 μs	0.20	[99, 101] (2011)
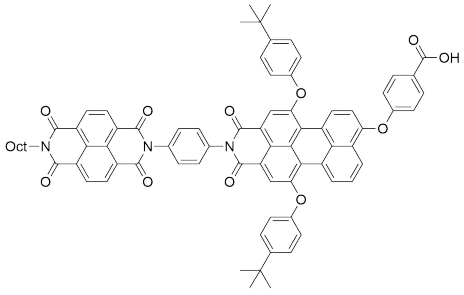	3 μs, 55 μs	0.074	[101] (2011)

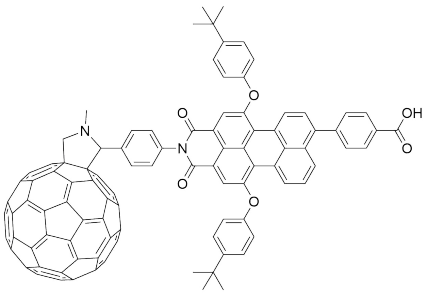	2.4 μs	0.058	[101] (2011)
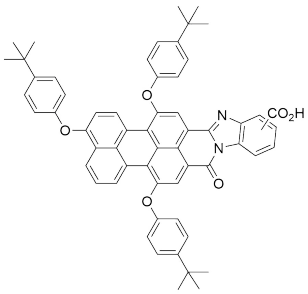	111 ps	-	[57] (2012)
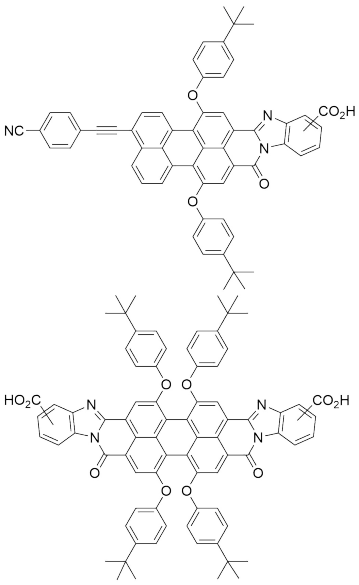	147 ps	-	[57] (2012)
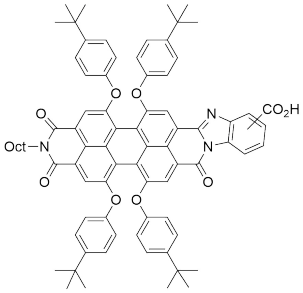	260 ps	-	[57] (2012)
Squaraine			
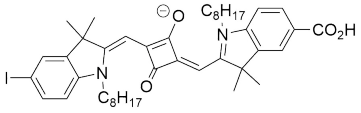	2.2 ps, 53 ps	0.034	[123] (2014)

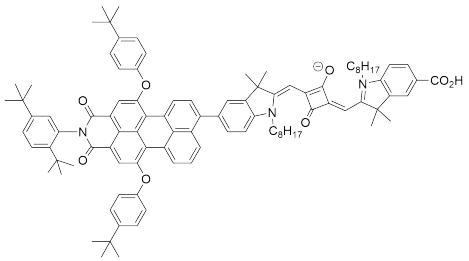	3 ps, 112 ps	0.026	[123] (2014)
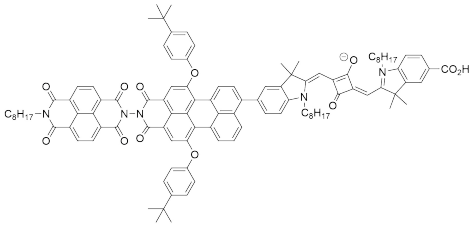	4.8 ps, 130 ps	0.083	[123] (2014)
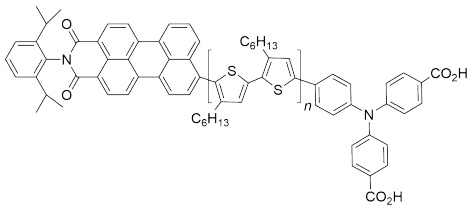	n=1: 177 ns, 1.34 μs n=2: 1.22 μs, 12.2 μs n=3: 2.54 μs, 13.6 μs	0.1 0.19 1.30 2.51	[46] (2010) [103] (2013) [126] (2015)
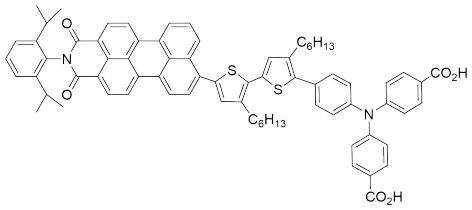	250 ns	0.04	[127] (2012)
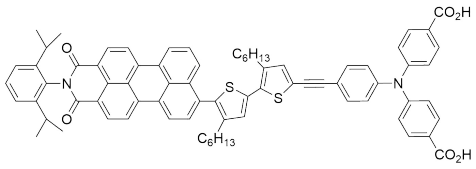	300 ns	0.10	[127] (2012)
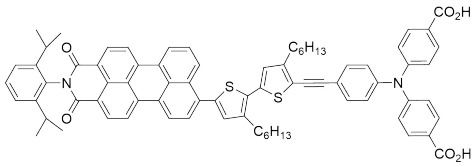	250 ns	0.05	[127] (2012)
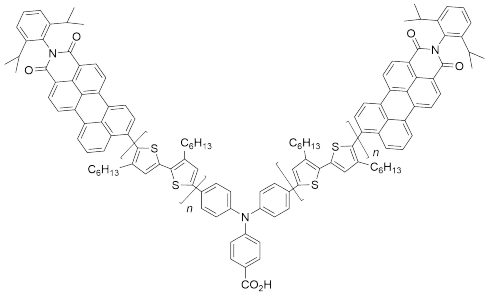	n=1: 0.37 μs n=2: 4.5 μs n=3: 13 μs	- - -	[128] (2017)

Push-pull

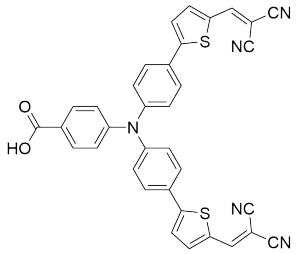

2.7 ps, 17 ps, 205 ps | 0.15 | [69] (2010) [93] (2017)

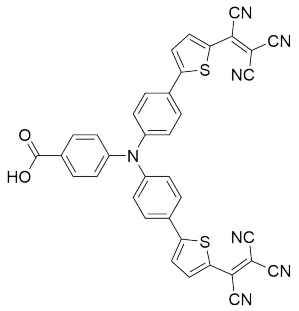

2.4 ps, 20 ps, 317 ps | 0.03 | [69] (2010)

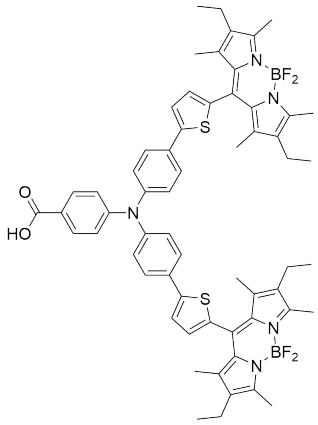

177 ns | 0.08 | [70] (2014)

Cationic

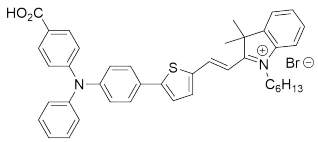

300 ps | 0.09 | [121] (2014)

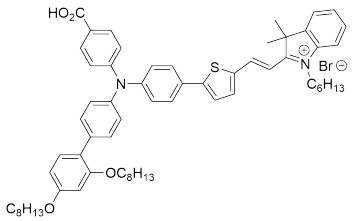

100 ps | 0.10 | [121] (2014)

Oligothiophene

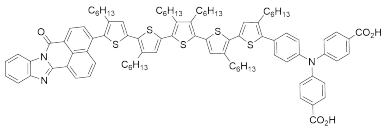

392 ps | 0.13 | [129] (2016)

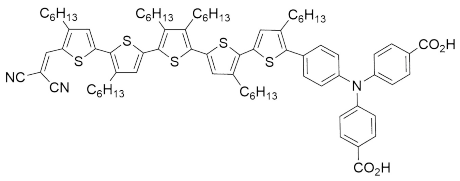	62 ps	0.10	[129] (2016)

Diketopyrrolopyrrole

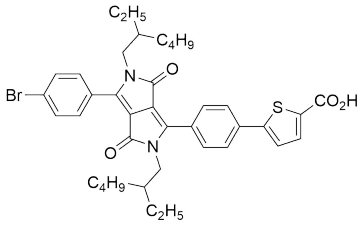	8.6 ps, 75 ps	0.03	[71, 130] (2016)
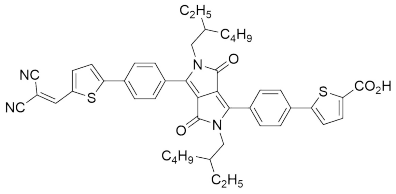	6.1 ps, 94 ps	0.07	[71, 130] (2016)
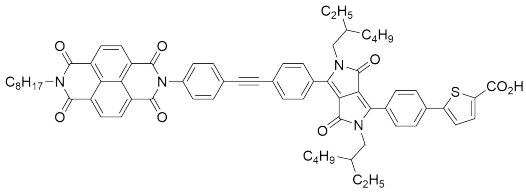	13 ps, 260 ps, 140 μs	0.09	[71, 130] (2016)
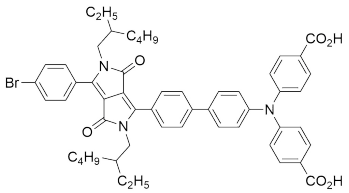	61 ps	0.063	[131] (2016)
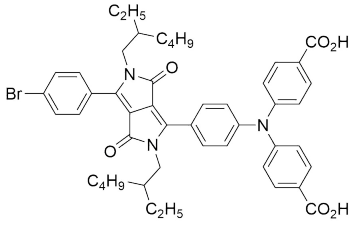	57 ps	0.04	[131] (2016)
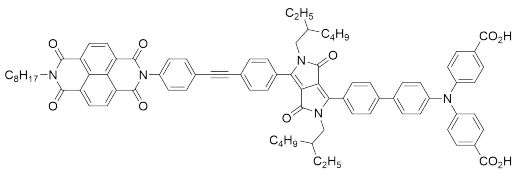	49 μs, 570 μs	0.21	[131] (2016)

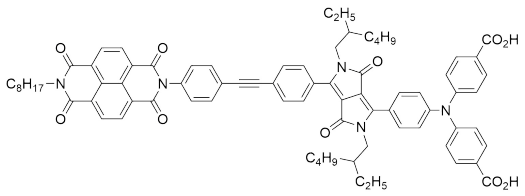	47 μs, 476 μs	0.21	[131] (2016)

Table 1.1: Structures and charge-separated state lifetimes of dyes adsorbed on nickel oxide films. When data is not given it is indicated with (-). The lifetimes of each component are given where a multi-exponential fit was used.

The charge-separated state lifetimes and efficiencies given in Table 1.1 are compared in Figure 1.15, and in general there is little correlation. However, the majority of the data shown in Figure 1.15 represents p-type dyes which achieve efficiencies of less than 0.5 %, as there are few systems which achieve over 1.0 % where the charge-separated state lifetime has been reported. Exceptions include P1 and PMI-6T-TPA, whose values are labelled in Figure 1.15.

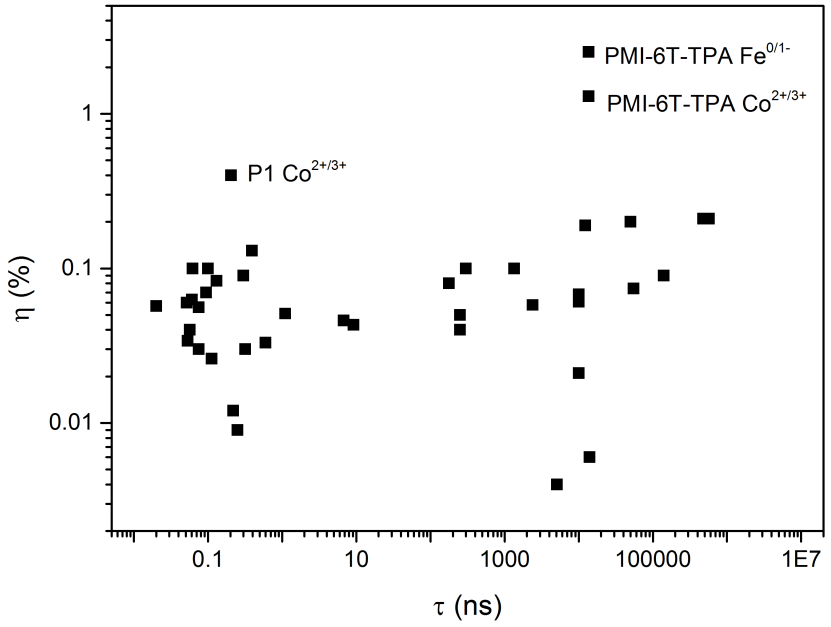

Figure 1.15: A comparison of the power conversion efficiencies (η) and corresponding charge-separated state lifetimes (τ) for the p-type dyes shown in Table 1.1. Three systems are labelled: P1 ref [93]; PMI-6T-TPA ref [103] and ref [126].

These two dyes have very different structures, P1 is a small push-pull dye and PMI-6T-TPA has a long, extended thiophene bridge with a long-lived charge-separated state, yet

the efficiencies of both are higher than average for a p-type system.

1.4.4 Measuring lifetimes

The rates of charge-injection and charge-recombination processes are commonly investigated using time-resolved spectroscopy.[65,132] For dye-sensitised titanium dioxide systems, the inhomogeneous distribution of trap states in the metal oxide film leads to a variety of recombination rates, so stretched exponential functions or multiple components are used to fit recombination kinetics.[133,134] The decay of $dye^-|NiO^+$ systems are also commonly fit with multi-exponential decay functions.[71,72,74,123,129] In this work single-point analysis is used to extract kinetic information from time-resolved spectroscopy data, and is described further in Section 2.3.2. Where multiple species or intermediates are present, a global analysis technique is used. Briefly, the full spectra are fit to multiple time components and the amplitudes of each component are plotted against the detection wavelength. This gives decay-associated difference spectra (DADS) and evolution-associated difference spectra (EADS).[135] This is especially useful for conjugated molecules which absorb broadly.

Time-resolved infrared spectroscopy is used to gain kinetic information about photoinduced dynamics by monitoring changes in bond strength following laser excitation. This technique has been used extensively to study dye|semiconductor systems,[132,136–138] and our group has observed changes in the ν(C=O) of the carboxylic anchoring group on a dye|NiO system using time-resolved infrared analysis.[121]

References

(1) Lewis, N.; Crabtree, G., *Basic Research Needs for Solar Energy Utilization: Report of the Basic Energy Sciences Workshop on Solar Energy Utilization*; US Department of Energy, Office of Basic Energy Science: Washington, DC, USA, 2005.

(2) International Energy Outlook 2017., `https://www.eia.gov/outlooks/ieo/exec_summ.php`, Accessed April 12th, 2018.

(3) Lewis, N. S. *Science* **2007**, *315*, 798–801.

(4) Crabtree, G. W.; Lewis, N. S. *Phys. Today* **2007**, *60*, 37–42.

(5) Gratzel, M. *Inorg. Chem.* **2005**, *44*, 6841–51.

(6) Harriman, A. *Philos. Trans. A Math. Phys. Eng. Sci.* **2013**, *371*, 20110415.

(7) Department for Business, Energy and Industrial Strategy. UK solar installation statistics., `https://www.gov.uk/government/statistics/solar-photovoltaics-deployment`, Accessed October 13th, 2017. Last updated 28th September, 2017.

(8) Specific (Swansea)., `http://www.specific.eu.com/`, Accessed April 13th, 2018.

(9) Green, M. A. *Energy Policy* **2000**, *28*, 989–998.

(10) Xiao, S.; Xu, S., *High-Efficiency Solar Cells: Physics, Materials, and Devices*; Springer: 2014; Chapter 1: Status and Progress of High-efficiency Silicon Solar Cells.

(11) Goetzberger, A.; Knobloch, J.; Voß, B., *Crystalline Silicon Solar Cells*; John Wiley & Sons, Ltd: 2014; Chapter 6: High Efficiency Solar Cells, pp 87–131.

(12) Green, M. A., *Practical Handbook of Photovoltaics: Fundamentals and Applications*, Second; Elsevier Science: 2012; Chapter IB-2 – High-Efficiency Silicon Solar Cell Concepts, pp 99–128.

(13) Rau, U.; Schock, H. W., *Practical Handbook of Photovoltaics: Fundamentals and Applications*, Second; Elsevier Science: 2012; Chapter IC-3: Cu(In,Ga)Se2 Thin-Film Solar Cells, pp 323–371.

(14) Bonnet, D., *Practical Handbook of Photovoltaics: Fundamentals and Applications*, Second; Elsevier Science: 2012; Chapter IC-2: CdTe Thin-Film PV Modules, pp 283–322.

(15) American Society for Testing and Materials (ASTM) Terrestrial Reference Spectra for Photovoltaic Performance Evaluation, NREL Renewable Resource Data Center., `http://rredc.nrel.gov/solar/spectra/am1.5/`, Accessed December 6th, 2017.

(16) Shockley, W.; Queisser, H. J. *J. Appl. Phys.* **1961**, *32*, 510–519.

(17) Henry, C. H. *J. Appl. Phys.* **1980**, *51*, 4494.

(18) Brown, A. S.; Green, M. A. *Physica E Low Dimens. Syst. Nanostruct.* **2002**, *14*, 96–100.

(19) He, J.; Lindström, H.; Hagfeldt, A.; Lindquist, S. E. *Sol. Energy Mater. Sol. Cells* **2000**, *62*, 265–273.

(20) Bremner, S. P.; Levy, M. Y.; Honsberg, C. B. *Prog. Photovoltaics* **2008**, *16*, 225–233.

(21) Martí, A.; Araújo, G. L. *Sol. Energy Mater. Sol. Cells* **1996**, *43*, 203–222.

(22) National Renewable Energy Laboratory Solar Cell Efficiency Chart., `https://www.nrel.gov/pv/assets/images/efficiency-chart.png`, Accessed April 25th, 2018.

(23) Kakiage, K.; Aoyama, Y.; Yano, T.; Oya, K.; Fujisawa, J.; Hanaya, M. *Chem. Commun.* **2015**, *51*, 15894–7.

(24) Hagfeldt, A.; Graetzel, M. *Chem. Rev.* **1995**, *95*, 49–68.

(25) Freitag, M.; Teuscher, J.; Saygili, Y.; Zhang, X.; Giordano, F.; Liska, P.; Hua, J.; Zakeeruddin, S. M.; Moser, J.-. E.; Grätzel, M.; Hagfeldt, A. *Nat. Photonics* **2017**, *11*, 372–378.

(26) Ito, S.; Ha, N. L.; Rothenberger, G.; Liska, P.; Comte, P.; Zakeeruddin, S. M.; Pechy, P.; Nazeeruddin, M. K.; Gratzel, M. *Chem. Commun.* **2006**, *38*, 4004–6.

(27) Brown, T. M.; De Rossi, F.; Di Giacomo, F.; Mincuzzi, G.; Zardetto, V.; Reale, A.; Di Carlo, A. *J. Mater. Chem. A* **2014**, *2*, 10788.

(28) Tributsch, H.; Calvin, M. *J. Photochem. Photobiol.* **1971**, *14*, 95–112.

(29) Kamat, P. V.; Fox, M. A. *Chem. Phys. Lett.* **1983**, *102*, 379–384.

(30) Moser, J.; Graetzel, M. *J. Am. Chem. Soc.* **1984**, *106*, 6557–6564.

(31) Matsumura, M.; Nomura, Y.; Tsubomura, H. *Bull. Chem. Soc. Jpn.* **1977**, *50*, 2533–2537.

(32) Nakao, M.; Itoh, K.; Honda, K. *J. Phys. Chem.* **1984**, *88*, 4906–4907.

(33) O'Regan, B.; Grätzel, M. *Nature* **1991**, *353*, 737–740.

(34) Snaith, H. J. *J. Phys. Chem. Lett.* **2013**, *4*, 3623–3630.

(35) Yang, W. S.; Park, B. W.; Jung, E. H.; Jeon, N. J.; Kim, Y. C.; Lee, D. U.; Shin, S. S.; Seo, J.; Kim, E. K.; Noh, J. H.; Seok, S. I. *Science* **2017**, *356*, 1376–1379.

(36) Assadi, M. K.; Bakhoda, S.; Saidur, R.; Hanaei, H. *Renew. Sust. Energ. Rev.* **2018**, *81*, 2812–2822.

(37) Correa-Baena, J. P.; Saliba, M.; Buonassisi, T.; Gratzel, M.; Abate, A.; Tress, W.; Hagfeldt, A. *Science* **2017**, *358*, 739–744.

(38) Hagfeldt, A.; Boschloo, G.; Sun, L.; Kloo, L.; Pettersson, H. *Chem. Rev.* **2010**, *110*, 6595–6663.

(39) Odobel, F.; Pellegrin, Y.; Gibson, E. A.; Hagfeldt, A.; Smeigh, A. L.; Hammarström, L. *Coord. Chem. Rev.* **2012**, *256*, 414–2423.

(40) Boschloo, G.; Hagfeldt, A. *Acc. Chem. Res.* **2009**, *42*, 1819–26.

(41) Datta, J.; Bhattacharya, A.; Kundu, K. K. *Bull. Chem. Soc. Jpn.* **1988**, *61*, 1735–1742.

(42) Richards, C. E.; Anderson, A. Y.; Martiniani, S.; Law, C.; O'Regan, B. C. *J. Phys. Chem. Lett.* **2012**, *3*, 1980–1984.

(43) Gibson, E. A.; Le Pleux, L.; Fortage, J.; Pellegrin, Y.; Blart, E.; Odobel, F.; Hagfeldt, A.; Boschloo, G. *Langmuir* **2012**, *28*, 6485–93.

(44) Zhu, H.; Hagfeldt, A.; Boschloo, G. *J. Phys. Chem. C* **2007**, *111*, 17455–17458.

(45) Nattestad, A.; Ferguson, M.; Kerr, R.; Cheng, Y. B.; Bach, U. *Nanotechnology* **2008**, *19*, 295304.

(46) Nattestad, A.; Mozer, A. J.; Fischer, M. K.; Cheng, Y. B.; Mishra, A.; Bauerle, P.; Bach, U. *Nat. Mater.* **2010**, *9*, 31–5.

(47) Hagfeldt, A.; Boschloo, G.; Sun, L.; Kloo, L.; Pettersson, H. *Chem. Rev.* **2010**, *110*, 6595–663.

(48) Gratzel, M. *Acc. Chem. Res.* **2009**, *42*, 1788–98.

(49) He, J.; Lindström, H.; Hagfeldt, A.; Lindquist, S.-E. *J. Phys. Chem. B* **1999**, *103*, 8940–8943.

(50) Feldt, S. M.; Lohse, P. W.; Kessler, F.; Nazeeruddin, M. K.; Gratzel, M.; Boschloo, G.; Hagfeldt, A. *Phys. Chem. Chem. Phys.* **2013**, *15*, 7087–97.

(51) Daeneke, T.; Mozer, A. J.; Uemura, Y.; Makuta, S.; Fekete, M.; Tachibana, Y.; Koumura, N.; Bach, U.; Spiccia, L. *J. Am. Chem. Soc.* **2012**, *134*, 16925–8.

(52) Odobel, F.; Pellegrin, Y.; Anne, F. B.; Jacquemin, D., *High-Efficiency Solar Cells: Physics, Materials, and Devices*; Springer: 2014; Chapter 8: Molecular Engineering of Efficient Dyes for p-Type Semiconductor Sensitization.

(53) Kuciauskas, D.; Freund, M. S.; Gray, H. B.; Winkler, J. R.; Lewis, N. S. *J. Phys. Chem. B* **2001**, *105*, 392–403.

(54) Ardo, S.; Meyer, G. J. *Chem. Soc. Rev.* **2009**, *38*, 115–64.

(55) Moser, J. E.; Grätzel, M. *Chem. Phys.* **1993**, *176*, 493–500.

(56) Odobel, F.; Pellegrin, Y. *J. Phys. Chem. Lett.* **2013**, *4*, 2551–2564.

(57) Smeigh, A. L.; Le Pleux, L.; Fortage, J.; Pellegrin, Y.; Blart, E.; Odobel, F.; Hammarstrom, L. *Chem. Commun.* **2012**, *48*, 678–80.

(58) Tachibana, Y.; Haque, S. A.; Mercer, I. P.; Durrant, J. R.; Klug, D. R. *J. Phys. Chem. B* **2000**, *104*, 1198–1205.

(59) Hilgendorff, M.; Sundström, V. *J. Phys. Chem. B* **1998**, *102*, 10505–10514.

(60) Wiberg, J.; Marinado, T.; Hagberg, D. P.; Sun, L.; Hagfeldt, A.; Albinsson, B. *J. Phys. Chem. C* **2009**, *113*, 3881–3886.

(61) Bartelt, A. F.; Schütz, R.; Neubauer, A.; Hannappel, T.; Eichberger, R. *J. Phys. Chem. C* **2009**, *113*, 21233–21241.

(62) Tachibana, Y.; Rubtsov, I. V.; Montanari, I.; Yoshihara, K.; Klug, D. R.; Durrant, J. R. *J. Photochem. Photobiol. A* **2001**, *142*, 215–220.

(63) Anderson, N. A.; Lian, T. *Annu. Rev. Phys. Chem.* **2005**, *56*, 491–519.

(64) Nelson, J.; Chandler, R. E. *Coord. Chem. Rev.* **2004**, *56*, 1181–1194.

(65) Pazoki, M.; Cappel, U. B.; Johansson, E. M. J.; Hagfeldt, A.; Boschloo, G. *Energy Environ. Sci.* **2017**, *10*, 672–709.

(66) Zaban, A.; Greenshtein, M.; Bisquert, J. *ChemPhysChem* **2003**, *4*, 859–64.

(67) Van de Lagemaat, J.; Park, N. G.; Frank, A. J. *J. Phys. Chem. B* **2000**, *104*, 2044–2052.

(68) O'Regan, B. C.; Bakker, K.; Kroeze, J.; Smit, H.; Sommeling, P.; Durrant, J. R. *J. Phys. Chem. B* **2006**, *110*, 17155–60.

(69) Qin, P.; Wiberg, J.; Gibson, E. A.; Linder, M.; Li, L.; Brinck, T.; Hagfeldt, A.; Albinsson, B.; Sun, L. *J. Phys. Chem. C* **2010**, *114*, 4738–4748.

(70) Lefebvre, J. F.; Sun, X. Z.; Calladine, J. A.; George, M. W.; Gibson, E. A. *Chem. Commun.* **2014**, *50*, 5258–5260.

(71) Zhang, L.; Favereau, L.; Farre, Y.; Mijangos, E.; Pellegrin, Y.; Blart, E.; Odobel, F.; Hammarstrom, L. *Phys. Chem. Chem. Phys.* **2016**, *18*, 18515–27.

(72) D'Amario, L.; Antila, L. J.; Pettersson Rimgard, B.; Boschloo, G.; Hammarström, L. *J. Phys. Chem. Lett.* **2015**, *6*, 779–783.

(73) Odobel, F.; Pellegrin, Y. *J. Phys. Chem. Lett.* **2013**, *4*, 2551–2564.

(74) Dillon, R. J.; Alibabaei, L.; Meyer, T. J.; Papanikolas, J. M. *ACS Appl. Mater. Interfaces* **2017**, *9*, 26786–26796.

(75) Lunkenheimer, P.; Loidl, A.; Ottermann, C. R.; Bange, K. *Phys. Rev. B* **1991**, *44*, 5927–5930.

(76) D'Amario, L.; Jiang, R.; Cappel, U. B.; Gibson, E. A.; Boschloo, G.; Rensmo, H.; Sun, L.; Hammarstrom, L.; Tian, H. *ACS Appl. Mater. Interfaces* **2017**, *9*, 33470–33477.

(77) Nattestad, A.; Perera, I.; Spiccia, L. *J. Photochem. Photobiol. C* **2016**, *28*, 44–71.

(78) Nikolaou, V.; Charisiadis, A.; Charalambidis, G.; Coutsolelos, A. G.; Odobel, F. *J. Mater. Chem. A* **2017**, *5*, 21077–21113.

(79) Li, L.; Duan, L.; Wen, F.; Li, C.; Wang, M.; Hagfeldt, A.; Sun, L. *Chem. Commun.* **2012**, *48*, 988–90.

(80) Tong, L.; Iwase, A.; Nattestad, A.; Bach, U.; Weidelener, M.; Götz, G.; Mishra, A.; Bäuerle, P.; Amal, R.; Wallace, G. G.; Mozer, A. J. *Energ. Environ. Sci.* **2012**, *5*, 9472–9475.

(81) Zhang, K. H.; Xi, K.; Blamire, M. G.; Egdell, R. G. *J. Phys. Condens. Matter* **2016**, *28*, 383002.

(82) Boschloo, G.; Hagfeldt, A. *J. Phys. Chem. B* **2001**, *105*, 3039–3044.

(83) Borgstrom, M.; Blart, E.; Boschloo, G.; Mukhtar, E.; Hagfeldt, A.; Hammarstrom, L.; Odobel, F. *J. Phys. Chem. B* **2005**, *109*, 22928–34.

(84) Morandeira, A.; Boschloo, G.; Hagfeldt, A.; Hammarström, L. *J. Phys. Chem. C* **2008**, *112*, 9530–9537.

(85) Mori, S.; Fukuda, S.; Sumikura, S.; Takeda, Y.; Tamaki, Y.; Suzuki, E.; Abe, T. *J. Phys. Chem. C* **2008**, *112*, 16134–16139.

(86) Li, L.; Gibson, E. A.; Qin, P.; Boschloo, G.; Gorlov, M.; Hagfeldt, A.; Sun, L. *Adv. Mater.* **2010**, *22*, 1759–62.

(87) Mizoguchi, Y.; Fujihara, S. *Electrochem. Solid State Lett.* **2008**, *11*, K78–K80.

(88) Morandeira, A.; Boschloo, G.; Hagfeldt, A.; Hammarstrom, L. *J. Phys. Chem. B* **2005**, *109*, 19403–10.

(89) Nakasa, A.; Usami, H.; Sumikura, S.; Hasegawa, S.; Koyama, T.; Suzuki, E. *Chem. Lett.* **2005**, *34*, 500–501.

(90) Qin, P.; Zhu, H.; Edvinsson, T.; Boschloo, G.; Hagfeldt, A.; Sun, L. *J. Am. Chem. Soc.* **2008**, *130*, 8570–1.

(91) Zhu, L.; Yang, H.; Zhong, C.; Li, C. M. *Chem. Asian J.* **2012**, *7*, 2791–5.

(92) Qin, P.; Linder, M.; Brinck, T.; Boschloo, G.; Hagfeldt, A.; Sun, L. *Adv. Mater.* **2009**, *21*, 2993–2996.

(93) Liu, H.; Xiang, W.; Tao, H. *J. Photochem. Photobiol. A* **2017**, *344*, 199–205.

(94) Yen, Y. S.; Chen, W. T.; Hsu, C. Y.; Chou, H. H.; Lin, J. T.; Yeh, M. C. *Org. Lett.* **2011**, *13*, 4930–3.

(95) Hsu, C.-Y.; Chen, W.-T.; Chen, Y.-C.; Wei, H.-Y.; Yen, Y.-S.; Huang, K.-C.; Ho, K.-C.; Chu, C.-W.; Lin, J. T. *Electrochim. Acta* **2012**, *66*, 210–215.

(96) Chang, C. H.; Chen, Y. C.; Hsu, C. Y.; Chou, H. H.; Lin, J. T. *Org. Lett.* **2012**, *14*, 4726–9.

(97) Zhu, L.; Yang, H. B.; Zhong, C.; Li, C. M. *Dyes Pigm.* **2014**, *105*, 97–104.

(98) Zhang, Q.-Q.; Jiang, K.-J.; Huang, J.-H.; Zhao, C.-W.; Zhang, L.-P.; Cui, X.-P.; Su, M.-J.; Yang, L.-M.; Song, Y.-L.; Zhou, X.-Q. *J. Mater. Chem. A* **2015**, *3*, 7695–7698.

(99) Gibson, E. A.; Smeigh, A. L.; Le Pleux, L.; Fortage, J.; Boschloo, G.; Blart, E.; Pellegrin, Y.; Odobel, F.; Hagfeldt, A.; Hammarstrom, L. *Angew. Chem. Int. Ed.* **2009**, *48*, 4402–5.

(100) Morandeira, A.; Fortage, J.; Edvinsson, T.; LePleux, L.; Blart, E.; Boschloo, G.; Hagfeldt, A.; Hammarstrom, L.; Odobel, F. *J. Phys. Chem. C* **2008**, *112*, 1721–1728.

(101) Le Pleux, L.; Smeigh, A. L.; Gibson, E.; Pellegrin, Y.; Blart, E.; Boschloo, G.; Hagfeldt, A.; Hammarström, L.; Odobel, F. *Energy Environ. Sci.* **2011**, *4*, 2075–2084.

(102) Gibson, E. A.; Smeigh, A. L.; Le Pleux, L.; Hammarström, L.; Odobel, F.; Boschloo, G.; Hagfeldt, A. *J. Phys. Chem. C* **2011**, *115*, 9772–9779.

(103) Powar, S.; Daeneke, T.; Ma, M. T.; Fu, D.; Duffy, N. W.; Gotz, G.; Weidelener, M.; Mishra, A.; Bauerle, P.; Spiccia, L.; Bach, U. *Angew. Chem. Int. Ed.* **2013**, *52*, 602–5.

(104) Naponiello, G.; Venditti, I.; Zardetto, V.; Saccone, D.; Di Carlo, A.; Fratoddi, I.; Barolo, C.; Dini, D. *Appl. Surf. Sci.* **2015**, *356*, 911–920.

(105) Bonomo, M.; Barbero, N.; Matteocci, F.; Carlo, A. D.; Barolo, C.; Dini, D. *J. Phys. Chem. C* **2015**, *120*, 16340–16353.

(106) Bonomo, M.; Saccone, D.; Magistris, C.; Di Carlo, A.; Barolo, C.; Dini, D. *ChemElectroChem* **2017**, *4*, 2385–2397.

(107) Langmar, O.; Saccone, D.; Amat, A.; Fantacci, S.; Viscardi, G.; Barolo, C.; Costa, R. D.; Guldi, D. M. *ChemSusChem* **2017**, *10*, 2385–2393.

(108) Tian, H.; Oscarsson, J.; Gabrielsson, E.; Eriksson, S. K.; Lindblad, R.; Xu, B.; Hao, Y.; Boschloo, G.; Johansson, E. M.; Gardner, J. M.; Hagfeldt, A.; Rensmo, H.; Sun, L. *Sci. Rep.* **2014**, *4*, 4282.

(109) Maufroy, A.; Favereau, L.; Anne, F. B.; Pellegrin, Y.; Blart, E.; Hissler, M.; Jacquemin, D.; Odobel, F. *J. Mater. Chem. A* **2015**, *3*, 3908–3917.

(110) Zhang, L.; Favereau, L.; Farre, Y.; Maufroy, A.; Pellegrin, Y.; Blart, E.; Hissler, M.; Jacquemin, D.; Odobel, F.; Hammarström, L. *RSC Adv.* **2016**, *6*, 77184–77194.

(111) Safari-Alamuti, F.; Jennings, J. R.; Hossain, M. A.; Yung, L. Y.; Wang, Q. *Phys. Chem. Chem. Phys.* **2013**, *15*, 4767–74.

(112) Kong, W.; Li, S.; Chen, Z.; Wei, C.; Li, W.; Li, T.; Yan, Y.; Jia, X.; Xu, B.; Zhang, W. *Part. Part. Syst. Charact.* **2015**, *32*, 1078–1082.

(113) Raissi, M.; Pellegrin, Y.; Jobic, S.; Boujtita, M.; Odobel, F. *Sci. Rep.* **2016**, *6*, 24908.

(114) Raissi, M.; Sajjad, M. T.; Pellegrin, Y.; Roland, T. J.; Jobic, S.; Boujtita, M.; Ruseckas, A.; Samuel, I. D. W.; Odobel, F. *Nanoscale* **2017**, *9*, 15566–15575.

(115) Feihl, S.; Costa, R. D.; Pflock, S.; Schmidt, C.; Schönamsgruber, J.; Backes, S.; Hirsch, A.; Guldi, D. M. *RSC Adv.* **2012**, *2*, 11495–11503.

(116) Bian, Z.; Tachikawa, T.; Cui, S.-C.; Fujitsuka, M.; Majima, T. *Chem. Sci.* **2012**, *3*, 370–379.

(117) Pellegrin, Y.; Le Pleux, L.; Blart, E.; Renaud, A.; Chavillon, B.; Szuwarski, N.; Boujtita, M.; Cario, L.; Jobic, S.; Jacquemin, D.; Odobel, F. *J. Photochem. Photobiol. A* **2011**, *219*, 235–242.

(118) Freys, J. C.; Gardner, J. M.; D'Amario, L.; Brown, A. M.; Hammarstrom, L. *Dalton Trans.* **2012**, *41*, 13105–11.

(119) Ji, Z.; Natu, G.; Huang, Z.; Kokhan, O.; Zhang, X.; Wu, Y. *J. Phys. Chem. C* **2012**, *116*, 16854–16863.

(120) Gennari, M.; Legalite, F.; Zhang, L.; Pellegrin, Y.; Blart, E.; Fortage, J.; Brown, A. M.; Deronzier, A.; Collomb, M. N.; Boujtita, M.; Jacquemin, D.; Hammarstrom, L.; Odobel, F. *J. Phys. Chem. Lett.* **2014**, *5*, 2254–8.

(121) Wood, C. J.; Cheng, M.; Clark, C. A.; Horvath, R.; Clark, I. P.; Hamilton, M. L.; Towrie, M.; George, M. W.; Sun, L.; Yang, X.; Gibson, E. A. *J. Phys. Chem. C* **2014**, *118*, 16536–16546.

(122) Wood, C. J.; Summers, G. H.; Gibson, E. A. *Chem. Commun.* **2015**, *51*, 3915–3918.

(123) Warnan, J.; Gardner, J.; Le Pleux, L.; Petersson, J.; Pellegrin, Y.; Blart, E.; Hammarström, L.; Odobel, F. *J. Phys. Chem. C* **2014**, *118*, 103–113.

(124) Farre, Y.; Raissi, M.; Fihey, A.; Pellegrin, Y.; Blart, E.; Jacquemin, D.; Odobel, F. *ChemSusChem* **2017**, *10*, 2618–2625.

(125) Ji, Z.; Wu, Y. *J. Phys. Chem. C* **2013**, *117*, 18315–18324.

(126) Perera, I. R.; Daeneke, T.; Makuta, S.; Yu, Z.; Tachibana, Y.; Mishra, A.; Bauerle, P.; Ohlin, C. A.; Bach, U.; Spiccia, L. *Angew. Chem. Int. Ed.* **2015**, *54*, 3758–62.

(127) Weidelener, M.; Mishra, A.; Nattestad, A.; Powar, S.; Mozer, A. J.; Mena-Osteritz, E.; Cheng, Y.-B.; Bach, U.; Bäuerle, P. *J. Mater. Chem.* **2012**, *22*, 7366–7379.

(128) Yu, Y.; Click, K. A.; Polen, S. M.; He, M.; Hadad, C. M.; Wu, Y. *J. Phys. Chem. C* **2017**, *121*, 20720–20728.

(129) Sheibani, E.; Zhang, L.; Liu, P.; Xu, B.; Mijangos, E.; Boschloo, G.; Hagfeldt, A.; Hammarström, L.; Kloo, L.; Tian, H. *RSC Adv.* **2016**, *6*, 18165–18177.

(130) Favereau, L.; Warnan, J.; Pellegrin, Y.; Blart, E.; Boujtita, M.; Jacquemin, D.; Odobel, F. *Chem. Commun.* **2013**, *49*, 8018–20.

(131) Farré, Y.; Zhang, L.; Pellegrin, Y.; Planchat, A.; Blart, E.; Boujtita, M.; Hammarström, L.; Jacquemin, D.; Odobel, F. *J. Phys. Chem. C* **2016**, *120*, 7923-7940.

(132) Ponseca C. S., J.; Chabera, P.; Uhlig, J.; Persson, P.; Sundstrom, V. *Chem. Rev.* **2017**, *117*, 10940–11024.

(133) Clifford, J. N.; Yahioglu, G.; Milgrom, L. R.; Durrant, J. R. *Chem. Commun.* **2002**, 1260–1261.

(134) Hirata, N.; Lagref, J. J.; Palomares, E. J.; Durrant, J. R.; Nazeeruddin, M. K.; Gratzel, M.; Di Censo, D. *Chem. Eur. J* **2004**, *10*, 595–602.

(135) Slavov, C.; Hartmann, H.; Wachtveitl, J. *Anal. Chem.* **2015**, *87*, 2328–36.

(136) Asbury, J. B.; Hao, E.; Wang, Y.; Ghosh, H. N.; Lian, T. *J. Phys. Chem. B* **2001**, *105*, 4545–4557.

(137) Asbury, J. B.; Hao, E.; Wang, Y.; Ghosh, H. N.; Lian, T. *J. Am. Chem. Soc.* **2008**, *130*, 5632–3.

(138) Dereka, B.; Koch, M.; Vauthey, E. *Acc. Chem. Res.* **2017**, *50*, 426–434.

Chapter 2

Theory

2.1 Solar cells

The principles behind the standard solar cell characterisation methods which have been used to evaluate the performance of dye-sensitised solar cells are presented in this chapter.

2.1.1 Current-voltage characteristics

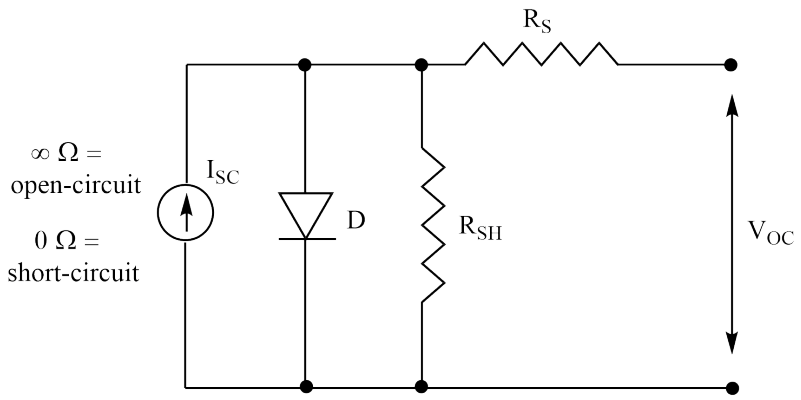

Figure 2.1: Equivalent circuit of a dye-sensitised solar cell under open-circuit and short-circuit conditions.

A dye-sensitised solar cell is commonly modelled by the equivalent circuit shown in Figure 2.1, where D is the diode element, R_S is the series resistance, R_{SH} is the shunt resistance, V_{OC} is the open-circuit voltage and I_{SC} is the short-circuit current.[1,2] The open-circuit voltage and the short-circuit current are determined by recording the current as a function of potential under AM 1.5 illumination at 1 sun intensity (1000 W/m^2) to give a current-

voltage curve which has the shape shown in Figure 2.2.[3] When the working and counter electrodes are connected with negligible resistance, the cell is at short-circuit and the current which flows through the cell is the short-circuit current (I_{SC}). When there is infinite resistance between the electrodes the cell is at open-circuit and the potential difference across the cell is the open-circuit voltage (V_{OC}). I_{SC} values are generally given in terms of the photocurrent density which accounts for the active area of the electrode (J_{SC}, A cm^{-2}). The current which flows when the device is in the dark (dark current) is due to charge transfer at the semiconductor/electrolyte interface and is therefore determined by recombination.[1,4]

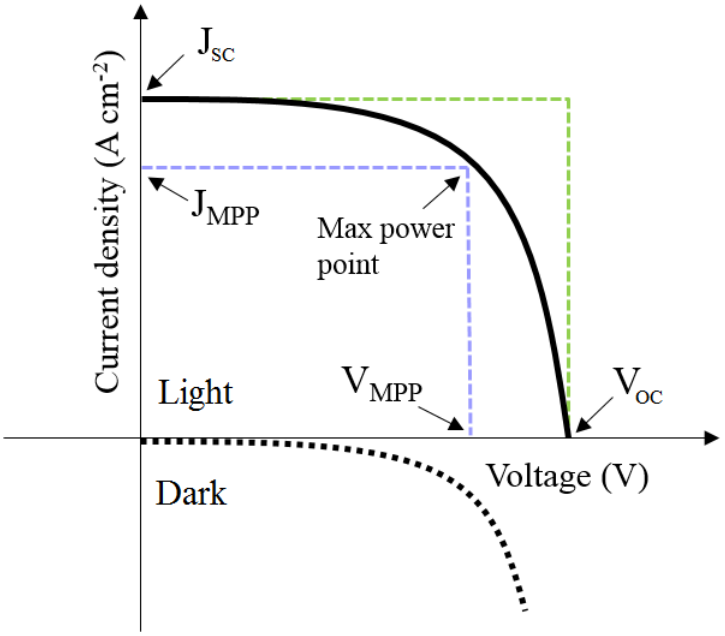

Figure 2.2: Current-voltage curve under illumination and in the dark. J_{SC} is the short-circuit current; Voc is the open-circuit voltage; J_{MPP} and V_{MPP} are the current density and voltage at the maximum power point, respectively.

The current density at the maximum power point, J_{MPP}, and the voltage at the maximum power point, V_{MPP}, are labelled in Figure 2.2. The product of J_{MPP} and V_{MPP} gives the maximum power output of the cell, P_{max}. For an ideal system the curve would be square, in which case $V_{OC} = V_{MPP}$ and $J_{SC} = J_{MPP}$. The deviation from this square is quantified by the fill factor, Equation 2.1. The magnitude of the fill factor depends on the series resistance, R_S, and the shunt resistance, R_{SH}, when a dye-sensitised solar cell is represented using the basic diode model shown in Figure 2.1, which cause the current-voltage curve

to slope as shown in Figure 2.3.[5,6] The R_{SH} is related to charge-recombination losses to the dye and electrolyte which impacts the dark current.

$$FF = \frac{J_{MPP} \times V_{MPP}}{J_{SC} \times V_{OC}} = \frac{P_{max}\ (mW cm^{-2})}{J_{SC}\ (mA\ cm^{-2}) \times V_{OC}\ (mV)} \tag{2.1}$$

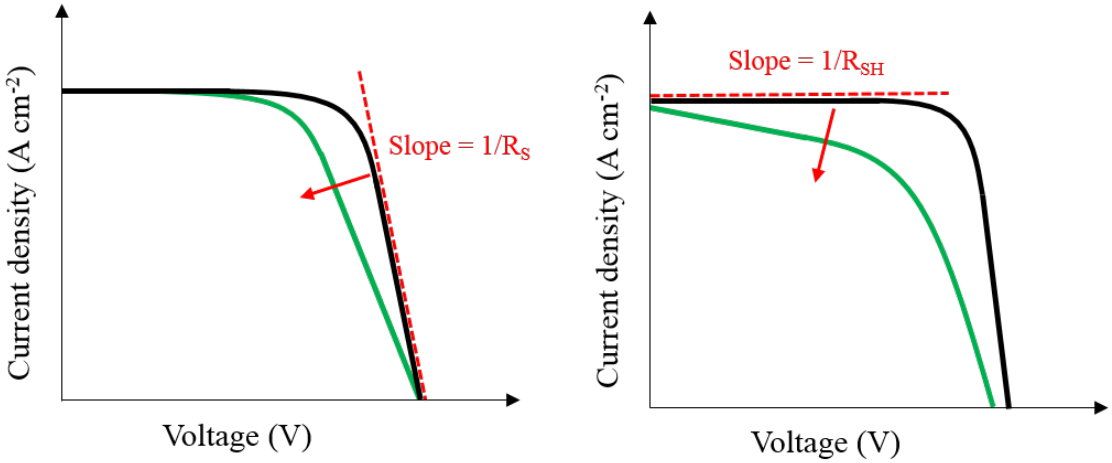

Figure 2.3: Illustration of the impact of resistance on the shape of a current-voltage curve. Left) series resistance, R_S; right) shunt resistance, R_{SH}.

The power conversion efficiency, η, is the ratio of power generated to the power of incident light (irradiance, I) as defined in Equation 2.2.

$$\eta = \frac{P_{max}}{I} = \frac{FF \times V_{OC}\ (V) \times J_{SC}\ (mA\ cm^{-2})}{100\ (mW\ cm^{-2})} \times 100(\%) \tag{2.2}$$

2.1.2 External quantum efficiency

The incident photon-to-current conversion efficiency (IPCE) is a measure of the spectral response of the cell at a given wavelength. The current response is measured as the cell is exposed to monochromatic light of varying wavelengths under short-circuit conditions. The IPCE is used to determine the performance of the sensitiser in a dye-sensitised solar cell and is defined by Equation 2.3.

$$IPCE_{\lambda} = \frac{\#\text{ collected electrons}}{\#\text{ incident photons}} \times 100\% \tag{2.3}$$

The number of collected electrons is calculated from the current density generated by the cell at a given wavelength, J_{SC}, and the charge of an electron, e , where $1C = 1A\,s$:

$$\#\text{ collected electrons } (s^{-1}\,cm^{-2}) = \frac{J_{SC}\ (A\,cm^{-2})}{e\ (C)} = \frac{J_{SC}}{1.602 \times 10^{-19}} \tag{2.4}$$

The number of incident photons is determined by measuring the power of the monochromatic light, P. The wavelength, λ, is converted to meters. The power and wavelength are converted to the number of photons per second, per area by dividing by Planck's constant, h, and the speed of light, c:

$$\#\text{ incident photons } (s^{-1}\,cm^{-2}) = \frac{P\ (W\,cm^{-2}) \times \lambda\ (nm) \times 10^{-9}}{h\ (Js)\ c\ (m\,s^{-1})} = \frac{P\lambda \times 10^{-9}}{1.986 \times 10^{-25}} \tag{2.5}$$

Combining Equations 2.3, 2.4 and 2.5 gives:

$$\begin{gathered}\frac{\#\text{ collected electrons}}{\#\text{ incident photons}} = \frac{J_{SC} \times 1.986 \times 10^{-25}}{1.602 \times 10^{-19} \times P\lambda \times 10^{-9}} \\ IPCE_{\lambda} = 1240 \times \frac{J_{SC}}{P\lambda} \times 100\%\end{gathered} \tag{2.6}$$

The IPCE is dependent on the light harvesting efficiency (LHE), the injection efficiency (η_{inj}), the regeneration efficiency (η_{reg}) and the charge collection efficiency (η_{cc}). The light harvesting efficiency is dependent on the film absorbance, $LHE = 1 - 10^{-A}$.

$$IPCE_{\lambda} = LHE \times \eta_{inj} \times \eta_{reg} \times \eta_{cc} \tag{2.7}$$

The internal quantum efficiency, (absorbed photon to current conversion efficiency, APCE) can be calculated if the absorbance of the sensitised film is known.

$$APCE = \frac{IPCE_{\lambda}}{LHE} \tag{2.8}$$

2.1.3 Charge lifetime, charge transport and charge extraction

The charge collection efficiency, η_{cc}, of a device depends on the charge transport time, τ_{tr}, and the charge lifetime, $\tau_{e/h}$ of an electron or hole:[7]

$$\eta_{cc} = 1 - \frac{\tau_{tr}}{\tau_{e/h}} \tag{2.9}$$

The charge lifetime, τ_e or τ_h, is a measure of recombination between charges in the semiconductor and species in the electrolyte.[1,8,9] Under open-circuit conditions no current flows between the two electrodes, and the voltage depends on the light intensity. Small (*ca.* 10 %) modulations of the bias light intensity are applied as changes in the voltage are monitored. As the bias light intensity is decreased the photovoltage decay represents recombination of photogenerated charges in the semiconductor with the electrolyte. Fitting the decay to an exponential function gives an average lifetime of τ_e or τ_h for a corresponding voltage.

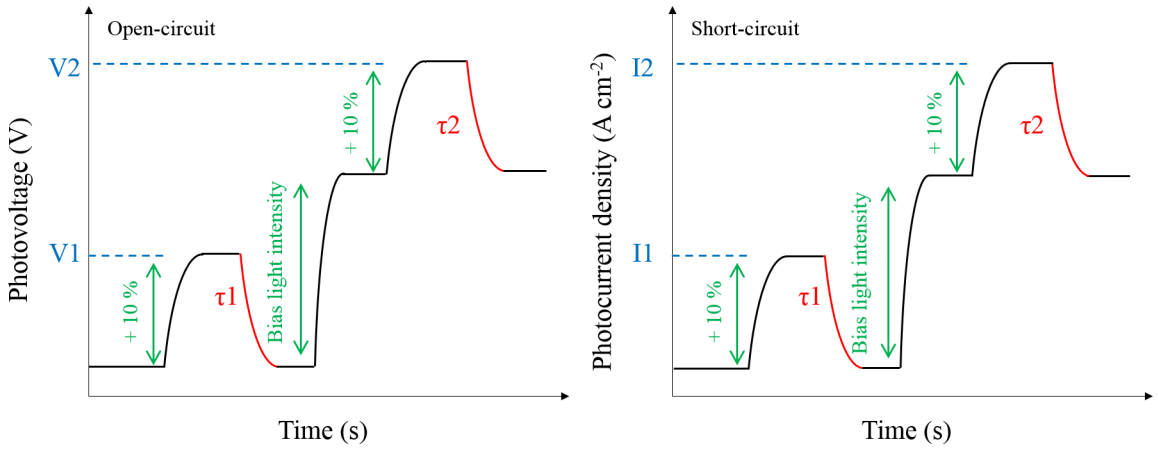

Figure 2.4: Representation of the typical shape of data recorded in a charge lifetime (left) and charge transport (right) experiment.

To determine τ_{tr}, the cell is illuminated under short-circuit conditions and the current flows as a result of injected charges in the semiconductor from the dye. The photocurrent is dependent on the light intensity. As the light is decreased by *ca.* 10 %, the photocurrent decreases and an exponential fit of the decay gives the charge transport time, τ_{tr}, for a corresponding photocurrent density.

Information about the Fermi level of electrons in the semiconductor can be determined using charge extraction experiments. According to Equation 2.10 for an n-type system and Equation 2.11 for a p-type system, the Fermi level depends on the charge concentration and density of states in the semiconductor, where $E_{F,n/p}$ is the Fermi level energy of an

n-type or p-type semiconductor, $E_{\mathrm{CB/VB}}$ is the conduction or valence band energy, $k_{\mathrm{B}}T$ is the thermal energy, $n_{\mathrm{CB/VB}}$ is the electron concentration in the conduction band or valence band and $N_{\mathrm{CB/VB}}$ is the density of states in the semiconductor.[10]

$$E_{\mathrm{F,n}} = E_{\mathrm{CB}} + k_{\mathrm{B}}T \ln(\frac{n_{\mathrm{CB}}}{N_{\mathrm{CB}}}) \tag{2.10}$$

$$E_{\mathrm{F,p}} = E_{\mathrm{VB}} + k_{\mathrm{B}}T \ln(\frac{N_{\mathrm{VB}}}{n_{\mathrm{VB}}}) \tag{2.11}$$

Charge extraction measurements are recorded under open-circuit conditions initially. At open-circuit conditions and under illumination a potential difference exists across the cell. The light is switched off for a set time and charges in the semiconductor recombine with the electrolyte. The conditions are then switched to short-circuit and a photocurrent spike corresponds to the extracted charge for the voltage at which the system was switched to short-circuit. A difference in the extracted charge at a given photovoltage for comparable devices suggests a shift in the band edge.[11] This experiment can also be combined with charge lifetime experiments to compare the charge lifetime for a given charge density. Further experimental information is given in the Experimental Chapter, Section 3.2.4.

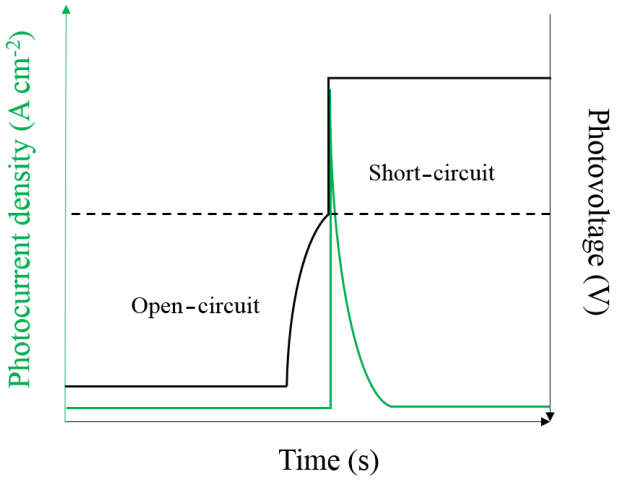

Figure 2.5: Representation of the typical shape of data recorded in a charge extraction experiment.

2.2 Electrochemistry

The oxidation and reduction potentials of dyes in a solution of supporting electrolyte are determined using cyclic voltammetry and differential pulse voltammetry. In a three electrode setup a potential is applied at the working electrode relative to a reference electrode, and current flows between the working and counter electrodes through a solution of supporting electrolyte containing the analyte. The redox potential of species at the working electrode is given by the Nernst equation:[1]

$$E = {E^{0'}}_{\text{redox}} - k_{\text{B}}T \ln(\frac{C_{\text{ox}}}{C_{\text{red}}}) \tag{2.12}$$

Where E is the electrode potential, ${E^{0'}}_{\text{redox}}$ is the redox formal energy, k_{B} and T are the Boltzmann constant and temperature. C_{ox} and C_{red} are the concentrations of oxidised and reduced species, respectively. The current is recorded as the applied voltage is scanned across a potential range in the forward and reverse directions to give a cyclic voltammogram, shown in Figure 2.6.

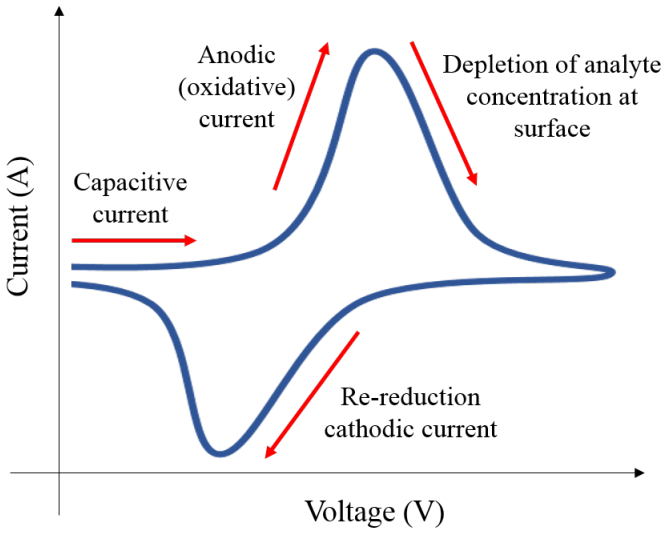

Figure 2.6: Representation of the typical shape of a cyclic voltammogram of a reversible process. E_{PA} and E_{PC} are the peak potentials of anodic and cathodic current, respectively; ΔE_P is the difference between E_{PA} and E_{PC}.

When scanning from positive to negative, capacitive current flows until ${E^{0'}}_{\text{redox}}$ is reached and reduction begins. The cathodic current increases until the surface concentration of

the species at the electrode drops. In the case of a reversible reduction, the backward scan will cause the species to be re-oxidised and anodic current will flow.

For an organic molecule the oxidation potential determined from cyclic voltammetry is the potential at which an electron is removed from the HOMO level, and the reduction potential is the potential at which an electron is accepted by the LUMO level. From the cyclic voltammogram of oxidative and reductive processes, the HOMO-LUMO energy can be estimated. Typically this is used in conjunction with visible absorption and emission spectroscopy to give an estimate of the excited state energy.

2.3 Spectroscopic techniques

2.3.1 Steady state spectroscopy

Ultraviolet-visible spectroscopy probes valence electron transitions. The wavelength of absorption is a measure of the energy separation between electronic states, with accompanying changes in vibrational and rotational structure causing a broad absorption peak. The solar spectrum has maximum irradiance in the visible region so materials which have energy transitions between 1.4 eV to 4.0 eV absorb in this region. Transitions corresponding to this energy range are from p, d and π orbitals.

The molar absorption coefficient (ε, dm^3 mol^{-1} cm^{-1}) of a molecule gives a measure of how well the molecule absorbs light, and is defined by the Beer-Lambert Law:

$$log_{10}\frac{I_0}{I} = \varepsilon \times c \times l \tag{2.13}$$

Where I_0 and I are the intensities of incident and transmitted light, respectively. ε is the molar absorption coefficient, c is the concentration of the sample in solution, and l is the path length of the sample.

Fluorescence spectroscopy is used to evaluate the radiative decay process of photogenerated singlet excited states,[1,12] and this process is labelled on the Jablonksi diagram in Figure 2.7. The energy where the absorption and emission spectra intersect is the $E_{0\text{-}0}$ energy, which is the energy difference between the S_0 ground state and the S_1 excited state. This gives an estimate of the HOMO-LUMO energy transition.

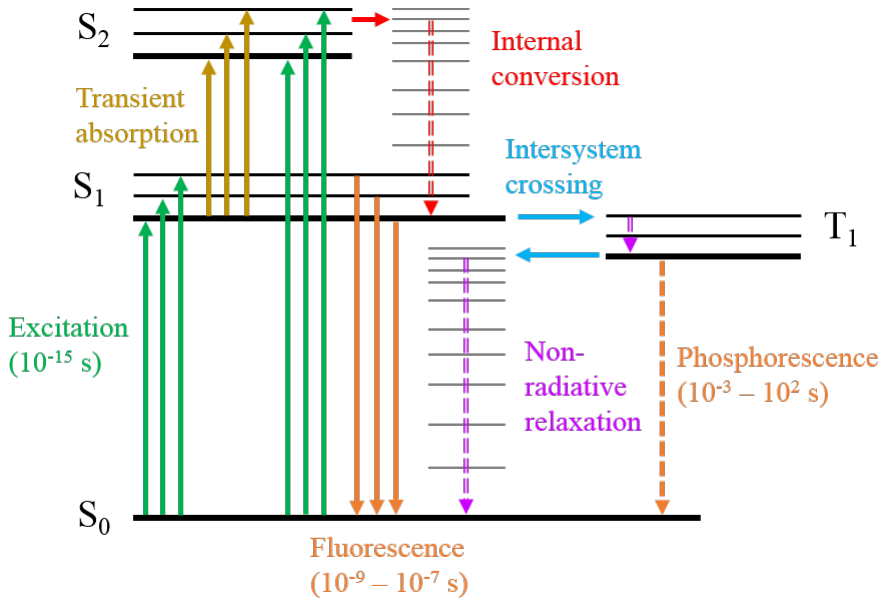

Figure 2.7: An example Jablonski diagram, S_0 is the ground state, S_1 and S_2 are excited singlet states. T_1 is an excited triplet state.

The quantum yield of fluorescence (Φ_F) is the ratio of photons emitted as fluorescence to photons absorbed. This is determined by comparing the integration of the fluorescence spectrum of a sample with unknown quantum yield to that of a reference sample with known quantum yield.

2.3.2 Time-resolved spectroscopy

Time-resolved spectroscopic techniques are commonly used for the analysis of dye-sensitised films,[1,13,14] and involve monitoring the evolution and decay of short-lived species which have been generated by a laser pulse. Samples are excited with a short laser pulse and visible (transient absorption) or infrared (time-resolved infrared) spectra are recorded at various time delays after excitation. The excitation process is labelled in Figure 2.7. Transient species decay to the ground state via a radiative or non-radiative process which can include the formation of charge-transfer intermediates. In this work these techniques are used to monitor intramolecular charge transfer processes in solution and the formation of a charge-separated state on a dye|semiconductor system, which occur on the picosecond to nanosecond timescale. Figure 2.8 shows the general setup of a time-resolved spectroscopy experiment. The wavelength of the excitation (pump) beam is usually in the visible re-

gion. The probe beam is a white light beam for transient absorption or infrared beam for time-resolved infrared spectroscopy. The delay time between the pump pulse and the probe pulse is varied.

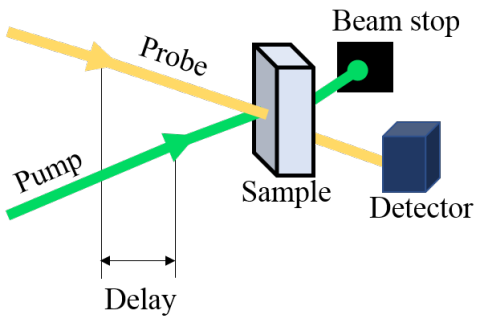

Figure 2.8: The main components of a time-resolved spectroscopy setup.

The information is presented as the absorption change over time for a specific wavelength, or the absorption change for the measured spectral range at a specific time delay. The decay of transient species can be fit using single-point or global analysis. For single-point analysis the exponential decay is fit for a given wavelength. Where there are multiple time components associated with the decay, multi-exponential fits are used. In some cases the components of a multi-exponential fit are averaged with a fractional amplitude weighting, where A is the amplitude for a given time component, τ:

$$\tau_{\mathrm{Av}} = (A_1 \times \tau_1) + (A_2 \times \tau_2)..... \tag{2.14}$$

Global analysis is used to extract the spectra of the transient species associated with each time component where multiple species are present.[15–18] Briefly, a model function for each detection wavelength is constructed, with a number of starting lifetime values to calculate each of the basic functions. The values are then optimised iteratively to obtain a fit.[19] The amplitudes of each function are plotted against the detection wavelength to give decay-associated difference spectra (DADS). Evolution-associated difference spectra (EADS) are also generated and represent the spectral evolution for each time component.

2.3.3 Spectroelectrochemistry

Intramolecular charge-separated states or dye|semiconductor charge-transfer intermediates contain species which have partial charges, and are observed in time-resolved spectroscopy experiments. To identify the nature of these species, oxidation and reduction of a sample is performed electrochemically whilst visible or infrared absorption spectra are taken. This requires an infrared or optically transparent cell which contains the sample in a supporting electrolyte solution, which is placed in the path of a spectrometer. Reference, working and counter electrodes within the cell are connected to a potentiostat. As a potential is applied and the reduced or oxidised species are generated, a series of spectra are taken.

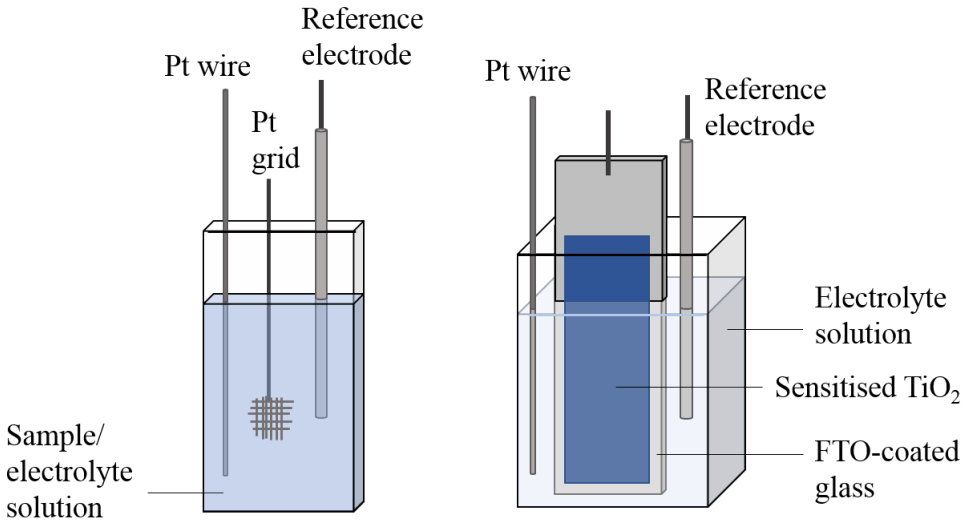

Figure 2.9: Spectroelectrochemical setup for solution (left) and film (right) experiments.

Alternatively a sensitised metal oxide film can be used as the working electrode, for example titanium dioxide. This requires a smaller amount of material. When a potential is applied, charge is passed through the metal oxide to the sensitiser which is oxidised or reduced.

References

(1) Pazoki, M.; Cappel, U. B.; Johansson, E. M. J.; Hagfeldt, A.; Boschloo, G. *Energy Environ. Sci.* **2017**, *10*, 672–709.

(2) Yong, V.; Ho, S.-T.; Chang, R. P. H. *Appl. Phys. Lett.* **2008**, *92*, 143506.

(3) Bard, A. J.; Faulkner, L. R., *Electrochemical Methods: Fundamentals and Applications*, Second; John Wiley & Sons, Inc: 2001.

(4) Gibson, E. A.; Hagfeldt, A., *Energy Materials*; John Wiley & Sons, Inc: 2011; Chapter 3: Solar Energy Materials.

(5) Halme, J.; Vahermaa, P.; Miettunen, K.; Lund, P. *Adv. Mater.* **2010**, *22*, E210–34.

(6) Huang, Z.; Natu, G.; Ji, Z.; He, M.; Yu, M.; Wu, Y. *J. Phys. Chem. C* **2012**, *116*, 26239–26246.

(7) Zhu, H.; Hagfeldt, A.; Boschloo, G. *J. Phys. Chem. C* **2007**, *111*, 17455–17458.

(8) Hagfeldt, A.; Boschloo, G.; Sun, L.; Kloo, L.; Pettersson, H. *Chem. Rev.* **2010**, *110*, 6595–6663.

(9) Duffy, N. W.; Peter, L. M.; Rajapakse, R. M. G.; Wijayantha, K. G. U. *Electrochem. Commun.* **2000**, *2*, 658–662.

(10) Hagfeldt, A.; Cappel, U. B.; Boschloo, G.; Sun, L.; Kloo, L.; Pettersson, H.; Gibson, E. A., *Solar Cells: Materials, Manufacture and Operation*, Second; Elsevier Ltd.: 2012; Chapter ID-1: Dye-Sensitized Photoelectrochemical Cells, pp 479–542.

(11) Kopidakis, N.; Neale, N. R.; Frank, A. J. *J. Phys. Chem. B* **2006**, *110*, 12485–9.

(12) Lakowicz, J. R., *Principles of Fluorescence Spectroscopy*; Springer: 2006; Chapter 1: Introduction to Fluorescence.

(13) Ponseca C. S., J.; Chabera, P.; Uhlig, J.; Persson, P.; Sundstrom, V. *Chem. Rev.* **2017**, *117*, 10940–11024.

(14) Berera, R.; van Grondelle, R.; Kennis, J. T. *Photosynth. Res.* **2009**, *101*, 105–18.

(15) Dillon, R. J.; Alibabaei, L.; Meyer, T. J.; Papanikolas, J. M. *ACS Appl. Mater. Interfaces* **2017**, *9*, 26786–26796.

(16) Lee, S. H.; Chan, C. T.; Wong, K. M.; Lam, W. H.; Kwok, W. M.; Yam, V. W. *J. Am. Chem. Soc.* **2014**, *136*, 10041–52.

(17) Le Pleux, L.; Smeigh, A. L.; Gibson, E.; Pellegrin, Y.; Blart, E.; Boschloo, G.; Hagfeldt, A.; Hammarström, L.; Odobel, F. *Energy Environ. Sci.* **2011**, *4*, 2075–2084.

(18) Farré, Y.; Zhang, L.; Pellegrin, Y.; Planchat, A.; Blart, E.; Boujtita, M.; Hammarström, L.; Jacquemin, D.; Odobel, F. *J. Phys. Chem. C* **2016**, *120*, 7923-7940.

(19) Slavov, C.; Hartmann, H.; Wachtveitl, J. *Anal. Chem.* **2015**, *87*, 2328–36.

Chapter 3

Experimental

3.1 General methods

Anhydrous solvents were used for electrolyte solutions, dye baths, electrochemical measurements, spectroelectrochemical measurements, time-resolved spectroscopy and synthesis. Anhydrous acetonitrile was purchased from Fisher Scientific (99.9 %, over molecular sieves). Dichloromethane was distilled over calcium hydride. Deuterated solvents were purchased from Fluorochem. All other reagents and chemicals were purchased from Sigma Aldrich unless stated otherwise.

3.2 Solar cells

3.2.1 Electrodes

Nickel oxide working electrode

Nanostructured nickel oxide films were prepared from a nickel solution according to a modified literature procedure.[1] Anhydrous nickel(II) chloride (1 g, Alfa Aesar) was dissolved in ethanol (7.6 mL) and distilled water (6 mL). A templating polymer (Pluronic® F108, poly(ethylene glycol)-block-poly(propylene glycol)-block-poly(ethylene glycol)) (1 g) was added and the solution was stirred overnight. The solution was left in the fridge to prevent evaporation of the solvent for 3-4 weeks, and centrifuged immediately prior to use. Solutions kept at room temperature became cloudy more quickly than those kept in

the fridge.

Fluorine-doped tin oxide (FTO) coated glass (Pilkington, TEC15, resistance 15 Ω/sq) was used as a conductive substrate for the working electrode. The glass was cleaned by immersing in soapy water (5 minutes, ultrasonic bath), 0.1 M hydrochloric acid in ethanol (5 minutes, ultrasonic bath) and ethanol (15 minutes, ultrasonic bath). The glass was then dried and a 0.25 cm^2 circular mask of Scotch® Magic™ tape was applied. A drop of the nickel solution was spread over the masked substrate using the side of a glass pipette. The mask was then removed and the film was sintered in a muffle furnace (Nabertherm) at 450 °C for 30 minutes with a ramp time of 30 minutes. The sintering establishes electrical contact between the nanoparticles.

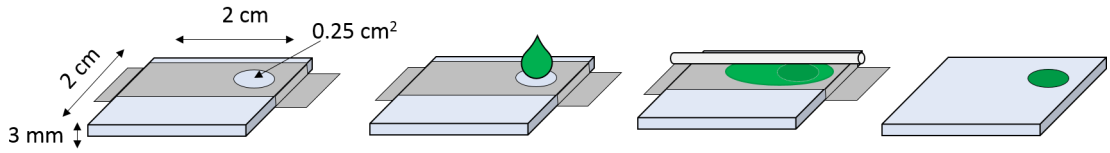

Figure 3.1: Representation of doctor-blading technique. From left to right, glass is masked; a drop of solution is applied; the solution is spread over the mask; the mask is removed.

When cool, subsequent layers of solution were applied and the films were sintered after each layer until the films were *ca.* 1.1 micrometer thick, which was usually after 4 applications of solution. Film thicknesses were measured on a Dektak^{3}ST profiler. The films were sensitised by immersion in a 0.3 mM solution of dye for at least 12 hours and assembled into dye-sensitised solar cells or used for spectroscopic analysis.

Titanium dioxide working electrode

FTO coated glass (TEC15) was cleaned as described for nickel oxide working electrodes. The glass was treated with a compact layer of titanium dioxide to adhere the nanoparticles to the substrate and to block FTO|electrolyte recombination. The addition of this blocking layer has been reported to increase the photovoltage of titanium dioxide dye-sensitised solar cells.[2,3] The glass was immersed in a 70 mM solution of titanium tetrachloride in water, which was prepared by careful dilution of liquid titanium tetrachloride to obtain a stock solution of 2 M concentration. The immersed glass was heated to 70 °C for 30 minutes. When cool, the glass was rinsed with water and ethanol and sintered at 450 °C

in a muffle furnace for 30 minutes. A layer of paste containing 20 nm titanium dioxide anatase particles (Dyesol/Greatcell Solar Limited, 18NR-T) was spread over the substrate by doctor-blading method, dried at 125 °C on a hotplate and a second layer was applied and dried. A scattering layer containing large titanium dioxide particles (Solaronix, Ti-Nanoxide R/SP) was applied and the films were sintered at 500 °C for 30 minutes with a ramp time of 30 minutes. A second titanium dioxide blocking layer was applied to the films as before to increase the surface roughness of the film, aid dye adsorption and increase the photocurrent.[2,4] The films were sensitised as described for the nickel oxide electrodes, by immersion in a dye bath containing 0.3 mM dye for at least 12 hours.

Counter electrode

Platinum counter electrodes were fabricated from FTO coated glass (Pilkington, TEC8, resistance 8 Ω/sq). A 1 mm hole was first drilled into a corner of the glass which was then cleaned by the same method as for the working electrodes. 1 μL/mm of chloroplatinic acid in ethanol (H_2PtCl_6, 4.8 mM) was dropped onto each electrode. The electrodes were then heated to 400 °C for 15 minutes.

3.2.2 Redox couples

Iodide/triiodide For nickel oxide dye-sensitised solar cells a typical electrolyte contained 0.1 M iodine (0.025 g) and 1.0 M lithium iodide (0.134 g) dissolved in acetonitrile (1 mL). For titanium dioxide solar cells additives were also added and electrolyte solutions consisted of 0.01 M iodine (0.0038 g), 0.6 M tetrabutylammonium iodide (0.22 g), 0.5 M *tert*-butylpyridine (0.08 mL) and 0.1 M guanidinium thiocyanate (0.012 g) dissolved in acetonitrile (1 mL). Electrolyte solutions were prepared on the day of solar cell assembly.

[Co(II)(^{t}bbpy)$_3$ClO$_4$)$_2$] $CoCl_2.6H_2O$ (0.246 g, 1 mmol, 1.1 eq.) and 4,4'-di-*tert*-butyl-2,2'-dipyridyl (0.732 g, 2.73 mmol, 3 eq.) were suspended in a 5:1 H_2O:MeOH mixture and heated with stirring for 30 min. The solution turned dark brown over time. An excess of $LiClO_4$ in methanol was added and the solution was stirred for 30 min as a precipitate formed. The precipitate was washed with methanol and diethyl ether and dried, giving [Co(^{t}bbpy)$_3$ClO$_4$)$_2$] in 66 % yield (700 mg).

[Co(III)(^{t}bbpy)$_3$ClO$_4$)$_3$] $CoCl_2.6H_2O$ (0.225 g, 0.95 mmol, 1.1 eq.) and 4,4'-di-*tert*-

butyl-2,2'-dipyridyl (0.698 g, 2.6 mmol, 3 eq.) were suspended in a 5:1 H_2O:MeOH mixture and the solution was heated to near boiling with stirring for 30 min. H_2O_2 (0.82 mL, 9.5 mmol, 11 eq.) was added dropwise and stirred for 20 min. HCl (37 %) was added dropwise until the solution was pale yellow. Water was added until the solution became clear. The solution was cooled to room temperature and an excess of $LiClO_4$ in 1:1 H_2O:MeOH was added. The reaction was stirred for 1 hr and the precipitate was filtered and washed with H_2O and diethyl ether, giving the product in 91 % yield (1.0 g).

3.2.3 Cell assembly

Sensitised titanium dioxide and nickel oxide working electrodes were sandwiched to platinised counter electrodes using a thermoplastic frame (Surlyn, 60 μm). The electrolyte was introduced through the hole in the counter electrode using a vacuum-backfilling method. The hole was sealed with a square of thermoplastic and a glass cover slip. Improvements to the electrical contact were made by painting the exposed faces of working and counter electrodes with silver conductive paint (RS Components).

3.2.4 Current-voltage characteristics

Current-voltage curves were measured using an Ivium CompactStat potentiostat under simulated sunlight from an Oriel VeraSol-2 Class AAA LED solar simulator, with an intensity of 1000 W m^{-2}. To determine the photocurrent density and photovoltage for a particular system, an average of three solar cells were fabricated and tested.

Charge lifetime and charge transport experiments were carried out over a range of bias light intensities with a 10 % modulation, using an Ivium Modulight light source. An Ivium CompactStat potentiostat was programmed to modulate the light intensity and to monitor the changes in current and voltage. For charge lifetime experiments the cell was illuminated under open-circuit conditions and the voltage decay was recorded as the light intensity was modulated. For charge transport experiments the cell was illuminated at short-circuit and the current response was monitored. Voltage or current decays were fit to a single exponential function to give the lifetime for a corresponding current or voltage. Charge extraction experiments were carried out using the same equipment. The cell was illuminated at open-circuit until a constant voltage was reached. The light source was

then switched off and the voltage was allowed to decay over a range of time intervals, between 0.01 s and 5 s. The system was then switched to short-circuit and the current decay over 10 s was integrated to give the charge.

3.2.5 External quantum efficiency

Incident photon-to-current conversion efficiency (IPCE) spectra were recorded using monochromatic light from an Oriel 300 Watt Xenon lamp with an AM 1.5 filter and a Cornerstone monochromator. The system was calibrated against a certified silicon photodiode. A dye-sensitised solar cell was placed in the path of monochromatic light and the current response was measured using an Ivium CompactStat for wavelengths between 300 nm to 700 nm.

3.3 Synthesis

FAB2 (4-(di(1H-pyrrol-2-yl)methyl)benzonitrile)

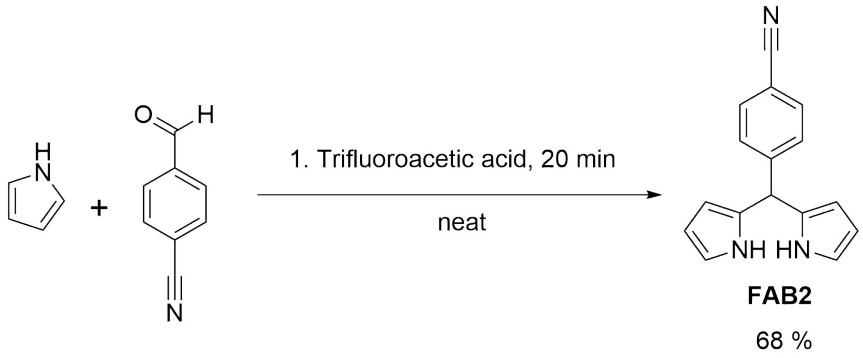

A three-necked round-bottomed flask was purged with nitrogen. Pyrrole (9 mL, 0.13 mol, 25 eq.) was added and nitrogen was bubbled through the liquid. 4-Cyanobenzaldehyde (0.68 g, 5.2 mmol, 1 eq.) was added and stirred for 10 minutes. Trifluoroacetic acid (40 μL, 52 mmol, 10 eq.) was added dropwise and stirred for a further 20 min. The reaction was quenched with aqueous sodium hydroxide (40 mL, 2 M) and diluted with ethyl acetate. The organic layer was washed with water and dried over magnesium sulphate. After filtration, the solvent was removed by rotary evaporation. The residue was taken up in warm ethanol and water was added to yield a cream-coloured precipitate in 68 % yield (875 mg). In chlorinated solvents the sample degrades over about 12 hours, visibly turning

brown. The product was characterised by ^{1}H and ^{13}C NMR spectroscopy. The full spectra are given in the Appendix, Figures A.6 and A.7.

^{1}H ($CDCl_3$; 300 MHz) 8.03-7.94 (2H, s, br, NH), 7.60 (2H, d, J = 8.4 Hz, phenyl) 7.31 (2H, d, J = 8.1 Hz, phenyl) 6.74 (2H, m, pyrrole), 6.16 (2H, dd, J = 5.89, 2.84 Hz, pyrrole), 5.87-5.84 (2H, m, pyrrole), 5.53 (1H, s, alkane) ppm. ^{13}C NMR ($CDCl_3$, 75 MHz): δ 132.38, 130.93, 129.17, 117.88, 108.74, 108.18, 107.76, 58.50, 44.03, 18.45 ppm. .

FAB3 (4-(5,5-difluoro-5H-4l4,5l4-dipyrrolo[1,2-c:2',1'-f][1,3,2]diazaborinin-10-yl)benzonitrile)

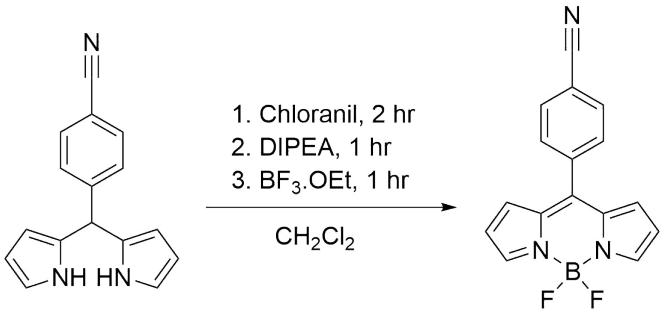

FAB2 **FAB3**

22 %

Dipyrromethane FAB2 (0.85 g, 3.4 mmol, 1 eq.) in 20 mL dichloromethane was added to a three-necked round-bottomed flask and the flask was purged with nitrogen. Chloranil (0.85 g, 3.4 mmol, 1 eq.) was added and the solution turned from a clear orange/brown to dark brown. After 2 hours stirring, diisopropylethylamine (DIPEA) (6.5 mL, 37.4 mmol, 11 eq.) was added and stirred for a further 1 hour. Boron trifluoride diethyl etherate (7.6 mL, 61.2 mmol, 18 eq.) was added dropwise and the reaction was stirred. After 1 hour the solution was diluted with dichloromethane and the organic layer was washed with water. The solution was dried over magnesium sulphate, filtered and concentrated by rotary evaporation. The crude product was purified by flash column chromatography over silica with dichloromethane eluent. The solvent was removed and the purified product was collected as a dark green powder in 22 % yield (220 mg). Crystals were grown by slow evaporation in dichloromethane and these were analysed by X-ray crystallography. The ^{13}C NMR spectrum was assigned based on the HSQC spectrum, which is shown in the Appendix together with the ^{1}H and ^{13}C spectra, Figures A.8, A.9 and A.10.

^{1}H NMR ($CDCl_3$; 300 MHz) 7.99 (2H, s, pyrrole), 7.85 (2H, d, J = 8.4 Hz, phenyl), 7.69 (2H, d, J = 8.4 Hz, phenyl), 6.84 (2H, d, J = 4.2 Hz, pyrrole), 6.58 (2H, d, J = 3.6 Hz, pyrrole) ppm. ^{13}C NMR ($CDCl_3$; 126 MHz) 145.4, 144.2, 138.1, 134.5, 132.2, 131.2, 130.9, 119.3, 117.8, 114.6 ppm. δ_B NMR (96 MHz) 0.23 (t, J = 29 Hz). δ_F NMR (282 MHz) -145.0 (q, J = 28 Hz). LC-MS: m/z calcd. for C16H10BF2N3Na; 316.0834, found; 316.1260 ($[M]^+$). FTIR (neat, transmission): ν = 2233, 1566, 1540, 1388 cm^{-1}.

FAB4 (10'-(4-cyanophenyl)-2l4,4'l4-spiro[benzo[d][1,3,2]dioxaborole-2,5'- dipyrrolo [1,2-c:2',1'-f][1,3,2]diazaborinine]-5-carboxylic acid)

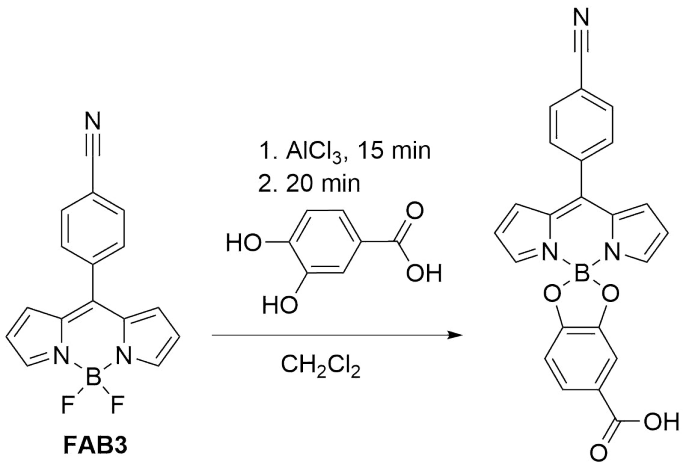

FAB3 (150 mg, 0.5 mmol, 1 eq.) was added to a two-necked round-bottomed flask which was purged with nitrogen. Distilled dichloromethane (30 mL) was added followed by aluminium chloride (340 mg, 2.6 mmol, 5 eq.). The flask was heated slightly and stirred for 15 min during which the solution turned from orange to dark pink. 3,4-Dihydroxybenzoic acid (0.39 g, 2.6 mmol, 5 eq.) in acetonitrile was added and the reaction was stirred for 20 min. The organic layer was washed with dilute aqueous hydrochloric acid (1 M, 20 mL), then with aqueous sodium bicarbonate (20 mL). The organic layer was dried over magnesium sulphate, filtered and the solvent was evaporated to afford a dark pink solid in 39 % yield (80 mg). Recrystallisation attempts were unsuccessful as catechol impurities did not separate from the product. The product was characterised by ^{1}H and ^{13}C NMR spectroscopy. The full spectra are given in the Appendix, Figures A.11 and A.12.

^{1}H NMR (*d*-DMSO, 700 MHz) 8.11 (2H, d, J = 8.5 Hz), 7.92 (2H, d, J = 8.5 Hz), 7.88 (2H, t, 1.5 Hz), 7.50-7.49 (1H, dd, J = 8.0, 1.8 Hz), 7.30 (1H, d, J = 1.9 Hz), 7.10-7.09 (2H, dd, J = 4.3, 1.1 Hz), 6.86 (1H, d, J = 8.1 Hz), 6.67-6.66 (2H, dd, J = 4.3, 2.0 Hz) ppm. ^{13}C NMR (*d*-DMSO, 175 MHz) δ 168.0, 155.7, 151.2, 147.0, 145.8, 145.1, 137.6, 134.4, 134.2, 133.1, 132.9, 131.4, 131.8, 129.6, 123.4, 122.5, 120.6, 118.7, 114.0, 110.2, 109.3 ppm. LC-MS: m/z calcd. for C23H14BN3O4Na; 430.0975, found; 430.0981 ([M]$^{+}$). FTIR (neat, transmission): 2231, 1673, 1568, 1541, 1413, 1386 cm^{-1}.

3.4 Electrochemistry

Cyclic voltammetry and differential pulse voltammetry experiments were recorded using an Ivium CompactStat or Ivium Stat potentiostat. Solutions were purged with nitrogen prior to the experiment and distilled solvents were used. Tetrabutylammonium hexafluorophosphate was recrystallised when received from Sigma Aldrich. Non-aqueous reference electrode kits were purchased from BASi and filled with a solution of supporting electrolyte containing 10 mM silver nitrate prior to using. Reference electrodes were stored in the fridge with the Vycor glass frits immersed in solvent when not in use.

3.5 Spectroelectrochemistry

For solution experiments, an OTTLE (optically transparent thin layer electrochemical) cell was used. The components of an OTTLE cell are shown in Figure 3.2. The holder contains a silver wire reference electrode, a platinum grid working electrode and a platinum wire counter electrode, sandwiched between two PTFE spacers. The spacers are held tightly between two calcium fluoride windows. The holder was manually tightened to ensure the cell did not leak. The electrodes were connected to an external circuit and the electrochemical parameters were controlled by an Ivium CompactStat potentiostat. An Ocean Optics USB2000+ VIS-NIR fibre optic spectrometer was used for experiments in the visible region. The OTTLE cell was placed in front of the spectrometer in the path of a tungsten/halogen light source. The cell was filled with a solution of supporting electrolyte and a background spectrum was taken prior to the experiment. When the analyte was added, the Ivium CompactStat was programmed to apply a potential range stepwise.

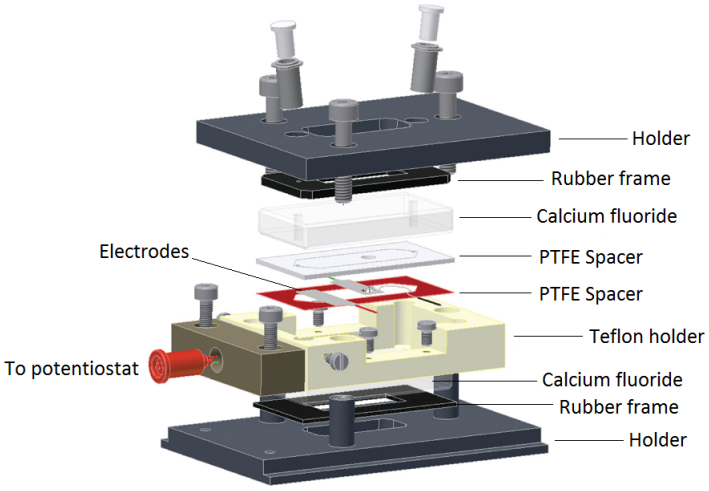

Figure 3.2: Setup of an OTTLE cell. Image adapted from ref [5].

Each potential step was held for *ca.* 10 seconds, allowing an absorption spectrum to be taken at each step. For infrared spectroelectrochemical experiments, deuterated chloroform was used as the solvent as it gave the fewest solvent bands in the measured window (2500 cm^{-1} to 1000 cm^{-1}).

For film experiments where little sample was available, a titanium dioxide film on FTO coated glass was used as the working electrode with a silver/silver^{+} reference electrode and a platinum wire counter electrode. Titanium dioxide films were prepared by doctor-blading one layer of transparent titanium dioxide paste onto a rectangle of FTO coated TEC15 glass as described in Section 3.2.1. The film was then sensitised by immersing in a solution of dye for a few hours. The sensitised film was placed in a quartz cuvette with a solution of supporting electrolyte in organic solvent. The cuvette was placed in the path of an Ocean Optics USB2000+ VIS-NIR fibre optic spectrometer, and absorption spectra were taken as a potential was applied to the titanium dioxide film.

3.6 Steady state spectroscopy

3.6.1 Ultraviolet-visible and fluorescence

Visible spectra of sensitised nickel oxide and titanium dioxide films were measured on an Ocean Optics USB2000+ VIS-NIR fibre optic spectrometer with a tungsten halogen light source. Electronic absorption and emission spectra in solution were recorded in

a 1 cm quartz cuvette. Electronic absorption spectra were measured on a Shimadzu UV-1800 UV Spectrophotometer. Fluorescence spectra were recorded on a Shimadzu RF-6000 Spectrofluorophotometer. Fluorescence lifetime measurements were recorded on a Horiba Easylife Fluorescence Lifetime system with an LED excitation bulb of *ca.* 400 nm. The lifetime was determined using the software provided on the instrument by iterative reconvolution of the instrument response function (IRF) and the true exponential decay combined with the least squares minimisation. Fluorescence decays were fit with a single or bi-exponential function. Quantum yields of fluorescence for samples in solution were recorded by integrating the emission spectra of samples of varying concentration with known absorbance values. Emission spectra of Rhodamine 6G were also taken. The integration was plotted against the absorbance value at the excitation wavelength and Equation 3.1 was used to calculate the emission quantum yield of the sample, Φ_X, relative to that of Rhodamine 6G, Φ_{ST}. (Φ_{ST} in ethanol is 0.95).

$$\Phi_X = \Phi_{ST} \frac{Grad_X}{Grad_{ST}} \frac{{\eta_X}^2}{{\eta_{ST}}^2} \tag{3.1}$$

$Grad_X$ and $Grad_{ST}$ are the gradients for each sample and η_X and η_{ST} are the refractive indexes of the solvents.

3.6.2 Infrared

Solid samples were mixed with potassium bromide (99 %, spectroscopic grade, Fisher Scientific) using a pestle and mortar and pressed into disks. The infrared spectra were measured on a Varian FTS 800 FT-IR spectrometer. For samples of dyes adsorbed on nickel oxide, sensitised films were removed from the FTO substrate with a spatula and potassium bromide disks were prepared as described above.

3.7 Time-resolved spectroscopy

3.7.1 Transient absorption

Two transient absorption setups were used, both operating a general pump-probe technique. The first (Lund University, research group of Tönu Pullerits) consisted of a Ti:Sapphire laser (Mai-Tai, Spitfire; Spectra Physics) which generates 800 nm, 80 fs pulses

at a rate of 1 kHz.

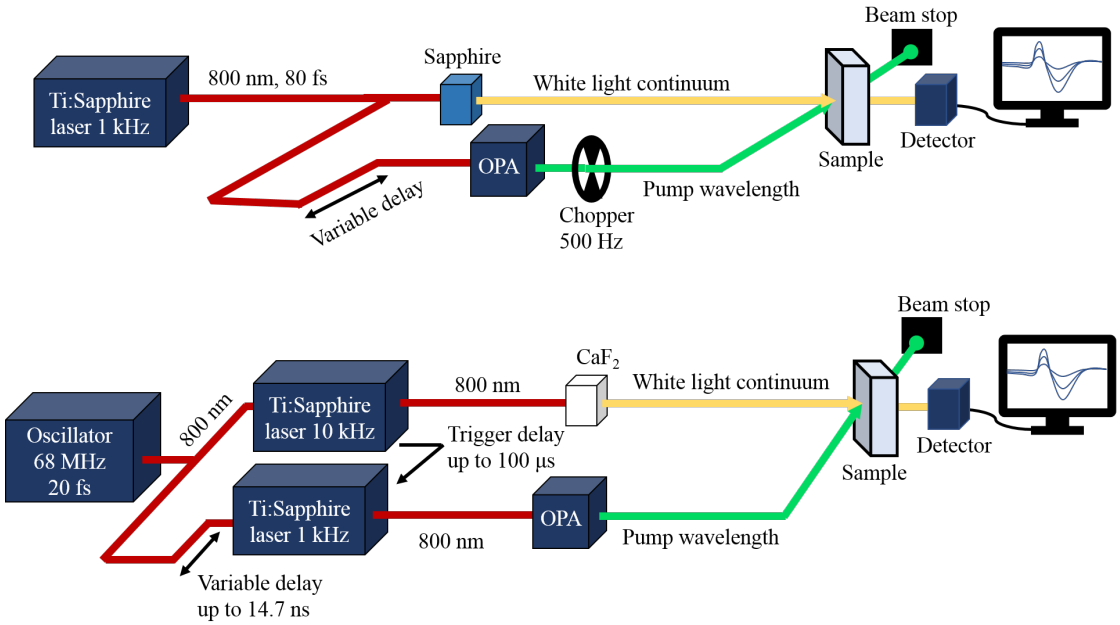

Figure 3.3: General pump-probe time-resolved spectroscopy setup. Top: Lund Laser Centre, Lund University. Bottom: ULTRA, Rutherford Appleton Laboratory, Harwell Research Campus.

The beam is split into a pump beam and a probe beam. The pump wavelength is generated with a non-collinear optical parametric amplifier (OPA, Topas, Light Conversion) and the probe beam is passed through a thin sapphire plate to generate a white light continuum. The two beams are set to overlap at the sample, at a 'magic angle' of 54.7 degrees to avoid the observation of dynamics connected to transition dipole rotation. The probe beam is dispersed on a photodiode array coupled to a spectrograph (Pascher Instruments). The pump beam is intermittently blocked with a 500 Hz chopper, and the transient absorption signal was calculated from the difference between spectra of two consecutive probe pulses passing through excited and unexcited sample, respectively. The excitation intensity used (80 μJ cm^{-2}, 2 x10^{-14} photons cm^{-2}) did not lead to any visible photodegredation of the samples over the measurement period.

The second setup (ULTRA, Central Laser Facility, Rutherford Appleton Laboratory, Harwell Research Campus) operates a time-resolved multiple probe (TRMPS)[6,7] setup to allow short (sub picosecond) and long (up to millisecond) processes to be monitored in the same experiment. Two Ti:Sapphire lasers (Thales Laser) are seeded by a 68 MHz oscillator. The 68 MHz oscillator is divided down to operate the probe laser at a rate of 10 kHz.

This is then divided down to trigger the pump laser at 1 kHz. For short pump/probe delays ($\leq$14.7 ns) the oscillator beam is sent along a translational stage. For longer delays up to 100 μs a combination of translation delay and electronic delay of the pump beam trigger are used. The first probe pulse catches processes up to 100 ns, subsequent probe beams catch processes up to 1 ms. The pump wavelength is tuned by an OPA and the probe beam is focused on calcium fluoride to generate the white light continuum.

The setup at Lund University was used for BOD1-5 discussed in Section 4.3, with an excitation wavelength of 532 nm and a pump energy of 80 μJ cm^{-2} (2 x10^{14} photons cm^{-2}). The setup at the Central Laser Facility was used for CAD dyes in Section 4.4 and bodipy-polyoxometalate hybrids in Chapter 5 with an excitation wavelength of 532 nm and a pump energy of 1.3 μJ cm^{-2} (3 x10^{12} photons cm^{-2}).

3.7.2 Time-resolved infrared

Time-resolved infrared experiments were performed on the ULTRA system, Central Laser Facility, Rutherford Appleton Laboratory, Harwell Research Campus. The general experimental principles are similar to transient absorption spectroscopy except that a mid-IR infrared probe beam and IR detector were used. Two titanium:sapphire amplifiers (10 kHz and 1 kHz) were synchronised using a 65 MHz oscillator. The 1 kHz pump beam was tuned to 532 nm by an OPA. The mid-IR was set to generate 10 kHz, 50 fs infrared pulses by difference frequency generation of an OPA. A mercury cadmium telluride array detector measured IR spectra over a 500 cm^{-1} spectral window. This setup was used for P1 and BOD2 in Section 4.5 and CAD dyes in Section 4.4.

3.7.3 Sample preparation

For samples in solution, a Harrick cell (Harrick Scientific Products) with two calcium fluoride windows and a 200 μm spacer was filled with a solution of dye to give an absorbance around 0.3 and the cell was sealed. For experiments on nickel oxide films, a compact nickel oxide layer was first applied to a calcium fluoride window by spraying a saturated solution of anhydrous nickel chloride dissolved in acetylacetone onto the surface of the calcium fluoride on a hot plate set to 450 °C. The compact layer creates a transparent, rough surface to help nanoparticles adhere to the window and create a transparent film. A layer

of nickel chloride solution (described in Section 3.2.1) was then applied by doctor-blading method and the films were sintered. The films were then sensitised by immersing in a solution of dye overnight. One layer of nickel solution is generally thick enough to give an absorbance of 0.3 at the excitation wavelength when sensitised. Sensitised NiO|CaF_2 windows were placed in a Harrick cell and either flushed with nitrogen (dry film experiments) or filled with electrolyte or solvent. Samples were rastered during the experiment to avoid degradation of the sample.

References

(1) Sumikura, S.; Mori, S.; Shimizu, S.; Usami, H.; Suzuki, E. *J. Photochem. Photobiol. A* **2008**, *199*, 1–7.

(2) Ito, S.; Murakami, T. N.; Comte, P.; Liska, P.; Grätzel, C.; Nazeeruddin, M. K.; Grätzel, M. *Thin Solid Films* **2008**, *516*, 4613–4619.

(3) Zhu, K.; Schiff, E. A.; Park, N. G.; van de Lagemaat, J.; Frank, A. J. *Appl. Phys. Lett.* **2002**, *80*, 685.

(4) Ito, S.; Liska, P.; Comte, P.; Charvet, R.; Pechy, P.; Bach, U.; Schmidt-Mende, L.; Zakeeruddin, S. M.; Kay, A.; Nazeeruddin, M. K.; Gratzel, M. *Chem. Commun.* **2004**, 4351.

(5) Domingos, S. R.; Luyten, H.; van Anrooij, F.; Sanders, H. J.; Bakker, B. H.; Buma, W. J.; Hartl, F.; Woutersen, S. *Rev. Sci. Instrum.* **2013**, *84*, 1–4.

(6) Greetham, G. M.; Sole, D.; Clark, I. P.; Parker, A. W.; Pollard, M. R.; Towrie, M. *Rev. Sci. Instrum.* **2012**, *83*, 103107.

(7) Greetham, G. M.; Burgos, P.; Cao, Q.; Clark, I. P.; Codd, P. S.; Farrow, R. C.; George, M. W.; Kogimtzis, M.; Matousek, P.; Parker, A. W.; Pollard, M. R.; Robinson, D. A.; Xin, Z.-J.; Towrie, M. *Appl. Spectrosc.* **2010**, *64*, 1311–1319.

Chapter 4

Photoinduced Charge Transfer of Push-pull Dyes at the NiO Interface

4.1 Aims

The aim of this chapter is to monitor the photoinduced charge transfer processes of dyes with a push-pull structure when adsorbed onto p-type nickel oxide films. Charge-separated state lifetimes were determined using ultrafast time-resolved spectroscopy for boron dipyrromethene and cationic dyes on nickel oxide in the presence and absence of a redox electrolyte. The excited state dynamics are related to the performances of p-type dye-sensitised solar cells assembled with these compounds.

4.2 Introduction

As discussed in the introduction to this thesis, a major limiting factor of nickel oxide p-type dye-sensitised solar cells is the fast charge-recombination which occurs between the reduced dye and holes in nickel oxide following charge-injection. Long-lived (microsecond) charge-separated state lifetimes on nickel oxide have been observed for some metal complexes[1,2] and molecules with long π bridges (commonly oligothiophene) attached to naphthalenediimide acceptor groups.[3–7] Similarly, dyes with a push-pull design aim to reduce the rate of charge-recombination by moving electron density in the dye away from the nickel oxide surface towards acceptor groups, as shown by the representation in Figure 4.1. In these systems the anchor group is attached at the donor to locate the acceptor group

furthest from the surface when adsorbed on nickel oxide, which is the opposite structure to push-pull dyes for n-type titanium dioxide systems where the anchor is located near to the acceptor group.

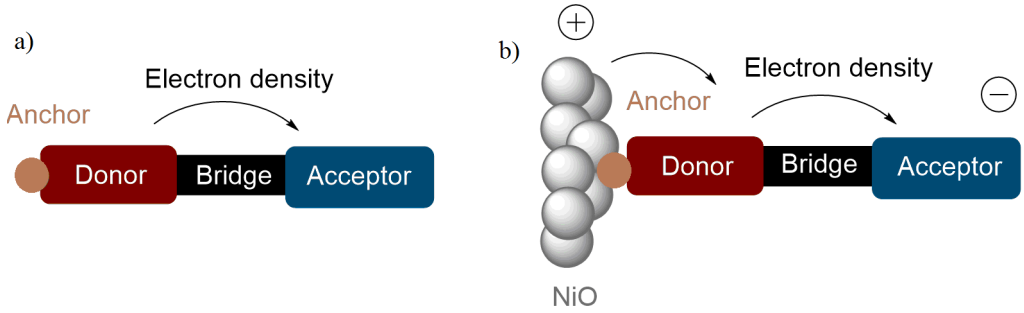

Figure 4.1: The general structure of a push-pull dye. a) When dissolved in solution; b) when adsorbed onto a nickel oxide film.

Push-pull dyes for p-type nickel oxide dye-sensitised solar cells were first introduced by Qin *et al.* with the dye P1.[8–11] This dye gave a particularly high solar cell performance which was attributed to the favourable alignment of energy levels between the dye, valence band of nickel oxide and the iodide/triiodide redox couple, and also the interactions of the malononitrile acceptor groups with species in the electrolyte which was reported to promote regeneration. There are many examples of dyes with similar structures to P1, containing a triphenylamine donor group and malononitrile acceptor groups,[12–16] though P1 is still used as a benchmark dye. Variations to this structure have included modifying the acceptor groups, the anchor-donor bridge and the donor-acceptor bridge.[16–20] Some of these structures are shown in Figure 4.2. Our group has reported a number of push-pull dyes for p-type dye-sensitised solar cells, including those with cationic indolium acceptor groups (CAD1-3)[19,21] and boron dipyrromethene (bodipy) acceptor groups[18] (BOD2, labelled as 1 in Figure 4.2). The photoinduced dynamics of P1, BOD2 and CAD3 will be discussed in this chapter, along with those of some new dyes which have not been reported prior to this work.

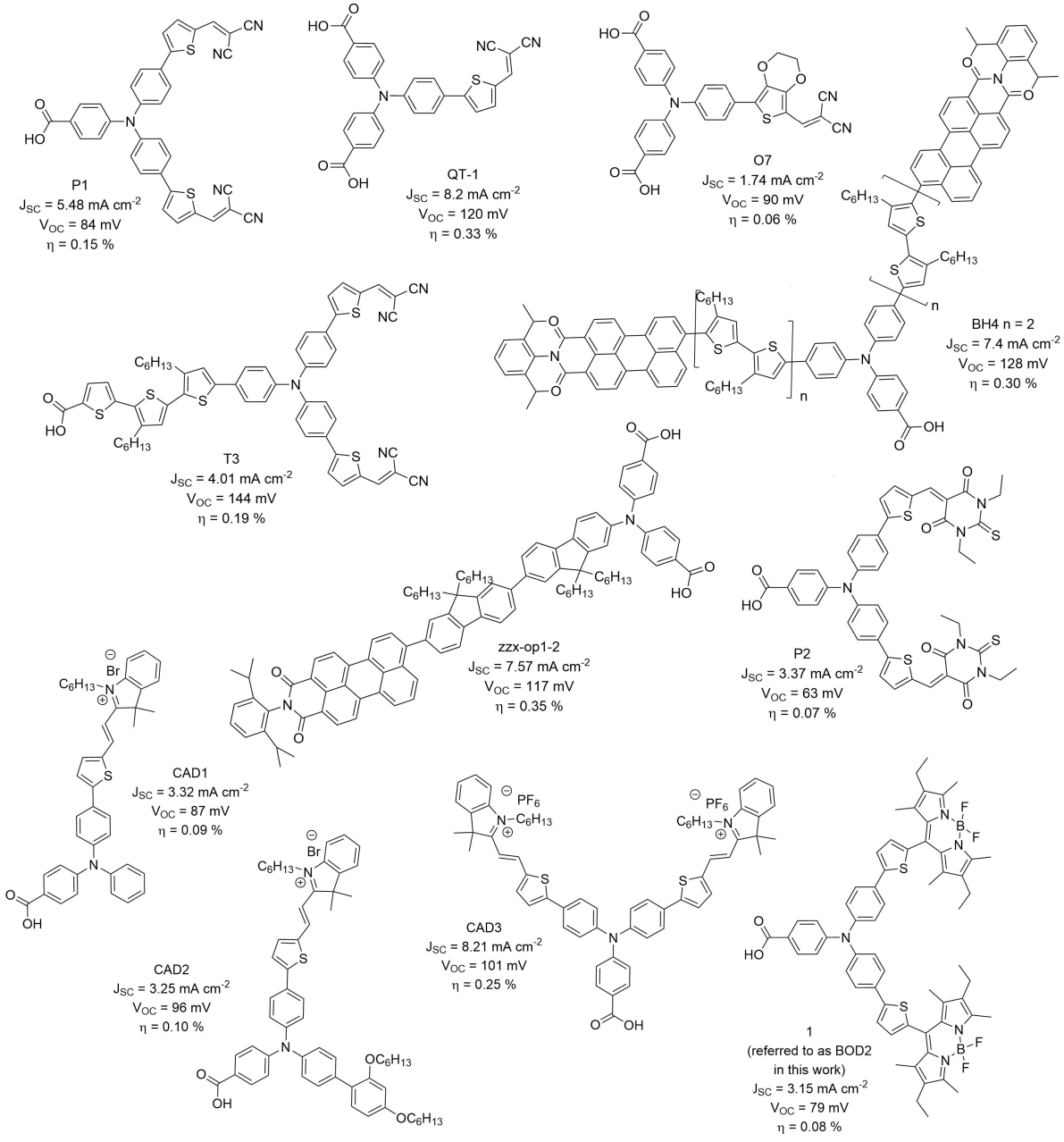

Figure 4.2: Structures of push-pull dyes with triphenylamine donor groups which have been used in p-type nickel oxide dye-sensitised solar cells. P1, ref [8]; T3, ref [14]; QT-1, ref [15]; O7, ref [13]; BH4, ref [17]; P2, ref [8], zzx-op1-2, ref [22]; 1, ref [18]; CAD1,CAD2 ref [21]; CAD3, ref [19].

4.3 Boron dipyrromethene

Contributions for Section 4.3: Transient absorption spectroscopy and photovoltaic measurements of bodipy dyes were carried out by the author except for the transient absorption spectroscopy of BOD2 and the photovoltaic properties of BOD3 which have been reported previously by our group.[18,19] Any other spectroscopic analysis was performed by members of the group.

4.3.1 Introduction

Boron dipyrromethene (bodipy) molecules are a class of organic molecules known for their high molar absorption coefficients, good chemical stability and wide variety of synthetically available structures.[23] The full name 4,4-difluoro-4-bora-3a,4a-diaza-*s*-indacene refers to a dipyrromethene ligand chelated to a boron atom, usually a boron difluoride group. There are many examples of n-type titanium dioxide dye-sensitised systems which use molecules containing bodipy groups and these have been reviewed by Singh *et al.*[24] In such systems, bodipy groups are most commonly used as acceptors in a push-pull design appended to a triphenylamine donor, with power conversion efficiencies reaching over 6 %.[25] Despite this, the only research into bodipy photosensitisers for p-type dye-sensitised solar cells has been carried out by our research group.

The synthesis and photovoltaic properties of a bodipy analogue of P1 have been reported by the group of Gibson with the molecule BOD2, shown in Figure 4.2.[18] Transient absorption spectroscopy of BOD2 revealed the formation of a long-lived charge-separated state on nickel oxide, τ = 180 ns. Despite a slower charge-recombination rate for BOD2|NiO relative to P1|NiO (τ = 200 ps), the photovoltaic performance of BOD2 was lower. An in-depth time-resolved infrared study of P1 and BOD2 is presented later in this chapter in Section 4.5. Here, the photovoltaic performances and charge-separated state lifetimes of a series of triphenylamine-bodipy push-pull dyes are compared with those of BOD2 to determine the relationship between structure and solar cell performance for this class of sensitisers. The structures of these bodipy dyes (BOD1-5) are shown in Figure 4.3, differing in the substituents around the bodipy acceptors and the lengths of donor-acceptor and anchor-donor bridges.

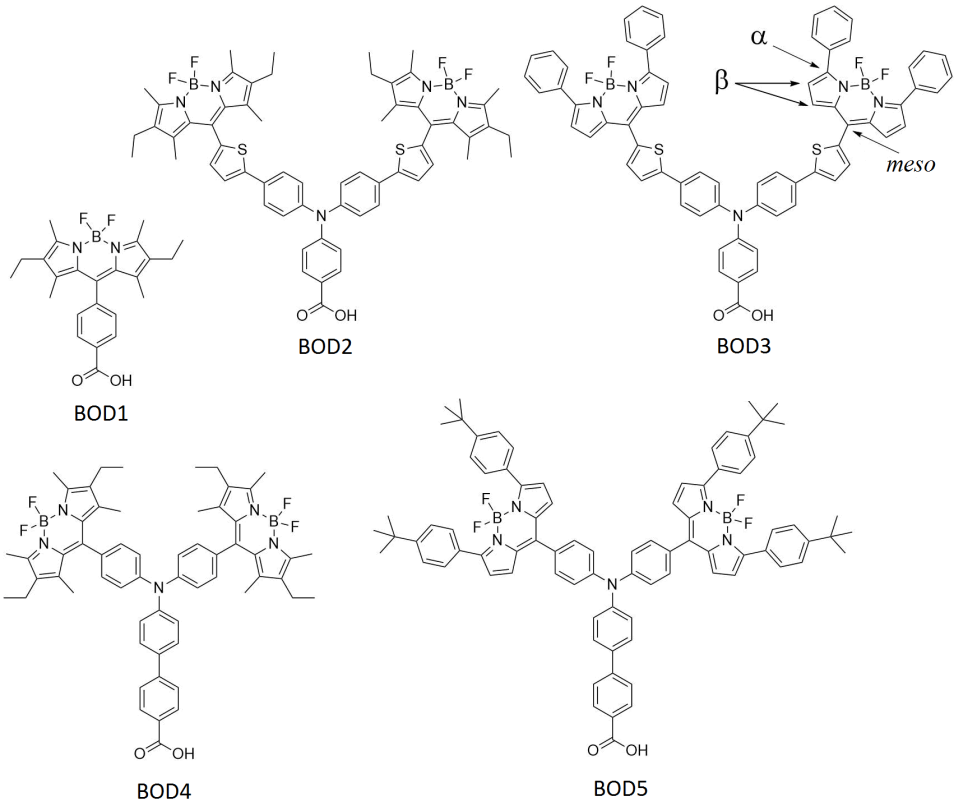

Figure 4.3: Structures of boron dipyrromethene push-pull dyes studied in this section.

BOD1 contains a 2,8-diethyl-1,3,7,9-tetramethyl bodipy core with a benzoic acid anchor group at the *meso* position, and is used here as a reference molecule for the bodipy group. BOD2 and BOD4 contain bodipy groups with the same substituents as BOD1, connected to a triphenylamine donor group directly or via a thiophene π bridge for BOD4 and BOD2, respectively. The bodipy groups of BOD3 and BOD5 are unsubstituted at the β positions, allowing greater rotational freedom around the bond at the *meso* position. BOD4 and BOD5 contain an extra phenyl spacer on the anchor-donor bridge.

4.3.2 Steady state absorption

The electronic absorption spectra of BOD1-5 in dichloromethane solution were recorded by members of the group and are shown in Figure 4.4. The full photophysical properties of these dyes are listed in ref [26], and selected values are given in the Appendix in Table A.1. The absorption profiles of BOD1 and BOD4 are similar, with a sharp S_0-S_1 absorption band between 500 nm and 550 nm with a shoulder at higher energy which is typical of the absorption spectrum of a bodipy.[23]

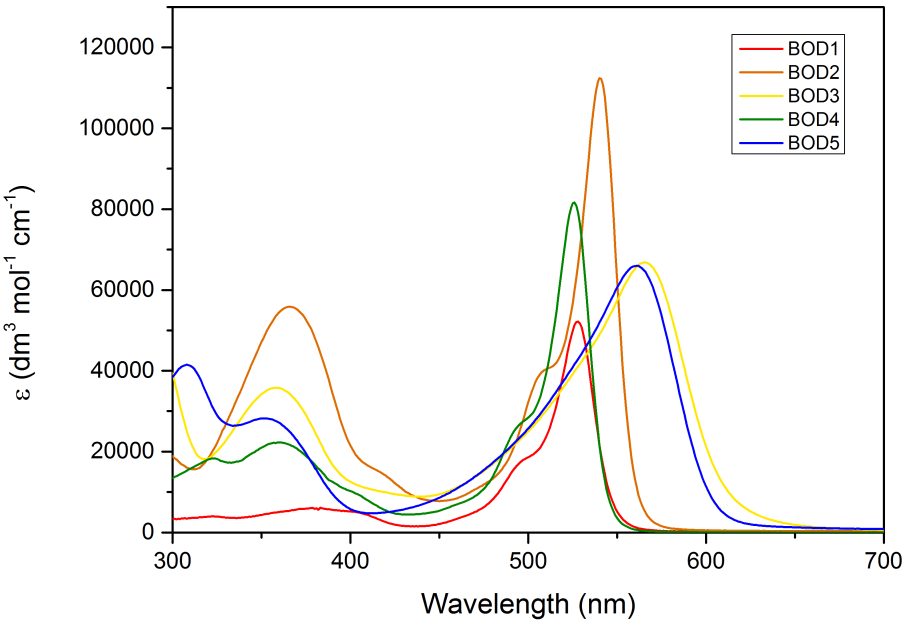

Figure 4.4: Electronic absorption spectra of BOD1-5 in dichloromethane, plotted from raw data provided by members of the group.[26]

BOD2-5 absorb strongly in the visible region with molar absorption coefficient values higher than that of P1 (ε = 57 900 dm^3 mol^{-1} cm^{-1}). The molar absorption coefficient of BOD1 is lower than BOD2-5 due to the increased probability of a π-π* transition when two bodipys are present in one molecule. The addition of a thiophene π bridge shifts the absorption band of BOD2 to lower energy by 15 nm relative to BOD1 and BOD4. The molar absorption coefficients of BOD3 and BOD5 are slightly lower than BOD2 and BOD4 which is likely due to a switch from π-π* transitions to charge transfer transitions for BOD3 and BOD5, which is consistent with their solvatochromic nature and decrease in the emission quantum yield of BOD3 and BOD5 relative to the other dyes.[26] The shape of the main absorption bands of BOD3 and BOD5 are also broader and red-shifted by 20 nm relative to BOD2 due to more extensive conjugation in the former systems as there is greater rotational freedom around the bodipy groups at the *meso* position. This is consistent with density functional theory calculations which were performed for these molecules by members of the group and can be found in the ESI of ref [26]. A red-shifted absorption profile minimises spectral overlap of the photoanode and photocathode in a tandem dye-sensitised solar cell, as has been demonstrated for a BOD3|NiO photocathode

with a D35|TiO_2 photoanode.[19]

4.3.3 Transient absorption spectroscopy

Ultrafast transient absorption spectroscopy was used to investigate the formation and subsequent recombination of the dye$^-$|NiO^+ charge-separated state. The full experimental setup is given in Section 3.7. Briefly, solution and film samples were excited with a 532 nm laser pulse, and the electronic absorption spectrum was probed with a white light beam at various time delays after excitation. The data was analysed using a single-point method, where the change in absorbance at selected wavelengths was fit to a single or multi-exponential decay function. For BOD3 and BOD5 global analysis of the transient absorption spectra was used to extract the lifetimes associated with species whose spectra overlap. The transient absorption spectra of BOD1, BOD3, BOD4 and BOD5 in dichloromethane solution and absorbed on films of nickel oxide are given in Figure 4.5, with the lifetimes from single-point analysis given in Table 4.1.

The transient absorption spectra of BOD1 and BOD4 contain similar features both in dichloromethane and when adsorbed on nickel oxide. In dichloromethane the negative signal which extends from 550 nm to 650 nm is attributed mainly to stimulated emission, as the ground state absorption band is narrow for these dyes and is masked by laser scatter. This decays with $\tau = 2.3$ ns for BOD1 which is similar to the fluorescence lifetime of this dye, $\tau_{FL} = 3.3$ ns, whereas the stimulated emission decay of BOD4 contains an additional fast component ($\tau_1 = 18$ ps). The fluorescence lifetimes can be found in the ESI of ref [26] and the emission spectra are given in the Appendix, Figure A.2. This stimulated emission arises from the interaction between an excited molecule and the probe pulse, which results in the emission of a photon.[27] The sharp transient signal which absorbs between 460 nm and 500 nm for BOD1 and BOD4 in dichloromethane is assigned to the first singlet excited state, and is similar to the initial species formed in the transient absorption spectra of BOD2.[18] For BOD2 this band evolved over 400 ps to form a long-lived triplet excited state with a sharp absorption at 425 nm ($\tau = 300$ ns). For BOD1 and BOD4 however, this band forms within the time resolution of the experiment (*ca.* 0.5 ps) and decays to the ground state with $\tau = 1.1$ ns for BOD1 and $\tau = 800$ ps for BOD4.

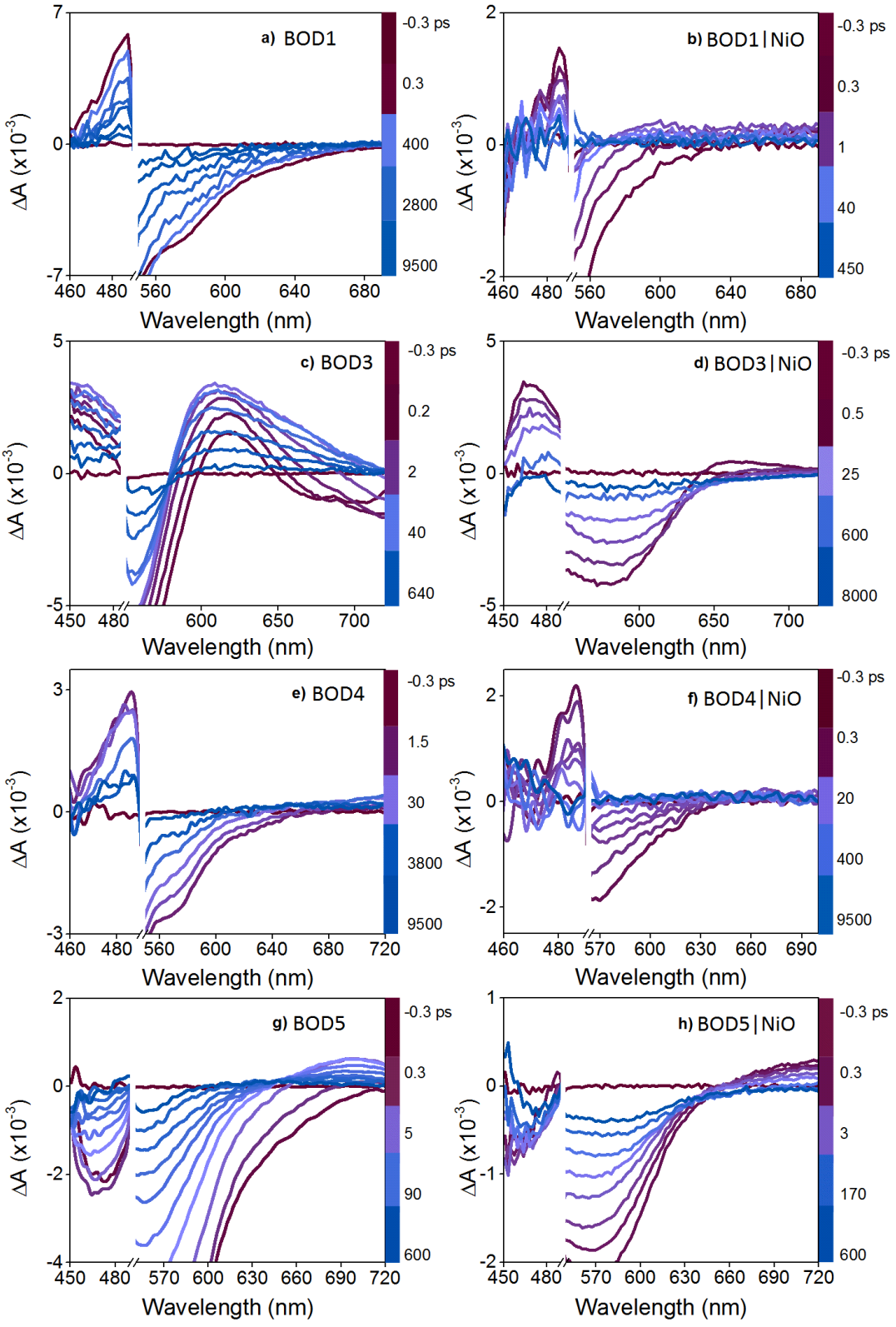

Figure 4.5: Transient absorption difference spectra of bodipy photosensitisers at selected time delays following excitation at 532 nm. Left) in dichloromethane solution; right) adsorbed on nickel oxide.

	Lifetime, ps	
	Dichloromethane	NiO
BOD1	τ_{472} = 1100 ±90	τ_{488} = 4.1 ±0.6
	τ_{594} = 2300 ±300	τ_{560} = 0.7 ±0.1
[a]BOD2	τ_{425} = 21 ±3 (11%), 864 000 ±28 000 (89%)	τ_{425} = 13 ±3 (70%), 49 000 ±28 000 (30%)
	τ_{470}(growth) = 9.52 ±0.91	τ_{515} = 10 ±1 (86%), 23 000 ±10 000 (14%)
	τ_{470} = 396 000 ±33 000	τ_{575} = 24 ±3 (78%), 177 000 ±59 000 (22%)
	τ_{500}(growth) = 14.1 ±1.2	
	τ_{500} = 413 ±50 (20%), 896 000 ±26 000 (80%)	
	τ_{650} = 292 000 ±31 000	
BOD3	τ_{472}(growth) = 0.8 ±0.04	τ_{472} = 4.9 ±0.1 (45%), 580 ±40 (55%)
	τ_{472} = 190 ±10	τ_{609} = 7.2 ±0.6 (65%), 443 ±64 (35%)
	τ_{563} = 0.6 ±0.03 (45%), 190 ±10 (55%)	τ_{700} = 6.5 ±0.4
	τ_{650}(growth) = 1.3 ±0.1	τ_{700}(rise) = 780 ±500
	τ_{650} = 210 ±100	
	τ_{680}(bleach decay) = 1.3 ±0.1	
BOD4	τ_{481} = 800 ±100	τ_{485} = 5.0 ±1.0
	τ_{596} = 18 ±1 (70%), 2700 ±600 (30%)	τ_{578} = 2.6 ±0.5
	τ_{710}(growth) = 25 ±3	
	τ_{710} = 3800 ±900	
BOD5	τ_{475} = 5.8 ±0.7 (39%), 61 ±4 (61%)	
	τ_{611} = 3.8 ±0.1 (65%), 68 ±4 (35%)	τ_{606} = 1.1 ±0.1 (60%), 470 ±70 (40%)
	τ_{705}(growth) = 1.2 ±0.1	τ_{693} = 0.1 ±0.01 (76%), 13 ±1 (24%)
	τ_{705} = 68 ±2	

Table 4.1: Lifetimes derived from single-point analysis of transient absorption spectra at selected wavelengths. Where a bi-exponential function is used, the amplitudes of each component are given in brackets. [a]Values taken from ref [18]. λ_{exc} = 532 nm.

For all BOD1 and BOD3-5, the experiment was performed in the region where the triplet excited state was observed for BOD2 (*ca.* 400 nm to 450 nm) but no signal was present for any of the dyes. The regions where signals were observed are therefore shown in Figure 4.5.

There was no long-lived signal unaccounted for in the ground state bleach of any of BOD1 or BOD3-5 which supports that no triplet excited state was formed. The kinetic traces of the negative signals are given in the Appendix, Figure A.3. An additional positive signal is present for BOD4 at later time delays which absorbs weakly around 680 nm, and resembles an oxidised form of triphenylamine ($TPA^{\bullet+}$).[28] This suggests the formation of an intramolecular charge-transfer excited state, though the bodipy radical ($bodipy^{\bullet-}$), which has been reported at 580 nm for similar systems and from spectroelectrochemical measurements, is not observed. This may be due to overlap of this species with stimulated emission.

When adsorbed on a nickel oxide film, a small amount of stimulated emission is present for both BOD1 and BOD4. The positive signal between 450 nm and 500 nm grows within the time resolution of the experiment and decays on a much shorter timescale compared to solution, $\tau = 4.1$ ps and $\tau = 5.0$ ps for BOD1 and BOD4, respectively. The spectra of BOD1|NiO contain a broad absorption from 600 nm across the measured wavelengths to 720 nm, which is suggestive of holes in nickel oxide.[29] A small positive signal at 580 nm is also present for both BOD1 and BOD4, which resembles $bodipy^{\bullet-}$, but the signal is too weak to resolve meaningful kinetics in either case. The presence of this signal, which is shown in an expansion of this region in Figure 4.6, suggests that the first singlet excited state is rapidly quenched by charge-injection from nickel oxide. Fast charge-recombination is expected for BOD1 as there is very small spacial separation between the bodipy acceptor and the nickel oxide surface.

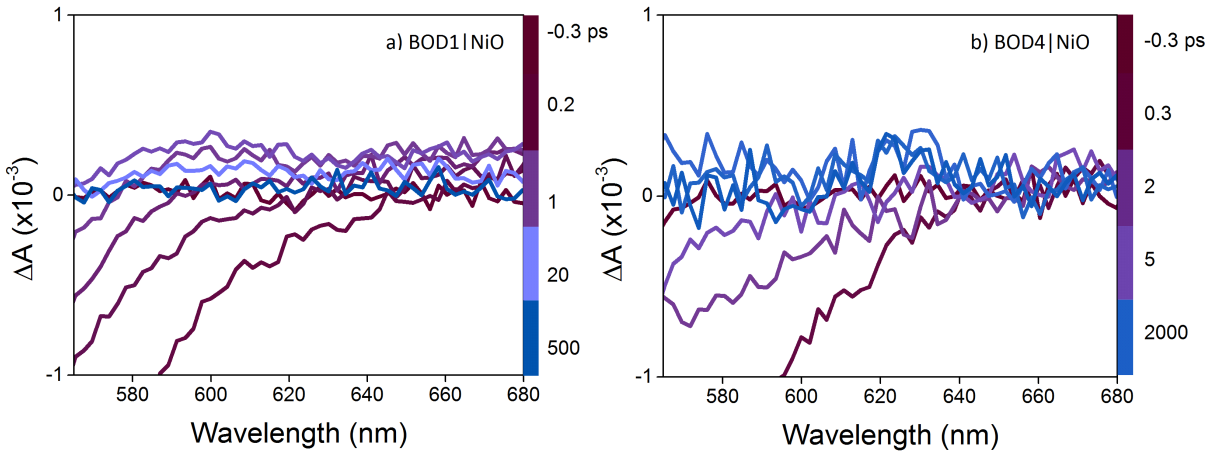

Figure 4.6: Expansion of the transient absorption spectra of BOD1 and BOD4 adsorbed on nickel oxide, at selected time delays following excitation at 532 nm, showing weak signals resembling $bodipy^{\bullet-}$.

The transient absorption spectra of BOD3 and BOD5 have much broader ground state bleaches relative to the other bodipy dyes in this series, which is consistent with their respective ground state absorption profiles. The transient absorption spectra of BOD3 in dichloromethane contains a broad negative signal between 650 nm and 720 nm at early time delays which is attributed to stimulated emission, and a second bleach between 530 nm and 600 nm which is attributed to the ground state absorption. A transient band which absorbs between 600 nm and 650 nm grows over 1.3 ps, as the stimulated emission decays on the same timescale. This transient is attributed to the first excited singlet state, and broadens and blue-shifts over 1 ps to resemble bodipy$^{\bullet-}$. This peak decays with τ = 210 ps, together with the positive signal at 460 nm (τ = 190 ps). This suggests the formation of the intramolecular charge-transfer excited state TPA^{+}bodipy^{-}, although the broad peak of TPA$^{\bullet+}$ which absorbs between 650 nm and 720 nm which was observed for BOD4 in solution is not present for BOD3. As the spectra of the first excited singlet state and the charge-transfer excited state overlap, a global analysis method of the transient absorption data was used,[30] as described in the Theory Section 2.3.2, and the results are shown in Figure 4.7. Lifetimes given by the decay-associated difference spectra are consistent with those obtained from single-point analysis, and the evolution-associated difference spectra show the first excited singlet state and emission (black line), and the charge-transfer excited state (red line).

When BOD3 is adsorbed on nickel oxide, the bleach indicating stimulated emission is absent, and the ground state bleach is red-shifted and broadened due to interactions between the dye and nickel oxide. The transient species which absorbs between 460 nm and 500 nm and at wavelengths longer than 650 nm resembles BOD3^{-} which was generated electrochemically[26] and is consistent with rapid formation of the charge-separated state. The transient which absorbs at 472 nm was fit to a bi-exponential decay function to give fast and slow components (τ_1 = 4.9 ps, τ_2 = 580 ps), but the transient at longer wavelengths overlaps with the ground state absorption and as a result kinetic information was difficult to extract. Global analysis of the transient absorption spectra of BOD3|NiO (Figure 4.7) extracted the spectrum of the charge-separated state (blue line), which is slightly red-shifted from the charge-transfer excited state at 475 nm (green line). The charge-separated state lifetime of BOD3 is considerably longer than BOD1 and BOD4.

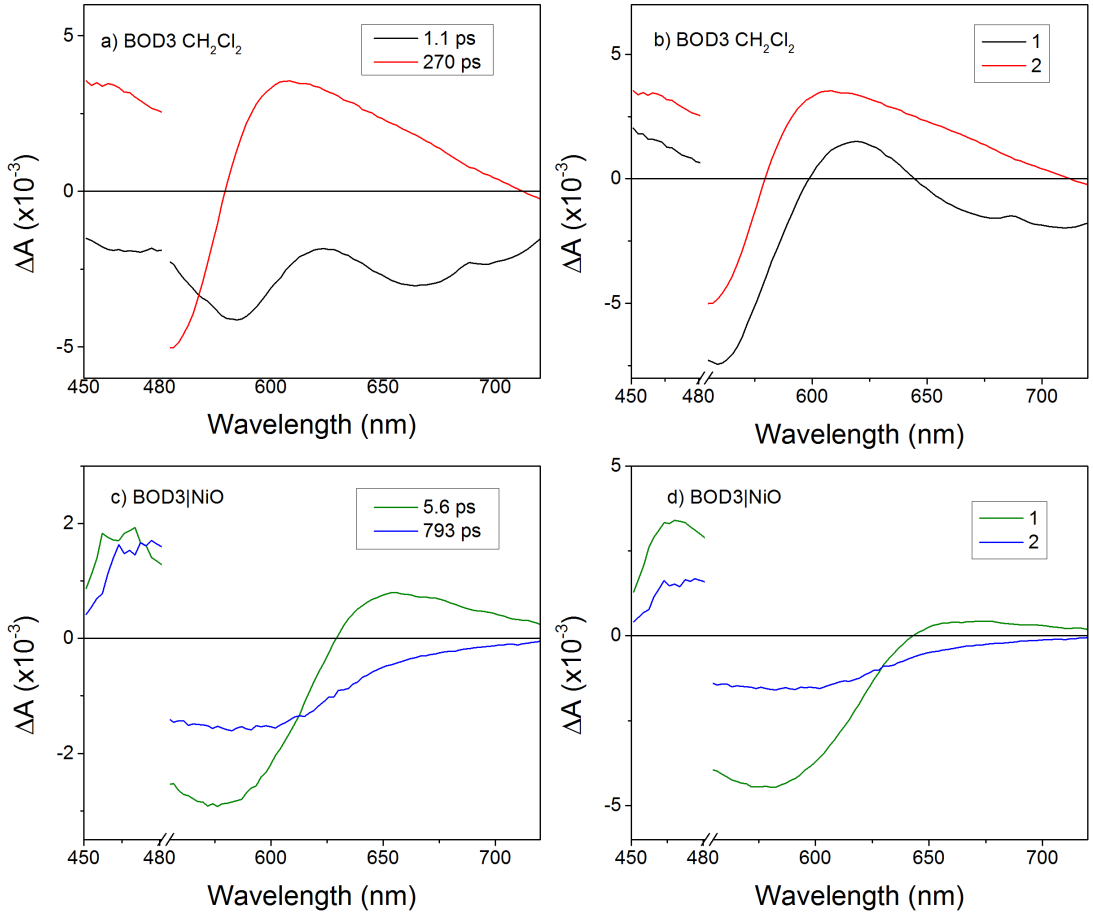

Figure 4.7: Results from global analysis of transient absorption data of BOD3. Left) decay-associated difference spectra; right) evolution-associated difference spectra.

The photoinduced dynamics of BOD5 in dichloromethane are less complicated than for BOD3. The negative signal which contains the ground state bleach and the stimulated emission extends from 450 nm to 650 nm, and was fit to a bi-exponential function which contained two components on a picosecond timescale ($\tau_1 = 3.8$ ps, $\tau_2 = 68$ ps). A transient species which absorbs between 660 nm and 720 nm grows with $\tau = 1.2$ ps, then decays with $\tau = 68$ ps, and is attributed to the charge-transfer excited state. When BOD5 is adsorbed on nickel oxide the ground state bleach is red-shifted but narrower than for the solution spectra, which is consistent with quenching of stimulated emission on nickel oxide. Single-point analysis of the broad transient at longer wavelengths suggests fast dynamics. However results from global analysis (Figure 4.8) reveal a longer-lived species (500 ps, blue line) which has a weak absorption at longer wavelengths and this is attributed to the charge-separated state.

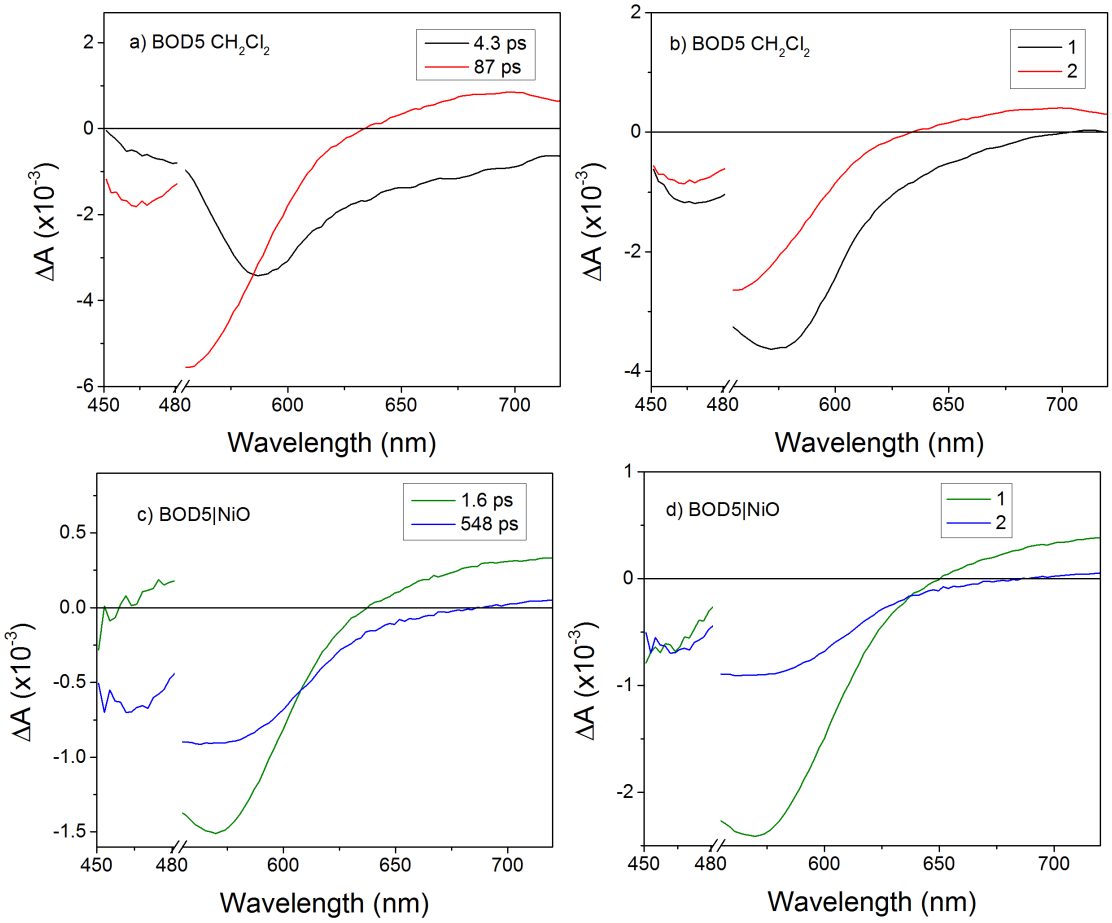

Figure 4.8: Results from global analysis of transient absorption data of BOD5. Left) decay-associated difference spectra; right) evolution-associated difference spectra.

In general, the absorption spectra of the charge-transfer excited state and the charge-separated state for BOD3 and BOD5 are more difficult to distinguish than for the other dyes in this series due to their broad absorption, and global analysis showed that the spectra of the charge-separated states are weakly absorbing for both dyes adsorbed on nickel oxide. However, the charge-separated state lifetimes of BOD3|NiO and BOD5|NiO are considerably longer than BOD1 and BOD4. Decay traces at selected wavelengths from the transient absorption spectra are shown in Figure 4.9. In dichloromethane solution the first singlet excited states of BOD1 and BOD4 are longer-lived than those of BOD3 and BOD5 ($\tau_{\mathrm{BOD1,\ BOD4}} = \textit{ca.}$ 2 ns and $\tau_{\mathrm{BOD3,\ BOD5}} = <$ 100 ps). The charge-separated state lifetimes of BOD1|NiO, BOD3|NiO, BOD4|NiO and BOD5|NiO were all on a picosecond timescale, shorter than that previously observed for BOD2|NiO (τ = ca. 180 ns).

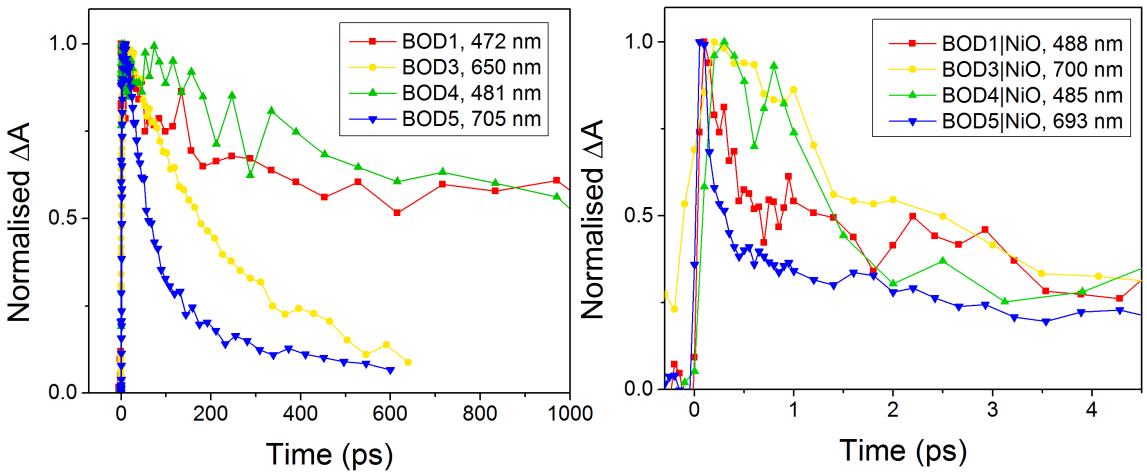

Figure 4.9: Decay traces at given wavelengths from transient absorption spectroscopy of BOD1-5. a) In dichloromethane; b) on NiO. The amplitudes have been normalised for visual comparison. λ_{exc} = 532 nm.

During previous work from our group, it was possible to determine the injection efficiency of BOD2 (η_{inj} = 50 %) because the spectrum of the reduced bodipy was distinguishable from the excited state.[18] This value was determined by comparing the relative amplitudes of the dye excited state with that of the charge-separated state in the transient absorption spectra of BOD2|NiO. For BOD1 and BOD3-5 it was not possible to directly distinguish the spectra of the first excited state and charge-separated state, especially for BOD3 and BOD5 which absorb broadly, however, the results from global analysis of BOD3|NiO showed that the amplitude of the charge-separated state was *ca.* 50 % of the excited state in the evolution-associated spectra, which is similar to that of BOD2. For BOD5|NiO the charge-separated state has only a small absorption so this value is considerably decreased.

4.3.4 Dye-sensitised solar cells

BOD1-5 were tested in p-type dye-sensitised solar cells with an iodide/triiodide electrolyte containing 0.1 M iodine and 1.0 M lithium iodide in acetonitrile. The performance of the solar cells was evaluated by photocurrent density-voltage curves under 1 sun illumination, and incident photon-to-current conversion efficiency (IPCE) experiments, as described in the Experimental Chapter, Section 3.2. Solar cell characteristics of BOD3 have been reported by our group previously with the same electrolyte as used here, and the values given for this dye in Table 4.2 are taken from ref [19]. The photovoltaic performance of

BOD2 has also been previously reported,[18] but with an electrolyte containing a higher concentration of iodine, so BOD2|NiO dye-sensitised solar cells with an electrolyte containing 0.1 M iodine and 1.0 M lithium iodide were fabricated by the author. It should be noted that when a cobalt$^{2+/3+}$ electrolyte was used there was no significant photocurrent generated by any of the dyes, which is likely due to the fast (picosecond to nanosecond) charge-recombination for BOD1-5. Charge-separated state lifetimes on a microsecond timescale are required when using redox couples with large reorganisation energies, for example cobalt tris-bipyridine complexes.[3,4] The errors are determined from three cells which were fabricated for each dye.

A surprisingly good performance was obtained from the simple BOD1 molecule, despite the fast charge-recombination determined by transient absorption experiments, and the close proximity of the holes in nickel oxide to the reduced dye. This dye performed similarly to the structurally more complex BOD2 and BOD4.

	Voc (mV)	Jsc (mA cm^{-2})	FF (%)	η (%)	IPCE (%)	APCE (%)
BOD1	95 ±7.5	1.48 ±0.03	0.36 ±0.01	0.05 ±0.005	20 ±0.5	27 ±1.0
BOD2	95 ±3.0	1.58 ±0.22	0.35 ±0.01	0.05 ±0.005	23 ±4.0	24 ±4.0
[a]BOD3	106	5.87	0.31	0.20	53	53
BOD4	97 ±0.5	1.60 ±0.07	0.38 ±0.005	0.06 ±0.005	27 ±0.5	30 ±0.5
BOD5	109 ±1.5	3.70 ±0.17	0.35 ±0.005	0.14 ±0.005	44 ±3.0	45 ±3.0

Table 4.2: Photovoltaic performance of nickel oxide dye-sensitised solar cells containing BOD1-5 and an electrolyte of 0.1 M I_2 and 1.0 M LiI in acetonitrile. [a]Taken from ref [19]. FF is the fill factor; η is the power conversion efficiency; IPCE is the incident photon-to-current conversion efficiency; APCE is the absorbed photon-to-current conversion efficiency.

These three dyes, which all contain bodipy groups with the same substituents achieved modest photocurrent density values of 1.48 mA cm^{-2} to 1.60 mA cm^{-2}, and open-circuit photovoltage values of 95 mV to 97 mV, which are similar to the performances of the push-pull dyes shown in Figure 4.2. The photocurrent generated by BOD2 in this study was 50 % lower than the previously reported system which contained an electrolyte with a higher concentration of iodine, however, IPCE and fill factor values were similar, and the photovoltage was higher for the system shown in Table 4.2.

BOD3 and BOD5 performed considerably better than the other dyes, which is shown by their higher relative photocurrent densities and voltages in Figure 4.10. This is consistent with the broader absorption and longer-lived charge-separated state lifetimes of BOD3 and BOD5 compared to BOD1 and BOD4. BOD5 achieved an overall power conversion efficiency of 0.14 %, nearly twice that of the previously reported efficiency of BOD2, and only slightly lower than that of P1 ($\eta = 0.15$ %).[10]

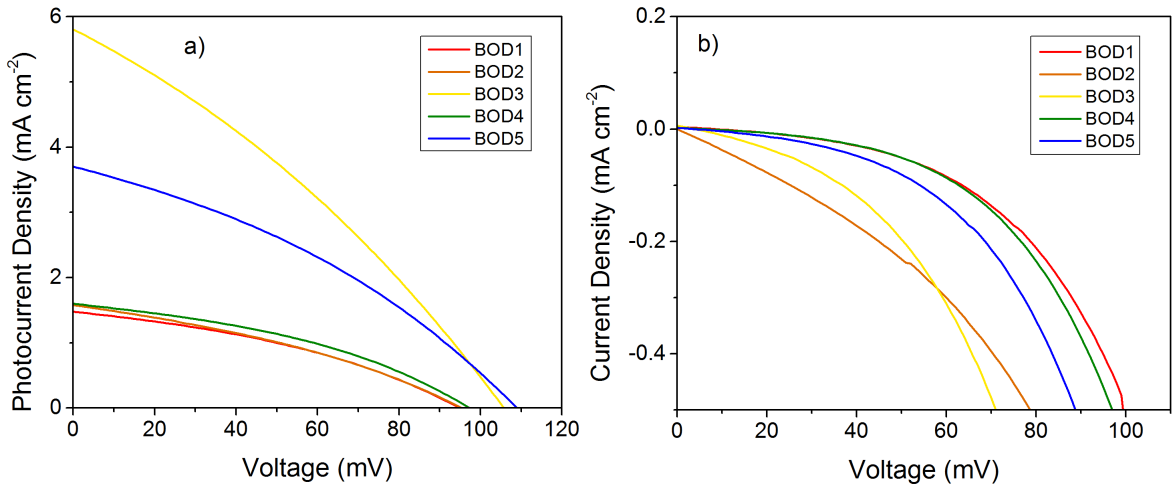

Figure 4.10: Photocurrent density-voltage curves for nickel oxide dye-sensitised solar cells containing BOD1-5 and an electrolyte of 0.1 M I_2 and 1.0 M LiI in acetonitrile. a) Under 1 sun illumination; b) in the dark.

The photocurrent densities generated by dye-sensitised solar cells containing BOD3 with a thiophene donor-acceptor bridge are significantly higher than those containing BOD5. This suggests that increasing the distance between the nickel oxide surface and the acceptor group improves the solar cell performance, and is likely related to the slight increase in the charge-separated state lifetime of BOD3 relative to BOD5. BOD3 also absorbs more broadly than BOD5, and this is shown in the ground state absorption on nickel oxide and the IPCE spectra in Figure 4.11. The highest IPCE values of BOD1, BOD2 and BOD4 are between 475 nm and 575 nm, whereas BOD3 and BOD5 still generate a considerable photocurrent above 600 nm.

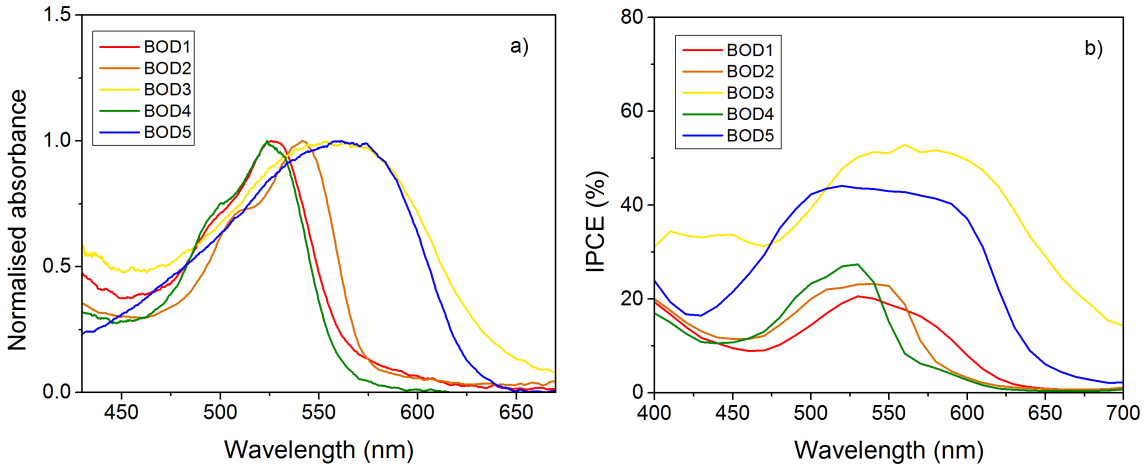

Figure 4.11: a) Normalised absorption spectra of dye-sensitised nickel oxide films recorded prior to solar cell fabrication; b) IPCE plots of p-type dye-sensitised solar cells assembled with 0.1 M I_2 and 1.0 M LiI in acetonitrile. IPCE experiments were performed on dye-sensitised solar cells which were used for the current-voltage measurements shown in Figure 4.10.

As discussed in Theory Section 2.1.2, the IPCE is related to the light harvesting efficiency (LHE), the injection efficiency (η_{inj}), the regeneration efficiency (η_{reg}) and the charge collection efficiency (η_{cc}), as shown in Equation 4.1.

$$IPCE_{\lambda} = LHE \times \eta_{\text{inj}} \times \eta_{\text{reg}} \times \eta_{\text{cc}} \tag{4.1}$$

η_{inj} can be estimated from a comparison of the lifetimes associated with the dye in the presence and absence of nickel oxide. For all photosensitsers BOD1-5, the charge-separated state was formed on nickel oxide and this suggests that charge-injection is not the major factor responsible for the difference in IPCE observed, though the yield of the charge-separated state was lower for BOD2, BOD3 and BOD5.

Charge lifetime and charge extraction experiments were performed for the solar cells which gave the current-voltage characteristics shown in Figure 4.10, and give an estimate of η_{cc}, as discussed in Theory Section 2.1.3. Details of the setup are given in Experimental Section 3.2.4. Briefly, for charge lifetime measurements the current decay is measured under short-circuit conditions while small modulations to the bias light intensity are applied. The decays are fit to a single exponential decay function and plotted against the photovoltage determined by the light intensity. Charge extraction experiments are

performed by switching from open-circuit to short-circuit conditions and monitoring the current. A plot of charge lifetime vs charge density is shown in Figure 4.12, and plots of charge lifetime and charge density vs photovoltage are given in the Appendix in Figure A.1.

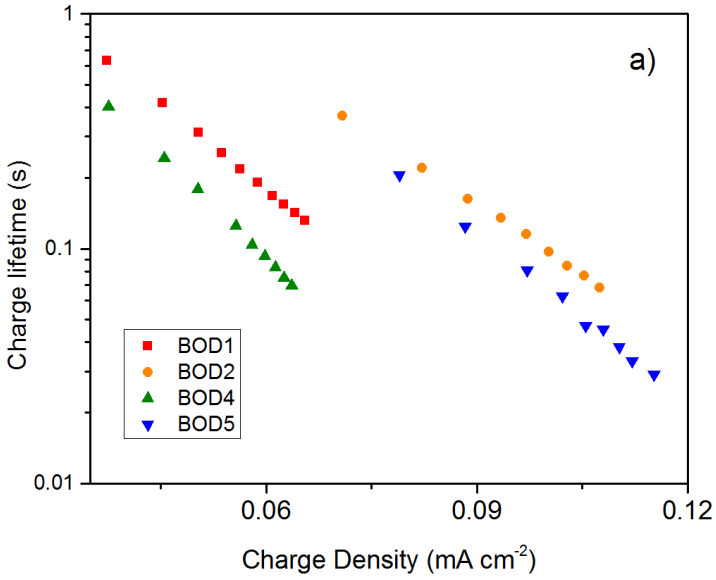

Figure 4.12: Charge transient measurements of p-type dye-sensitised solar cells with BOD1, BOD2, BOD4 and BOD5. The cells were the same as those used for the current-voltage curves shown in Figure 4.10 and IPCE plots in Figure 4.11.

In general, the charge lifetime and extracted charge at a given photovoltage are similar for all systems. There is a slight increase in the charge lifetime at a given charge density for cells assembled with BOD2 and BOD5 relative to cells assembled with BOD1 or BOD4, which is consistent with the higher photovoltaic performance of the former systems. The process of dye-regeneration is therefore likely responsible for the differences in IPCE of these dyes. The driving force for regeneration, ΔG_{reg}, is the energy difference between the reduction potential of the dye, $E(D/D^-)$ and the redox potential of the electrolyte, $E(I_3^-/I_2^{-\bullet})$, as shown in Equation 4.2.

$$\Delta G_{reg} \approx E(D/D^-) - E(I_3^-/I_2^{-\bullet}) \tag{4.2}$$

The values of ΔG_{reg} for BOD1-5 with an iodide/triiodide redox couple are given in Table 4.3 and are determined from the electrochemical and photophysical properties of BOD1-

5 which were performed by members of the group and are detailed in the Appendix in Table A.1. The driving forces for injection, ΔG_{inj}, are also given, and this parameter is defined as the energy difference between the excited state reduction potential of the dye, $E(D^*/D^-)$, and the valence band potential of nickel oxide, $E(NiO_{VB})$.[31] The energy of the NiO valence band edge is -0.12 V vs fc/fc^+, and the energy of the iodide/triioide redox couple is -0.82 V vs fc/fc^+.[32] The excited state reduction potential is determined as described in Equation 4.4, where $E_{0\text{-}0}$ is the energy difference between the S_0 ground state and the S_1 excited state.

$$\Delta G_{inj} \approx E(NiO_{VB}) - E(D^*/D^-) \tag{4.3}$$

$$E(D^*/D^-) = D/D^- + E_{0\text{-}0} \tag{4.4}$$

	ΔG_{inj} (eV)	ΔG_{reg} (eV)
BOD1	-0.80	-0.81
BOD2	-0.91	-0.66
BOD3	-0.94	-0.47
BOD4	-0.79	-0.84
BOD5	-0.99	-0.45

Table 4.3: Values for the driving forces for charge-injection, ΔG_{inj}, and dye-regeneration, ΔG_{reg}, determined from electrochemical data provided in ref [26] according to Equations 4.2 and 4.3.

For BOD1 and BOD4, ΔG_{inj} is slightly lower than for the other dyes by *ca.* 100 mV, which is consistent with our transient absorption experiments where a small amount of stimulated emission was observed on nickel oxide, suggesting that the rate of charge-injection was slower for these systems. The ΔG_{reg} for BOD3 and BOD5 are lower than that of BOD2 which also has the longest-lived charge-separated state. This suggests that regeneration with the iodide/triiodide redox couple is more efficient for BOD3 and BOD5, but further studies are required to investigate this process.

4.3.5 Conclusions

This study aimed to determine the effect of modifying the donor-acceptor π bridge, the anchor-donor π bridge and the structure of the bodipy acceptor groups on the charge-separated state lifetimes and photovoltaic performances of a series push-pull dyes. In general the dyes generated reasonable photocurrent densities in p-type nickel oxide dye-sensitised solar cells despite the fast picosecond to nanosecond charge-recombination which was observed for all systems. This is similar behaviour to that of P1, which generated over 5 mA cm^{-2} but has a short charge-separated state lifetime (τ = 200 ps).

In solution the excited state lifetimes of BOD1-5 are between 50 ps and 5 ns, which is different to the long-lived triplet excited state which was previously observed for BOD2.[18] BOD3 and BOD5 contain bodipy groups which are unsubstituted at the β positions, allowing greater rotational freedom around the donor-acceptor bridge. These dyes therefore have broader, red-shifted absorption profiles relative to BOD1, BOD2 and BOD4, which leads to an increased IPCE at longer wavelengths. BOD3 and BOD5 also have slightly longer charge-separated state lifetimes relative to BOD1 and BOD4, which may contribute to the higher performance of the former systems. The charge transfer nature of the electronic transition for BOD3 and BOD5 results in electron density residing further from the nickel surface relative to BOD1 and BOD4 which have π-π^* transitions. The increased distance between the electron density in the reduced dye and the nickel oxide likely decreases the rate of recombination. BOD2 has the longest-lived charge-separated state (τ = 180 ns), but a lower IPCE than BOD3 and BOD5, which is attributed to differences in the efficiency of the dye-regeneration process.

In general this study shows that push-pull dyes containing a triphenylamine donor group and bodipy acceptors are useful photosensitisers, as they are highly-absorbant and many structures can be accessed through synthetic modifications to the bodipy core. The highest photovoltaic performance was achieved for systems where the β position is unsubstituted and a thiophene π bridge connects the donor to the acceptors. Despite the promising solar cell performance of these dyes, our group still provides the only examples of bodipy-containing photosensitisers used in nickel oxide dye-sensitised solar cells.

In the following section transient absorption spectroscopy is performed for another series

of push-pull dyes, and a significant difference in the excited state dynamics is observed in the presence and absence of an electrolyte containing an iodide/triiodide redox couple. This is an important factor when translating the kinetic behaviour of dyes absorbed onto a dry film to the inner workings of a dye-sensitised solar cell and any future studies on BOD1-5 should include experiments in the presence of the redox electrolyte. Also, BOD1-5 are all assumed to bind through the carboxylic anchoring group and this was not investigated as there are many examples of dyes which are assumed to bind to nickel oxide in this way.[6,33–36] In some cases photoelectron spectroscopy studies on sensitised nickel oxide surfaces have been used to investigate this binding.[37] However, the dyes have large structures with multiple functional groups and in the following sections infrared spectroscopy is used to try determine the method of binding, as this may affect the comparability of the dyes.

4.4 Cationic acceptor dyes

Contributions for Section 4.4: The synthesis and photovoltaic properties of cationic dyes was performed by members of the Gibson group. Spectroelectrochemistry, infrared spectroscopy, transient absorption spectroscopy and time-resolved infrared spectroscopy were performed by the author.

4.4.1 Introduction

In the previous section we observed that the photophysical properties of push-pull dyes were affected by the structure of the acceptor groups. Dyes containing bodipy groups which were unsubstituted in the β positions had red-shifted absorption bands and gave higher IPCE values than those which had methyl substituents. For tandem dye-sensitised solar cells, a p-type dye which absorbs above 600 nm is required to minimise the spectral overlap between the photoanode and the photocathode.[19] Despite their favourable photophysical properties, the bodipy photosensitisers in the previous section showed relatively short charge-separated state lifetimes on nickel oxide, and no photocurrent was generated when a cobalt$^{2+/3+}$ electrolyte was used.

The push-pull dyes discussed in this section contain cationic acceptor groups with the structure 1-hexyl-2,3,3-trimethyl-3H-indolium. Relative to bodipy photosensitisers, there

are fewer examples of dye-sensitised solar cells which use cationic dyes.[38,39] In fact, the systems reported by Lin *et al.* and by our group are the only examples of cationic push-pull dyes used in p-type nickel oxide dye-sensitised solar cells.[19,21,40] The charged nature of the acceptor is of particular interest as this may promote a pre-association of the dye with species in the iodide/triiodide electrolyte and result in fast regeneration, as has been reported for P1 by Qin *et al.*[8] The dyes CAD1-3 which are shown in Figure 4.13 have been reported previously by our group and contain a triphenylamine donor group and a carboxylic acid anchor.[19,21] Dyes with alkyl substituents have been reported to slow charge-recombination at the surface,[41] such as those around the donor group of CAD2. CAD4 contains a different donor and anchor moiety and has not been reported in the literature prior to this work.

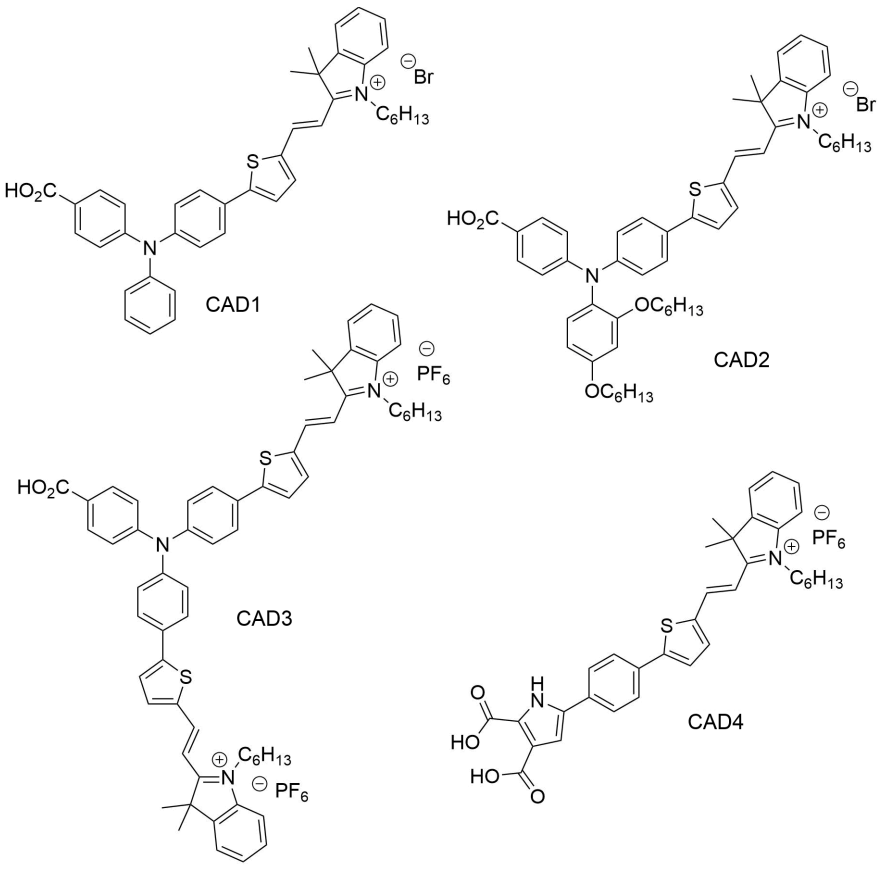

Figure 4.13: Structures of cationic acceptor dyes synthesised by members of the group. The synthesis, photophysical and photovoltaic properties of CAD1, CAD2 and CAD3 have been reported in ref [21] and ref [19].

The photophysical, electrochemical and photovoltaic properties of CAD1-3 are given in

ref [21] and ref [19] and selected data is shown in Table 4.4 together with that of CAD4. CAD1-3 have absorption maxima above 600 nm, and CAD3 has a molar absorption coefficient over three times higher than the other dyes due to the increased probability of an electronic transition when two indolium groups are present. The driving forces for charge-injection and regeneration (ΔG_{inj} and ΔG_{reg}) are calculated from photophysical and electrochemical data, as for BOD1-5 using Equations 4.2 and 4.3. It has been reported that for a series of push-pull dyes which contained different acceptor groups that those which had lower LUMO levels had insufficient ΔG_{reg} and did not perform well in a dye-sensitised solar cell.[8] This is consistent with CAD1 and CAD2 which have red-shifted absorption bands due to lower LUMO levels and therefore have values of ΔG_{reg} which are 200 mV lower than that of P1 and generate lower photocurrent densities. However, CAD3 also has a lower ΔG_{reg} than P1 (ΔG_{reg} = -0.48 V)[8] but performs better in a p-type solar cell.

	λ_{max}[a] (nm)	ε (dm^3 mol^{-1} cm^{-1})	V_{OC} (mV)	J_{SC} (mA cm^{-2})	IPCE (%)	ΔG_{inj} (eV)	ΔG_{reg} (eV)	τ $dye^-|NiO^+$[b] (ps)
CAD1	608	22 900	87	3.32	27	-0.79	-0.23	300
CAD2	629	25 300	96	3.25	20	-0.81	-0.15	100
CAD3	614	94 580	101	8.21	50	-0.91	-0.17	-
CAD4	532	12 625	84	3.96	35	-1.02	-0.16	-

Table 4.4: Important electrochemical and photophysical properties for CAD dyes, from ref [21], ref [19] and ref [42]. [a]Absorbance maximum in dichloromethane solution. Solar cells characteristics are for nickel oxide dye-sensitised solar cells with an electrolyte containing 0.1 M I_2 and 1.0 M LiI in acetonitrile. The IPCE values given are at the λ_{max}. [b]Charge-separated state lifetimes on nickel oxide. The charge-shift state and charge-separated state lifetimes of CAD3 and CAD4 are investigated in this work.

CAD4 contains a different binding moiety and a dicarboxypyrrole anchoring group which was developed in collaboration with the group of Dr. Camp. There has been comparatively less research into alternative anchoring systems for p-type dyes[34,43] relative to n-type dyes,[44–48] and carboxylic anchors are still most commonly used. Changes to the electron density on the anchor group affects the HOMO energy which influences ΔG_{inj}, and should not significantly affect ΔG_{reg}. Therefore, CAD4 has a larger value of ΔG_{inj} than for CAD1-3 but a similar value of ΔG_{reg}. CAD1 nickel oxide p-DSCs performed slightly better than CAD2, and CAD3 outperformed both dyes with devices achieving a photocurrent density

8.21 mA cm^{-2}, and 5.2 mA cm^{-2} in a tandem cell with a D35|TiO_2 photoanode, in which the photocurrent response of CAD3 was well above 600 nm. CAD4 p-DSCs performed similarly to CAD1 and CAD2, which is encouraging for potential dyes using this new binding moiety. The charge-separated state lifetimes of CAD1 and CAD2 are also given in Table 4.4, and were on a similar timescale to the bodipy photosensitisers studied in the previous section of this thesis. CAD1 has a slightly longer-lived charge-separated state relative to CAD2, despite the alkyl groups which aimed to slow charge-recombination in the latter dye. The charge-separated state lifetimes of CAD3 and CAD4 are investigated in this work using transient absorption and time-resolved infrared spectroscopies.

4.4.2 Steady state absorption

The ground state absorption of CAD3 and CAD4 are characterised by their electronic absorption profiles in dichloromethane and acetonitrile solutions, which are shown in Figure 4.14. Both dyes have a broad absorption band between 500 nm and 600 nm, and this extends to 700 nm for CAD3. Both CAD3 and CAD4 also show a strong solvatochromic shift when dissolved in dichloromethane relative to in acetonitrile (*ca.* +55 nm for CAD3 and +30 nm for CAD4), which suggests that the main absorption peak is due to a charge transfer transition.

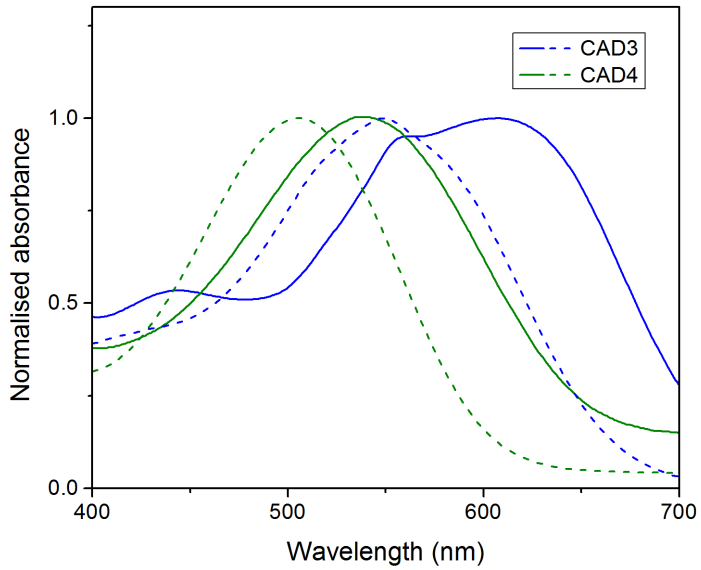

Figure 4.14: Electronic absorption spectra of CAD3 and CAD4 in dichloromethane (solid lines) and in acetonitrile (dashed lines).

The ground state infrared spectra of CAD3 and CAD4 were recorded as powders crushed and pressed into potassium bromide disks. The spectra are shown in Figure 4.15 along with thiophene, triphenylamine and the indolium acceptor group which were recorded to assign the vibrations in the dyes. The assignments of the major bands are given in Table 4.5. The infrared spectra of CAD3 and CAD4 both contain intense bands at 1575 cm^{-1} and 1290 cm^{-1}, which are attributed to the ν(C=C) of the phenyl groups due to their similarity to the major bands present in the infrared spectra of triphenylamine.

Assignment	Wavenumber, cm^{-1}	
	CAD3	CAD4
C=O	1699 br	1699 br
C=C (Phenyl)	1574, 1288	1576, 1298
C=C (Indolium)	1456, 1368	1456, 1368
C=C (Thiophene)	1422	1422

Table 4.5: Assignments and frequencies of the major bands in the ground state infrared spectra of CAD3 and CAD4 shown in Figure 4.15.

The infrared spectra of the indolium acceptor group has three distinctive bands at 1628 cm^{-1} to 1593 cm^{-1}, though this is not observed for CAD3 or CAD4 and may be masked by other vibrations. The indolium group also has a strong band at 1460 cm^{-1} and a weak band at 1377 cm^{-1} which appear in the infrared spectra of CAD3 and CAD4 at 1456 cm^{-1} and 1386 cm^{-1}, though are weak. A band at 1422 cm^{-1} in the infrared spectra of CAD3 and CAD4 is attributed to the ν(C=C) of the thiophene group, and a weak broad band centered at 1699 cm^{-1} is attributed to the ν(C=O) of the anchor groups.

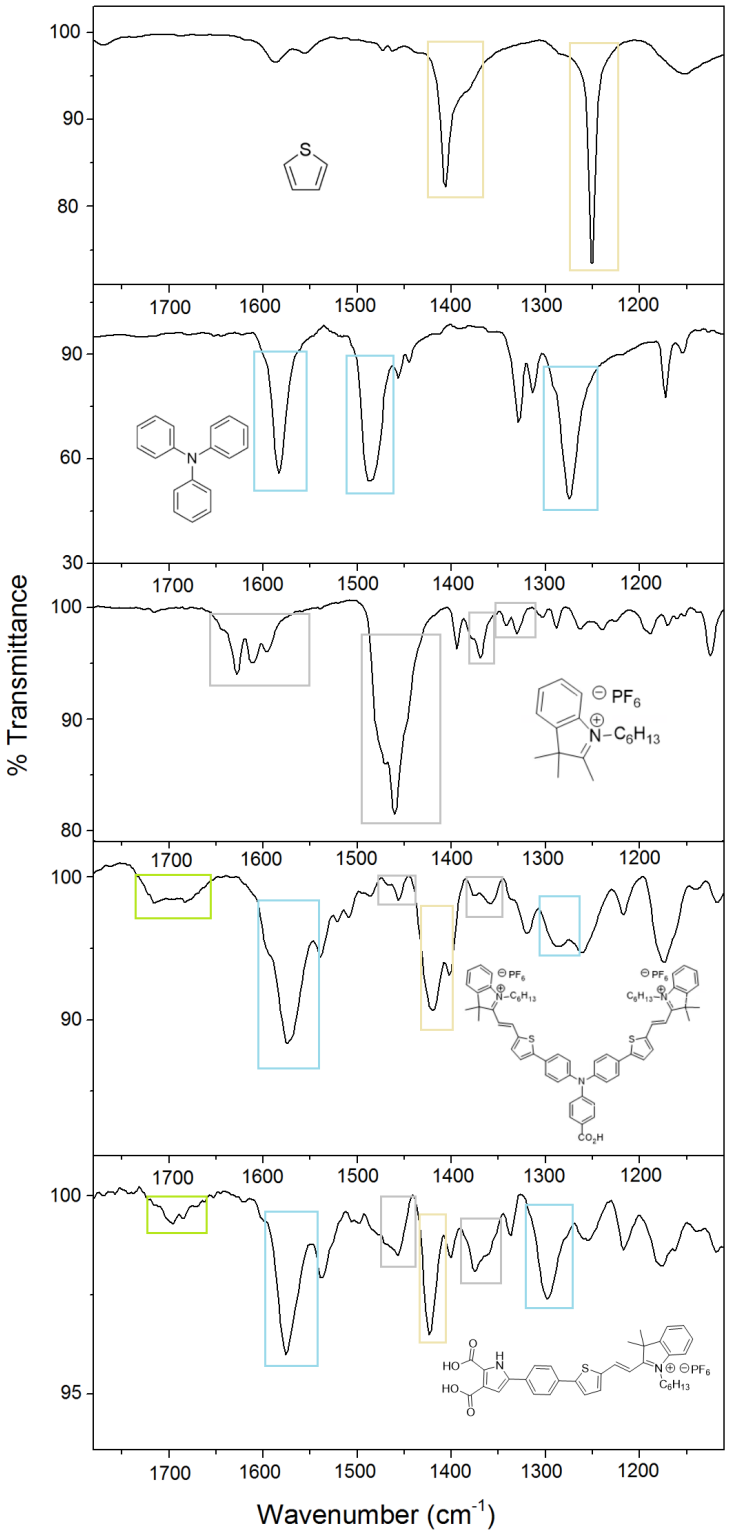

Figure 4.15: Ground state vibrational spectra of thiophene, triphenylamine, the indolium acceptor, CAD3 and CAD4. The infrared spectra of CAD3, CAD4, the acceptor and triphenylamine were measured as powders crushed and pressed into potassium bromide disks. The infrared spectrum of thiophene was recorded as a neat liquid.

To investigate the method of binding of the new pyrrole anchor group, the infrared spectrum of CAD4 adsorbed on a nickel oxide film was recorded and is shown in Figure 4.16.

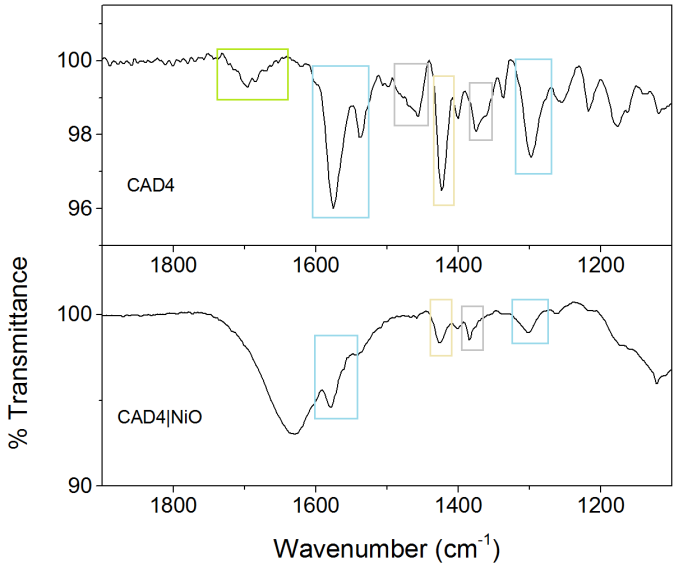

Figure 4.16: Ground state infrared spectra of CAD4 as a powder and adsorbed on nickel oxide. Samples were crushed and pressed into potassium bromide disks for analysis.

Sensitised nickel oxide films were prepared as outlined in Section 3.2.1, and were then scraped from the substrate and ground and pressed into potassium bromide disks. The infrared spectrum of CAD4|NiO contains ν(C=C) vibrations relating to phenyl, thiophene and indolium groups. The weak carbonyl stretch is considerably reduced, which may suggest that both carboxylic groups bind to the nickel oxide surface during sensitisation, or that the stretch is masked by the broad band at 1620 cm^{-1} which is due to the nickel oxide.[49]

4.4.3 Spectroelectrochemistry

Spectroelectrochemistry in the visible and infrared regions was used to characterise the reduced forms of CAD3 and CAD4 for comparison with transient absorption and time-resolved infrared spectra. A thin-film method was used for experiments in the visible region as little sample was available, as described in Section 3.5. Briefly, a titanium dioxide film on FTO coated glass was sensitised with CAD3 or CAD4 and placed in a quartz cuvette which was filled with a solution of lithium perchlorate in acetonitrile. The

film was connected to a potentiostat together with a platinum mesh counter electrode and a silver/silver^{+} wire reference electrode. The cuvette was placed in the path of a visible spectrometer and the potentiostat was set to apply a reducing potential stepwise to that of the first reduction. In Figure 4.17 the absorbance and absorbance difference spectra are shown.

The visible spectrum of CAD3^{-} is sharper and blue-shifted relative to that of CAD3, and contains an additional broad peak which absorbs between 700 nm and 800 nm. The visible spectrum of CAD4^{-} was red-shifted relative to that of CAD4, and contains a broad absorption at longer wavelengths similar to that observed for CAD3^{-}.

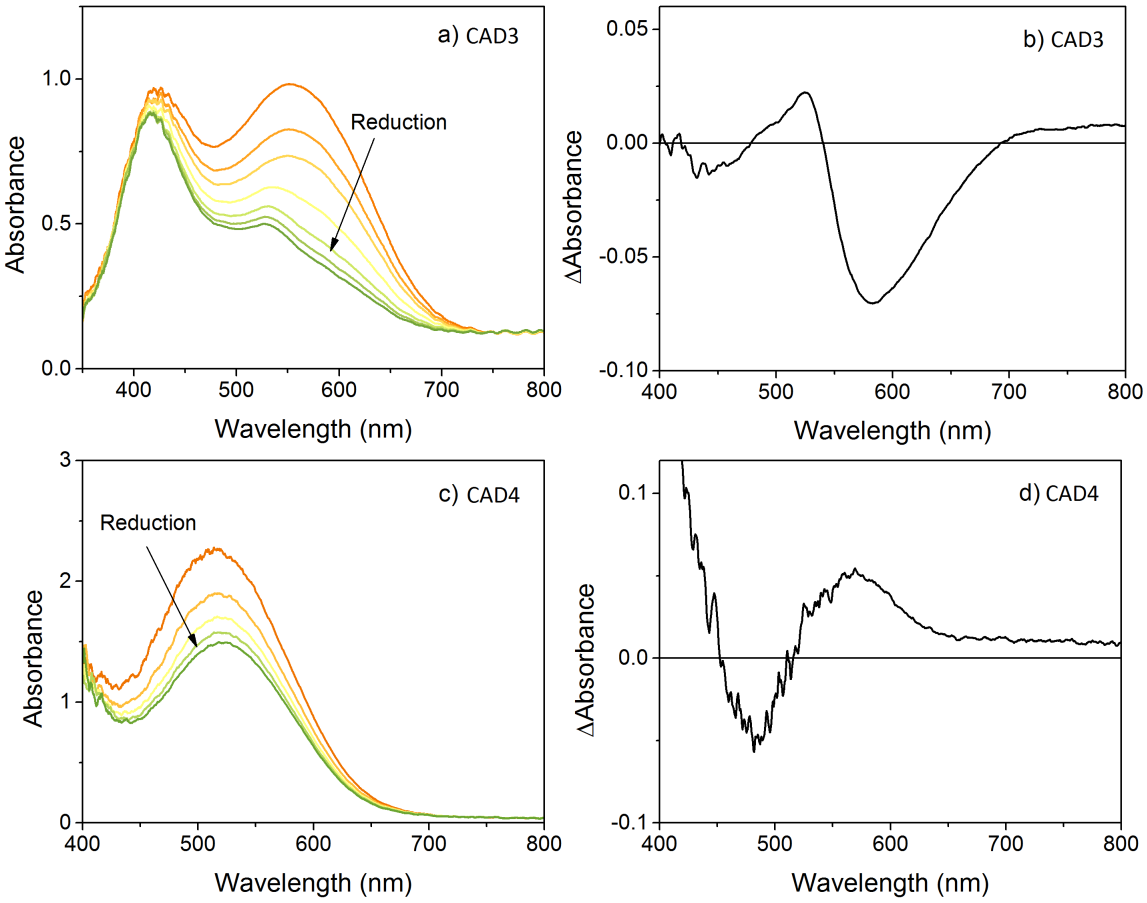

Figure 4.17: Absorbance spectra of CAD3 and CAD4 as a reducing potential from 0 V to -0.9 V vs Ag/Ag^{+} was applied electrochemically to sensitised titanium dioxide films. Left) evolution of the visible spectra; right) visible difference spectra.

For spectroelectrochemical experiments in the infrared region, triphenylamine and the indolium acceptor were used to investigate the behaviour of the donor (D) and acceptor

(A) groups upon oxidation and reduction, respectively. The indolium acceptor (A) was reduced to A^- using two methods to confirm the results, an electrochemical reduction using an OTTLE cell, and by chemical reduction with cobaltocene. The setup of the OTTLE cell is given in the Experimental Section 3.5. The cell was filled with a dichloromethane solution of the acceptor in tetrabutylammonium perchlorate and was placed in the path of an infrared spectrometer.

A reducing potential was applied and an infrared spectrum was taken. The spectra before and after reduction are shown in Figure 4.18, a). Reduction of A to A^- leads to the appearance of a band at 1650 cm^{-1} and the band at 1610 cm^{-1} increases in intensity.

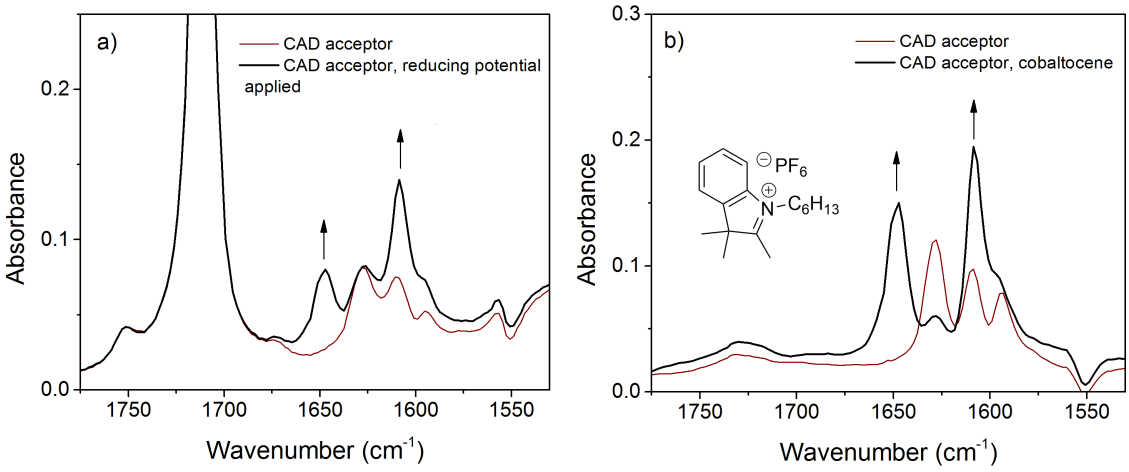

Figure 4.18: Spectroelectrochemical reduction of the indolium acceptor group (A) (structure shown inset). a) Electrochemical reduction in an OTTLE cell with 10 mM indolium acceptor in 0.1 M tetrabutylammonium perchlorate in dichloromethane. The reducing potential was -1.0 V vs Ag/Ag^+; b) chemical reduction with cobaltocene in a Harrick solution cell with a *ca.* 200 μm PTFE spacer and 10 mM solution of A in dichloromethane.

When A is chemically reduced by cobaltocene to A^-, the infrared spectra are similar relative to when reduced electrochemically. A Harrick solution cell[50] with calcium fluoride windows was purged with nitrogen and filled with a degassed solution of the acceptor group in dichloromethane. An infrared spectrum was taken before and after the addition of cobaltocene to the solution. The spectrum of A^- is shown in Figure 4.18 b), and resembles that of the electrochemically reduced A^-.

The donor group triphenylamine (D) was electrochemically oxidised to D^+ in an OTTLE cell as an infrared spectrum was taken, as described for A. The supporting electrolyte

contained tetrabutylammonium perchlorate in deuterated chloroform, and the spectra are shown in Figure 4.19. The infrared spectrum of D contains a sharp band at 1587 cm^{-1}, which is broadened in the spectrum of D^+. Bands at 1607 cm^{-1} and 1348 cm^{-1} are also present in the infrared spectrum of D^+.

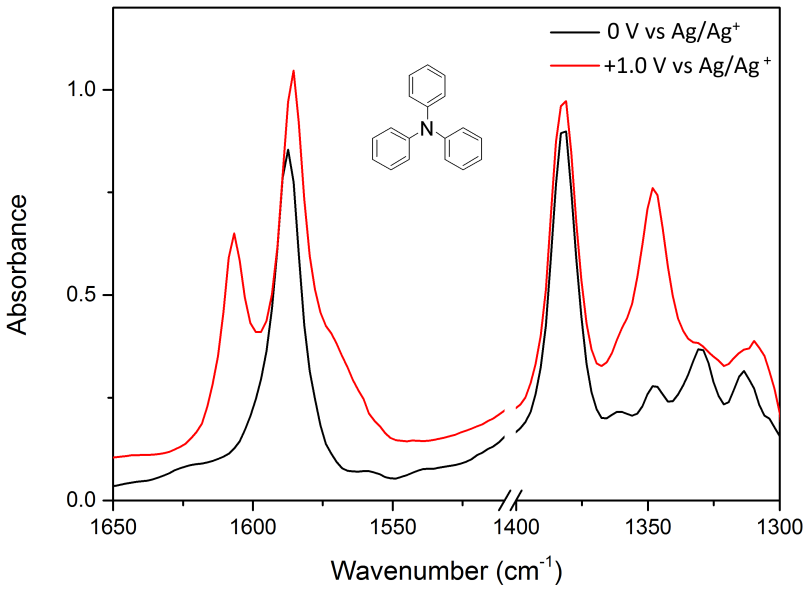

Figure 4.19: Infrared spectra of triphenylamine (D) (structure shown inset) and D^+ generated electrochemically in 0.1 M tetrabutylammonium perchlorate in deuterated chloroform. The oxidising potential was 1.0 V vs Ag/Ag^+.

4.4.4 Transient absorption spectroscopy

Ultrafast transient absorption spectroscopy was used to determine the excited state and charge-shift state lifetimes of CAD3 and CAD4 in solution and the charge-separated state lifetimes of CAD3 and CAD4 adsorbed on nickel oxide. Experiments on nickel oxide films were also performed in the presence of an electrolyte containing 3 mM iodine and 0.1 M lithium iodide in acetonitrile to investigate the dye-regeneration process. A lower concentration of iodine was used relative to a typical dye-senisitised solar cell to minimise the contribution from the electrolyte in the absorption spectrum. The experiments were run in dichloromethane and deuterated acetonitrile to investigate the effect of the solvent on the charge transfer dynamics. A Harrick cell was filled with either a solution of dye or a film of dye-sensitised nickel oxide, which were prepared as described in Experimental Section 3.7. The sample was excited with a 532 nm laser pulse and the visible spectra were

probed with a white light beam. Single-point analysis of the data was used to estimate the lifetimes of each process. The transient absorption difference spectra of CAD3 and CAD4 are shown in Figure 4.20 and Figure 4.21.

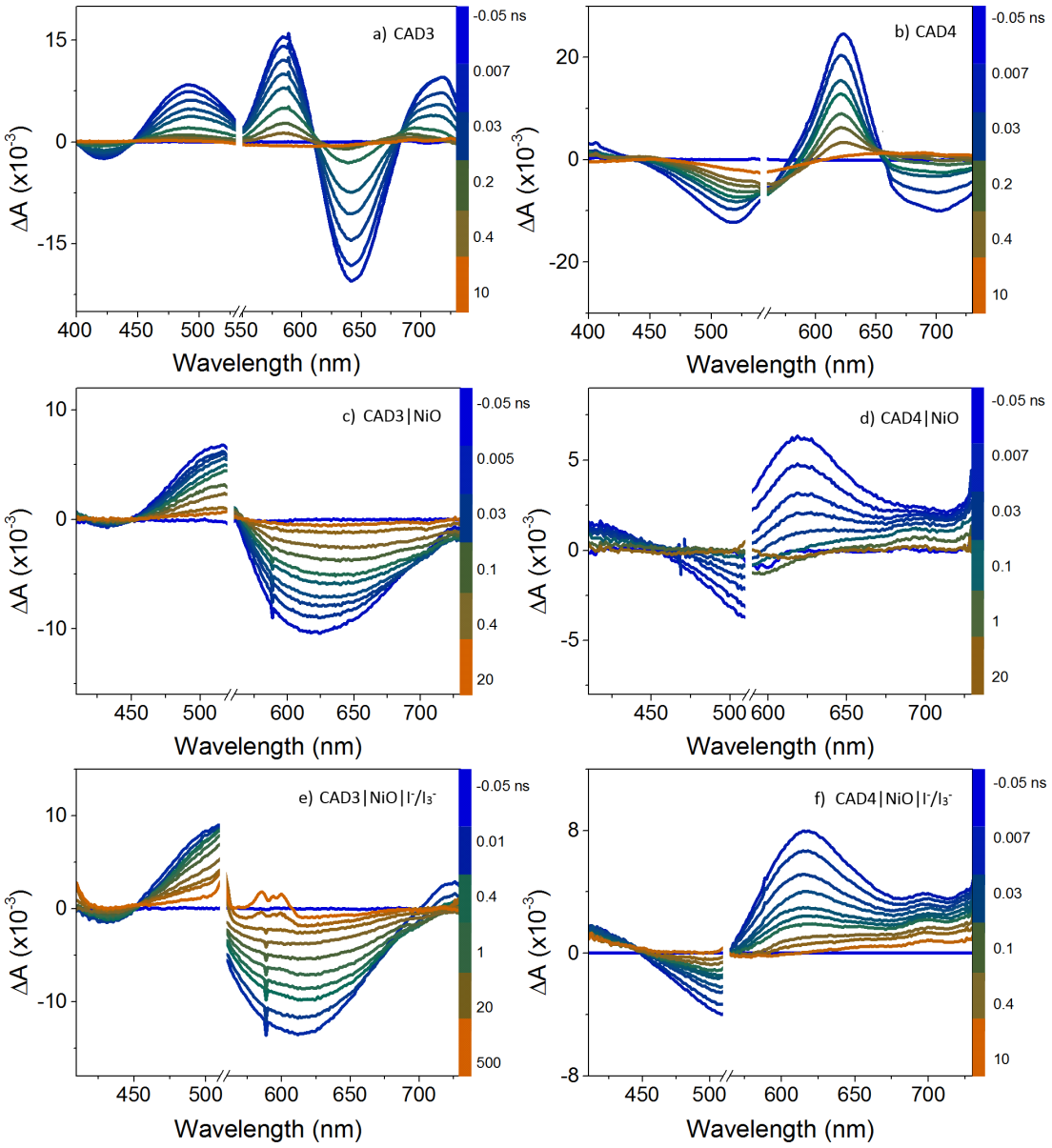

Figure 4.20: Transient absorption difference spectra of CAD3 and CAD4 at selected time delays following excitation at 532 nm. a),b) in dichloromethane; c),d) adsorbed in nickel oxide ; e),f) on nickel oxide in the presence of an electrolyte containing 3 mM I_2 and 0.1 M LiI in acetonitrile.

Results from single-point analysis are given in Tables 4.7 and 4.6. Table 4.8 contains amplitude-weighted average lifetimes, which were calculated for selected wavelengths as described in Theory Section 2.3.2 using Equation 4.5.

$$\tau_{\mathrm{Av}} = (A_1 \times \tau_1) + (A_2 \times \tau_2)..... \tag{4.5}$$

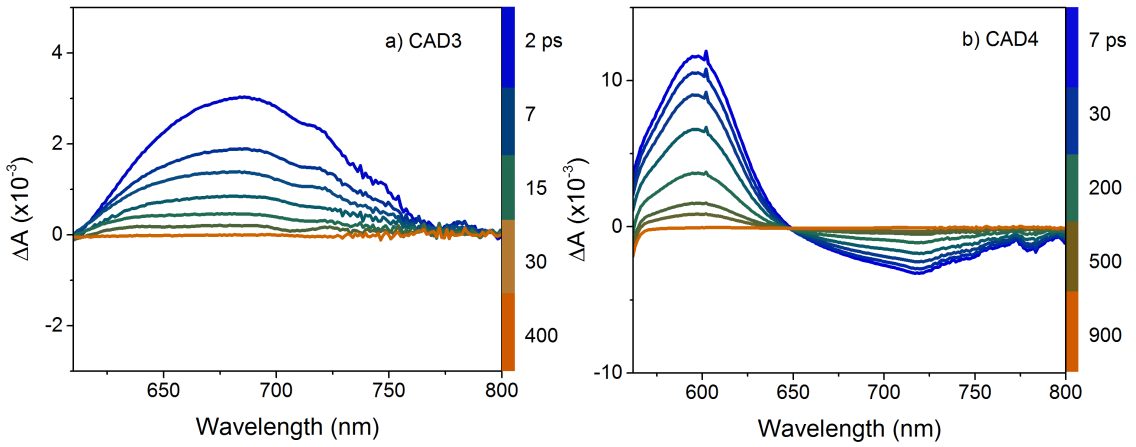

Figure 4.21: Transient absorption difference spectra of CAD3 and CAD4 in deuterated acetonitrile solution at selected time delays following excitation at 532 nm.

Laser excitation of CAD3 at 532 nm in dichloromethane generates a negative signal between 610 nm and 680 nm which is attributed to the ground state absorption. A broad transient signal which resembles the spectrum of $CAD3^-$ (Figure 4.17) absorbs between 450 nm and 600 nm and at wavelengths above 700 nm, and is attributed to the charge-transfer excited state. This signal decays with τ = 55 ps in dichloromethane and τ = 7 ps in deuterated acetonitrile, which is between that of CAD1 and CAD2 (τ_{CAD1} = 120 ps, τ_{CAD2} = 25 ps in dichloromethane). The transient absorption spectra of CAD4 in dichloromethane resemble $CAD4^-$ generated by spectroelectrochemical methods. The decay of the sharp absorption between 590 nm and 650 nm was fit to a bi-exponential function due to a slight red-shift of the peak at later delay times. This shift was not observed in the transient absorption spectra of CAD4 in deuterated acetonitrile solution (Figure 4.21). Unlike for BOD1-5, stimulated emission is not observed for CAD3 or CAD4 in solution, and was also absent for transient absorption experiments of CAD1 and CAD2.[21]

On nickel oxide the transient absorption spectra of CAD3 and CAD4 are broadened relative to solution, which is consistent with interactions between the dye and nickel oxide. For CAD4|NiO the presence of a broad absorption at longer wavelengths is characteristic

of holes in nickel oxide which suggests that the charge-separated state is formed. For CAD3|NiO the ground state absorption extends further to the red-region and masks this signal. Transient species in the spectra of CAD3|NiO were fit to a multi-exponential function which is consistent with heterogeneous recombination of the dye with holes in nickel oxide,[2,51–55] with $\tau_{\mathrm{Av}} = 1.2$ ns. The bleach at 428 nm has a shorter lifetime than that of the main transient and ground state bleach. An additional small positive peak at 700 nm is present in the transient absorption spectra of CAD3|NiO in the presence of iodine and lithium iodide. The dynamics of this band were more difficult to resolve due to overlap with the bleach, so a stretched exponential was used, as described by Equation 4.6.

$$Abs(t) = Abs(t0)\, exp(-(t/\tau)\beta) \tag{4.6}$$

Where $Abs(t)$ is the change in absorbance at time t, τ is the lifetime and β is the stretch parameter.

In general, transient species decayed over a longer timescale in the presence of an iodide/triiodide redox couple. The experiment was repeated with a solution of lithium perchlorate in acetonitrile to ensure that this effect wasn't due to the presence of solvent, and the transient species were only slightly longer-lived in this case, (Appendix Table A.4).

	Lifetime, ps	
	CH_2Cl_2	CD_3CN
CAD3	$\tau_{425} = 73 \pm 2$	
	$\tau_{485} = 55 \pm 4$	
	$\tau_{575} = 90 \pm 7$	$\tau_{688} = 6.7 \pm 0.2$
	$\tau_{635} = 48 \pm 1$	
	$\tau_{701} = 63 \pm 3$	
CAD4	$\tau_{518} = 9 \pm 2$ (35%), 200 ±20 (50%)	$\tau_{605} = 166 \pm 2$
	$\tau_{627} = 43 \pm 8$ (50%), 240 ±50 (47%)	$\tau_{704} = 1.1 \pm 0.04$ (55%), 180 ±3 (45%)
	$\tau_{702} = 5 \pm 3$ (32%), 590 ±10 (68%)	

Table 4.6: Lifetimes derived from single-point analysis of the transient absorption spectra of CAD3 and CAD4 in solution. Where a bi-exponential fit is used, the amplitudes of each component are given in brackets. $\lambda_{\mathrm{exc}} = 532$ nm.

	Lifetime, ps	
	NiO	NiO|I^-/I_3^-
CAD3	τ_{428} = 7 ±3 (55%), 270 ±90 (45%)	τ_{435} = 150 ±50 (42%), 22 000 ±6000 (58%)
	τ_{485} = 5 ±1 (37%), 120 ±30 (34%), 4500 ±1000 (26%)	τ_{485} = 24 ±4 (30%), 9100 ±1800 (35%), 311 000 ±84 000(29%)
	τ_{610} = 12 ±2 (38%), 180 ±30 (40%), 7300 ±1600 (22%)	τ_{615} = 18 ±3 (32%), 760 ±130 (34%), 54 000 ±10 000 (28%)
		τ_{720} = 16 ±7
CAD4	τ_{500} = 3 ±0.3 (73%), 43 ±6 (27%)	τ_{495} = 3 ±0.1 (59%), 33 ±9 (25%), 1400 ±400 (18%)
	τ_{640} = 2 ±0.1 (79%), 35 ±6 (21%)	τ_{625} = 3 ±0.1 (64%), 28 ±4 (25%), 740 ±200 (11%)
		τ_{696} = 0.8 ±0.3 (66%), 20 ±8 (15%), 1000 ±400 (14%)
		τ_{704} = 3 ±1 (45%), 110 ±50 (26%), 6100 ±3000 (20%)

Table 4.7: Lifetimes derived from single-point analysis of transient absorption spectra of CAD3 and CAD4 on nickel oxide in the presence and absence of 3 mM I_2 and 0.1 M LiI in acetonitrile. Where a multi-exponential fit is used, the amplitudes of each component are given in brackets. λ_{exc} = 532 nm.

	Lifetime, ps			
	CH_2Cl_2	CD_3CN	NiO	NiO|I^-/I_3^-
CAD3	τ_{425} = 73		τ_{428} = 125	τ_{435} = 12 823
	τ_{485} = 55		τ_{485} = 1212	τ_{485} = 93 382
	τ_{575} = 90	τ_{688} = 6.7	τ_{610} = 1682	τ_{615} = 15 384
	τ_{635} = 48			τ_{720} = 16
	τ_{701} = 63			
CAD4	τ_{518} = 103	τ_{605} = 166	τ_{500} = 14	τ_{495} = 262
	τ_{627} = 134	τ_{704} = 82	τ_{640} = 9	τ_{625} = 90
	τ_{702} = 403			τ_{696} = 144
				τ_{704} = 1250

Table 4.8: Average lifetimes derived from single-point analysis of transient absorption spectra of CAD3 and CAD4.

These results suggest that an interaction between $CAD3^-|NiO^+$ and species in the redox

electrolyte occurs and leads to a reduction in the rate of charge-recombination. Wood *et al.* observed that I^- reacts with Ni^{3+} at the surface,[56] which may inhibit recombination. We therefore suggest that the charged nature of CAD3 promotes this reaction, possibly by associating with I^- and increasing the concentration of this species at the surface.

The charge-separated state of CAD4|NiO recombines considerably faster than CAD3|NiO, with τ_{AV} = *ca.* 10 ps for CAD4|NiO and τ_{AV} = *ca.* 200 ps for CAD4|NiO|I^-/I_3^-. This fast charge-recombination is likely related to the lower performance of CAD4 relative to CAD3. The increase in lifetime in the presence of electrolyte for CAD4|NiO is consistent with our conclusion that this behaviour is due to the charged nature of the dye, though the effect is not as large for CAD4. The relative lifetimes of the charge-shift and charge-separated states of CAD3 and CAD4 are summarised by the decay traces at given wavelengths shown in Figure 4.22.

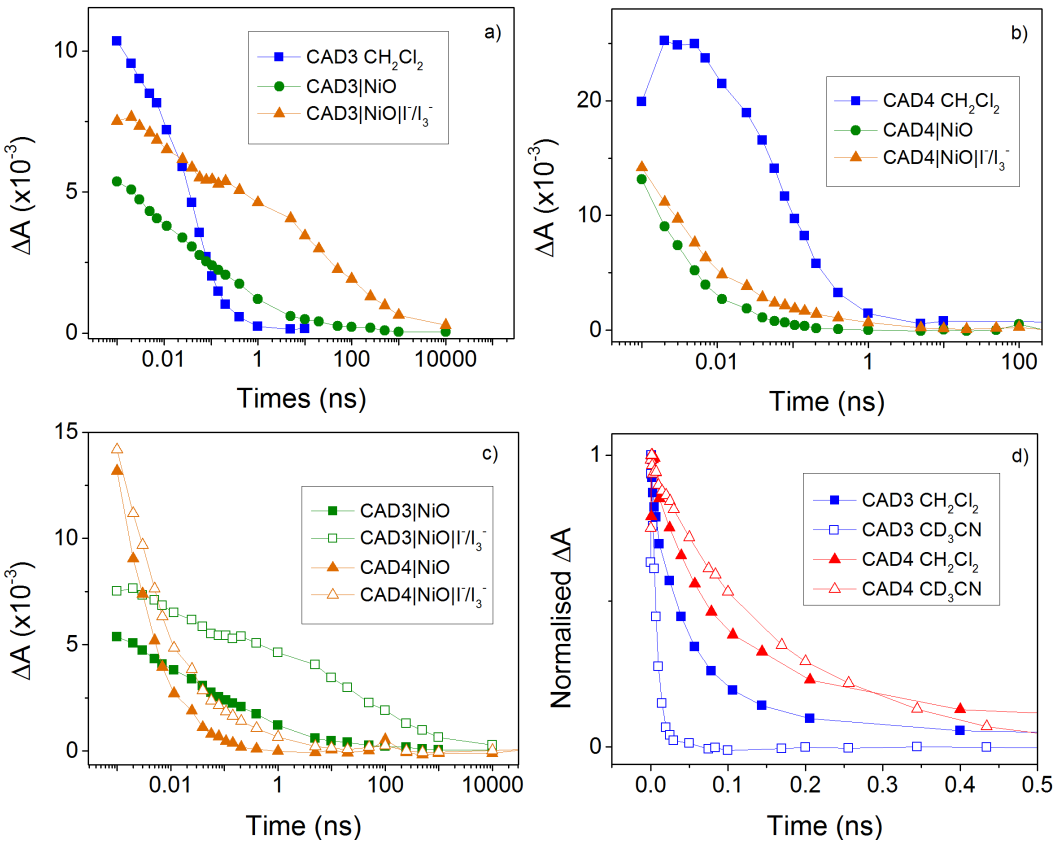

Figure 4.22: Decay traces from transient absorption experiments of CAD3 and CAD4. For d), the amplitude of the change in absorbance is normalised for comparison. Probe wavelengths are at 485 nm for CAD3 and 630 nm for CAD4.

There is a clear increase in the lifetime of CAD3^{-}|NiO^{+} in the presence of iodide/triiodide, and the fast recombination of CAD4|NiO relative to CAD3|NiO is also apparent, despite the longer-lived excited state of CAD4 in both dichloromethane and deuterated acetonitrile solutions.

4.4.5 Time-resolved infrared spectroscopy

Time-resolved infrared spectroscopy was used to probe the vibrational changes of CAD3 in the fingerprint region upon excitation at 532 nm. The experimental setup was the same as described for transient absorption spectroscopy except an infrared probe beam and infrared detector were used. The absorbance difference spectra are shown in Figure 4.23.

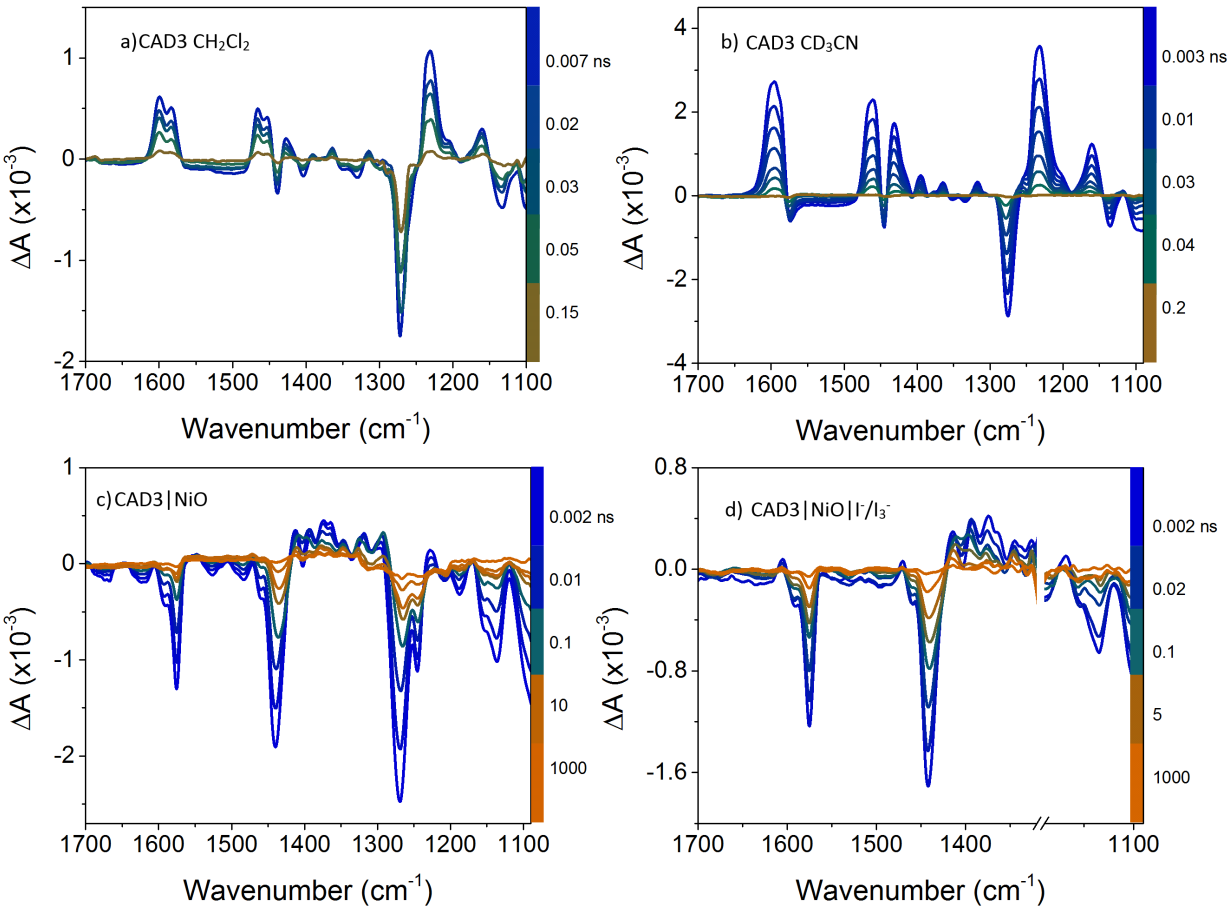

Figure 4.23: Time-resolved infrared difference spectra of CAD3 at selected time delays following excitation at 532 nm. a) In dichloromethane; b) in deuterated acetonitrile; c) on nickel oxide; d) on nickel oxide in the presence of 3 mM I_2 and 0.1 M LiI in deuterated acetonitrile.

Lifetimes obtained from single-point analysis of time-resolved infrared spectra were generally consistent with those obtained from transient absorption data, and are given for selected bands in Table 4.9. The spectral features in the time-resolved infrared spectra of CAD3 in dichloromethane and deuterated acetonitrile are similar, though signals are weaker in dichloromethane, which may be due to a difference in the molar absorption coefficient of the excited species in the two solvents. A negative signal is present at 1275 cm^{-1}, with a sharp transient band at 1230 cm^{-1}. This is attributed to the ν(C=C) of the phenyl groups, along with weaker bleaches at 1551 cm^{-1} in dichloromethane and 1574 cm^{-1} in deuterated acetonitrile. The ν(C=C) at 1601 cm^{-1} is similar to the band observed in the infrared spectrum of D^+ (Figure 4.19). The transient band masks the main bleach which is also consistent with broadening of the oxidised species observed in spectroelectrochemical experiments. The presence of these features is consistent with the formation of the charge-transfer excited state.

Lifetime, ps			
CH_2Cl_2	CD_3CN	NiO	NiO|I^-/I_{3^-}
τ_{1272} = 68 ±30	τ_{1276} = 13 ±0.3	τ_{1268} = 2 ±0.3 (70%),	
τ_{1230} = 42 ±2	τ_{1230} = 7 ±0.3	37 ±8 (19%), 11 000 ± 4000 (11%)	τ_{1574} = 1.1 ±0.2 (59%),
τ_{1601} = 51 ±2	τ_{1597} = 9 ±0.4		37 ±7 (22%),
τ_{1551} = 33 ±4	τ_{1574} = 19 ±0.8	τ_{1574} = 2 ±0.2 (66%),	16 000 ±5000 (19%)
τ_{1463} = 54 ±2	τ_{1460} = 9 ±0.4	36 ±8 (22%), 8800 ± 3300 (12%)	
τ_{1429} = 36 ±2	τ_{1429} = 7 ±0.3		
τ_{1440} = 41 ±3	τ_{1444} = 16 ±0.4	τ_{1440} = 1.0 ±0.1 (73%),	τ_{1318} = 0.6 ±0.1 (69%),
τ_{1329} = 36 ±3	τ_{1333} = 4 ±0.3	30 ±6 (14%), 7800 ±1600 (13%)	27 ±3 (20%),
τ_{1318} = 44 ±3	τ_{1318} = 10 ±0.4	τ_{1318} = 0.6 ±0.1 (71%),	9000 ±2000 (12 %)
τ_{1364} = 41 ±3	τ_{1364} = 13 ±0.6	34 ±6 (16%), 6300 ±1400 (14%)	

Table 4.9: Lifetimes derived from single-point analysis of time-resolved infrared spectra of CAD3. λ_{exc} = 532 nm. Where a multi-exponential fit is used, the amplitudes of each component are given in brackets.

A small bleach at 1440 cm^{-1} in dichloromethane and 1444 cm^{-1} in deuterated acetonitrile is attributed to the indolium acceptor. In the ground state this band appears at 1456 cm^{-1}. The transient band is split around the bleach as it is broader than the ground state absorption. A second weak bleach is attributed to the indolium acceptor at 1329 cm^{-1} in dichloromethane and 1333 cm^{-1} in deuterated acetonitrile. This is at a similar frequency to

the ground state signal at 1368 cm^{-1}. ν (C=O) and ν(C=C) stretches of the carbonyl and thiophene groups are not observed. The lifetimes of the transient bands are consistent with those recorded for CAD3 in transient absorption experiments. In dichloromethane, bands decay with a time constant of *ca.* 50 ps, and in deuterated acetonitrile this is shortened to *ca.* 10 ps. The time-resolved infrared spectra of CAD3 are different when adsorbed on nickel oxide and the signals are generally weaker. The transient signals observed at 1230 cm^{-1}, 1601 cm^{-1}, 1463 cm^{-1} and 1429 cm^{-1} are absent and instead an intense bleach at 1574 cm^{-1} and a series of weak transient bands around 1318 cm^{-1} are present. The decay of the bands is consistent with the charge-shift state determined in transient absorption experiments. Similarly, in the presence of an iodide/triiodide electrolyte, the spectral features are similar to that of CAD3|NiO and the lifetimes are generally longer.

4.4.6 Conclusions

This study aimed to investigate the effect of the cationic indolium acceptor group on the charge-separated state lifetime of two push-pull dyes. It was proposed that a pre-association of the dye and species in the electrolyte may occur and increase the efficiency of dye-regeneration. CAD3 and CAD4 both absorb above 600 nm, and CAD3 generates high photocurrents in a nickel oxide dye-sensitised solar cell despite a relatively small driving force for regeneration. CAD4, which contains a dicarboxypyrrole binding moiety and larger ΔG_{inj} performs better than previously reported CAD1 and CAD2 but does not generate high photocurrents relative to CAD3. This is attributed to the broader absorption of CAD3 and fast charge-recombination which is observed for CAD4 when adsorbed on nickel oxide. Interestingly, the charge-separated state lifetime of CAD3|NiO is on the order of nanoseconds, despite a common assumption that a lifetime on the order of microseconds is required for efficient regeneration. This is similar for P1, BOD3 and BOD5 which have a relatively short charge-separated state lifetimes but generate high photocurrents in nickel oxide dye-sensitised solar cells. Time-resolved spectroscopy experiments showed that the charge-separated state decays over a longer timescale in the presence of a solution of iodine and lithium iodide, which suggested that species in the electrolyte associate with the cationic dyes adsorbed on nickel oxide. This association slows recombination rather than increases the rate of regeneration as was expected, and

the effect is attributed to the promotion of the reaction between I^- and Ni^{3+}.

In general cationic push-pull dyes are a promising class of sensitiser for dye-sensitised solar cells due to their red absorption, good photovoltaic performances and charged nature. However, the broad absorption of these dyes makes spectroscopic analysis of excited states difficult and the charge-separated state did not give a characteristic signal when absorbed on nickel oxide. Also, time-resolved infrared spectroscopy of CAD3 did not give a strong infrared vibration relating to the indolium acceptor group. The following study describes an investigation of two push-pull dyes using time-resolved infrared spectroscopy, and highlights the difficulties of analysing the vibrational spectra of conjugated organic systems which do not contain strong infrared markers.

4.5 Probing vibrational dynamics

Contributions for Section 4.5: Electrochemical, photovoltaic and transient absorption studies of BOD2 and P1 have been reported previously. Synthesis and time-resolved infrared experiments were performed by members of the group. Infrared spectroscopy and analysis of time-resolved infrared data was performed by the author.

4.5.1 Introduction

Increasing the driving force for intramolecular charge-separation within a push-pull dye is anticipated to slow $dye^-|NiO^+$ charge-recombination and therefore improve the performance of dye-sensitised solar cells. However, as discussed in the introduction to this thesis, there is little correlation between the charge-separated state lifetime and solar cell performance when comparing p-type dyes reported in the literature, and a report by Troisi *et al.* reported a similar trend for the donor-acceptor character of n-type dyes.[57] This suggests that charge-recombination dynamics are complex and are influenced by a variety of factors. Here we compare the photophysical, electrochemical and excited state properties of two push pull dyes (P1 and BOD2) which contain different acceptor groups, to determine how their charge-recombination dynamics influence the performance of solar cells fabricated with these dyes.

P1 is widely used as a benchmark dye for p-type nickel oxide dye-sensitised solar cells, and the analogue BOD2, which contains boron dipyrromethene acceptor groups, has been

reported previously by our group.[18] Their structures are given in Figure 4.24, and both contain a triphenylamine donor group, a carboxylic anchor group and a thiophene π bridge to the acceptor moieties.

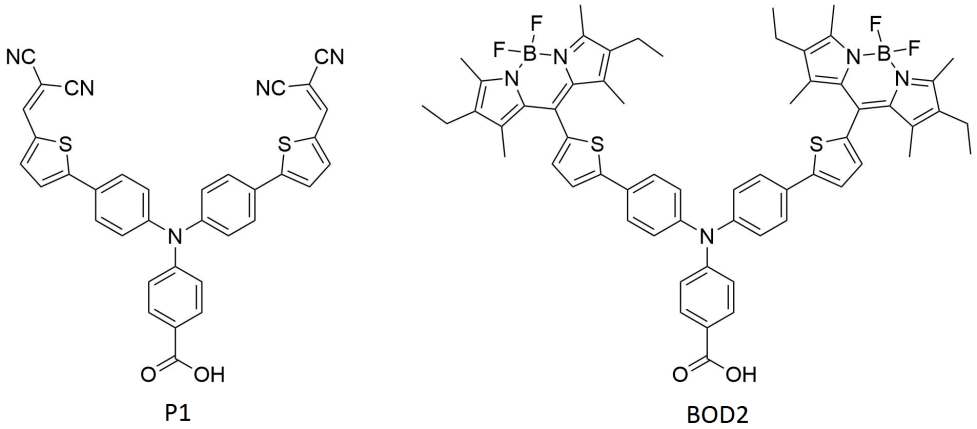

Figure 4.24: Structures of push-pull dyes P1 and BOD2 discussed in this section.

Selected photophysical, electrochemical and photovoltaic data is shown in Table 4.10, and the oxidation and reduction potentials are given in the Appendix in Table A.5. P1 performs significantly better in a p-type dye-sensitised solar cell than BOD2 despite having similar values of ΔG_{reg}, a factor which is related to the LUMO energy level and has previously been reported to contribute to the high performance of P1.[8] ΔG_{inj} is also consistent for both dyes.

	λ_{max}[a] (nm)	ε[b] ($dm^3\ mol^{-1}\ cm^{-1}$)	V_{OC} (mV)	J_{SC} ($mA\ cm^{-2}$)	IPCE[c] (%)	ΔG_{inj}[d] (eV)	ΔG_{reg}[d] (eV)	τ $dye^-|NiO^+$[e] (ps)
P1	481	57 900	84	5.48	63	-0.91	-0.64	2-200
BOD2	540	112 000	79	3.15	28	-0.91	-0.66	180 000

Table 4.10: Electrochemical and photophysical properties and highest photovoltaic performances of P1 and BOD2, taken from ref [8] and ref [18]. [a]Absorbance maxima in dichloromethane. [b]Molar absorption coefficient in dichloromethane. [c]Solar cells characteristics for nickel oxide dye-sensitised solar cells with an electrolyte containing and 0.1 M I_2 for P1 and 0.5 M I_2 for BOD2, and 1.0 M LiI in acetonitrile. [d]The driving forces for injection and regeneration were determined using Equations 4.3 and 4.2 as described in Section 4.3. [e]Charge-separated state lifetimes determined by transient absorption spectroscopy.

P1 has a molar absorption coefficient nearly half that of BOD2, however the absorption spectrum of P1 is much broader, as shown in Figure 4.25 for both dyes adsorbed on nickel

oxide. The solar cell results of BOD2 shown in Table 4.10 are for cells assembled with an electrolyte containing a higher concentration of iodine,[18] and it was shown in Section 4.3 that the efficiencies of BOD2 cells assembled with an electrolyte containing 0.1 M iodine were lower than those assembled with 0.5 M iodine. The IPCE plots in Figure 4.25 are for cells containing 0.1 M iodine, both of which were fabricated by the author for direct comparison of the two dyes.

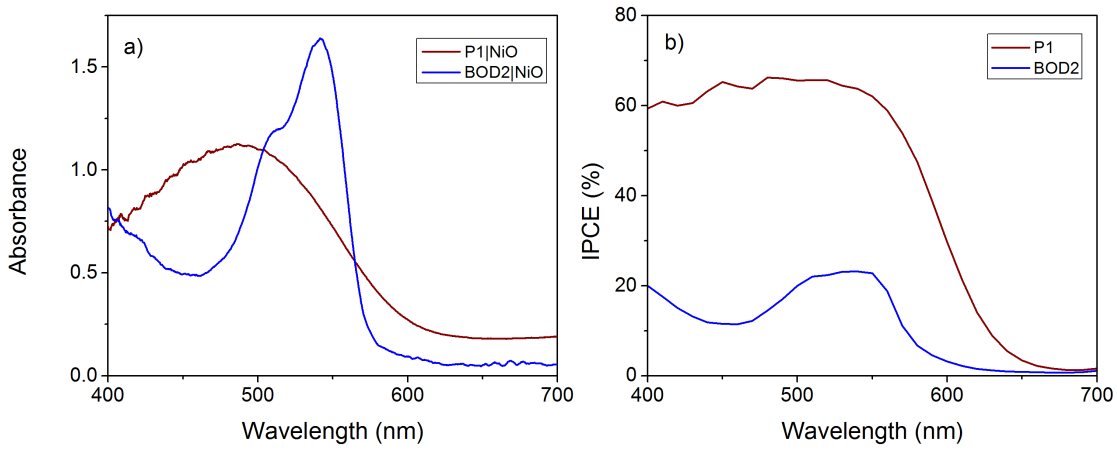

Figure 4.25: a) Absorbance spectra of P1|NiO and BOD2|NiO; b) IPCE spectra of P1 and BOD2 nickel oxide dye-senisitsed solar cells with an electrolyte containing 0.1 M I_2 and 0.1 M LiI in acetonitrile. The IPCE plot of P1 is for a cell which gave similar IPCE to that reported in ref [8].

The singlet excited state lifetime of P1 in acetonitrile solution from transient absorption experiments was relatively short (τ = 30 ps) which was attributed to intermolecular charge transfer caused by aggregation.[8] The first excited singlet state of BOD2 in dichloromethane decayed over 400 ps to form a long-lived triplet excited state with τ = 300 ns. The charge-separated state lifetime of BOD2 (*ca.* 180 ns) is considerably longer than that of P1 (*ca.* 200 ps). The decay of the charge-separated state of P1 was fit to a multi-exponential with lifetimes of 2.7 ps, 17 ps and 205 ps. In the presence of an electrolyte containing an iodide/triiodide redox couple, the $BOD2^{-}|NiO^{+}$ charge-separated state decayed with τ = 23 ns, showing efficient regeneration. In this study time-resolved infrared spectroscopy is used to gain more detailed information about the charge-recombination and dye-regeneration dynamics to explain why these two dyes give such different solar cell performances.

Time-resolved infrared spectroscopy is commonly used in the analysis of charge trans-

fer dynamics for dyes containing metal-carbonyl bonds adsorbed on titanium dioxide films.[58–62]
Our group has used time-resolved infrared spectroscopy in the carbonyl region to investigate the dynamics of the anchor groups of CAD1 and CAD2 which are described in ref [21]. Section 4.4.5 of this chapter described time-resolved infrared spectroscopy of CAD3 and CAD4 in the fingerprint region, where bands relating the the ν(C=C) of the triphenylamine group confirmed the formation of the charge-separated state. Here it is proposed that the malononitrile group of P1 and the bodipy acceptor of BOD2 will be suitable infrared handles to give significant signals in the nitrile and fingerprint regions.

4.5.2 Steady state vibrational absorption

The infrared spectra of P1 and BOD2 were recorded as powders and adsorbed on nickel oxide to characterise the vibrational spectra of the dyes in the ground state. The infrared spectra of thiophene, triphenylamine and the bodipy acceptor group were also measured to assign the bands in the two dyes, and the spectra are shown in Figure 4.26. Vibrational spectra of P1 and BOD2 on nickel oxide are shown in Figure 4.27. Samples for spectroscopic analysis were prepared as potassium bromide disks as described in the Experimental Section 3.6.2. The frequencies of major bands for P1 and BOD2 are given in Table 4.11.

The sharp ν(C=C) bands present in the infrared spectrum of thiophene were described in Section 4.4, and are identified in the infrared spectra of P1 (1427 cm^{-1}, 1244 cm^{-1}) and BOD2 (1423 cm^{-1}, 1224 cm^{-1}). Similarly, three sharp bands corresponding to the ν(C=C) of triphenylamine are present for both P1 (1568 cm^{-1}, 1491 cm^{-1}, 1263 cm^{-1}) and BOD2 (1595 cm^{-1}, 1481 cm^{-1}, 1261 cm^{-1}). The ν(C=O) of the carbonyl anchor group is strong and broad for both dyes, and a sharp band is observed for the ν(CN) of the malononitrile acceptor groups of P1. The ν(C=C) of the bodipy acceptor groups of BOD2 are weaker, but bands at 1543 cm^{-1} and 1385 cm^{-1} in the infrared spectrum of BOD2 are attributed to these vibrations. When the dyes are adsorbed on nickel oxide the ν(C=O) vibration of the carbonyl is absent, which is consistent with the anchoring of the dye to the nickel oxide surface. For BOD2|NiO a small shoulder is present in the carbonyl region but this is difficult to identify due to the overlap of this band with the infrared vibrations of nickel oxide.

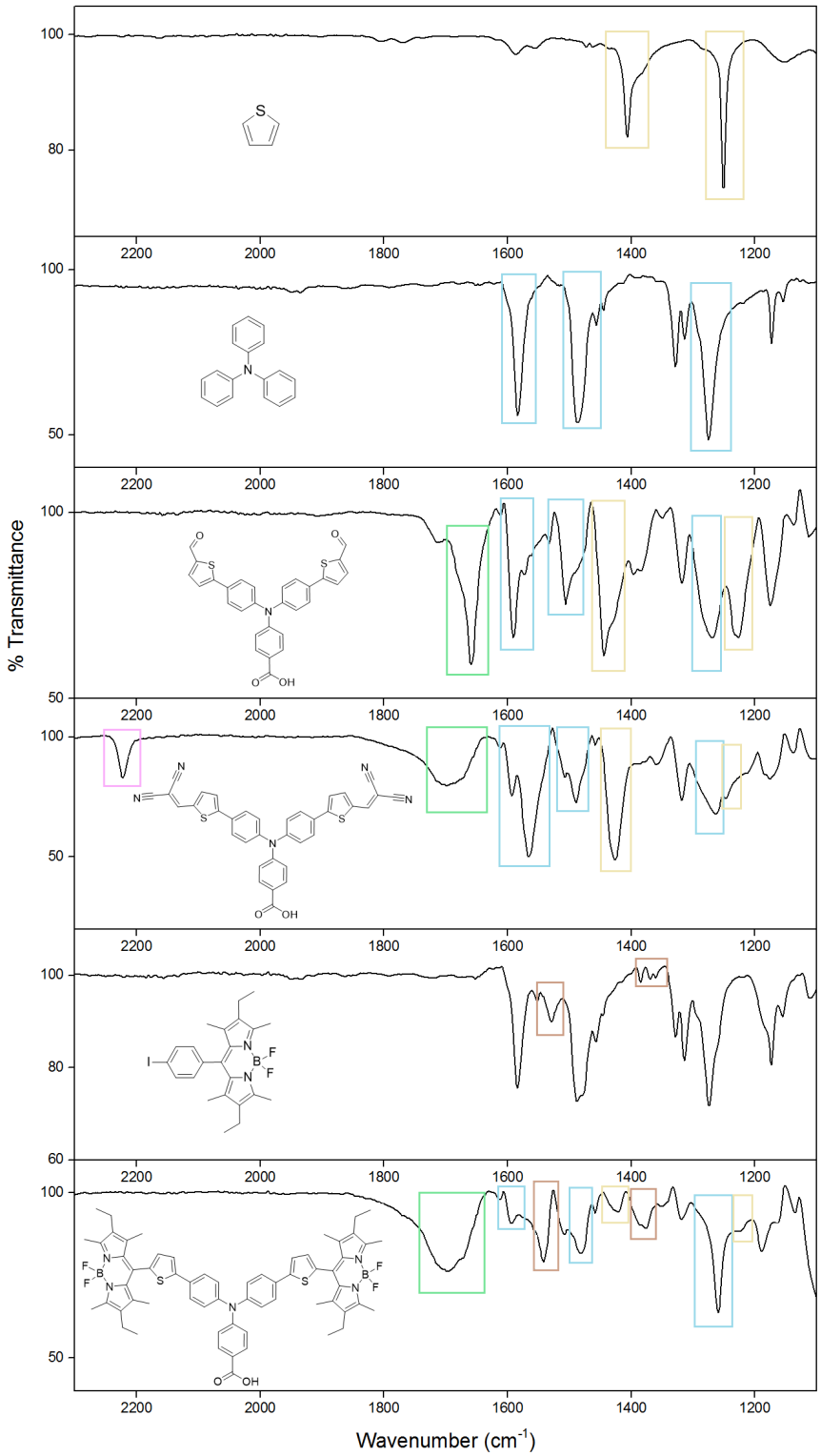

Figure 4.26: Ground state infrared spectra of P1, BOD2 and their precursor molecules. Coloured boxes indicate bands relating to ν(C=C) of thiophene (yellow), triphenylamine (blue), and bodipy (brown) vibrations. Green boxes indicate the ν(C=O) of the carbonyl and pink boxes indicate the ν(CN) of the nitrile stretch. All samples were crushed and pressed into potassium bromide disks except for thiophene which was run neat.

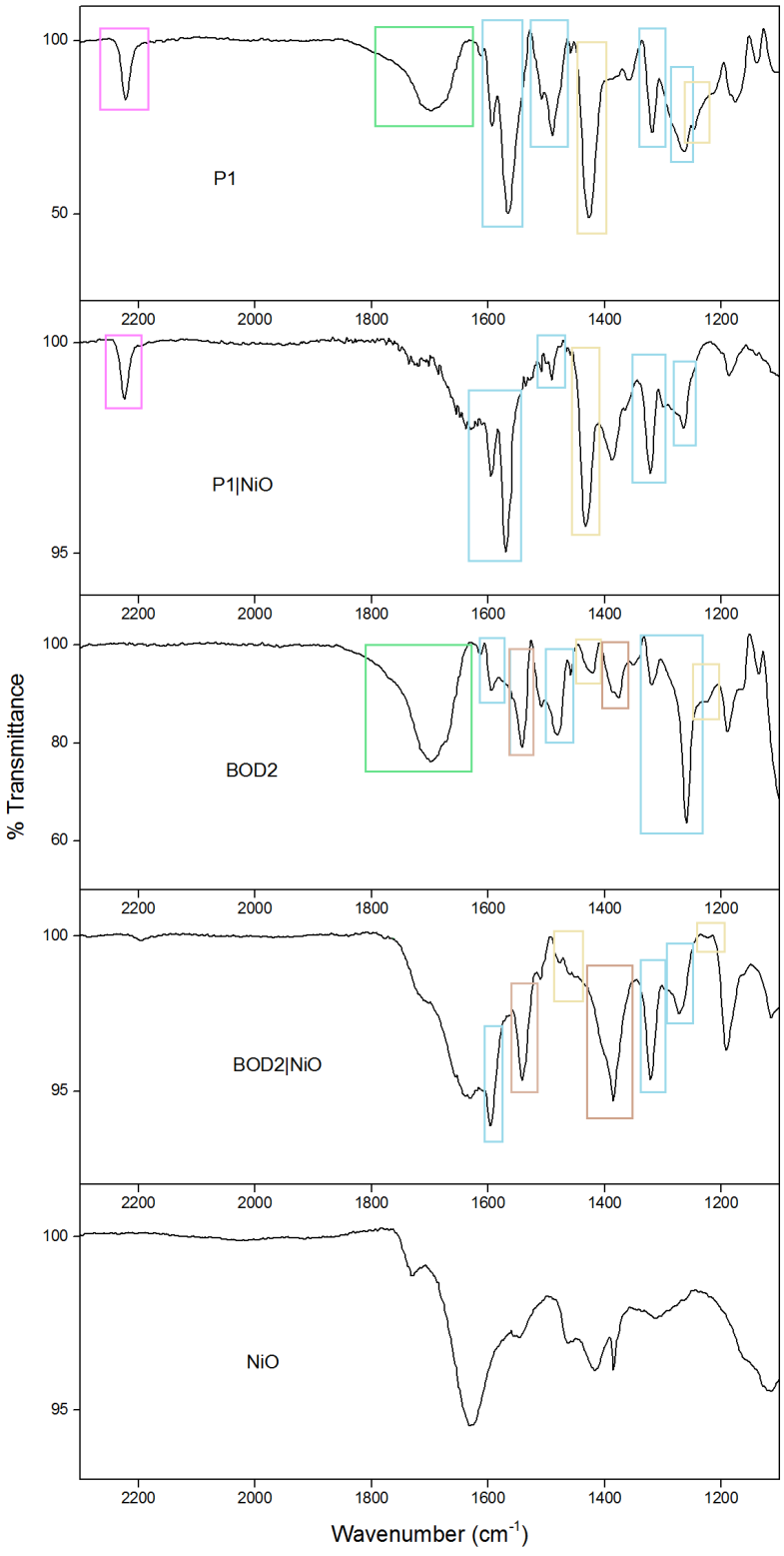

Figure 4.27: Comparison of the ground state vibrational spectra of P1 and BOD2 as powders and when adsorbed on nickel oxide. Sensitised films on FTO coated glass were scraped, crushed and pressed into potassium bromide disks.

Assignment	Wavenumber, cm^{-1}	
	P1	P1|NiO
CN	2222	2224
C=O	1693 br	
C=C (Phenyl)	1568, 1491, 1319, 1263, 1179	1570, 1491, 1321, 1265, 1188
C=C (Thiophene)	1427, 1244	1433
	BOD2	BOD|NiO
C=O	1693 br	
C=C (Phenyl)	1595, 1481, 1317, 1261, 1188	1597, 1321, 1271, 1188
C=C (Bodipy)	1541, 1381	1543, 1385
C=C (Thiophene)	1423, 1224	1458, 1227

Table 4.11: Assignment of bands from ground state infrared spectra, characterised from the ground state infrared spectra of precursor molecules. Assignments are from the spectra shown in Figure 4.26.

4.5.3 Infrared spectroelectrochemistry

Spectroelectrochemical analysis in the infrared region was performed for a triphenylamine derivative, the bodipy acceptor and a precursor molecule which contained a triphenylamine donor, thiophene π bridge and carboxylic anchor group, to characterise the infrared spectra of the oxidised donor (D^+) and the reduced acceptor (A^-) for BOD2. The structures of these molecules are shown in Figure 4.28 and Figure 4.29. The experiment was run in an OTTLE cell using methods described in Experimental Section 3.5, with a supporting electrolyte of tetrabutylammonium perchlorate in deuterated chloroform as this solvent was found to give the fewest bands in the region of interest (2000 cm^{-1} to 1000 cm^{-1}). The cell containing the sample in supporting electrolyte was placed in the path of an infrared spectrometer, and a reducing or oxidising potential was applied and held whilst consecutive spectra were taken. The potentials of the first reduction or oxidation were checked via cyclic voltammetry prior to the experiment and these values were chosen for chronoamperometry. In most cases the spectra did not fully return to the ground state after the applied potential was returned to zero, which is likely to be due to reactions between electrochemically generated species and oxygen in the cell, as it was not possible to effectively degas the system. The spectra are plotted as absorbance difference spectra for comparison with time-resolved infrared spectra.

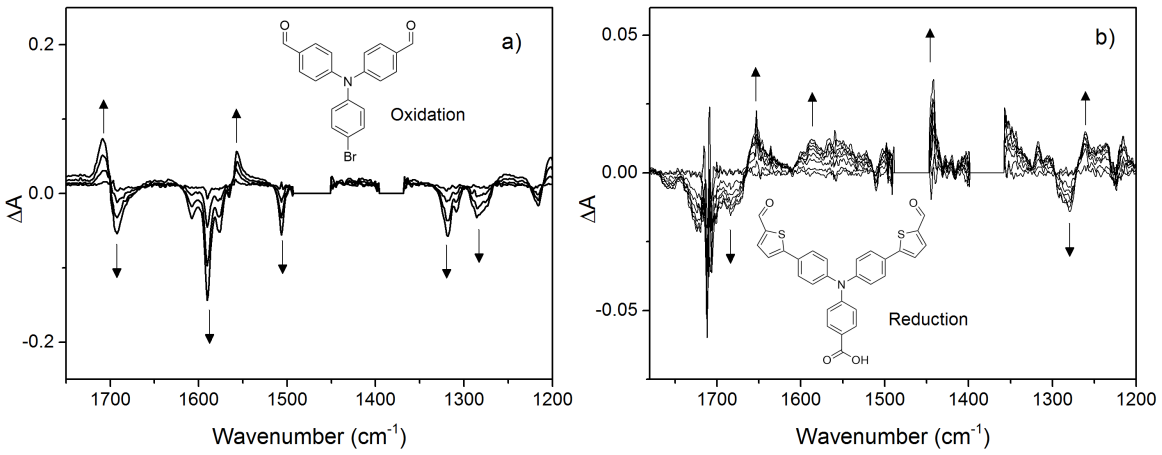

Figure 4.28: Absorbance difference spectra in the infrared region as an oxidising or reducing potential is applied to triphenylamine-based molecules (shown inset) in an OTTLE cell with 0.1 M $TBAClO_4$ in deuterated chloroform. a) 0 to 1.0 V vs Ag/Ag^+; b) 0 to -1.4 V vs Ag/Ag^+. Regions relating to solvent and supporting electrolyte species which saturate the detector have been set to zero.

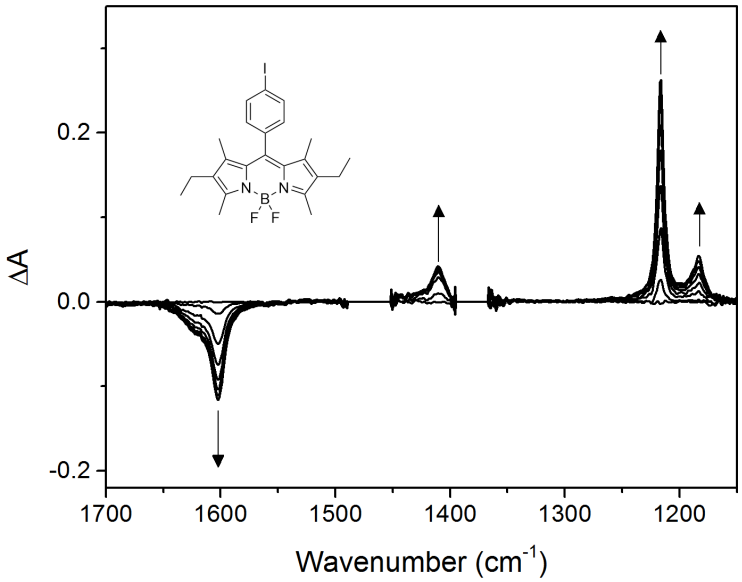

Figure 4.29: Absorbance difference spectra in the infrared region as the bodipy acceptor (shown inset) is electrochemically reduced in an OTTLE cell with 0.1 M $TBAClO_4$ in deuterated chloroform. 0 to -1.0 V vs Ag/Ag^+. Regions relating to solvent and supporting electrolyte species which saturate the detector have been set to zero.

Changes in the infrared spectrum of a simple triphenylamine compound (D) as an oxidative potential was applied are shown in Figure 4.28 a). Upon oxidation, the ν(C=O) of the carbonyl groups at 1700 cm^{-1} shift to higher energy, and the ν(C=C) phenyl vibrations at

1590 cm^{-1}, 1506 cm^{-1}, 1319 cm^{-1} and 1286 cm^{-1} decrease, as a sharp band grows at 1550 cm^{-1}, together with a weaker band at 1252 cm^{-1}. When a reducing potential was applied to a triphenylamine molecule with a thiophene π bridge, a band at 1442 cm^{-1} grows and is attributed to the ν(C=C) of the thiophene bridge, due to similarity with the ground state infrared spectrum of this molecule (Figure 4.26). Infrared difference spectra of the electrochemical reduction of a bodipy molecule (A), which has similar structure to the acceptor group of BOD2 are shown in Figure 4.29. Upon reduction, a band at 1602 cm^{-1} decreases and bands at 1410 cm^{-1}, 1216 cm^{-1} and 1183 cm^{-1} grow.

4.5.4 Time-resolved infrared spectroscopy

The infrared analysis presented in the previous sections indicates that both P1 and BOD2 have suitable infrared handles, as the ν(C=O) of the carboxylic anchor groups and the ν(C=C) of the triphenylamine donor and thiophene bridges give strong signals which shift upon reduction or oxidation. The ν(CN) of the malononitrile acceptor groups of P1 and the ν(C=C) of the bodipy acceptor of BOD2 also give characteristic vibrations. Ultrafast time-resolved infrared spectroscopy was used to investigate the changes in these bands upon excitation with a 532 nm laser pulse. The setup was the same as for time-resolved infrared experiments of CAD3 and CAD4 in Section 4.4.5 and details are given in the Experimental Section 3.7. Dichloromethane and deuterated acetonitrile solutions of P1 and BOD2 were added to a Harrick solution cell and infrared spectra were taken following laser excitation. These solvents were used to compare the results with previously reported transient absorption spectra of P1 and BOD2.[8,26]

Infrared spectra were recorded at various time delays following excitation, and were repeated for sensitised nickel oxide films in the presence and absence of an electrolyte containing 3 mM iodine and 0.1 M lithium iodide in deuterated acetonitrile. The time-resolved infrared difference spectra are shown in Figure 4.30. The spectra were analysed with a single-point method at selected frequencies and also a global analysis method. As the dynamics of the time-resolved infrared spectra were complex, average lifetimes were calculated from single-point analysis using Equation 4.5 for each band and are given in Tables 4.12 and 4.13. Full single-point analysis which gives the multi-exponential fits for both dyes is detailed in the Appendix in Tables A.6 and A.7.

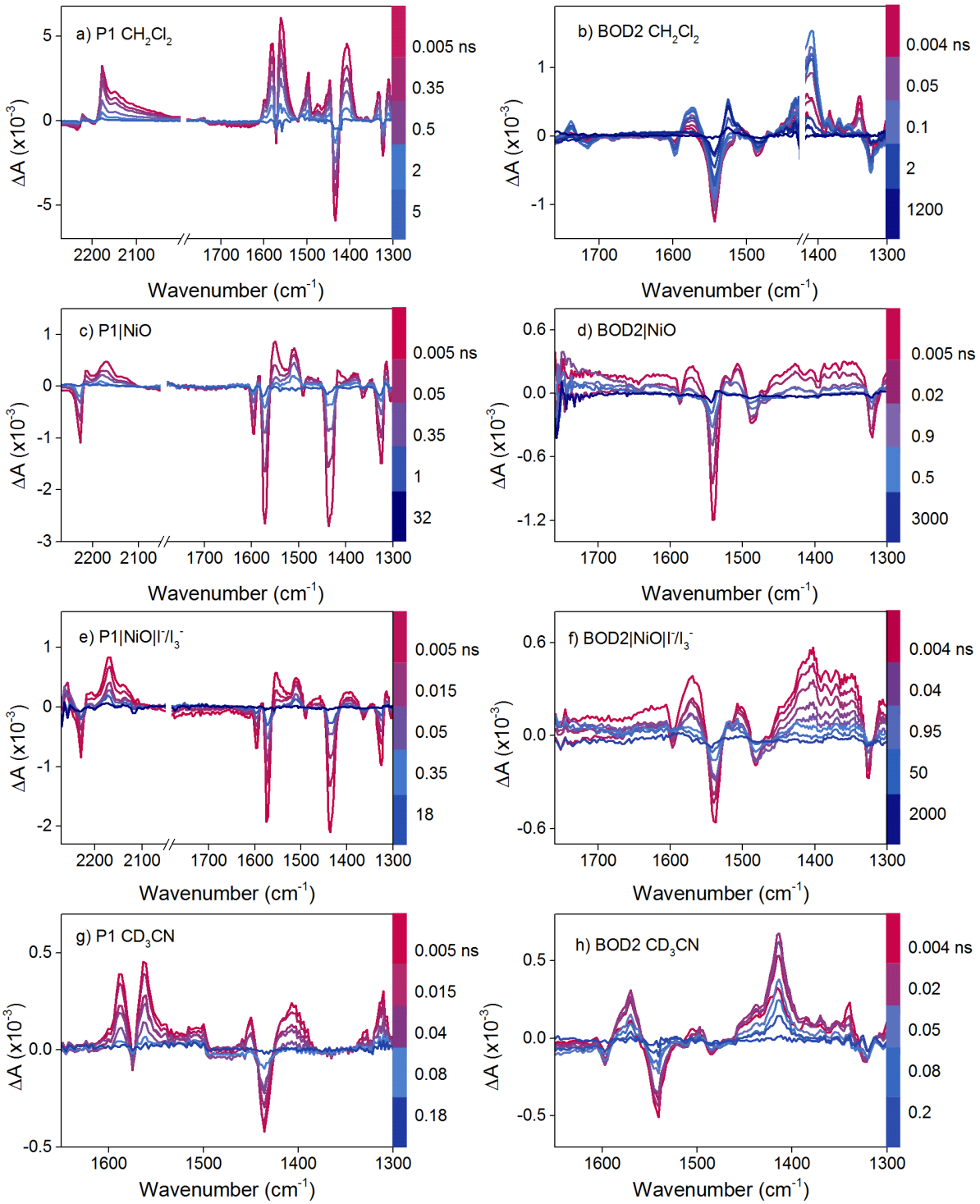

Figure 4.30: Time-resolved infrared difference spectra of P1 and BOD2 at selected time delays following excitation at 532 nm. a),b) In dichloromethane solution; c),d) on nickel oxide; e),f) on nickel oxide with 3 mM I_2 and 0.1 M LiI in deuterated acetonitrile; g),h) in deuterated acetonitrile.

Assignment	Lifetime, ps			
	CH_2Cl_2	CD_3CN	NiO	NiO|I^-/I_3^-
CN	τ_{2234} = 836 ±127		τ_{2228} = 54 ±19	τ_{2228} = 143 ±143
	τ_{2223} = 1094 ±139		τ_{2217} = 30 ±15	τ_{2211} = 87 ±24
	τ_{2178} = 892 ±91		τ_{2173} = 13 ±0.3	τ_{2173} = 86 ±30
	τ_{2146} = 968 ±104		τ_{2130} = 48 ±24	τ_{2130} = 238 ±42
C=O	τ_{1742} = 1091 ±192			
	τ_{1719} = 978 ±172			
C=C (Phenyl)	τ_{1583} = 1139 ±28	τ_{1589} = 37 ±3	τ_{1598} = 97 ±24	τ_{1595} = 188 ±27
	τ_{1561} = 1163 ±28	τ_{1564} = 39 ±3	τ_{1572} = 102 ±12	τ_{1575} = 202 ±28
	τ_{1498} = 1103 ±27	τ_{1450} = 34 ±6	τ_{1553} = 50 ±14	τ_{1555} = 33 ±5
	τ_{1447} = 1148 ±64	τ_{1329} = 29 ±4	τ_{1509} = 47 ±5	τ_{1510} = 296 ±31
	τ_{1333} = 1153 ±76	τ_{1310} = 36 ±3	τ_{1326} = 98 ±14	τ_{1325} = 186 ±24
	τ_{1324} = 1100 ±67		τ_{1314} = 51 ±9	τ_{1314} = 122 ±21
	τ_{1310} = 1127 ±65			
C=C (Thiophene)	τ_{1434} = 1184 ±45	τ_{1436} = 42 ±4	τ_{1434} = 87 ±12	τ_{1436} = 172 ±22
	τ_{1407} = 1073 ±29	τ_{1407} = 35 ±3	τ_{1382} = 220 ±47	τ_{1396} = 263 ±48

Table 4.12: Amplitude weighted average lifetimes derived from single-point analysis of time-resolved infrared spectra of P1. λ_{exc} = 532 nm.

In dichloromethane the time-resolved infrared spectra of P1 contain negative bands at 2234 cm^{-1} and 1434 cm^{-1} which correspond to the ground state ν(CN) of the malononitrile and ν(C=C) vibration of the thiophene, respectively, consistent with the ground state infrared spectra. These bands shift to lower energy upon excitation with a sharp transient band at 1407 cm^{-1} for the thiophene ν(C=C) vibration and multiple bands at 2221 cm^{-1}, 2178 cm^{-1} and 2146 cm^{-1} for the ν(CN) stretch. The shift to lower energy of these bands is consistent with an increase in electron density on the bridges and acceptor groups upon excitation, which suggests the formation of an intramolecular charge-transfer excited state. The presence of multiple bands in the ν(CN) region indicates multiple conformations, which is consistent with computational studies performed by Dr. Penfold which showed asymmetrical distribution of the charge on the acceptor groups in the first excited singlet state.[63]

A weak negative band at 1719 cm^{-1} is attributed to the ν(C=O) of the carboxylic anchor which shifts to 1742 cm^{-1} upon excitation, signifying a decrease in electron density on the anchor group in the charge-transfer excited state. The intensity and shift of this band is similar to that observed for the CAD1 and CAD2,[21] and an expansion of this region is shown in Figure 4.31.

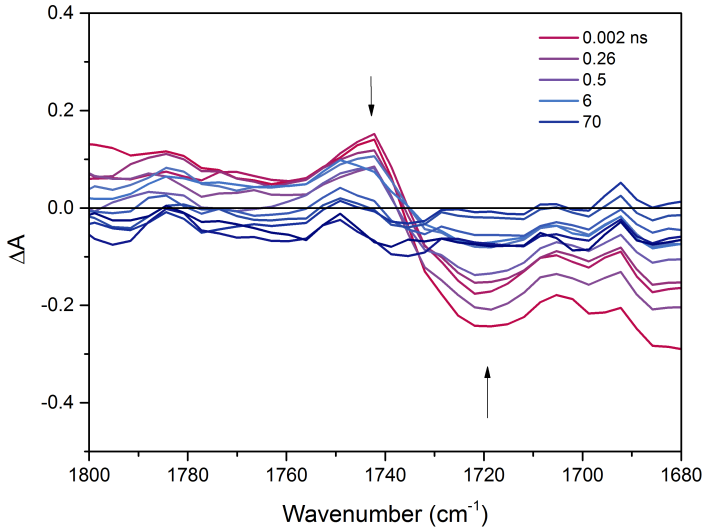

Figure 4.31: Expansion of the carbonyl region of the time-resolved infrared spectra of P1 in dichloromethane solution at selected time delays following excitation at 532 nm. This region has been smoothed using adjacent averaging.

Sharp transient signals at 1583 cm^{-1} to 1561 cm^{-1} and 1498 cm^{-1} to 1447 cm^{-1} are attributed to phenyl ν(C=C) stretches which overlap with the ground state vibrations and mask the bleach in this region. For P1 in dichloromethane, the transient and negative signals decay with similar lifetimes (τ = *ca.* 1.1 ns). In deuterated acetonitrile the spectral features in the fingerprint region are similar to those in dichloromethane, except that the phenyl bands at 1589 cm^{-1} to 1564 cm^{-1} are shifted slightly to higher energy by *ca.* 5 cm^{-1} and the transient band relating to ν(C=C) of the thiophene groups at 1407 cm^{-1} is weaker. The first excited singlet state decays faster, τ = *ca.* 35 ps, in deuterated acetonitrile, which is similar to the singlet excited state lifetime of P1 in acetonitrile previously reported from transient absorption experiments by Qin *et al.*[8] In Qin's work, the fast excited state lifetime was attributed to aggregation and intermolecular charge transfer, generating an intermolecular $P1^{+}P1^{-}$ charge-separated state. However, we would expect a solvent dependence if an intermolecular charge-separated state were present and no difference is

observed in the spectral shape for P1 in dichloromethane and deuterated acetonitrile in the fingerprint region. Another possibility is that the energy of the lowest singlet excited state is lowered when P1 is dissolved in acetonitrile which is more polar, as this could also affect the excited state lifetime.

The time-resolved infrared spectra of P1 adsorbed on nickel oxide contain similar spectral features in the ν(CN) region to those of P1 in dichloromethane. The bleach at 2228 cm^{-1} for P1|NiO is shifted to higher energy relative to solution, which is consistent with the ground state spectra. Multiple transient bands in this region suggest that the asymmetry is retained when P1 is adsorbed on nickel oxide. In the fingerprint region however, the spectra are different to in solution. Negative signals at 1598 cm^{-1} to 1572 cm^{-1} are attributed to the ground state ν(C=C) vibrations of the phenyl groups, and mask the transient signals which were observed in solution. This suggests that the ν(C=C) transient bands in this region are narrower than their corresponding ground state bands, which is similar to the infrared spectrum of D^+ relative to D from spectroelectrochemical analysis of triphenylamine (Figure 4.19). This species is therefore attributed to the charge-separated state, and the transient bands decay with similar lifetimes which suggests that only one species is formed. The decay was fit to a bi-exponential function which is consistent with heterogeneous recombination dynamics previously reported for P1 adsorbed on nickel oxide.[8] In the presence of an electrolyte containing iodine and lithium iodide, the lifetimes associated with P1|NiO are generally longer. This may be due to a similar process which was observed for CAD3 and CAD4 where an association with species in the electrolyte reduced recombination.

The transient infrared spectra of BOD2 in dichloromethane are more complex than that of P1. For clarity, the spectra of BOD2 in dichloromethane are shown at early (up to ten picoseconds) and late (up to one nanosecond) delay times following excitation in Figure 4.32. Average lifetimes from single-point analysis of time-resolved infrared spectra are given in Table 4.13, and the full single-point analysis is given in Table A.7. Upon excitation at 532 nm, negative signals at 1543 cm^{-1} and 1324 cm^{-1} are formed within the time resolution of the experiment, and are attributed to the ground state ν(C=C) vibrations of the bodipy groups due to similarity with the ground state spectrum.

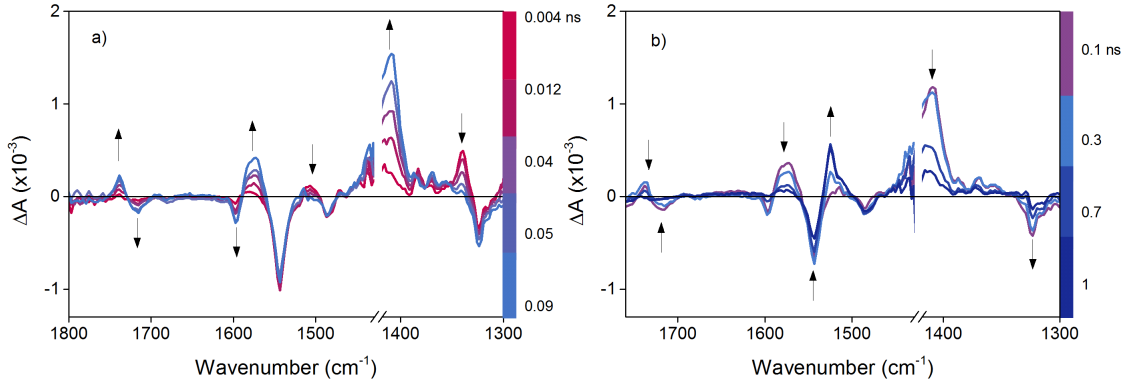

Figure 4.32: Time-resolved infrared difference spectra of BOD2 in dichloromethane at selected time delays following excitation at 532 nm. a) At short delay times (5 ps to 90 ps); b) at long delay times (100 ps to 1 ns).

Assignment	Lifetime			
	CH_2Cl_2 (ps)	CD_3CN (ps)	NiO (ns)	NiO|I^-/I_3^- (ns)
C=O	τ_{1738} rise = 21 ±8 τ_{1738} = 509 ±72 τ_{1715} rise = 30 ±10 τ_{1715} = 368 ±70			
C=C (Phenyl)	τ_{1598} rise = 20 ±8 τ_{1598} = 492 ±102 τ_{1573} rise = 23 ±6 τ_{1573} = 499 ±89	τ_{1497} rise = 8 ±2 τ_{1497} = 43 ±10 τ_{1597} rise = 6 ±2 τ_{1597} = 69 ±10 τ_{1570} rise = 7 ±3 τ_{1570} = 41 ±8	τ_{1573} = 0.028 ±0.009	τ_{1570} = 0.37 ±0.12
C=C (Bodipy)	τ_{1543} = 458 ±30 τ_{1525} rise = 405 ±66 τ_{1525} = 616 000 ±100 000 τ_{1507} = 44 ±5 τ_{1339} = 28 ±3 τ_{1324} = 233 271 ±59 000	τ_{1543} = 60 ±5 τ_{1507} = 7 ±0.9 τ_{1340} = 18 ±2 τ_{1324} = 59 ±9	τ_{1543} =2.74 ±0.57 τ_{1530} = 2.36 ±0.53 τ_{1522} = 2.11 ±0.36 τ_{1507} = 2.30 ±0.48	τ_{1550} = 14.4 ±1.9 τ_{1520} = 29 ±9 τ_{1505} = 8.86 ±1.65
C=C (Thiophene)	τ_{1409} rise = 22 ±4 τ_{1409} = 495 ±49	τ_{1416} rise = 5 ±1 τ_{1416} = 61 ±6	τ_{1484} = 6.53 ±1.7	τ_{1480} = 111 ±39 τ_{1405} = 3.04 ±0.97

Table 4.13: Average lifetimes obtained from single-point analysis of the time-resolved infrared spectra of BOD2, at selected frequencies following excitation at 532 nm.

A sharp positive band at 1339 cm^{-1} is also formed on this timescale, and is attributed to the bodipy singlet excited state, along with a weak band at 1507 cm^{-1}. As these bands decay with τ = 25 ps, a weak bleach and transient grow at 1715 cm^{-1} and 1738 cm^{-1}, respectively, and resemble the ν(C=O) of the carbonyl group. The shift of the ν(C=O) to higher energy upon excitation suggests the formation of the charge-transfer excited state. A strong transient signal relating to the ν(C=C) of the thiophene group at 1409 cm^{-1} also grows in on the same timescale as that of the carbonyl, together with a bleach of the ν(C=C) of the phenyl group at 1598 cm^{-1} and its corresponding transient band at 1573 cm^{-1}.

This second transient species decays with τ = *ca.* 500 ps, as sharp transient band grows in at 1525 cm^{-1}. This final species decays with τ = *ca.* 600 ns, and is attributed to a bodipy-localised triplet excited state, as this was observed previously in transient absorption experiments of BOD2 in dichloromethane, and decayed with a similar lifetime.[18] A small shoulder on this band at 1517 cm^{-1} grows with the triplet band, but decays faster. Due to overlap with bands at 1507 $^{-1}$ and 1525 cm^{-1}, the decay of the band at 1517 cm^{-1} could not be sensibly fit. An expansion of this region is shown in Figure 4.33.

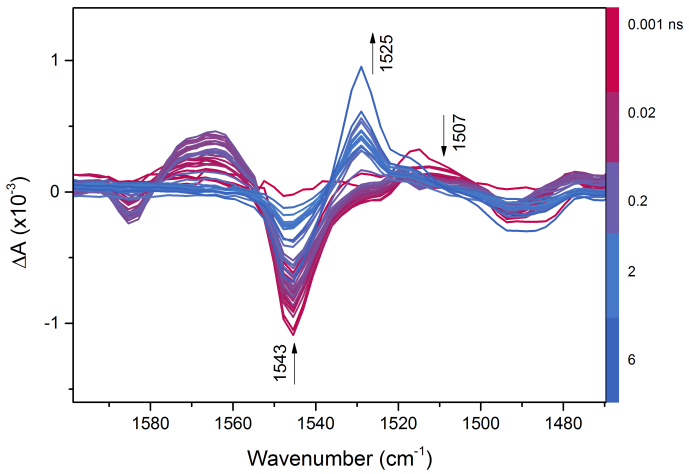

Figure 4.33: Expansion of the time-resolved infrared spectra of BOD2 in dichloromethane, showing the region containing the bodipy-localised triplet excited state at selected time delays following excitation at 532 nm.

To separate the infrared spectra of each species, a global analysis method was used for

BOD2 in dichloromethane and the results are shown in Figure 4.34. In the region 1500 cm^{-1} to 1525 cm^{-1}, the infrared spectra of the bodipy excited singlet state (species 1, blue), the charge-transfer excited state (species 2, red) and the bodipy triplet excited state (species 3, green) overlap.

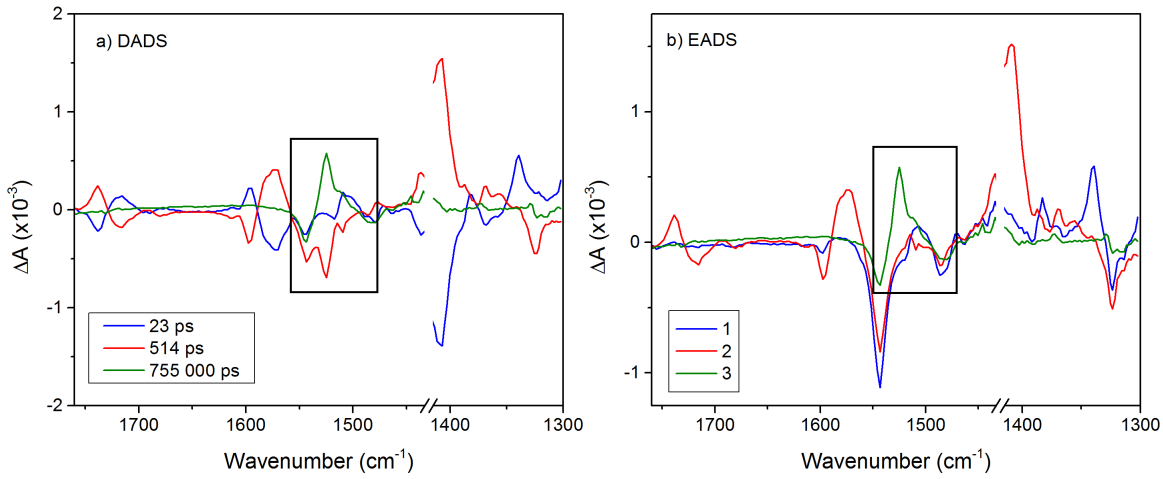

Figure 4.34: Results from global analysis of time-resolved infrared spectra of BOD2 in dichloromethane. λ_{exc} = 532 nm. a) Decay-associated difference spectra; b) evolution-associated difference spectra.

In deuterated acetonitrile, the ν(C=C) of the thiophene band shifts to 1417 cm^{-1}, and the ν(C=O) of the carbonyl group is weaker. Bands at 1507 cm^{-1} and 1340 cm^{-1} are assigned to singlet bodipy excited state, as observed for BOD2 in dichloromethane, with ground state bleaches at 1543 cm^{-1} and 1324 cm^{-1}. The sharp band at 1525 cm^{-1} which was attributed to the triplet excited state in dichloromethane is not present in deuterated acetonitrile. The bodipy singlet excited state decays with τ = *ca.* 10 ps as bands relating to the ν(C=C) of the phenyl groups at 1597 cm^{-1}, 1570 cm^{-1} and 1497 cm^{-1} grow. This is attributed to the formation of the charge-transfer excited state, and this species decays to the ground state with τ = *ca.* 60 ps. The decay of the charge-transfer state is on a shorter timescale than in dichloromethane, which is consistent with the trend observed for P1.

When BOD2 is adsorbed on nickel oxide in the presence and absence of an electrolyte containing iodine and lithium iodide in deuterated acetonitrile, the time-resolved infrared spectra contain similar features to the charge-transfer excited state, which was observed in solution at *ca.* 20 ps. A broad signal is present across the recorded frequencies for

BOD2|NiO and also BOD2|NiO|I^-/I_3^- which was not observed for P1|NiO, though this is likely due to noise as the amplitudes of transient signals are considerably smaller for BOD2. The ν(C=C) of the thiophene group which appeared at 1409 cm^{-1} in solution is not as intense for BOD2|NiO, which is also similar to P1|NiO. The bleach of the phenyl band at 1587 cm^{-1} was too weak to resolve meaningful kinetics. The band at 1507 cm^{-1} is attributed to the bodipy singlet excited state, together with the strong bleach at 1543 cm^{-1}. Spectroelectrochemical reduction of a simple bodipy (Figure 4.29) showed the growth of a band at 1410 cm^{-1}, which unfortunately overlaps with the band at 1409 cm^{-1} which is attributed to the ν(C=C) of the thiophene in the time-resolved infrared spectra, so the presence of $bodipy^-$ could not be confirmed.

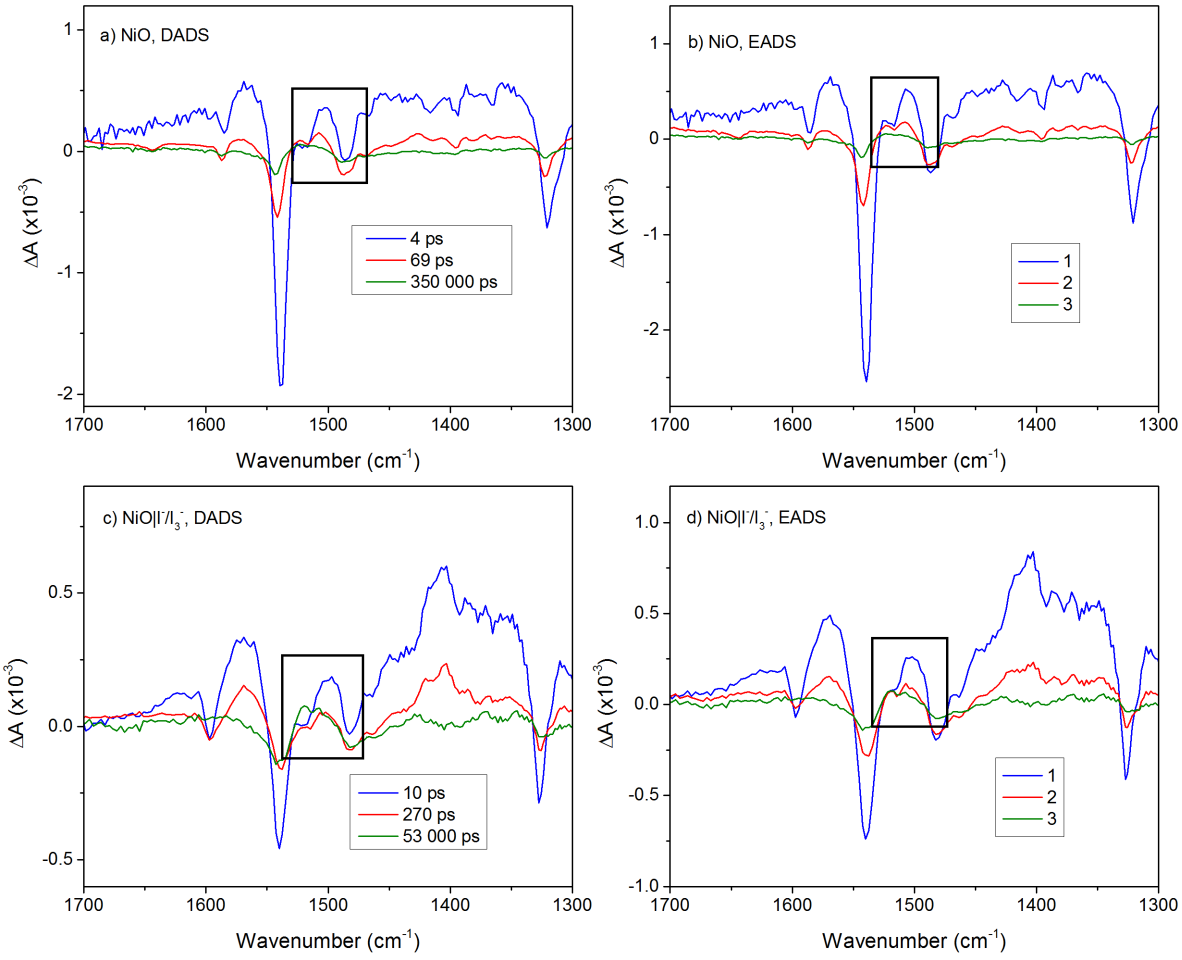

Figure 4.35: Results from global analysis of the time-resolved infrared spectra of BOD2 adsorbed on nickel oxide in the presence and absence of 3 mM I_2 and 0.1 M LiI in deuterated acetonitrile. Left) decay-associated difference spectra; right) evolution-associated difference spectra. The region which contains signals from the charge-transfer excited state and charge-separated state is highlighted with a black box.

In general the features do not evolve over time which is different to BOD2 in solution. Instead the spectra resemble the charge-transfer excited state. However the bands do not all decay with consistent time components, which suggests that more than one species is present. Average lifetimes from single-point analysis of the time-resolved infrared spectra on nickel oxide are shown in Table 4.13. Long-lived components are present for bodipy ν(C=C) bands, and phenyl ν(C=C) bands generally decay faster. Results from global analysis in Figure 4.35 show an overlap of signals around 1510 cm^{-1}. The long-lived signal is attributed to the charge-separated state and does not have a strong signal in the infrared region.

Only the charge-separated state is observed in the time-resolved infrared spectra of P1 adsorbed on nickel oxide which suggests efficient injection and this agrees with the results from transient absorption data.[8] In the time-resolved infrared spectra of BOD2 absorbed on nickel oxide, however, the charge-transfer excited state is observed together with the charge-separated state, which suggests less efficient formation of the charge-separated state for this system which is likely the reason for the lower quantum efficiency of BOD2 relative to P1. The presence of both excited and reduced species has been observed for ruthenium dyes on nickel oxide previously by Queyriaux *et al.*[64]

4.5.5 Conclusions

The aim of this study, and of this chapter in general, was to investigate the charge-recombination process of push-pull dyes adsorbed on nickel oxide to relate the photophysical, electrochemical and excited state dynamics to the photovoltaic performance. In the case of P1 and BOD2, time-resolved infrared spectroscopy revealed that the formation of the charge-separated state was less efficient for BOD2|NiO than for P1|NiO, and this is consistent with the relative performance of these dyes in p-type nickel oxide dye-sensitised solar cells. Global analysis of the time-resolved infrared spectra of BOD2|NiO was used to extract the spectrum of the charge-separated state and it was revealed that this overlaps with the charge-transfer excited state. For P1 the ν(CN) stretch of the malononitrile acceptor group was a useful infrared handle in the nitrile region, and is more easily distinguished than bands in the fingerprint region, such as those observed for CAD3 and CAD4, and also for BOD2.

Importantly, this study characterised the infrared spectrum of a bodipy-localised triplet excited state which is present as a sharp band at *ca.* 1525 cm^{-1} for BOD2 in dichloromethane, but is not present in acetonitrile. The presence of the bodipy singlet excited state confirmed that the triplet excited state is formed through the decay of the charge-transfer excited state. Interestingly, this triplet excited state was not observed for BOD1 and BOD3-5 which have similar structures to BOD2.

References

(1) Freys, J. C.; Gardner, J. M.; D'Amario, L.; Brown, A. M.; Hammarstrom, L. *Dalton Trans.* **2012**, *41*, 13105–11.

(2) Gennari, M.; Legalite, F.; Zhang, L.; Pellegrin, Y.; Blart, E.; Fortage, J.; Brown, A. M.; Deronzier, A.; Collomb, M. N.; Boujtita, M.; Jacquemin, D.; Hammarstrom, L.; Odobel, F. *J. Phys. Chem. Lett.* **2014**, *5*, 2254–8.

(3) Gibson, E. A.; Smeigh, A. L.; Le Pleux, L.; Fortage, J.; Boschloo, G.; Blart, E.; Pellegrin, Y.; Odobel, F.; Hagfeldt, A.; Hammarstrom, L. *Angew. Chem. Int. Ed.* **2009**, *48*, 4402–5.

(4) Le Pleux, L.; Smeigh, A. L.; Gibson, E.; Pellegrin, Y.; Blart, E.; Boschloo, G.; Hagfeldt, A.; Hammarström, L.; Odobel, F. *Energy Environ. Sci.* **2011**, *4*, 2075–2084.

(5) Nattestad, A.; Mozer, A. J.; Fischer, M. K.; Cheng, Y. B.; Mishra, A.; Bauerle, P.; Bach, U. *Nat. Mater.* **2010**, *9*, 31–5.

(6) Yu, Y.; Click, K. A.; Polen, S. M.; He, M.; Hadad, C. M.; Wu, Y. *J. Phys. Chem. C* **2017**, *121*, 20720–20728.

(7) Farré, Y.; Zhang, L.; Pellegrin, Y.; Planchat, A.; Blart, E.; Boujtita, M.; Hammarström, L.; Jacquemin, D.; Odobel, F. *J. Phys. Chem. C* **2016**, *120*, 7923-7940.

(8) Qin, P.; Wiberg, J.; Gibson, E. A.; Linder, M.; Li, L.; Brinck, T.; Hagfeldt, A.; Albinsson, B.; Sun, L. *J. Phys. Chem. C* **2010**, *114*, 4738–4748.

(9) Qin, P.; Linder, M.; Brinck, T.; Boschloo, G.; Hagfeldt, A.; Sun, L. *Adv. Mater.* **2009**, *21*, 2993–2996.

(10) Li, L.; Gibson, E. A.; Qin, P.; Boschloo, G.; Gorlov, M.; Hagfeldt, A.; Sun, L. *Adv. Mater.* **2010**, *22*, 1759–62.

(11) Qin, P.; Zhu, H.; Edvinsson, T.; Boschloo, G.; Hagfeldt, A.; Sun, L. *J. Am. Chem. Soc.* **2008**, *130*, 8570–1.

(12) Zhu, L.; Yang, H.; Zhong, C.; Li, C. M. *Chem. Asian J.* **2012**, *7*, 2791–5.

(13) Ji, Z.; Natu, G.; Huang, Z.; Wu, Y. *Energ. Environ. Sci.* **2011**, *4*, 2818.

(14) Zhu, L.; Yang, H. B.; Zhong, C.; Li, C. M. *Dyes Pigm.* **2014**, *105*, 97–104.

(15) Zhang, Q.-Q.; Jiang, K.-J.; Huang, J.-H.; Zhao, C.-W.; Zhang, L.-P.; Cui, X.-P.; Su, M.-J.; Yang, L.-M.; Song, Y.-L.; Zhou, X.-Q. *J. Mater. Chem. A* **2015**, *3*, 7695–7698.

(16) Zhang, F.; Yu, P.; Shen, W.; Li, M.; He, R. *RSC Adv.* **2015**, *5*, 64378–64386.

(17) Click, K. A.; Beauchamp, D. R.; Garrett, B. R.; Huang, Z.; Hadad, C. M.; Wu, Y. *Phys. Chem. Chem. Phys.* **2014**, *16*, 26103–11.

(18) Lefebvre, J. F.; Sun, X. Z.; Calladine, J. A.; George, M. W.; Gibson, E. A. *Chem. Commun.* **2014**, *50*, 5258–5260.

(19) Wood, C. J.; Summers, G. H.; Gibson, E. A. *Chem. Commun.* **2015**, *51*, 3915–3918.

(20) Sheibani, E.; Zhang, L.; Liu, P.; Xu, B.; Mijangos, E.; Boschloo, G.; Hagfeldt, A.; Hammarström, L.; Kloo, L.; Tian, H. *RSC Adv.* **2016**, *6*, 18165–18177.

(21) Wood, C. J.; Cheng, M.; Clark, C. A.; Horvath, R.; Clark, I. P.; Hamilton, M. L.; Towrie, M.; George, M. W.; Sun, L.; Yang, X.; Gibson, E. A. *J. Phys. Chem. C* **2014**, *118*, 16536–16546.

(22) Liu, Z.; Li, W.; Topa, S.; Xu, X.; Zeng, X.; Zhao, Z.; Wang, M.; Chen, W.; Wang, F.; Cheng, Y. B.; He, H. *ACS Appl. Mater. Interfaces* **2014**, *6*, 10614–22.

(23) Loudet, A.; Burgess, K. *Chem. Rev.* **2007**.

(24) Singh S. P.; Gayathri, T. *Eur. J. Org. Chem.* **2014**, *22*, 4689–4707.

(25) Kubo, Y.; Eguchi, D.; Matsumoto, A.; Nishiyabu, R.; Yakushiji, H.; Shigaki, K.; Kaneko, M. *J. Mater. Chem. A* **2014**, *2*, 5204.

(26) Summers, G. H.; Lefebvre, J. F.; Black, F. A.; Davies, E. S.; Gibson, E. A.; Pullerits, T.; Wood, C. J.; Zidek, K. *Phys. Chem. Chem. Phys.* **2015**, *18*, 1059–1070.

(27) Berera, R.; van Grondelle, R.; Kennis, J. T. *Photosynth. Res.* **2009**, *101*, 105–18.

(28) Seo, E. T.; Nelson, R. F.; Fritsch, J. M.; Marcoux, L. S.; Leedy, D. W.; Adams, R. N. *J. Am. Chem. Soc.* **1966**, *88*, 3498–3503.

(29) Boschloo, G.; Hagfeldt, A. *J. Phys. Chem. B* **2001**, *105*, 3039–3044.

(30) Slavov, C.; Hartmann, H.; Wachtveitl, J. *Anal. Chem.* **2015**, *87*, 2328–36.

(31) Feldt, S. M.; Lohse, P. W.; Kessler, F.; Nazeeruddin, M. K.; Gratzel, M.; Boschloo, G.; Hagfeldt, A. *Phys. Chem. Chem. Phys.* **2013**, *15*, 7087–97.

(32) Gibson, E. A.; Le Pleux, L.; Fortage, J.; Pellegrin, Y.; Blart, E.; Odobel, F.; Hagfeldt, A.; Boschloo, G. *Langmuir* **2012**, *28*, 6485–93.

(33) Ji, Z.; Natu, G.; Wu, Y. *ACS Appl. Mater. Interfaces* **2013**, *5*, 8641–8.

(34) Pellegrin, Y.; Le Pleux, L.; Blart, E.; Renaud, A.; Chavillon, B.; Szuwarski, N.; Boujtita, M.; Cario, L.; Jobic, S.; Jacquemin, D.; Odobel, F. *J. Photochem. Photobiol. A* **2011**, *219*, 235–242.

(35) Wu, F.; Zhu, L.; Zhao, S.; Song, Q.; Yang, C. *Dyes Pigm.* **2016**, *124*, 93–100.

(36) Wykes, M.; Odobel, F.; Adamo, C.; Ciofini, I.; Labat, F. *J. Mol. Model* **2016**, *22*, 289.

(37) Tian, H.; Oscarsson, J.; Gabrielsson, E.; Eriksson, S. K.; Lindblad, R.; Xu, B.; Hao, Y.; Boschloo, G.; Johansson, E. M.; Gardner, J. M.; Hagfeldt, A.; Rensmo, H.; Sun, L. *Sci. Rep.* **2014**, *4*, 4282.

(38) Cheng, M.; Yang, X.; Li, J.; Zhang, F.; Sun, L. *ChemSusChem* **2013**, *6*, 70–77.

(39) Hara, K.; Sato, T.; Katoh, R.; Furube, A.; Ohga, Y.; Shinpo, A.; Suga, S.; Sayama, K.; Sugihara, H.; Arakawa, H. *J. Phys. Chem. B* **2003**, *107*, 597–606.

(40) Chang, C. H.; Chen, Y. C.; Hsu, C. Y.; Chou, H. H.; Lin, J. T. *Org. Lett.* **2012**, *14*, 4726–9.

(41) Powar, S.; Daeneke, T.; Ma, M. T.; Fu, D.; Duffy, N. W.; Gotz, G.; Weidelener, M.; Mishra, A.; Bauerle, P.; Spiccia, L.; Bach, U. *Angew. Chem. Int. Ed.* **2013**, *52*, 602–5.

(42) Black, F. A.; Wood, C. J.; Ngwerume, S.; Summers, G. H.; Clark, I. P.; Towrie, M.; Camp, J. E.; Gibson, E. *Faraday Discuss.* **2017**, *198*, 449–461.

(43) Cui, J.; Lu, J.; Xu, X.; Cao, K.; Wang, Z.; Alemu, G.; Yuang, H.; Shen, Y.; Xu, J.; Cheng, Y.; Wang, M. *J. Phys. Chem. C* **2014**, *118*, 16433–16440.

(44) Hilgendorff, M.; Sundström, V. *J. Phys. Chem. B* **1998**, *102*, 10505–10514.

(45) Wiberg, J.; Marinado, T.; Hagberg, D. P.; Sun, L.; Hagfeldt, A.; Albinsson, B. *J. Phys. Chem. C* **2009**, *113*, 3881–3886.

(46) Pho, T. V.; Sheridan, M. V.; Morseth, Z. A.; Sherman, B. D.; Meyer, T. J.; Papanikolas, J. M.; Schanze, K. S.; Reynolds, J. R. *ACS Appl. Mater. Interfaces* **2016**, *8*, 9125–33.

(47) Zhang, L.; Cole, J. M. *ACS Appl. Mater. Interfaces* **2015**, *7*, 3427–55.

(48) McNamara, W. R.; Snoeberger R. C., 3.; Li, G.; Schleicher, J. M.; Cady, C. W.; Poyatos, M.; Schmuttenmaer, C. A.; Crabtree, R. H.; Brudvig, G. W.; Batista, V. S. *J Am. Chem. Soc.* **2008**, *130*, 14329–38.

(49) Zhu, Y.; Chu, W.; Wang, N.; Lin, T.; Yang, W.; Wen, J.; Zhao, X. S. *RSC Advances* **2015**, *5*, 77958–77964.

(50) Harrick Scientifical Products: Demountable liquid cells., `http://www.harrickscI.com/ftir/accessories/group/Demountable-Liquid-Cells`, Accessed May 25th, 2018.

(51) D'Amario, L.; Antila, L. J.; Pettersson Rimgard, B.; Boschloo, G.; Hammarström, L. *J. Phys. Chem. Lett.* **2015**, *6*, 779–783.

(52) Borgstrom, M.; Blart, E.; Boschloo, G.; Mukhtar, E.; Hagfeldt, A.; Hammarstrom, L.; Odobel, F. *J. Phys. Chem. B* **2005**, *109*, 22928–34.

(53) Morandeira, A.; Boschloo, G.; Hagfeldt, A.; Hammarstrom, L. *J. Phys. Chem. B* **2005**, *109*, 19403–10.

(54) D'Amario, L.; Jiang, R.; Cappel, U. B.; Gibson, E. A.; Boschloo, G.; Rensmo, H.; Sun, L.; Hammarstrom, L.; Tian, H. *ACS Appl. Mater. Interfaces* **2017**, *9*, 33470–33477.

(55) Zhang, L.; Favereau, L.; Farre, Y.; Mijangos, E.; Pellegrin, Y.; Blart, E.; Odobel, F.; Hammarstrom, L. *Phys. Chem. Chem. Phys.* **2016**, *18*, 18515–27.

(56) Wood, C. J.; McGregor, C. A.; Gibson, E. A. *ChemElectroChem* **2016**, *3*, 1827–1836.

(57) Ip, C. M.; Troisi, A. *J. Phys. Chem. Lett.* **2016**, *7*, 2989–93.

(58) Ponseca C. S., J.; Chabera, P.; Uhlig, J.; Persson, P.; Sundstrom, V. *Chem. Rev.* **2017**, *117*, 10940–11024.

(59) Asbury, J. B.; Hao, E.; Wang, Y.; Ghosh, H. N.; Lian, T. *J. Phys. Chem. B* **2001**, *105*, 4545–4557.

(60) Asbury, J. B.; Hao, E.; Wang, Y.; Ghosh, H. N.; Lian, T. *J. Am. Chem. Soc.* **2008**, *130*, 5632–3.

(61) Dereka, B.; Koch, M.; Vauthey, E. *Acc. Chem. Res.* **2017**, *50*, 426–434.

(62) Abdellah, M.; El-Zohry, A. M.; Antila, L. J.; Windle, C. D.; Reisner, E.; Hammarstrom, L. *J. Am. Chem. Soc.* **2017**, *139*, 1226–1232.

(63) Black, F. A.; Clark, C. A.; Summers, G. H.; Clark, I. P.; Towrie, M.; Penfold, T.; George, M. W.; Gibson, E. A. *Phys. Chem. Chem. Phys.* **2017**, *19*, 7877–7885.

(64) Queyriaux, N.; Wahyuono, R. A.; Fize, J.; Gablin, C.; Wachtler, M.; Martinez, E.; Leonard, D.; Dietzek, B.; Artero, V.; Chavarot-Kerlidou, M. *J. Phys. Chem. C Nanomater. Interfaces* **2017**, *121*, 5891–5904.

Chapter 5

Photoinduced Charge Transfer of Organic-Polyoxometalate Systems in Solution

5.1 Aims

This chapter presents the photoinduced dynamics of photosensitiser-polyoxometalate hybrid structures in solution. Laser excitation of the organic photosensitiser results in rapid charge transfer to the covalently-attached polyoxometalate. These dynamics are dependent on the polyoxometalate structure, metal atom, counter cation, structure of the linker group and the structure of the bridge between the polyoxometalate and photosensitiser. These materials have potential uses in solar energy conversion or photocatalysis which require multiple electrons to be stored and released.

5.2 Introduction

Contributions for Chapter 5: The design and synthesis of polyoxometalate hybrids were performed by Dr. Izzet, and the samples were provided to us for photophysical analysis. The electrochemical properties of the hybrids in acetonitrile were also provided to us by Dr. Izzet. Spectroscopic analysis and electrochemistry in dichloromethane was performed by the author of this thesis.

Polyoxometalates (POMs) are anionic clusters of d-block metals (M = Mo, W, V, Ta and Nb) in high oxidation states with oxygen ligands. They may also contain heteroatoms (X = P, As, Si, Ge). The structures of the polyoxometalates discussed in this chapter are based on Dawson [$X_2M_{18}O_{62}$] and Keggin [$XM_{12}O_{40}$] anions, but a large variety of structures with one or more types of metal have been reported.[1,2] Polyoxometalate anions are known to be able to accommodate multiple electrons without large reorganisation energies or degradation,[3–5] which makes them potentially useful for multi-electronic processes, for example electrocatalysis and photo(electro)catalysis.[3,6–8] These compounds have been investigated for applications such as water oxidation catalysis,[9–11] proton reduction[12–14] and energy storage.[15–18]

Electron donating or accepting groups can be attached to polyoxometalates through covalent or ionic interactions to produce hybrid materials, though covalent attachments are favourable as they can improve the solubility of the polyoxometalate and increase communication between the polyoxometalate and the appended group.[5,19] A successful route to covalent systems can be made through organotin or organosilicon linkers, which attach to lacunary anions where one or more metal centres of the polyoxometalate have been lost.[2,6,20] For photocatalysis applications, a light-absorbing group is needed as polyoxometalates only absorb in the ultraviolet region. In this case the photosensitiser transfers charge to the polyoxometalate through a conjugated bridge following excitation by light, as shown in Figure 5.1.

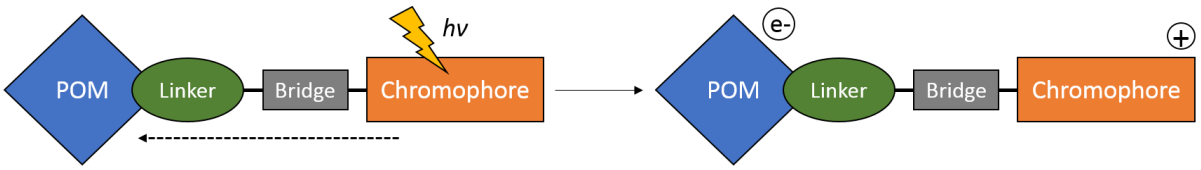

Figure 5.1: Representation of photoinduced charge transfer in a covalently-bound photosensitiser-polyoxometalate hybrid.

A number of hybrid structures with covalent bonds between polyoxometalates and photosensitiser moieties have been reported, including examples from the groups of Harriman, Odobel and Proust with chromophores such as spiropyran, pyrenes, porphyrins, perylenes and ruthenium complexes.[21–25] A study by Proust's group investigated the photoinduced dynamics exhibited by iridium complexes attached to both Dawson and Keggin poly-

oxometalates through organosilicon and organotin linkers.[26–28] The structures of these iridium-polyoxometalate hybrids are shown in Figure 5.2. The polyoxometalate structures are represented by octahedra of metal atoms or heteroatoms surrounded by oxygen ligands. The hybrids are named relating to their structure, K = Keggin, D = Dawson, W = tungsten, Mo = molybdenum, Si = organosilicon linker, Sn = organotin linker. The Keggin structure contains twelve tungsten or molybdenum metal atoms around one single heteroatom (P). The Dawson structure is formed from two lacunary Keggin monomers, $[XW_9O_{34}{}^{n-}]$. For all compounds the polyoxometalate was reduced following excitation of the iridium complex, and in the presence of a sacrificial electron donor a two-electron reduction on the polyoxometalate was achieved for the Dawson system with an organosilicon linker, $D^{W}{}_{Si}[Ir]$.[27]

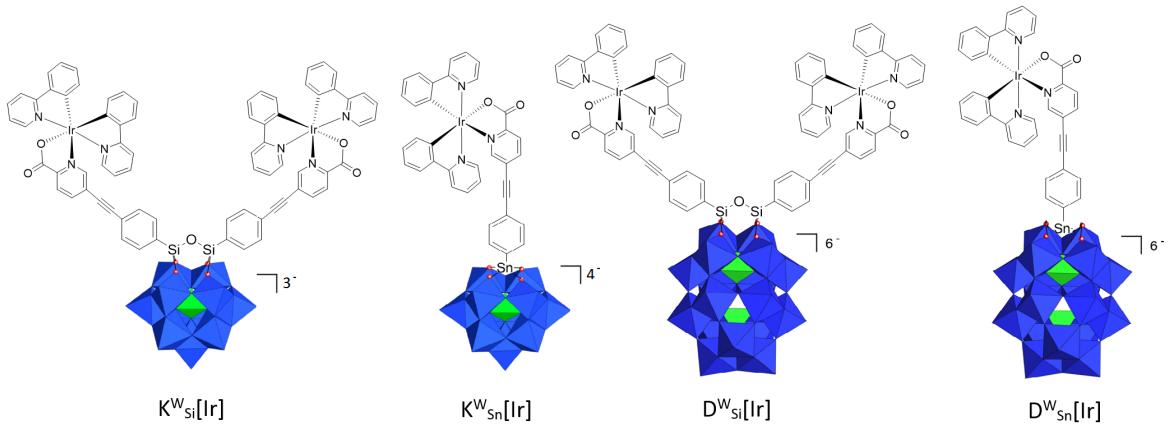

Figure 5.2: Iridium-polyoxometalate hybrid systems reported in ref [29]. Blue octahedra represent $[WO_6]$, green octahedra represent $[PO_4]$.

Both the structure of the polyoxotungstate and the π linker group were found to have an effect on the rates of intramolecular charge transfer.[28] In general, upon excitation of the iridium chromophore, intramolecular charge-separation occurred on a faster timescale for systems containing Keggin polyoxometalates than Dawson polyoxometalates. The linker group had an even more significant effect on the timescales of both charge-separation and charge-recombination, with charge-separation occurring on a picosecond timescale for systems containing an organosilicon linker group and on a nanosecond timescale for systems containing an organotin linker group. Similarly, charge-recombination occurred over a few nanoseconds for organosilicon systems and hundreds of nanoseconds for organotin

systems.

The polyoxometalate hybrid structures discussed in this chapter are shown in Figure 5.3 and contain covalently-bound boron dipyrromethene (bodipy) photosensitisers. As previously mentioned in Section 4.3, bodipy molecules are useful chromophores as they commonly have high molar absorption coefficients in the visible region and are synthetically simple to functionalise. This allows tuning of the bodipy-polyoxometalate hybrid through modifications to the bodipy group, for example an anchor group could be added to graft the photosensitser to a semiconductor surface. The hybrid systems described in this work are based on two polyoxometalate structures, Keggin ($K^{W}{}_{Si}[BOD_1]$, $K^{W}{}_{Sn}[BOD_2]$, $K^{Mo}{}_{Sn}[BOD_2]$) and Dawson ($D^{W}{}_{Si}[BOD_1]_{TBA}$, $D^{W}{}_{Si}[BOD_1]_{TEA}$, $D^{W}{}_{Si}[BOD_1]_{TMA}$).

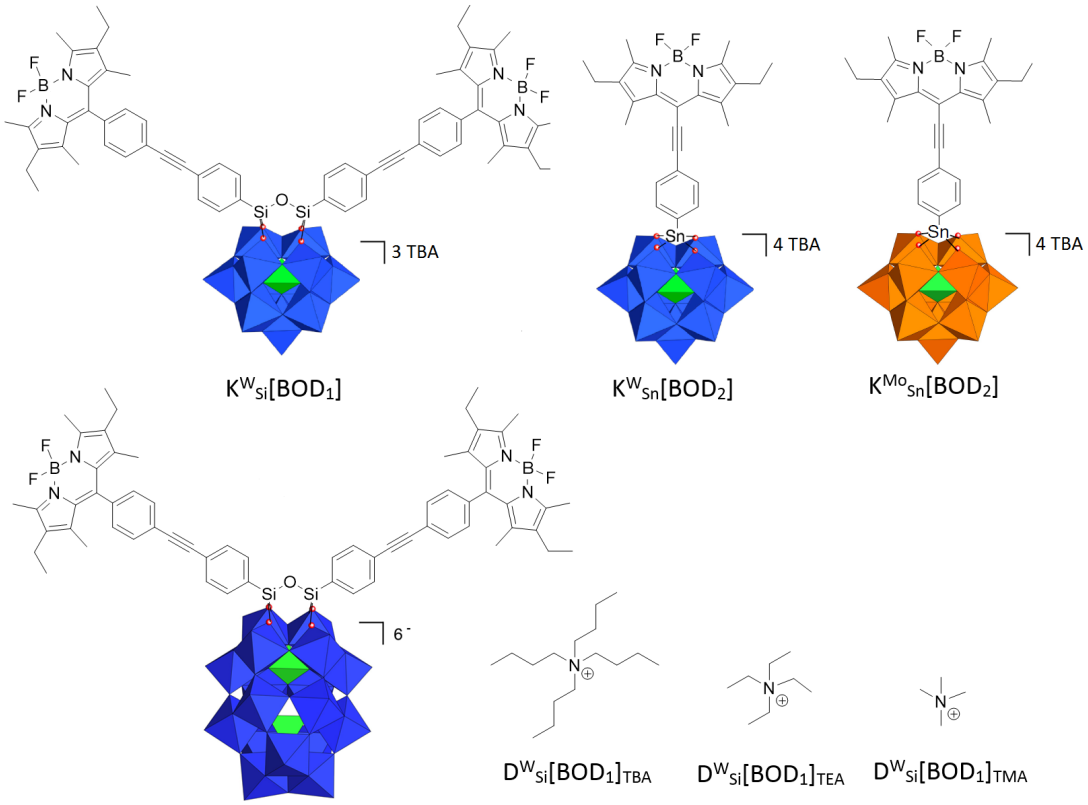

Figure 5.3: Structures of bodipy-polyoxometalate hybrids with organosilyl or organotin attachments. Blue octahedra represent $[WO_6]$, green octahedra represent $[PO_4]$ and orange octahedra represent $[MoO_6]$. TBA = tetrabutylammonium; TEA = tetraethylammonium; TMA = tetramethylammonium cations.

The Keggin structures $K^{W}{}_{Sn}[BOD_2]$ and $K^{Mo}{}_{Sn}[BOD_2]$ contain the same bodipy photosensitiser, with a 2,8-diethyl-1,3,7,9-tetramethyl bodipy core and an alkynyl group at the *meso* position, linking the bodipy to the POM via a phenyl-alkynyl bridge. $K^{W}{}_{Si}[BOD_1]$

contains an organosilicon linker and two bodipy photosensitisers with a phenyl group at the *meso* position so the bridge is phenyl-alkynyl-phenyl. These hybrids are the first examples of Keggin-type polyoxometalates covalently-bound to bodipys, with one other example of a bodipy-polyoxometalate system reported based on an Anderson-type polyoxometalate.[30] The Dawson structure $D^{W}{}_{Si}[BOD_1]_{TBA}$ is analogous to $K^{W}{}_{Si}[BOD_1]$, with an organosilicon linker, tungsten metal, tetrabutylammonium cations and a phenyl-alkynyl-phenyl bridge to the bodipy groups. $D^{W}{}_{Si}[BOD_1]_{TEA}$ and $D^{W}{}_{Si}[BOD_1]_{TMA}$ contain tetraethylammonium and tetramethylammonium counter cations, respectively. The structures of the bodipy photosensitisers are similar to those in Section 4.3 where the bodipy groups were used as acceptors. In this chapter we investigate the properties of the bodipys as donating groups.

Upon excitation of the bodipy there are a number of possible relaxation pathways which are represented by the energy level diagram in Figure 5.4. Excitation (green) can form bodipy-centred singlet or triplet excited states. From here a $BOD^{+}POM^{-}$ charge-transfer excited state can be formed (red), or the excited state can relax directly to the ground state (blue). The charge-transfer excited state can recombine to the ground state directly (purple) or via the triplet excited state (orange).

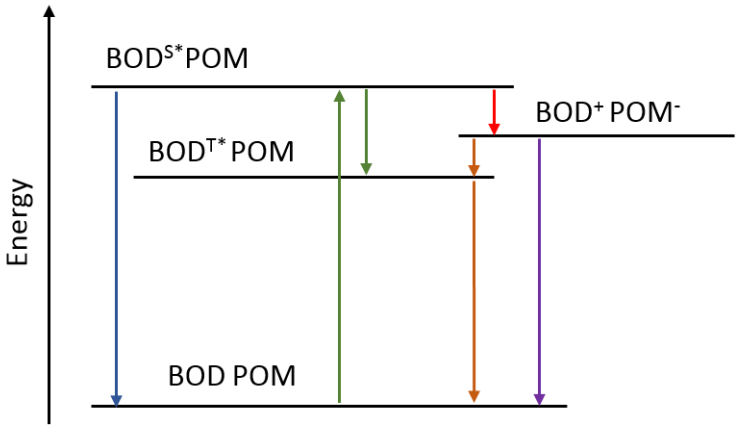

Figure 5.4: Energy level diagram of possible excitation and relaxation pathways for bodipy-polyoxometalate (BODPOM) hybrids.

The following sections outline the photoinduced charge transfer mechanisms of each bodipy-polyoxometalate hybrid using ultrafast time-resolved spectroscopies to investigate the effects of hybridisation, the linker group, the metal atom, the polyoxometalate

structure and the structure of the counter ion.

5.3 Effect of hybridisation

The photophysical and electrochemical properties of bodipy photosensitisers and polyoxometalate starting materials were compared to those of the hybrid compounds. Dawson and Keggin starting materials with organotin and organosilicon linker groups have been previously studied by Proust[29] and are shown in Figure 5.5. Organosilicon and organotin linker groups are coupled to BOD_1 and BOD_2 via phenyl-iodo groups to form the hybrid structures.

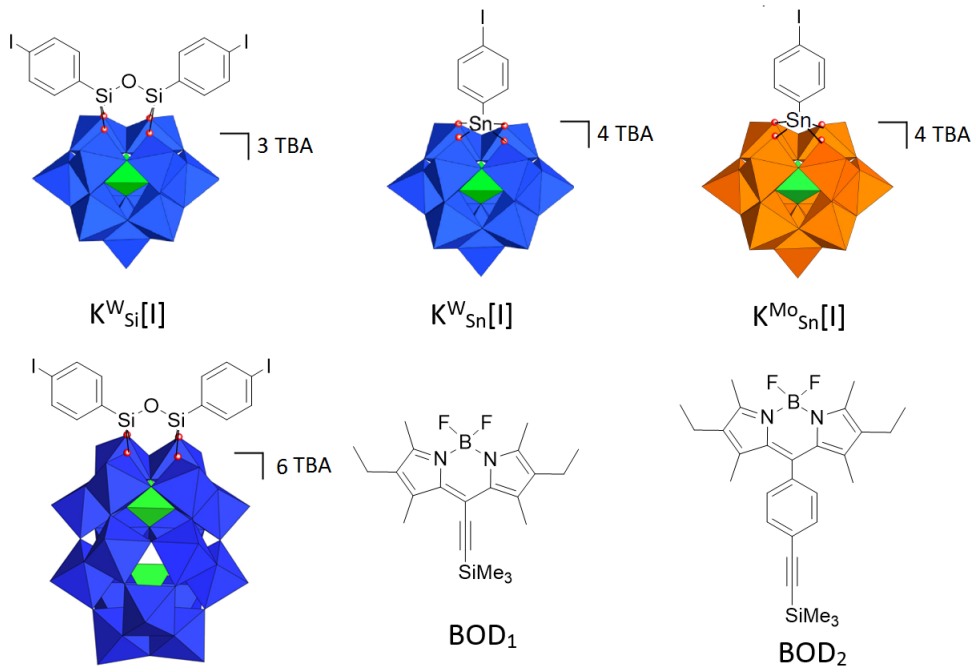

Figure 5.5: Structure of bodipy and polyoxometalate starting materials with organosilyl or organotin linker groups. Blue octahedra represent $[WO_6]$, green octahedra represent $[PO_4]$ and orange octahedra represent $[MoO_6]$.

The trimethylsilyl-protected bodipys BOD_1 and BOD_2 are used as reference compounds for the photosensitiser. BOD_1 has the same structure as the bodipy group in $K^{W}_{Si}[BOD_1]$, $D^{W}_{Si}[BOD_1]_{TBA}$, $D^{W}_{Si}[BOD_1]_{TEA}$ and $D^{W}_{Si}[BOD_1]_{TMA}$. BOD_2 has the same structure as the bodipy group in $K^{W}_{Sn}[BOD_2]$ and $K^{Mo}_{Sn}[BOD_2]$.

5.3.1 Photophysical properties

The absorption spectra of BOD_1, BOD_2, $K^{W}{}_{Si}[BOD_1]$, $K^{W}{}_{Sn}[BOD_2]$ and $K^{Mo}{}_{Sn}[BOD_2]$ in dichloromethane and acetonitrile solutions are shown in Figure 5.6, with the photophysical properties detailed in Table 5.1. The polyoxometalate group does not contribute to the absorption spectrum in the visible region and instead the spectra are dominated by the bodipy chromophores. In both solvents a typical sharp S_0-S_1 bodipy absorption band is present with a shoulder at higher energy. The absorption maximum of $K^{W}{}_{Si}[BOD_1]$ is consistent with that of BOD_1, whereas the absorption maxima of $K^{W}{}_{Sn}[BOD_2]$ and $K^{Mo}{}_{Sn}[BOD_2]$ are red-shifted slightly from BOD_2. This suggests a slight contribution from the organotin group to the π system of the bodipy and bridge.

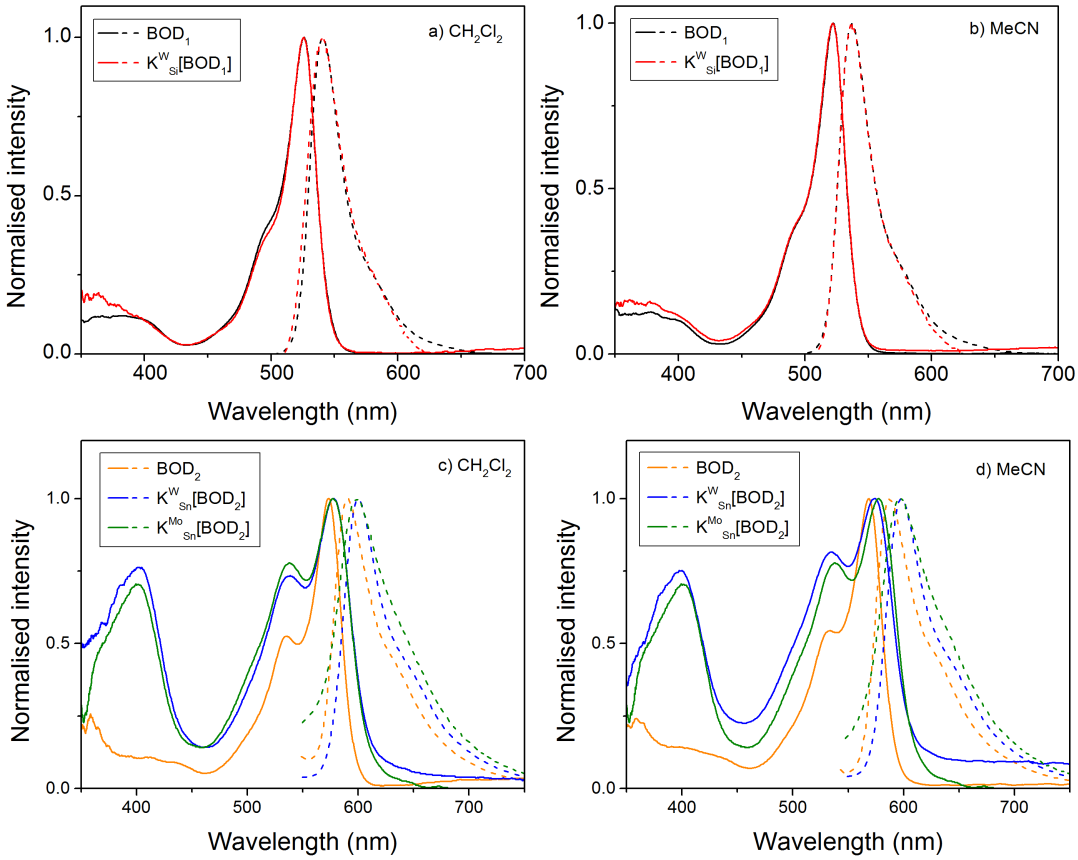

Figure 5.6: Normalised electronic absorption (solid lines) and emission (dashed lines) spectra of Keggin bodipy-polyoxometalate hybrids and bodipy photosensitisers in dichloromethane and acetonitrile solutions.

	Absorption λ_{max} (nm)	Emission λ_{max} (nm)	$E_{0\text{-}0}$ (eV)	ε^a (dm^3 mol^{-1} cm^{-1})	τ_{FL} (ns)	Φ_{FL}
Dichloromethane						
BOD_1	527	540	2.33	72 000	5.5	0.67
BOD_2	574	590	2.14	53 000	6.9	0.52
$K^{W}{}_{Si}[BOD_1]$	527	541	2.33	140 000	0.9 (63%), 4.3 (37%)	0.07
$K^{W}{}_{Sn}[BOD_2]$	579	600	2.10	55 000	5.4	0.22
$K^{Mo}{}_{Sn}[BOD_2]$	579	597	2.11	50 000	1.2	0.06
Acetonitrile						
BOD_1	522	538	2.34		5.4	0.60
BOD_2	568	588	2.15		5.9	0.43
$K^{W}{}_{Si}[BOD_1]$	522	538	2.34		1.1 (73%), 5.4 (27%)	0.06
$K^{W}{}_{Sn}[BOD_2]$	573	598	2.11		4.6	0.16
$K^{Mo}{}_{Sn}[BOD_2]$	573	596	2.12		0.94	0.02

Table 5.1: Photophysical properties of Keggin bodipy-polyoxometalate hybrids and bodipy photosensitisers. Fluorescence lifetimes, τ_{FL}, were determined by fitting single exponential decay functions, with the exception of $K^{W}{}_{Si}[BOD_1]$ which was fit using a bi-exponential decay function. The amplitude of each component is given in brackets. Φ_{FL} is the quantum yield of fluorescence. [a]Molar absorption coefficient values in dichloromethane were determined by Dr. Izzet.

In dichloromethane the absorption spectra are shifted by *ca.* +5 nm relative to acetonitrile. The absorption profiles of BOD_2, $K^{W}{}_{Sn}[BOD_2]$ and $K^{Mo}{}_{Sn}[BOD_2]$ are red-shifted and broadened relative to that of BOD_1 and $K^{W}{}_{Si}[BOD_1]$, which is a result of increased conjugation between the bodipy core and the group at the *meso* position for BOD_2 due to less rotational freedom around the bodipy-alkyne bond than the bodipy-phenyl bond. The electronic absorption spectra of Dawson bodipy-polyoxotungstate systems were also recorded, and are shown in acetonitrile solution in Figure 5.7. Their absorption profiles are also dominated by the bodipy groups and there is little difference when the cation is changed from tetrabutylammonium to tetraethylammonium or tetramethylammonium. Similar to the Keggin systems, the polyoxometalate does not contribute to the absorption spectrum in the visible region.

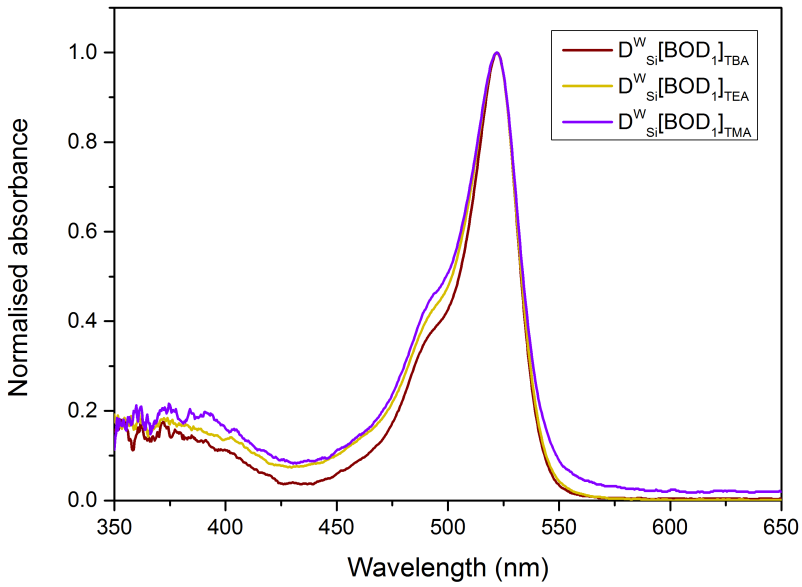

Figure 5.7: Normalised absorption spectra of $D^{W}_{Si}[BOD_1]_{TBA}$, $D^{W}_{Si}[BOD_1]_{TEA}$ and $D^{W}_{Si}[BOD_1]_{TMA}$ in acetonitrile.

The molar absorption coefficients of $K^{W}_{Sn}[BOD_2]$ and $K^{Mo}_{Sn}[BOD_2]$ are similar to BOD_2. When two bodipy groups are present in $K^{W}_{Si}[BOD_1]$, the molar absorption coefficient is twice that of BOD_1. This is higher than the molar absorption coefficients recorded for BOD2-5 studied in Section 4.3 which also contained structures with two bodipy chromophores.

Emission lifetime and fluorescence quantum yield values were measured as described in the Experimental Section 3.6.1, and the emission decays are shown in Figure 5.8. The fluorescence quantum yields of $K^{W}_{Si}[BOD_1]$ and $K^{Mo}_{Sn}[BOD_2]$ are *ca.* 90 % lower than their corresponding bodipy chromophores, BOD_1 and BOD_2, respectively, and the fluorescence lifetimes are shorter for the hybrid systems (τ_{FL} = *ca.* 1 ns) than the separate bodipy groups (τ_{FL} = *ca.* 6 ns). The emission lifetime of $K^{W}_{Si}[BOD_1]$ also contains a longer component which is on the same timescale as BOD_1, suggesting that quenching of the bodipy is less efficient for this system. This is even more significant for $K^{W}_{Sn}[BOD_2]$ which has an emission lifetime similar to that of BOD_2 and the fluorescence quantum yield is reduced by just 50 % upon hybridisation.

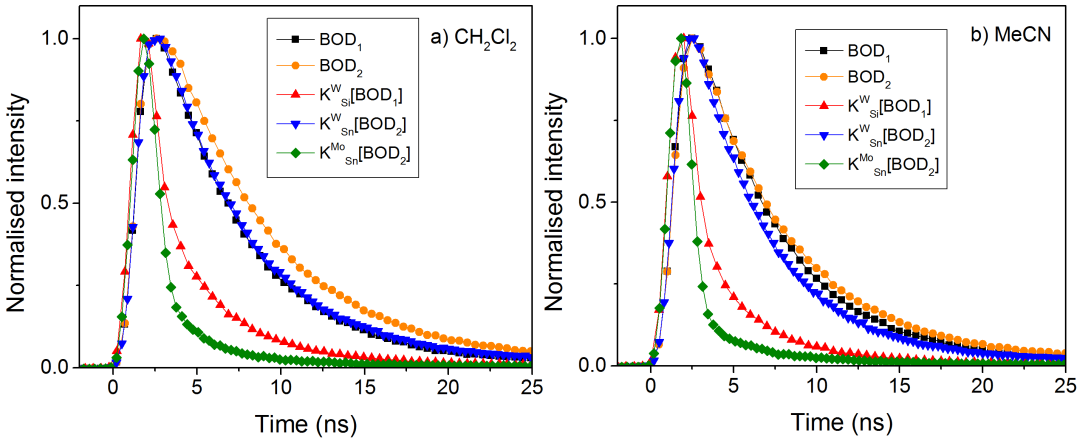

Figure 5.8: Fluorescence decay traces of BOD_1, BOD_2 and bodipy-polyoxometalate hybrids. a) In dichloromethane; b) In acetonitrile. Excitation with an LED bulb, λ = *ca.* 400 nm. The data was deconvoluted using the software on the instrument. The lifetimes of each decay, τ_{FL}, are given in Table 5.1.

5.3.2 Steady state vibrational absorption

The infrared spectra of BOD_1, BOD_2, $K^{W}{}_{Si}[BOD_1]$, $K^{W}{}_{Sn}[BOD_2]$ and $K^{Mo}{}_{Sn}[BOD_2]$ are shown in Figure 5.9 and the frequencies of the major bands are given in Table 5.2. The main bands in the fingerprint region are due to the bodipy groups and are similar to those observed for BOD2 in Section 4.5. Two intense bands at 1535 cm^{-1} to 1539 cm^{-1} and 1470 cm^{-1} to 1475 cm^{-1} and a sharp band at 1313 cm^{-1} to 1322 cm^{-1} are attributed to the ν(C=C) of the phenyl groups, highlighted in blue on the infrared spectra.

A weaker band at 1378 cm^{-1} is present in all spectra and was also present in the infrared spectrum of BOD2 suggesting that this band is related to the ν(C=C) of the bodipy groups. It is difficult to distinguish bands relating to the polyoxometalate from those of the bodipy, which may be due to the low relative intensity of the polyoxometalate vibrations. There are also no bands in the region between 2000 cm^{-1} to 2200 cm^{-1} where the alkyne stretch on the bridge would be expected. However, the bands highlighted in yellow in Figure 5.9 at 1272 cm^{-1} to 1248 cm^{-1} for BOD_1 and 1263 cm^{-1} to 1233 cm^{-1} for BOD_2 are different from those in the infrared spectra of the corresponding POMs. It is therefore proposed that these bands are related to the linker group. In this region there are two bands between 1275 cm^{-1} to 1263 cm^{-1} for $K^{W}{}_{Si}[BOD_1]$ which contains an organosilicon linker and one band at 1266 cm^{-1} for $K^{W}{}_{Sn}[BOD_2]$ and $K^{Mo}{}_{Sn}[BOD_2]$ which

contain organotin linkers.

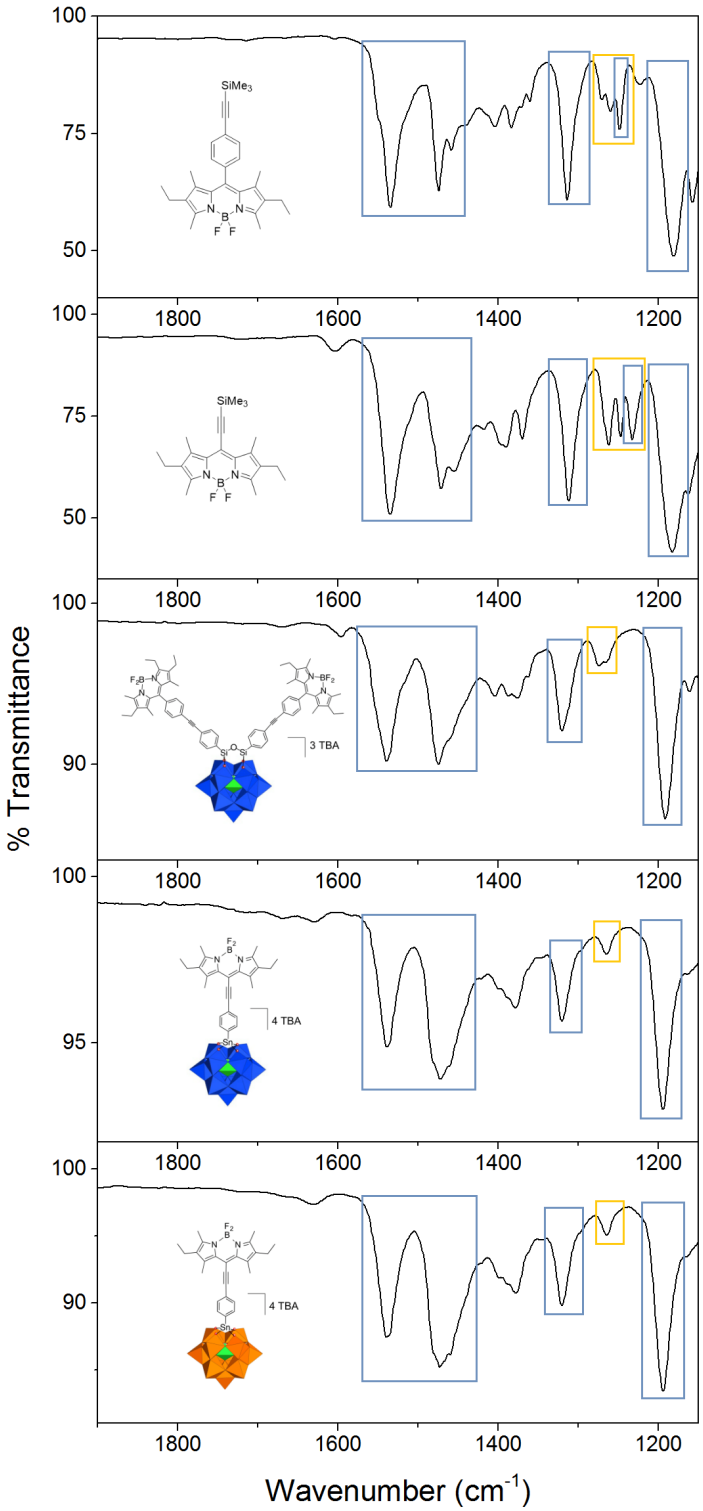

Figure 5.9: Ground state infrared spectra of BOD_1, BOD_2 and Keggin bodipy-polyoxometalate hydrids. Samples were crushed and pressed into potassium bromide disks. Coloured boxes indicate bodipy and phenyl vibrations ν(C=C) (blue) and vibrations relating to the linker group (yellow).

	Wavenumber, cm^{-1}
BOD_1	1535, 1475, 1457, 1314, 1181
	1271, 1261, 1249
BOD_2	1535, 1471, 1454, 1312, 1183
	1262, 1248, 1232
$K^{W}{}_{Si}[BOD_1]$	1539, 1475, 1320, 1190
	1274, 1264
$K^{W}{}_{Sn}[BOD_2]$	1539, 1472, 1320, 1195
	1265
$K^{Mo}{}_{Sn}[BOD_2]$	1538, 1472, 1320, 1194
	1265

Table 5.2: Frequencies of the major bands in the ground state infrared spectra of Keggin bodipy-polyoxometalate hybrids and their corresponding bodipy photosensitisers, from the infrared spectra in Figure 5.9.

5.3.3 Electrochemistry

The electrochemical properties of hybrid systems were investigated by cyclic voltammetry, and were compared to those of bodipy photosensitisers and polyoxometalate starting materials. The redox properties of $K^{W}{}_{Si}[I]$, $K^{W}{}_{Sn}[I]$ and $K^{Mo}{}_{Sn}[I]$ in acetonitrile solution have been previously reported and the values mentioned here are taken from ref [29]. The cyclic voltammograms and differential pulse voltammograms of $K^{W}{}_{Si}[I]$, $K^{W}{}_{Sn}[I]$, $K^{Mo}{}_{Sn}[I]$, $K^{W}{}_{Si}[BOD_1]$, $K^{W}{}_{Sn}[BOD_2]$ and $K^{Mo}{}_{Sn}[BOD_2]$ in dichloromethane (Figures 5.10 and 5.11) were recorded by the author of this thesis using a three electrode setup with a saturated calomel reference electrode, glassy carbon working electrode and platinum counter electrode. The values for BOD_1 and BOD_2 in dichloromethane and acetonitrile were provided to us by Dr. Izzet. The electrochemical properties including new and reported data are detailed in Table 5.3.

In general, the redox properties of the bodipy groups and polyoxometalate groups in the hybrid structures occur at similar potentials to those of the separate components, which suggests there is little electronic communication between the photosensitiser and the polyoxometalate. This is similar behaviour to previously reported iridium-polyoxometalate systems where the redox properties of the hybrids were similar to the separate polyox-

ometalates and photosensitisers.[28] A small additional process is observed at a similar potential to the second reduction of $K^{W}_{Si}[BOD_1]$ which is not present for $K^{W}_{Si}[I]$. However, this process is not assigned to a bodipy-centred reduction, as there is no process identified at this potential for the reduction of BOD_1.[31] The bodipy-centred oxidation processes in $K^{W}_{Sn}[BOD_2]$ and $K^{Mo}_{Sn}[BOD_2]$ occur at a slightly more positive potential than BOD_2. The first reduction potential of the polyoxotungstate in $K^{W}_{Sn}[BOD_2]$ occurs at a more negative potential by *ca.* 500 mV than $K^{W}_{Si}[BOD_1]$. This has been previously observed for $K^{W}_{Sn}[I]$ and $K^{W}_{Si}[I]$, and is due to the differences in charge, as the reduction of the organotin polyoxometalate involves one electron compared to the organosilicon which involves two electrons.[28,29] This relative potential difference is significant as the reduction potential of the polyoxometalate in $K^{W}_{Sn}[BOD_2]$ is positioned higher in energy than the reduction potential of the bodipy so charge transfer from the bodipy to the polyoxometalate is thermodynamically unfavourable for this system, whereas it is favourable for $K^{W}_{Si}[BOD_1]$.

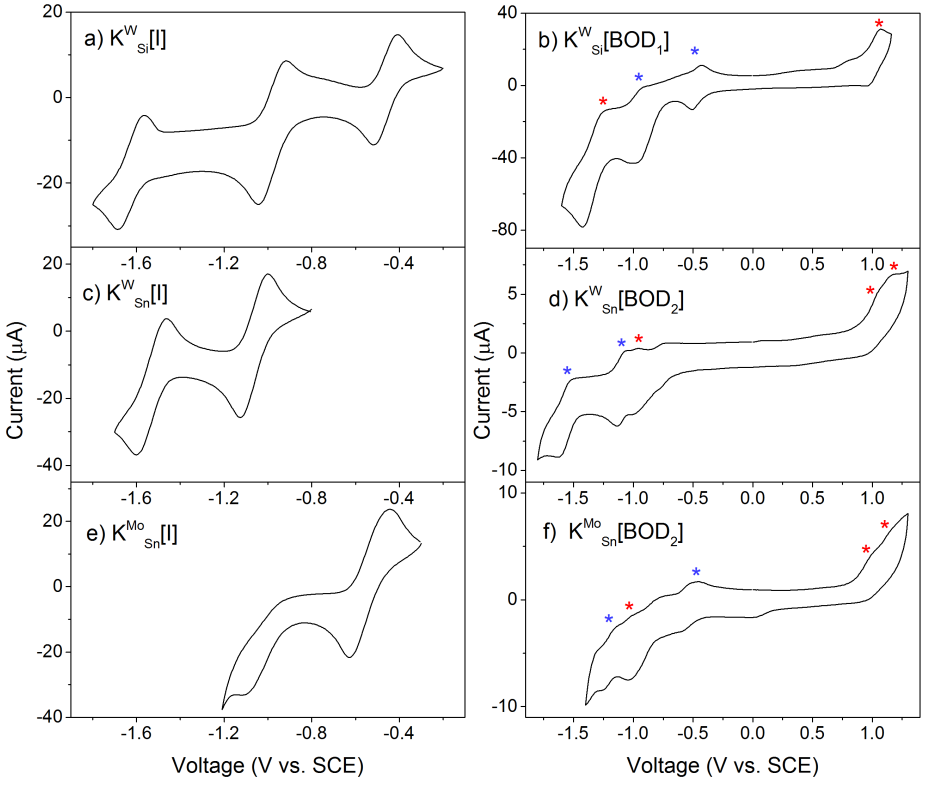

Figure 5.10: Cyclic voltammograms of $K^{W}_{Si}[I]$, $K^{W}_{Sn}[I]$, $K^{Mo}_{Sn}[I]$ and Keggin bodipy-polyoxometalate hybrids in dichloromethane solution with 0.1 M $TBAPF_6$. A glassy carbon working electrode, platinum wire counter electrode and saturated calomel reference electrode were used and the scan rate was 100 mV/s. Bodipy-centred and POM-centred processes are indicated with red and blue symbols respectively.

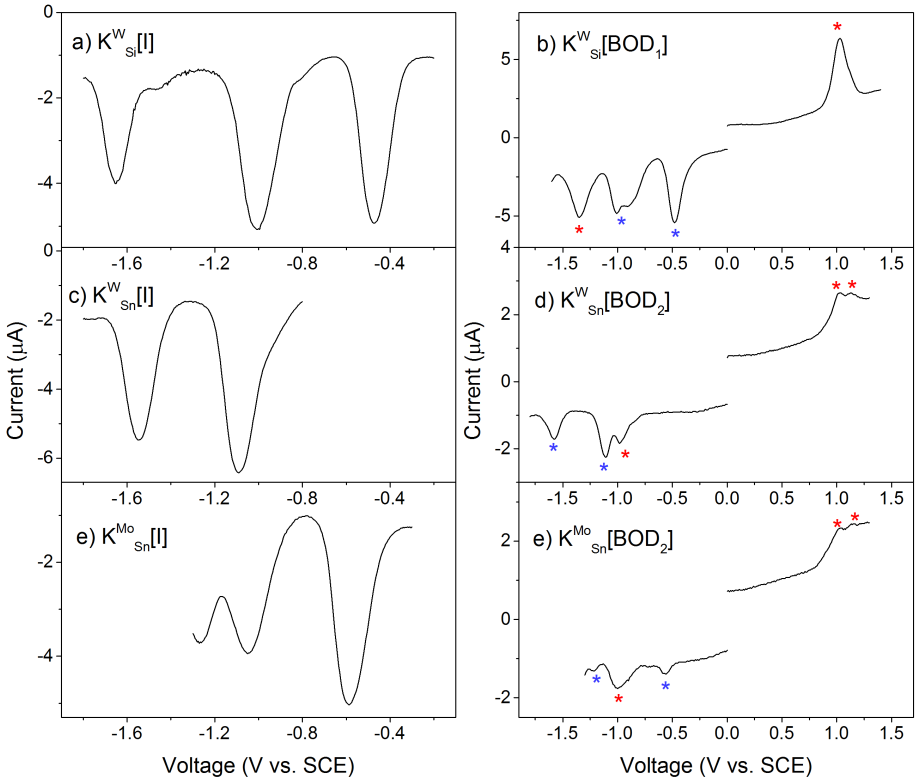

Figure 5.11: Differential pulse voltammograms of $K^{W}{}_{Si}[I]$, $K^{W}{}_{Sn}[I]$, $K^{Mo}{}_{Sn}[I]$ and Keggin bodipy-polyoxometalate hybrids in dichloromethane solution with 0.1 M $TBAPF_6$. A glassy carbon working electrode, platinum wire counter electrode and saturated calomel reference electrode were used and the scan rate was 100 mV/s. Bodipy-centred and POM-centred processes are indicated with red and blue symbols respectively.

The reduction potential of polyoxomolybdate in $K^{Mo}{}_{Sn}[BOD_2]$, which also contains an organotin linker, is shifted to a more negative potential by only *ca.* 100 mV relative to $K^{W}{}_{Si}[BOD_1]$, and there is still an enthalpic driving force for charge transfer in this system. A comparison of the relative driving forces will be discussed in Section 5.3.4. The reduction potentials of $K^{W}{}_{Si}[I]$, $K^{W}{}_{Sn}[I]$ and $K^{Mo}{}_{Sn}[I]$ are shifted to a more negative potential by *ca.* 150 mV in dichloromethane relative to the values reported in acetonitrile. The oxidation potentials of BOD_1 and BOD_2 are similar and are less affected by solvent than the polyoxometalates. The reduction potential of BOD_2 is more positive than BOD_1 by *ca.* 200 mV, which we propose is due to the π system extending over the alkyne group, favouring its reduction.

	BOD/BOD$^+$	BOD/BOD$^-$	POM/POM$^-$	POM-/POM^{2-}
		(V vs SCE)		
		Dichloromethane		
^{a}BOD$_1$	1.00	-1.35		
K$^W_{Si}$[I]			-0.49	-1.00
K$^W_{Si}$[BOD$_1$]	1.03	-1.35	-0.48	-1.01
^{a}BOD$_2$	0.98	-1.05		
K$^W_{Sn}$[I]			-1.11	-1.59
K$^W_{Sn}$[BOD$_2$]	1.13	-0.98	-1.11	-1.58
K$^{Mo}_{Sn}$[I]			-0.63	-1.10
K$^{Mo}_{Sn}$[BOD$_2$]	1.15	-1.00	-0.56	-1.21
		Acetonitrile		
^{a}BOD$_1$	1.07	-1.15		
^{a}K$^W_{Si}$[I]			-0.32	-0.83
^{a}K$^W_{Si}$[BOD$_1$]	1.03	-1.16	-0.31	-0.83
^{a}BOD$_2$	1.03	-0.92		
^{a}K$^W_{Sn}$[I]			-0.97	-1.42
^{a}K$^W_{Sn}$[BOD$_2$]	1.22	-0.89	-1.01	-1.49
^{a}K$^{Mo}_{Sn}$[I]			-0.47	-0.89
^{a}K$^{Mo}_{Sn}$[BOD$_2$]	1.16	-0.93	-0.46	-1.12

Table 5.3: Electrochemical properties of Keggin bodipy-polyoxometalate hybrids along with their corresponding bodipy photosensitisers and polyoxometalate starting materials in dichloromethane and acetonitrile solutions, with 0.1 M $TBAPF_6$ supporting electrolyte. A glassy carbon working electrode, platinum wire counter electrode and saturated calomel reference electrode were used. ^{a}The values in acetonitrile were provided to us by Dr. Izzet, along with the values for BOD_1 and BOD_2 in dichloromethane.

The electrochemical properties of the Dawson bodipy-polyoxometalates D$^W_{Si}$[BOD$_1$]$_{TBA}$, D$^W_{Si}$[BOD$_1$]$_{TEA}$ and D$^W_{Si}$[BOD$_1$]$_{TMA}$ were recorded by Dr. Izzet and are given in the Appendix, Figure A.4. The reduction potential of the polyoxometalate is shifted to a more negative potential by *ca.* 400 mV for the Dawson systems relative to K$^W_{Si}$[I], which is similar to behaviour previously reported by the group of Proust.[28] Changing the counter cations to tetramethylammonium shifts the first reduction of the polyoxometalate to a more positive potential and similar to that of K$^W_{Si}$[BOD$_1$].

5.3.4 Driving forces

The electrochemical and photophysical properties of the bodipy-polyoxometalate hybrids are combined to determine the excited state oxidation potential of the bodipy group (BOD^*/BOD^+) and the driving forces for intramolecular charge-separation and charge-recombination, ΔG_{CS} and ΔG_{rec}. (BOD^*/BOD^+) was determined from the bodipy-centred oxidation of the hybrid system (BOD/BOD^+) and the $E_{0\text{-}0}$ energy:

$$BOD^*/BOD^+ = BOD/BOD^+ - E_{0\text{-}0} \tag{5.1}$$

ΔG_{CS} is the energy difference between the excited state oxidation potential of the bodipy and the first reduction potential of the polyoxometalate group (POM/POM^-),as shown in Equation 5.2. ΔG_{rec} is determined according to Equation 5.3. The term for electrostatic interactions is not included,[32] which relates to the dielectric constant of the solvent and the distance between the charges. Despite being a simplification, this method of estimating is often used as it is unlikely to have a significant effect. The relevant values are detailed in Table 5.4.

$$\Delta G_{CS} \approx E(BOD^*/BOD^+) - E(POM/POM^-) \tag{5.2}$$

$$\Delta G_{rec} \approx E(POM/POM^-) - E(BOD^+/BOD) \tag{5.3}$$

	BOD^*/BOD^+ (V vs SCE)	POM/POM^- (V vs SCE)	ΔG_{CS} (eV)	ΔG_{rec} (eV)
		Dichloromethane		
$K^{W}{}_{Si}[BOD_1]$	-1.30	-0.48	-0.82	-1.51
$K^{W}{}_{Sn}[BOD_2]$	-0.97	-1.11	0.14	-2.24
$K^{Mo}{}_{Sn}[BOD_2]$	-0.96	-0.56	-0.40	-1.71
		Acetonitrile		
$K^{W}{}_{Si}[BOD_1]$	-1.31	-0.31	-1.00	-1.34
$K^{W}{}_{Sn}[BOD_2]$	-0.89	-1.01	0.12	-2.23
$K^{Mo}{}_{Sn}[BOD_2]$	-0.96	-0.46	-0.50	-1.62

Table 5.4: Driving forces for POM^-BOD^+ charge-separation and charge-recombination in bodipy-polyoxometalate hybrids.

The energy-level diagram in Figure 5.12 summarises the relative driving forces of charge-separation and charge-recombination for $K^{W}{}_{Si}[BOD_1]$, $K^{W}{}_{Sn}[BOD_2]$ and $K^{Mo}{}_{Sn}[BOD_2]$ in both dichloromethane and acetonitrile solutions.

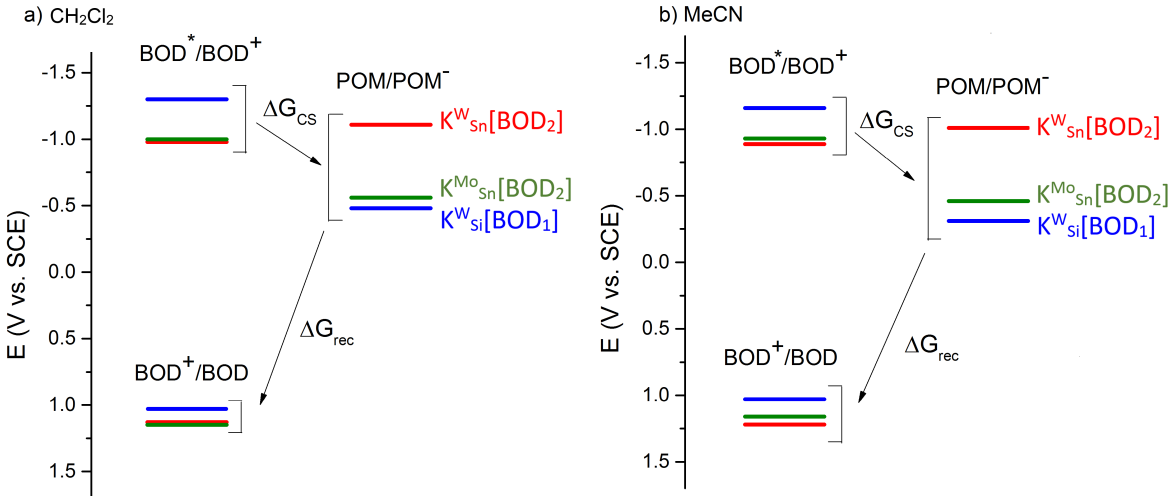

Figure 5.12: Energy level diagram of bodipy-polyoxometalate hybrids, representing the data in Table 5.4. a) In dichloromethane; b) in acetonitrile solution.

Charge transfer from the bodipy to the polyoxometalate for $K^{W}{}_{Si}[BOD_1]$ and $K^{Mo}{}_{Sn}[BOD_2]$ are thermodynamically favourable processes, whereas this process is unfavourable for $K^{W}{}_{Sn}[BOD_2]$ in both solvents. For all systems there is a large driving force for charge-recombination. In general the ΔG_{CS} is greater by *ca.* 100 mV for systems in acetonitrile compared to dichloromethane.

5.4 Linker and Bridge

In this section time-resolved spectroscopy of $K^{W}{}_{Si}[BOD_1]$ and $K^{W}{}_{Sn}[BOD_2]$ is used to compare the excited state dynamics of bodipy-polyoxotungstate systems with different linker groups. The bodipy of $K^{W}{}_{Si}[BOD_1]$ has a phenyl group at the *meso* position whereas $K^{W}{}_{Sn}[BOD_2]$ has a shorter bridge with an alkynyl group. The organosilicon analogue of $K^{W}{}_{Sn}[BOD_2]$ was unstable when synthesised, but this study still allows a sensible comparison of the two linker groups.

5.4.1 Spectroelectrochemistry

Spectroelectrochemical analysis was used to determine the visible spectra of oxidised bodipy and reduced polyoxometalate species. Samples in a solution of 0.1 M tetrabutylammonium hexafluorophosphate were added to an OTTLE cell as described in the Experimental Section 2.3.3, and a reducing or oxidising potential was applied as ultraviolet-visible spectra were taken. For polyoxometalates, the reducing potential was applied stepwise over the range of the first two reduction processes observed via cyclic voltammetry. The difference spectra of BOD_1 and BOD_2 in dichloromethane solution are shown in Figure 5.13. The ground state absorption saturates the detector causing spikes in the negative signal.

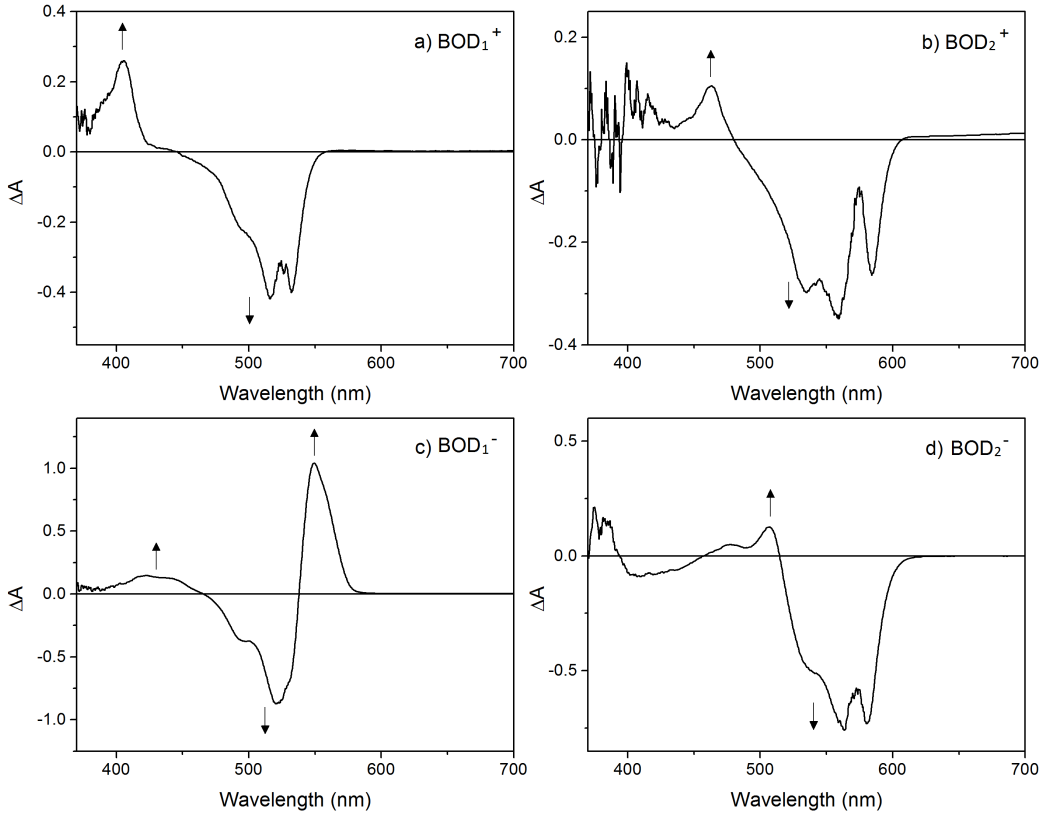

Figure 5.13: Absorbance difference spectra taken in the visible region as BOD_1 and BOD_2 were oxidised and reduced electrochemically in an OTTLE cell, with 0.1 M $TBAPF_6$ in dichloromethane as supporting electrolyte. a) BOD_1, 1.0 V vs fc/fc^+; b) BOD_2, 1.0 V vs fc/fc^+; c) BOD_1, -1.5 V vs fc/fc^+; d) BOD_2, -1.5 V vs fc/fc^+.

In general, signals for BOD_2^+ and BOD_2^- were weaker than those generated for BOD_1. Upon oxidation, the visible spectrum of BOD_1 in dichloromethane forms a sharp peak at

400 nm, as the ground state is depleted between 450 nm to 550 nm. Upon oxidation of BOD_2 a sharp peak also grows, but is red-shifted by 60 nm relative to that of BOD_1. The spectra of BOD_1^+ and BOD_2^+ resemble $BOD4^+$, a bodipy of similar structure which was discussed previously in Section 4.3 and whose spectroelectrochemistry is shown in ref [33]. The absorption band of BOD_1^- is red-shifted relative to its ground state and has a sharp peak at 550 nm and a broader peak at 400 nm to 450 nm. BOD_2^- is blue-shifted relative to its ground state. The spectrum of BOD_2^- is similar to the oxidised form, BOD_2^+, but the sharp peak is red-shifted to 500 nm. The spectrum of $BOD4^-$ contained a peak which was red-shifted relative to the ground state, which is consistent with that observed for BOD_1^-.

Spectroelectrochemical reductions of $K^W_{Si}[I]$ and $K^W_{Sn}[I]$ were performed in dichloromethane and acetonitrile solutions and the difference spectra are shown in Figure 5.14. Generally, the observed changes upon reduction were weaker in dichloromethane than in acetonitrile.

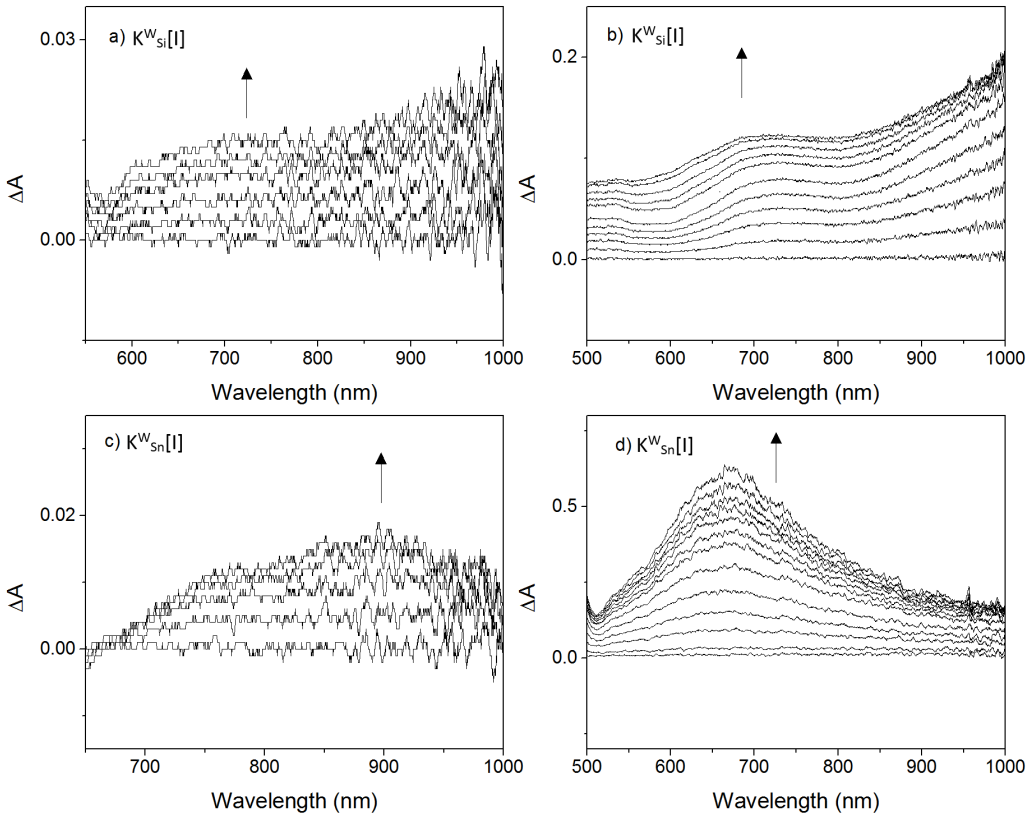

Figure 5.14: Absorption difference spectra as polyoxometalate starting materials are electrochemically reduced in an OTTLE cell with 0.1 $TBAPF_6$. a),c) In dichloromethane; b),d) in acetonitrile. $K^W_{Si}[I]$ 0 to -1.2 V vs Ag/Ag^+; $K^W_{Sn}[I]$ 0 to -2.0 V vs Ag/Ag^+.

The visible spectra of the $K^{W}_{Si}[I]^{-}$ and $K^{W}_{Sn}[I]^{-}$ contain broad bands at wavelengths above 700 nm. In acetonitrile this band is sharper for $K^{W}_{Sn}[I]^{-}$ than $K^{W}_{Si}[I]^{-}$.

5.4.2 Transient absorption spectroscopy

The excited state dynamics of $K^{W}_{Si}[BOD_1]$ and $K^{W}_{Sn}[BOD_2]$ were followed in the visible region using ultrafast transient absorption spectroscopy. These experiments were also performed for BOD_1 and BOD_2 to characterise the bodipy first excited singlet states. Dichloromethane and acetonitrile solutions of bodipy chromophores and bodipy-polyoxometalate hybrids were excited with a 540 nm laser pulse and visible spectra were recorded at various time delays following excitation, according to the experimental setup described in Section 3.7. Single-point analysis of the kinetic data was used to determine the lifetimes associated with each sample, and global analysis was used for bodipy-polyoxometalate hybrids where more complicated dynamics were evident.

Transient absorption difference spectra of BOD_1 and BOD_2 at selected time delays after excitation are shown in Figure 5.15, and lifetimes from single-point analysis are given in Table 5.5. The spectral features and singlet excited state lifetimes of BOD_1 are similar in both dichloromethane and acetonitrile solutions (τ = *ca.* 5 ns).

	Lifetime, ns	
	Dichloromethane	Acetonitrile
BOD_1	τ_{343} = 4.9±0.4	τ_{345} = 5.5±1.6
	τ_{430} = 5.3±0.2	τ_{435} = 4.3±0.2
	τ_{499} = 4.9±0.1	τ_{490} = 4.5±0.2
	τ_{581} = 5.1±0.2	τ_{585} = 4.1±0.2
BOD_2	τ_{430} = 1.6±0.07	τ_{380} = 4.3±0.1
	τ_{586} = 2.2±0.08	τ_{640} = 6.0±0.2
	τ_{690} = 2.4±0.07	

Table 5.5: Lifetimes derived from single-point analysis of transient absorption data of BOD_1 and BOD_2. A single exponential function was used to fit each decay. λ_{exc} = 540 nm.

A negative signal corresponds to the ground state bleach between 475 nm and 650 nm, with some stimulated emission at longer wavelengths. This is consistent with steady

state measurements where the ground state absorbs between 450 nm and 500 nm, and emission occurs between 500 nm and 600 nm. The transient signal contains a broad peak centred at 430 nm. The amplitude of the transient signal is considerably smaller for BOD_2 compared to BOD_1 in both solvents. A small peak at 430 nm decays with τ = 2.2 ns and a broad bleach extends past the laser wavelength. In acetonitrile the transient peak is blue-shifted to 380 nm. The photoinduced signals decay slightly slower in acetonitrile relative to dichloromethane (τ = *ca.* 5 ns in acetonitrile).

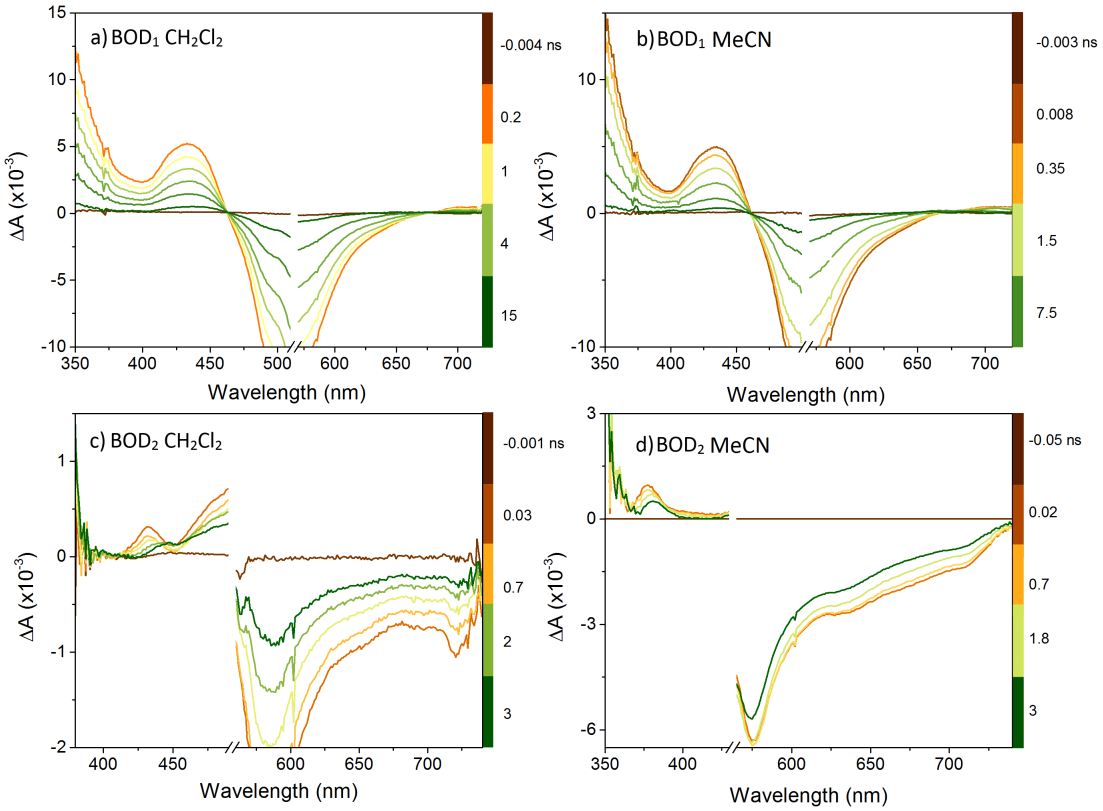

Figure 5.15: Transient absorption difference spectra of BOD_1 and BOD_2 at selected time delays following excitation at 540 nm. a),c) In dichloromethane; b),d) in acetonitrile.

The photoinduced dynamics of $K^{W}_{Si}[BOD_1]$ and $K^{W}_{Sn}[BOD_2]$ are shown in Figure 5.16 and are different to BOD_1 and BOD_2, with lifetimes from single-point analysis given in Table 5.6. At short delay times (0.5 ps to 300 ps) the transient absorption spectra of $K^{W}_{Si}[BOD_1]$ in both dichloromethane and acetonitrile resemble that of BOD_1, which is consistent with the formation of the bodipy first excited singlet state. This transient decays with τ = *ca.* 40 ps in dichloromethane, on the same timescale as the decay of the bleach at longer wavelengths, which is attributed to stimulated emission. The singlet

excited state decays slightly faster in acetonitrile (τ = *ca.* 25 ps).

A sharp absorption centred at 405 nm which closely resembles BOD_1^+ generated electrochemically (Figure 5.13), and a broad band which absorbs above 650 nm resembling $K^W_{Si}[I]^-$ (Figure 5.14) grow on the same timescale as the first excited singlet state decays. The appearance of these two peaks is convincing evidence of the formation of the POM^-BOD^+ intramolecular charge-separated state.

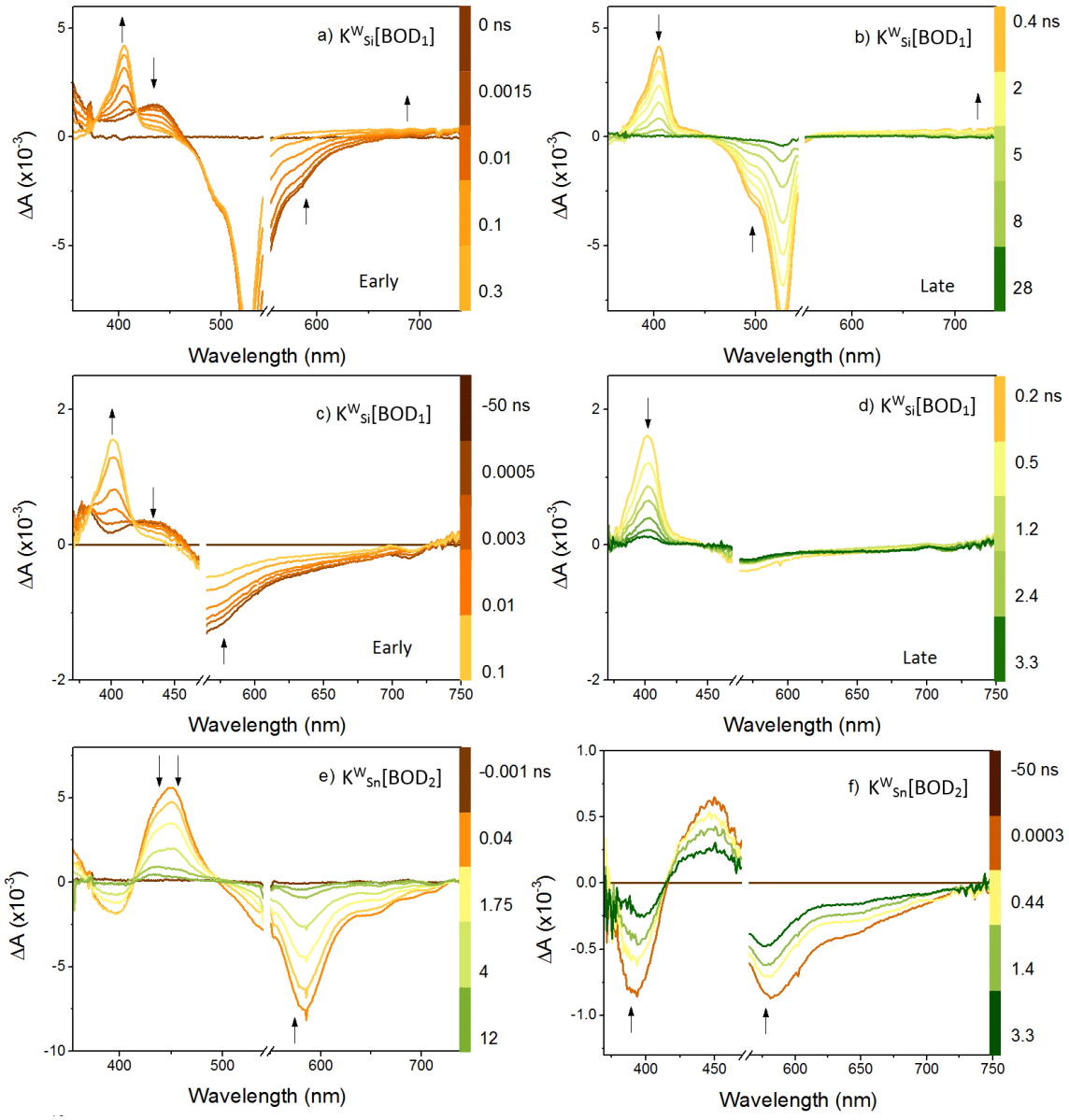

Figure 5.16: Transient absorption difference spectra of $K^W_{Si}[BOD_1]$ and $K^W_{Sn}[BOD_2]$. λ_{exc} = 540 nm. a),b) in dichloromethane after short and long delay times; c), d) in acetonitrile after short and long delay times; e) in dichloromethane; f) in acetonitrile.

	Lifetime, ns	
	Dichloromethane	Acetonitrile
$K^{W}_{Si}[BOD_1]$	τ_{352} = 0.046±0.004	
	τ_{405}(rise) = 0.035±0.002	τ_{402}(rise) = 0.032±0.003
	τ_{405} = 2.9±0.1	τ_{402} = 1.1±0.03
	τ_{445} = 0.047±0.003	τ_{438} = 0.06±0.02
	τ_{500} = 3.1±0.1	τ_{640} = 0.05±0.005
	τ_{585} = 0.047±0.002	τ_{779}(rise) = 0.023±0.005
	τ_{688}(rise) = 0.043±0.01	τ_{779} = 1.9±0.6
	τ_{688} = 3.3±0.3	
$K^{W}_{Sn}[BOD_2]$	τ_{396} = 4.2±0.3	τ_{396} = 2.2±0.1
	τ_{431} = 3.5±0.1 (86%), 100 (14%)[a]	τ_{449} = 3.6±0.2
	τ_{450} = 4.2±0.1	τ_{599} = 3.6±0.4
	τ_{599} = 2.6±0.3 (97%), 100 (3%)[a]	τ_{650} = 3.9±0.3
	τ_{650} = 3.4±0.2	

Table 5.6: Lifetimes derived from single-point analysis of transient absorption data of bodipy-polyoxometalate hybrids. [a]A component of 100 ns was fixed to account for long-lived species.

The charge-transfer excited state decays with τ = *ca.* 3.3 ns in dichloromethane and τ = *ca.* 2 ns in acetonitrile. An expansion of the transient absorption spectra of $K^{W}_{Si}[BOD_1]$ in dichloromethane is shown in Figure 5.17 and shows the growth and decay of POM^{-}.

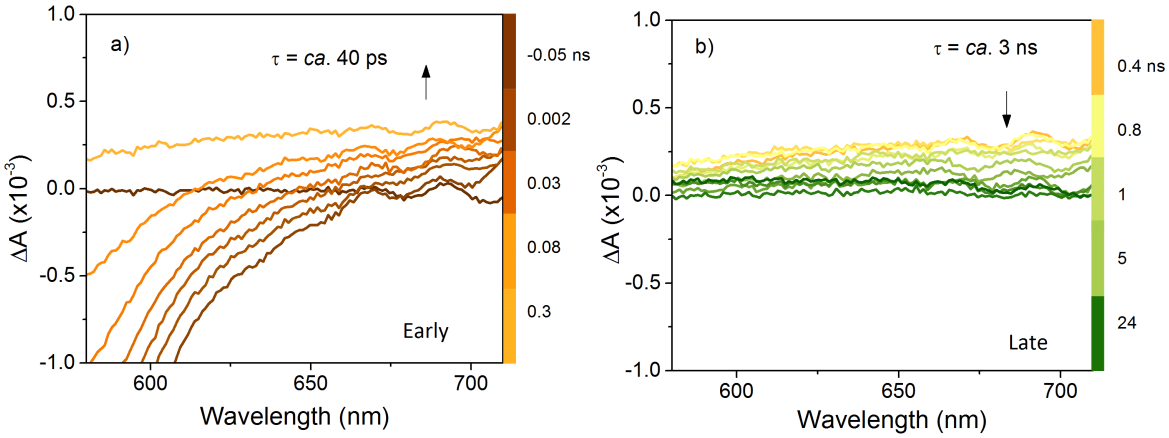

Figure 5.17: Expansion of the transient absorption spectra of $K^{W}_{Si}[BOD_1]$ showing POM^{-} in dichloromethane. a) At short delay times after excitation; b) at long delay times after excitation. λ_{exc} = 540 nm.

In a study by Matt *et al.* which has been discussed previously,[28] charge-separation of the iridium analogue of $K^{W}_{Si}[BOD_1]$ occurred with $\tau = 4$ ps in dimethylformamide, faster than observed for $K^{W}_{Si}[BOD_1]$ in both dichloromethane and acetonitrile. Charge-recombination of both systems was similar ($\tau = 1.5$ ns). The transient absorption spectra of $K^{W}_{Sn}[BOD_2]$ were simpler than that of $K^{W}_{Si}[BOD_1]$. In both solvents, a negative signal corresponding to the ground state bleach absorbs between 500 nm and 700 nm. This is red-shifted relative to $K^{W}_{Si}[BOD_1]$, which is consistent with the ground state absorption spectra (Figure 5.6). A second bleach is present at 400 nm, together with a transient signal at 450 nm. The transient signal resembles the singlet excited state of BOD_2, and decays with a similar lifetime in acetonitrile ($\tau = ca.$ 4 ns). In dichloromethane a residual transient signal is present at delay times longer than 10 ns, and a bi-exponential function was used to fix the slow component at 100 ns. This analysis suggests that the bodipy-centred singlet excited state is formed for $K^{W}_{Sn}[BOD_2]$ but the charge-transfer excited state is not formed.

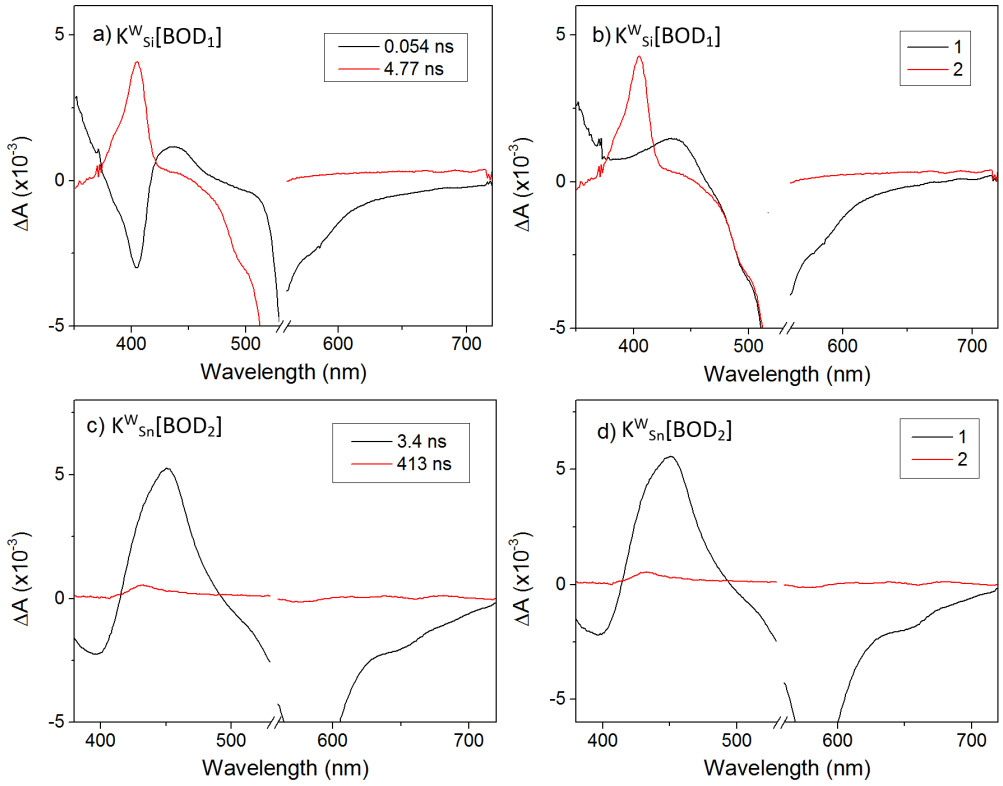

Figure 5.18: Global analysis of transient absorption data of $K^{W}_{Si}[BOD_1]$ and $K^{W}_{Sn}[BOD_2]$ in dichloromethane. a),c) Decay-associated difference spectra; b),d) evolution-associated difference spectra.

This agrees with electrochemical analysis which showed that charge transfer from the bodipy to the polyoxometalate was energetically unfavourable for $K^{W}_{Sn}[BOD_2]$ due to the more negative reduction potential of the polyoxotungstate with an organotin linker group. Results from global analysis of $K^{W}_{Si}[BOD_1]$ in dichloromethane are shown in Figure 5.18 along with that of $K^{W}_{Sn}[BOD_2]$. For $K^{W}_{Si}[BOD_1]$ the two time components, 54 ps and 4.77 ns, represent the first excited singlet state (species 1) and the charge-separated state (species 2). The decay-associated difference spectra of $K^{W}_{Sn}[BOD_2]$ in dichloromethane were also fit to two time components and the long component (τ = 413 ns) consists of a sharp absorption band similar to the bodipy-localised triplet excited state which was present for BOD2 previously reported by our group.[34] The absence of a charge-transfer excited state suggests that the triplet excited state is formed directly upon excitation.

5.4.3 Time-resolved infrared spectroscopy

Time-resolved infrared spectroscopy was used to probe vibrational changes of BOD_1, BOD_2, $K^{W}_{Si}[BOD_1]$ and $K^{W}_{Sn}[BOD_2]$ following excitation at 540 nm. The experimental setup was the same as for transient absorption spectroscopy, except an infrared probe pulse and infrared detector were used. Experiments were run using deuterated solvents as these gave the fewest infrared bands in the fingerprint region. In general the analysis was consistent with transient absorption experiments.

The time-resolved infrared spectra of BOD_1 and BOD_2 in deuterated acetonitrile are shown in Figure 5.19 and contain similar features in the fingerprint region. Negative bands at 1545 cm^{-1}, 1482 cm^{-1} and 1323 cm^{-1} are at similar positions to bands observed in the ground state spectra (1535 cm^{-1}, 1475 cm^{-1} and 1314 cm^{-1}). There are a number of sharp transient bands at 1503 cm^{-1}, 1427 cm^{-1}, 1385 cm^{-1}, 1343 cm^{-1} and 1295 cm^{-1}. The transient infrared bands for both BOD_1 and BOD_2 in deuterated acetonitrile all decayed with the same lifetime and did not evolve over time, and were similar to those determined from transient absorption spectroscopy. An average lifetime was calculated as described in Equation 2.14 in Experimental Section 2.3.2 and gave τ_{Av} = 3.6 ns for BOD_1 and τ_{Av} = 3.3 for BOD_2.

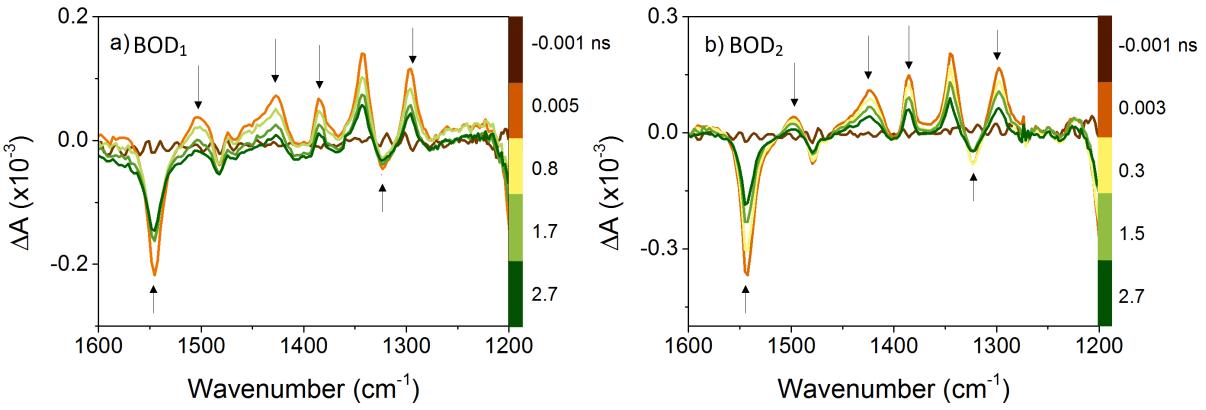

Figure 5.19: Time-resolved infrared difference spectra of bodipy photosensitisers in deuterated acetonitrile at selected time delays after excitation at 540 nm.

The time-resolved infrared spectra of $K^{W}_{Si}[BOD_1]$ and $K^{W}_{Sn}[BOD_2]$ were more complicated than that of BOD_1 and BOD_2 so decay-associated and evolution-associated difference spectra are used to represent the time components of each system instead of single-point analysis. Time-resolved infrared spectra are shown in Figure 5.20 and results from global analysis are shown in Figure 5.21.

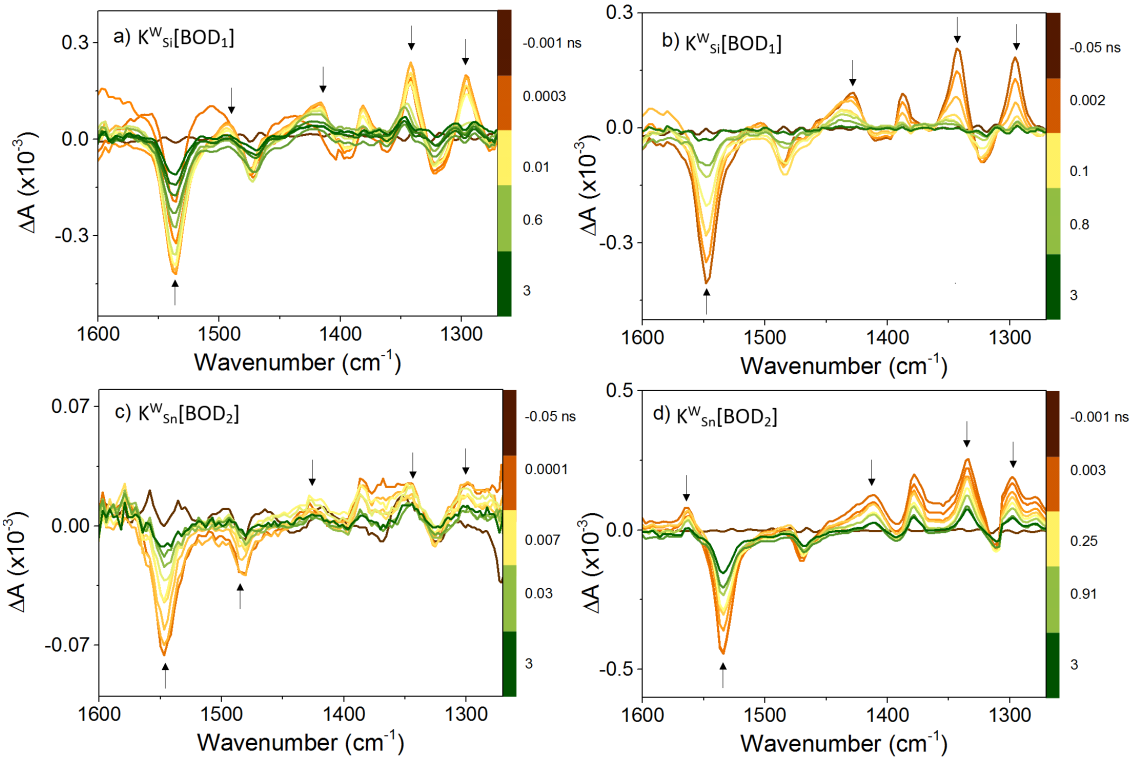

Figure 5.20: Time-resolved infrared spectra of $K^{W}_{Si}[BOD_1]$ and $K^{W}_{Sn}[BOD_2]$ at selected time delays following excitation at 540 nm. a),c) In dichloromethane; b),d) in deuterated acetonitrile.

For $K^{W}_{Si}[BOD_1]$ the bands present in deuterated dichloromethane and deuterated acetonitrile are similar, whereas the transient bands in the spectra of $K^{W}_{Sn}[BOD_2]$ in deuterated dichloromethane are considerably weaker are are harder to resolve. Initially, the time-resolved infrared spectra of $K^{W}_{Si}[BOD_1]$ and $K^{W}_{Sn}[BOD_2]$ resemble that of BOD_1 and BOD_2, respectively, confirming the formation of the bodipy singlet excited state at short delay times. The spectra of $K^{W}_{Sn}[BOD_2]$ contain an additional band at 1571 cm^{-1}. For $K^{W}_{Si}[BOD_1]$, the transient band at 1418 cm^{-1} in deuterated dichloromethane and 1427 cm^{-1} in deuterated acetonitrile evolves over time, and is attributed to the formation of the charge-separated state. Decay-associated difference spectra show this band more clearly (Figure 5.21 b) and d)). The broad band highlighted in a black box shifts to higher wavenumbers to give a second species which has a lifetime of τ = 2.5 ns in deuterated dichloromethane and τ = 1.3 ns in deuterated acetonitrile. This is on the same timescale as the charge-transfer excited state observed in transient absorption spectra for this system.

In the time-resolved infrared spectra of $K^{W}_{Sn}[BOD_2]$, the bodipy-centred triplet excited state which was observed in transient absorption experiments could not be distinguished. Instead, a fast (τ = 10 ps) component was present together with a nanosecond component which had a similar lifetime to the singlet excited state, τ = 4.2 ns. The short-lived component is likely due to fast relaxation processes. The band at *ca.* 1420 cm^{-1} does not evolve over time, which supports our conclusion that a charge-transfer excited state is not accessed for this system.

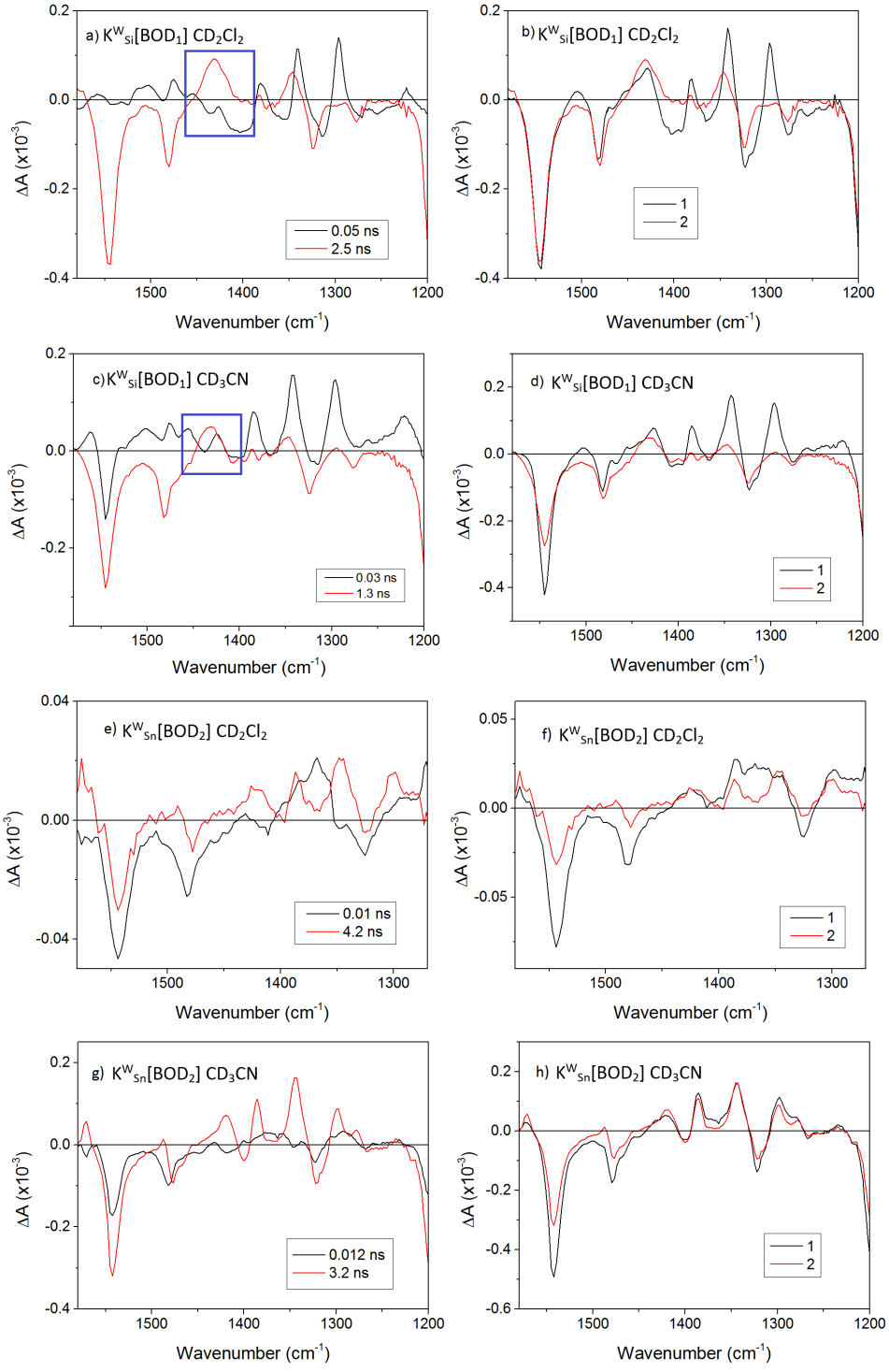

Figure 5.21: Results from global analysis of the time-resolved infrared spectra of $K^{W}_{Si}[BOD_1]$ and $K^{W}_{Sn}[BOD_2]$. Left) decay-associated difference spectra; right) evolution-associated difference spectra. Boxes highlight bands indicating the charge-separated state.

The energy level diagrams in Figure 5.22 are proposed for $K^{W}_{Si}[BOD_1]$ and $K^{W}_{Sn}[BOD_2]$ given the information gained from time-resolved spectroscopies.

For $K^{W}_{Si}[BOD_1]$ the excited state oxidation potential of the bodipy is more negative than for $K^{W}_{Sn}[BOD_2]$ so there is a large driving force for charge-separation in both solvents for the former system and the charge-transfer excited state is formed. Recombination is slightly faster in acetonitrile relative to dichloromethane.

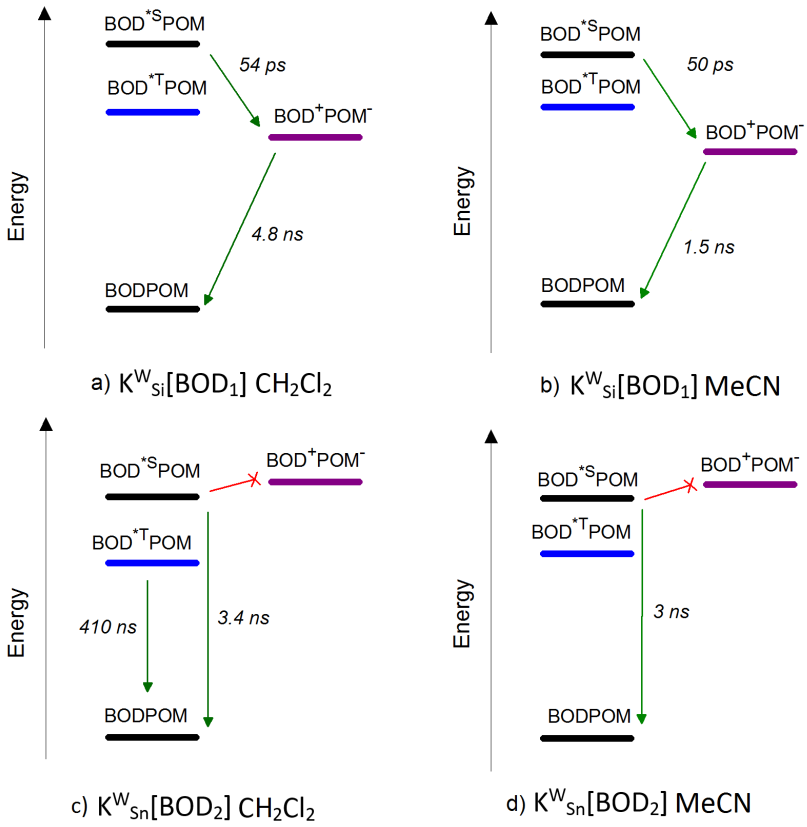

Figure 5.22: Energy level diagram showing the processes which occur when $K^{W}_{Si}[BOD_1]$ and $K^{W}_{Sn}[BOD_2]$ are excited at 540 nm in dichloromethane and acetonitrile solutions. Lifetimes are determined from global analysis of time-resolved data.

The first poyloxometalate-centred reduction of $K^{W}_{Si}[BOD_1]$ is also the most positive of all the systems studied here and the charge-transfer excited state recombines to the ground state without access to the triplet excited state. The charge-transfer excited state is not formed for $K^{W}_{Sn}[BOD_2]$ as the reduction potential of the polyoxometalate is more negative and there is no driving force for charge-separation. We also observe a small amount of the bodipy-centred triplet excited state in the transient absorption spectra of this system.

5.5 Tungsten vs molybdenum

The charge transfer dynamics of $K^{W}_{Sn}[BOD_2]$ and $K^{Mo}_{Sn}[BOD_2]$ are compared using time-resolved spectroscopy to investigate the effect of changing the polyoxotungstate to a polyoxomolybdate.

5.5.1 Spectroelectrochemistry

Changes in the visible absorption as $K^{Mo}_{Sn}[I]$ is reduced to $K^{Mo}_{Sn}[I]^{-}$ are shown in Figure 5.23. The spectrum of $K^{Mo}_{Sn}[I]^{-}$ consists of a broad peak above 650 nm, similar to that observed for $K^{W}_{Si}[I]^{-}$ and $K^{W}_{Sn}[I]^{-}$. The absorption difference spectra in dichloromethane are much weaker than in acetonitrile which was also observed for the polyoxometalates discussed in the previous section.

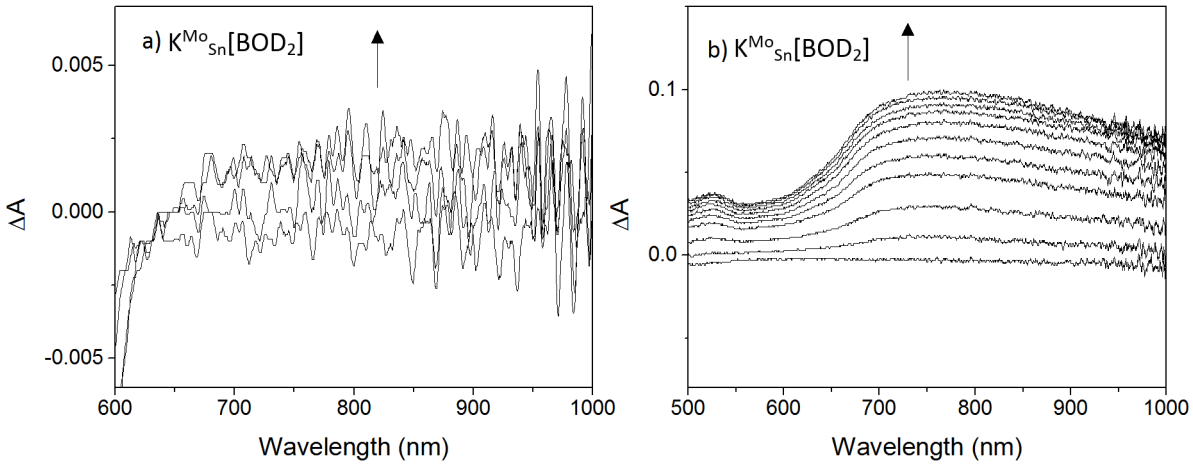

Figure 5.23: Absorbance difference spectra upon electrochemical reduction of $K^{Mo}_{Sn}[I]$ at 0 to -1.6 V vs Ag/Ag^{+}. a) In dichloromethane; b) in acetonitrile.

Figure 5.24 shows an overlay of the reduced spectra of $K^{W}_{Sn}[I]$ and $K^{Mo}_{Sn}[I]$. The peak of $K^{Mo}_{Sn}[I]$ is centred at 720 nm, and is broader and red-shifted by *ca.* 80 nm relative to that of $K^{W}_{Sn}[I]$.

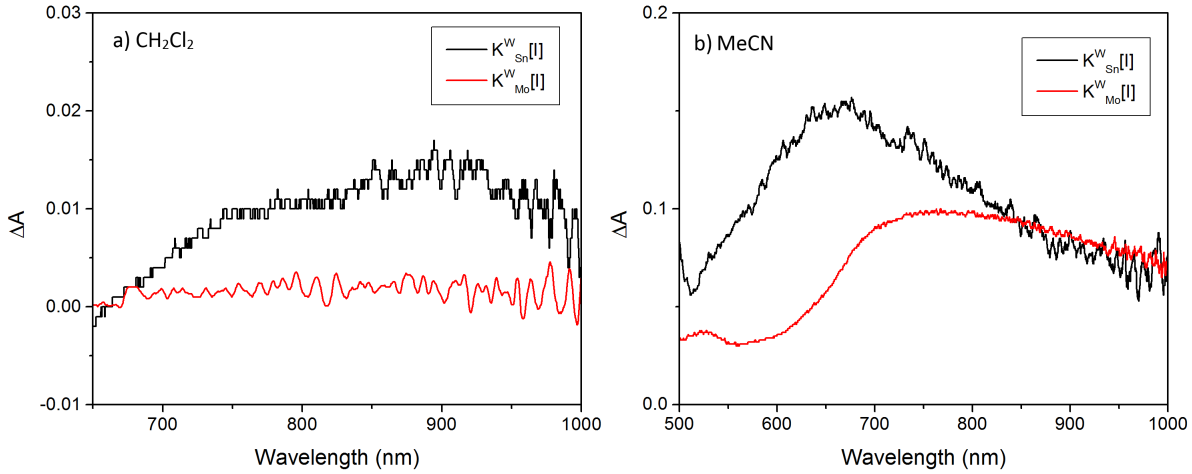

Figure 5.24: Overlay of the absorbance spectra of electrochemically generated $K^{W}{}_{Sn}[I]^{-}$ and $K^{Mo}{}_{Sn}[I]^{-}$. a) In dichloromethane; b) in acetonitrile.

5.5.2 Transient absorption spectroscopy

The previous section described the time-resolved spectroscopy of $K^{W}{}_{Sn}[BOD_2]$, which did not form a charge-transfer excited state in either solvent, but formed a small amount of bodipy-centred triplet excited state in dichloromethane. The first reduction potential of the polyoxomolybdate in $K^{Mo}{}_{Sn}[BOD_2]$ is more positive than that of the polyoxotungstate in $K^{W}{}_{Sn}[BOD_2]$, which we anticipate will allow access to the charge-transfer excited state.

The transient absorption spectra of polyoxomolybdate $K^{Mo}{}_{Sn}[BOD_2]$ show different dynamics in dichloromethane and acetonitrile. The spectra, shown in Figure 5.25, are different to that of both $K^{W}{}_{Si}[BOD_1]$ and $K^{W}{}_{Sn}[BOD_2]$. Results from single-point analysis are detailed in Table 5.7. In dichloromethane, a bleach which absorbs between 500 nm and 650 nm is attributed to the ground state absorption and was fit to a bi-exponential function with a 500 ps component and a longer *ca.* 500 ns component. At the edge of the bleach at longer wavelengths τ = 140 ps, which corresponds to the stimulated emission. A second bleach at 395 nm contains two time components which match the stimulated emission (τ = 130 ps) and the long-lived species present in the ground state bleach (τ = 382 ns).

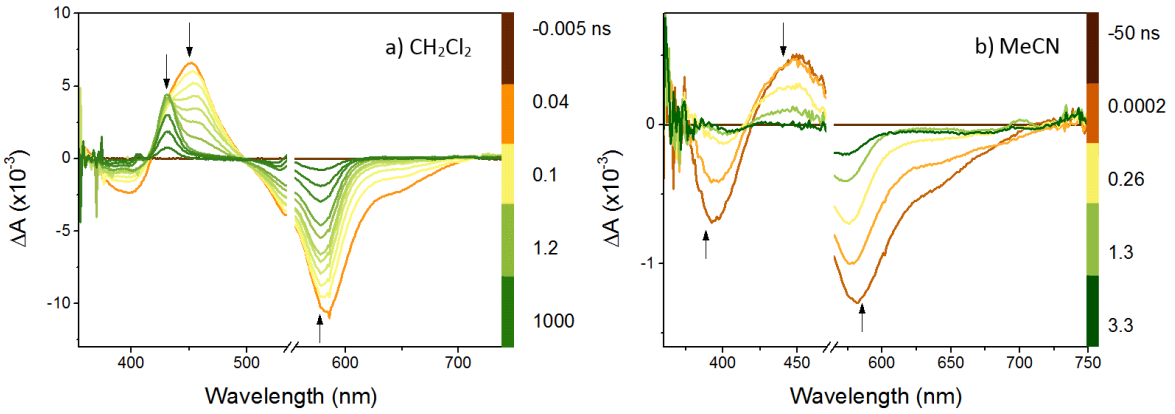

Figure 5.25: Transient absorption difference spectra of $K^{Mo}{}_{Sn}[BOD_2]$ at selected time delays following excitation at 540 nm. a) In dichloromethane; b) in acetontrile.

	Lifetime, ns	
	Dichloromethane	Acetonitrile
$K^{Mo}{}_{Sn}[BOD_2]$	τ_{395} = 0.13±0.009 (67%), 382±77 (33%)	
	τ_{431} = 562±26	τ_{394} = 0.13±0.01
	τ_{454} = 0.61±0.02 (92%), 486±206 (8%)	τ_{449} = 0.19±0.03 (56%), 2.4±0.4 (44%)
	τ_{482} = 0.75±0.05	τ_{583} = 0.02±0.005 (39%), 1.7±0.1 (61%)
	τ_{580} = 0.50±0.004 (56%), 532±69 (44%)	τ_{650} = 0.07±0.01 (78%), 4.5±2.5 (22%)
	τ_{652} = 0.14±0.005	

Table 5.7: Lifetimes derived from single-point analysis of transient absorption spectra of $K^{Mo}{}_{Sn}[BOD_2]$ in dichloromethane and acetonitrile solutions. λ_{exc} = 540 nm. Where a multi-exponential fit is used, the amplitudes of each component are given in brackets.

A transient signal which resembles the first excited singlet state of BOD_2 is formed around 450 nm, and contains multiple time components. This suggests that multiple species with similar absorption spectra are overlapping in this region. For this system which contains a bodipy with an alkyne group at the *meso* position, the ground state bleach is red-shifted relative to that of BOD_1 and masks the area where we observed a broad signal of POM^- for $K^{W}{}_{Si}[BOD_1]$. The initial transient evolves into a blue-shifted sharp absorption at 431 nm, which decays with τ = 562 ns. The long-lived species is similar to the weak signal observed for $K^{W}{}_{Sn}[BOD_2]$, which we attributed to a bodipy-centred triplet excited state. At 482 nm there is no contribution from the long-lived species and the decay is fit to τ = 750 ps. Global analysis of the transient absorption spectra of $K^{Mo}{}_{Sn}[BOD_2]$ in

dichloromethane is shown in Figure 5.26, and was best fit to three time components.

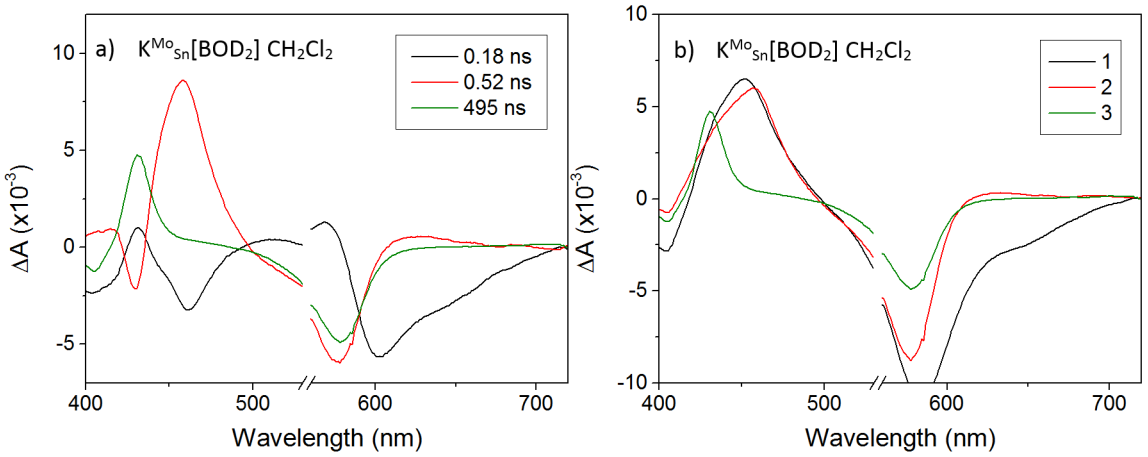

Figure 5.26: Results from global analysis of transient absorption data of $K^{Mo}_{Sn}[BOD_2]$ in dichloromethane. a) Decay-associated difference spectra; b) evolution-associated difference spectra.

The species associated with the first time component (180 ps) resembles the bodipy singlet excited state and contains stimulated emission. The species associated with the second time component (520 ps) is slightly red-shifted from the first species and evolves into the long-lived (500 ns) species which is attributed to a bodipy-centred triplet excited state. For this system charge transfer from the bodipy to the polyoxometalate is thermodynamically favourable, and our group has previously reported a push-pull bodipy system BOD2 which accesses the triplet excited state through intramolecular recombination of a charge-transfer excited state,[34] which was discussed in Section 4.5. We therefore suggest that the triplet excited state is accessed from a charge-transfer excited state which is species 2 in the evolution-associated difference spectra.

In acetonitrile the transient absorption spectra of $K^{Mo}_{Sn}[BOD_2]$ are similar to that of $K^{W}_{Sn}[BOD_2]$. A transient species resembling the excited sinlget state of BOD_2 is formed, and decays with a short (190 ps) and a long (2.4 ns) component. The negative signal was also fit to a bi-exponential function, containing stimulated emission at longer wavelengths. Global analysis of $K^{Mo}_{Sn}[BOD_2]$ in deuterated acetonitrile (Figure 5.27) confirms that the picosecond component contains stimulated emission and the nanosecond component is associated with a transient species which resembles the charge-transfer excited state observed in dichloromethane.

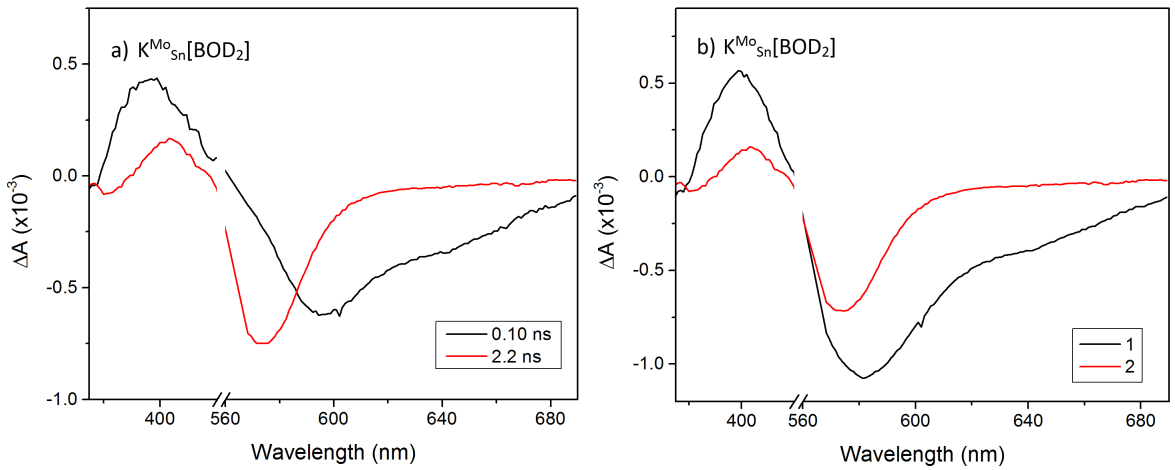

Figure 5.27: Results from global analysis of transient absorption spectra of $K^{Mo}{}_{Sn}[BOD_2]$ in acetonitrile. a) Decay-associated difference spectra; b) evolution-associated difference spectra.

The formation of the charge-separated state and absence of the triplet excited state in acetonitrile suggests that the BOD^+POM^- charge-transfer state is stabilised by the solvent with increased polarity, which drops the energy of this state to below the triplet excited state. The dynamics of $K^{Mo}{}_{Sn}[BOD_2]$ in dichloromethane and acetonitrile are shown by the decay traces at selected wavelengths in Figure 5.28.

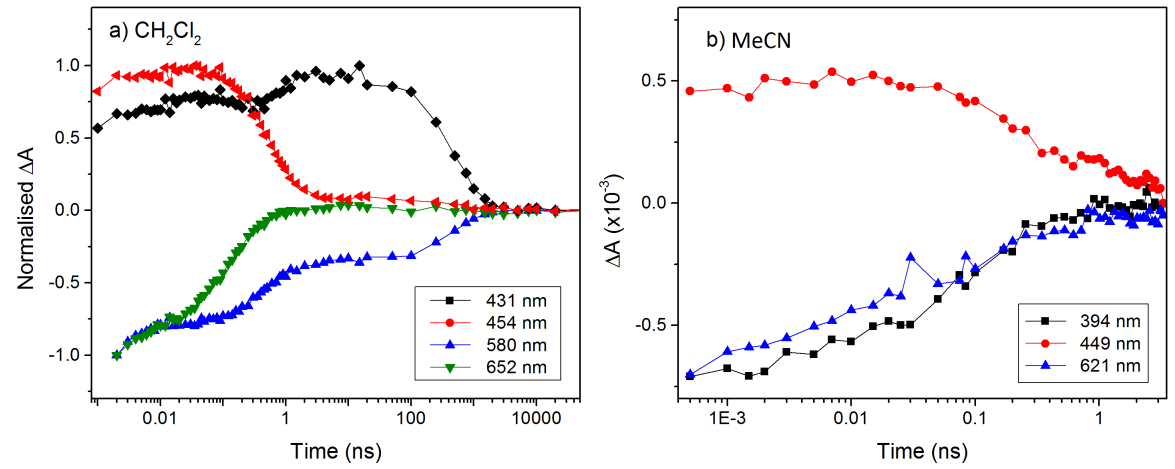

Figure 5.28: Decay traces from single-point analysis at given wavelengths from transient absorption spectra of $K^{Mo}{}_{Sn}[BOD_2]$. a) In dichloromethane; b) in acetonitrile.

The lifetimes of the transient at 431 nm and the bleach at 580 nm in dichloromethane are significantly longer than the transient species in acetonitrile, which consists of the first excited singlet state and charge-transfer excited state. Figure 5.29 shows a comparison of the evolution-associated difference spectra of $K^{W}{}_{Sn}[BOD_2]$ and $K^{Mo}{}_{Sn}[BOD_2]$ in dichloromethane. The initial species in both cases is the bodipy singlet excited state, which contains stimulated emission in the bleach at longer wavelengths. The charge-transfer excited state which is species 2 for $K^{Mo}{}_{Sn}[BOD_2]$ is slightly red-shifted from the singlet excited state and does not contain stimulated emission.

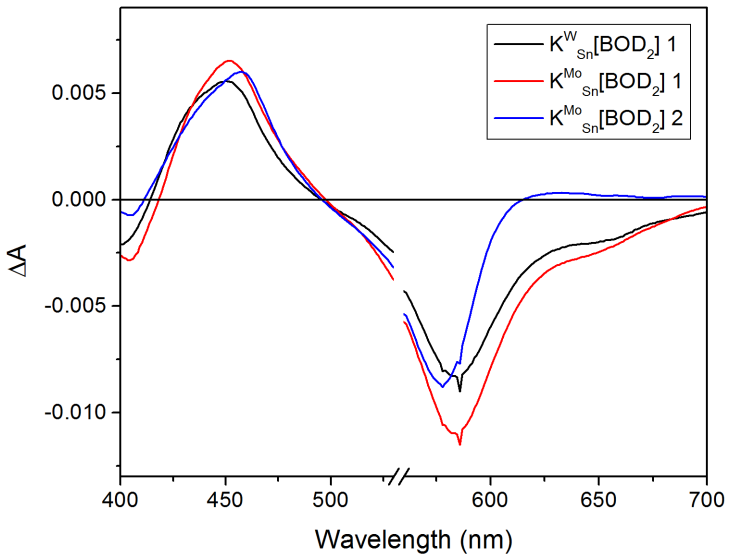

Figure 5.29: Overlay of evolution-associated difference spectra of $K^{W}{}_{Sn}[BOD_2]$ and $K^{Mo}{}_{Sn}[BOD_2]$ in dichloromethane, showing the singlet excited states of both systems (red and black lines), and charge-transfer excited state of $K^{Mo}{}_{Sn}[BOD_2]$ (blue line).

5.5.3 Time-resolved infrared spectroscopy

The time-resolved infrared spectra of $K^{Mo}{}_{Sn}[BOD_2]$ in deuterated dichloromethane initially resemble that of BOD_2 in the fingerprint region. A band at 1425 cm^{-1} is shifted to higher wavenumbers relative to the singlet excited state and resembles the charge-transfer excited state observed in the time-resolved infrared spectra of $K^{W}{}_{Si}[BOD_1]$. An additional band at 1523 cm^{-1} grows on longer timescales and occurs at a similar frequency to the bodipy-localised triplet band which we observed for BOD2 in Section 4.5, which appeared at 1525 cm^{-1} in dichloromethane.

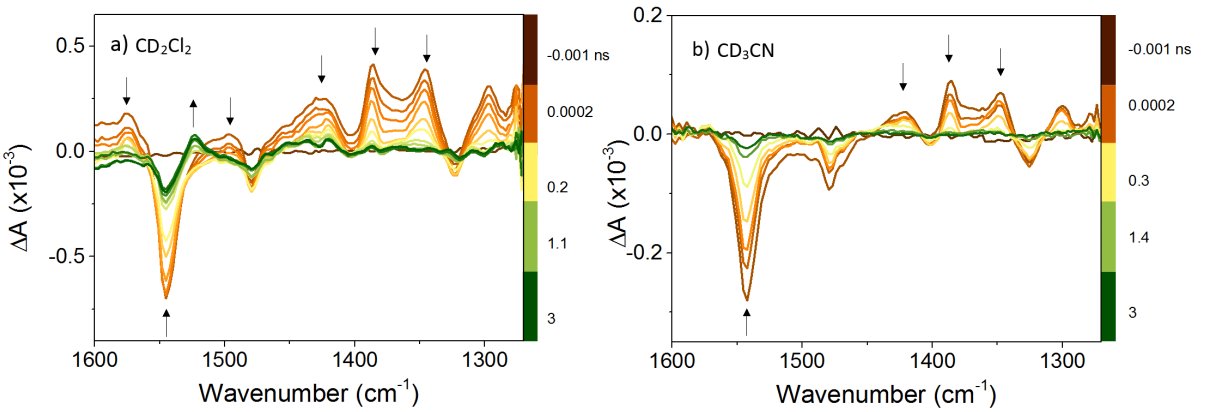

Figure 5.30: Time-resolved infrared difference spectra of $K^{Mo}{}_{Sn}[BOD_2]$ at selected time delays following excitation at 540 nm. a) In deuterated dichloromethane; b) in deuterated acetonitrile.

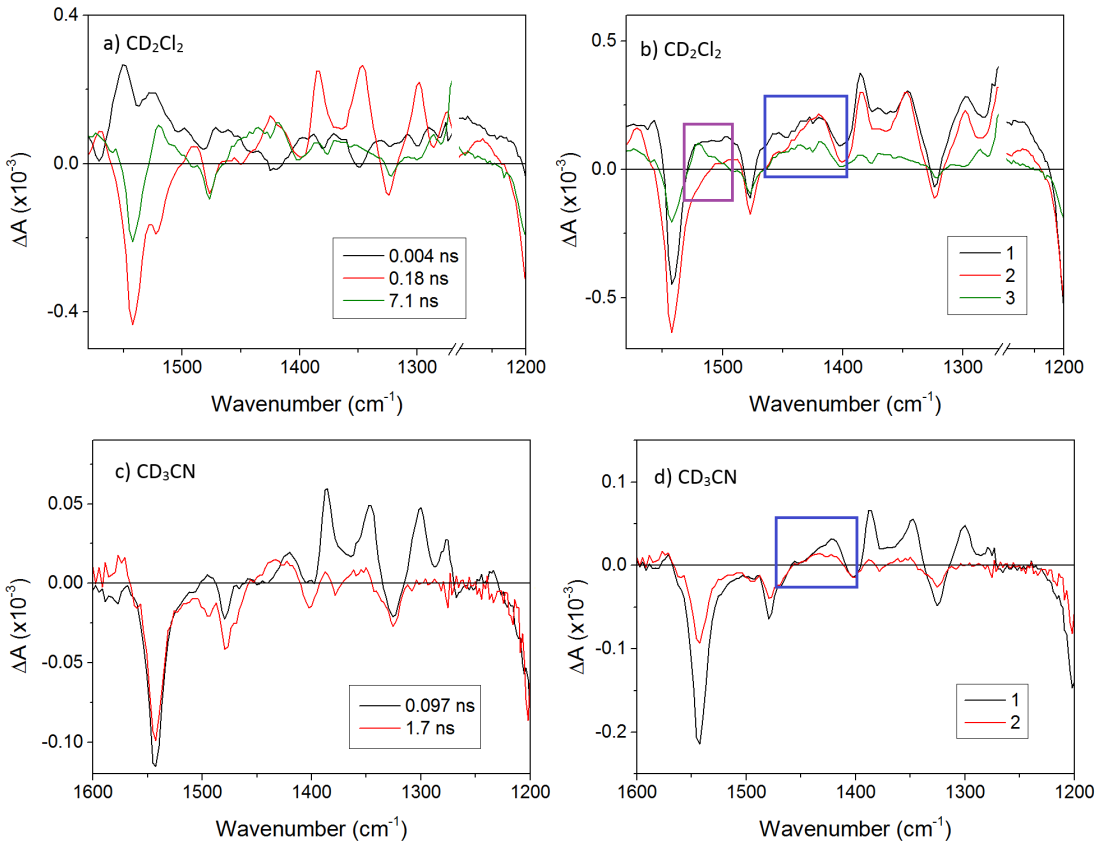

Figure 5.31: Results from global analysis of time-resolved infrared spectra of $K^{Mo}{}_{Sn}[BOD_2]$. a),c) Decay-associated and b),d) evolution-associated difference spectra.

Figure 5.31 shows results from global analysis of the time-resolved infrared spectra of $K^{Mo}{}_{Sn}[BOD_2]$ in deuterated dichloromethane. The data was best fit to three time com-

ponents, which are attributed to the bodipy singlet excited state, charge-transfer excited state and bodipy-centred triplet excited state. The time component of the triplet excited state (highlighted in purple) is underestimated as it did not decay fully on the timescale of this experiment. In deuterated acetonitrile the sharp bodipy-centred triplet excited state is absent, but the band at 1428 cm^{-1} is present. This is consistent with our analysis of transient absorption data which showed the formation of the charge-transfer excited state and triplet excited state in dichloromethane and the formation of the charge-transfer excited state in acetonitrile.

Given the information gained from time-resolved spectroscopies, the following energy level diagram can be deduced which shows the effect of changing the metal atom of a Keggin polyoxometalate from tungsten to molybdenum.

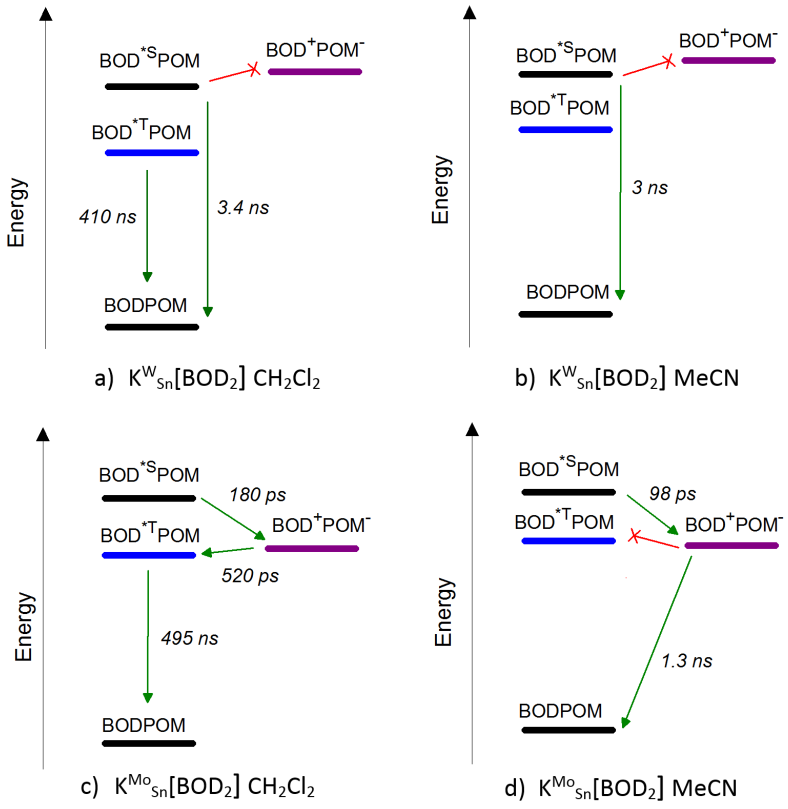

Figure 5.32: Energy level diagram showing the relaxation pathways and timescales of bodipy-polyoxometalate hybrids where the polyoxometalate is changed, following excitation of the bodipy.

The charge-transfer excited state is lower in energy for the polyoxomolybdate than the polyoxotungstate, so charge transfer is thermodynamically favourable and leads to rapid

charge-separation for $K^{Mo}{}_{Sn}[BOD_2]$ in both solvents. In dichloromethane this charge-transfer excited state is destabilised relative to acetonitrile and decays via a triplet excited state.

5.6 Polyoxometalate structure

In this section the photoinduced dynamics of $K^{W}{}_{Si}[BOD_1]$ are compared with that of $D^{W}{}_{Si}[BOD_1]_{TBA}$ which contains a polyoxotungstate with a different structure. It has been reported by Matt *et al.* that changing the Keggin anion to a Dawson anion increases the lifetime of the intramolecular charge-separated state for an iridium-polyoxometalate hybrid system.[28] In Section 5.4, charge-separation occurred with $\tau = 50$ ps following excitation of the bodipy, and charge-recombination occurred with $\tau = 5$ ns for the Keggin polyoxometalate $K^{W}{}_{Si}[BOD_1]$.

5.6.1 Spectroelectrochemistry

Spectroelectrochemical reduction of $D^{W}{}_{Si}[I]$ in dimethylformamide solution has been previously reported.[27] In the study, the growth of a broad absorption centred at 720 nm was observed in the visible spectrum upon the first reduction of the polyoxometalate, followed by a sharper, blue-shifted peak upon the second reduction. Here, spectroelectrochemical reduction of $D^{W}{}_{Si}[I]$ was performed in acetonitrile solution and the difference spectra are shown in Figure 5.33.

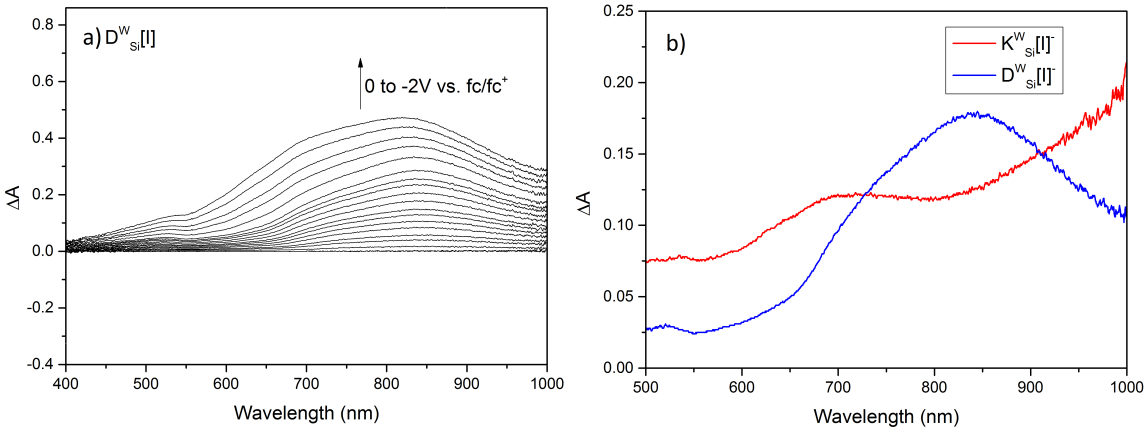

Figure 5.33: a) Absorption difference spectra of the reduction of $D^{W}{}_{Si}[I]$ in acetonitrile, 0 to 2.0 V vs fc/fc^{+}; b) an overlay of $K^{W}{}_{Si}[I]^{-}$ and $D^{W}{}_{Si}[I]^{-}$.

The experiment was performed in an OTTLE cell with the same setup as for $K^{W}_{Si}[I]$, $K^{W}_{Sn}[I]$ and $K^{Mo}_{Sn}[I]$. A reducing potential was applied stepwise from and visible spectra were taken. Ferrocene was added to the sample and the oxidation was recorded to calibrate the electrodes. The visible spectrum of $D^{W}_{Si}[I]^{-}$ contains a broad peak which absorbs above 600 nm and is centred at 840 nm. An overlay of the visible spectra of $K^{W}_{Si}[I]^{-}$ and $D^{W}_{Si}[I]^{-}$ is also shown in Figure 5.33. The spectrum of $D^{W}_{Si}[I]^{-}$ is sharper and red-shifted by *ca.* 100 nm relative to that of the Keggin analogue $K^{W}_{Si}[I]^{-}$.

5.6.2 Transient absorption spectroscopy

The transient absorption spectra of $D^{W}_{Si}[BOD_1]_{TBA}$ are shown in Figure 5.34 and lifetimes from single-point analysis are given in Table 5.8. Following laser excitation at 540 nm, the transient absorption spectra resemble that of $K^{W}_{Si}[BOD_1]$, except that the intensity of the POM^{-} transient signal is larger for the Dawson system relative to the BOD^{+} signal.

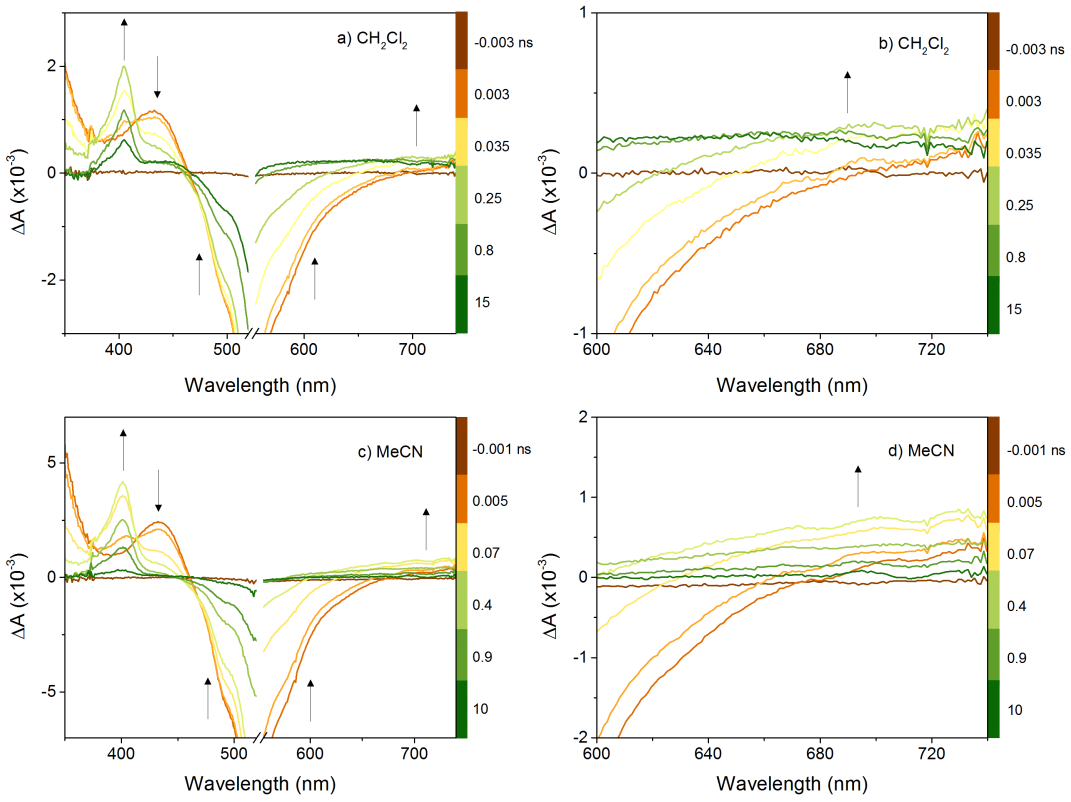

Figure 5.34: Transient absorption difference spectra of $D^{W}_{Si}[BOD_1]_{TBA}$ at selected time delays following excitation at 540 nm. a),b) In dichloromethane; c),d) in acetonitrile.

	Lifetime, ns	
	Dichloromethane	Acetonitrile
$D^{W}_{Si}[BOD_1]_{TBA}$	τ_{405} (rise) = 0.22±0.01	τ_{401} (rise) = 0.26±0.008
	τ_{405} = 12±0.5	τ_{401} = 3.6±0.1
	τ_{433} = 0.33±0.03 (65%), 11±2 (35%)	τ_{435} = 0.57±0.016
	τ_{502} = 0.8±0.2 (25%), 14±1 (75%)	τ_{492} = 2.7±0.06
	τ_{597} = 0.38±0.02	τ_{601} = 0.29±0.009
	τ_{709} (rise) = 0.29±0.07	τ_{711} (rise) = 0.23±0.03
	τ_{709} = 20±3	τ_{711} = 2.9±0.3

Table 5.8: Lifetimes derived from single-point analysis of transient absorption spectra of $D^{W}_{Si}[BOD_1]_{TBA}$. Where a multi-exponential fit was used, the amplitudes of each component are given in brackets.

An initial transient species is formed which has the same spectral features as BOD_1*. This decays over *ca.* 300 ps in both solvents as a sharp transient which resembles BOD_1^{+} grows at 405 nm, along with a broad absorption at 700 nm. The second species is attributed to the charge-transfer excited state which decays with τ = *ca.* 15 ns in dichloromethane and τ =*ca.* 3 ns in acetonitrile. A solvent dependence on charge-recombination is consistent with that observed for $K^{W}_{Si}[BOD_1]$, which showed faster charge-recombination in acetonitrile relative to in dichloromethane. A comparison of the lifetimes associated with the singlet excited state and charge-transfer excited state for $K^{W}_{Si}[BOD_1]$ and $D^{W}_{Si}[BOD_1]_{TBA}$ in dichloromethane is shown by global analysis in Figure 5.35.

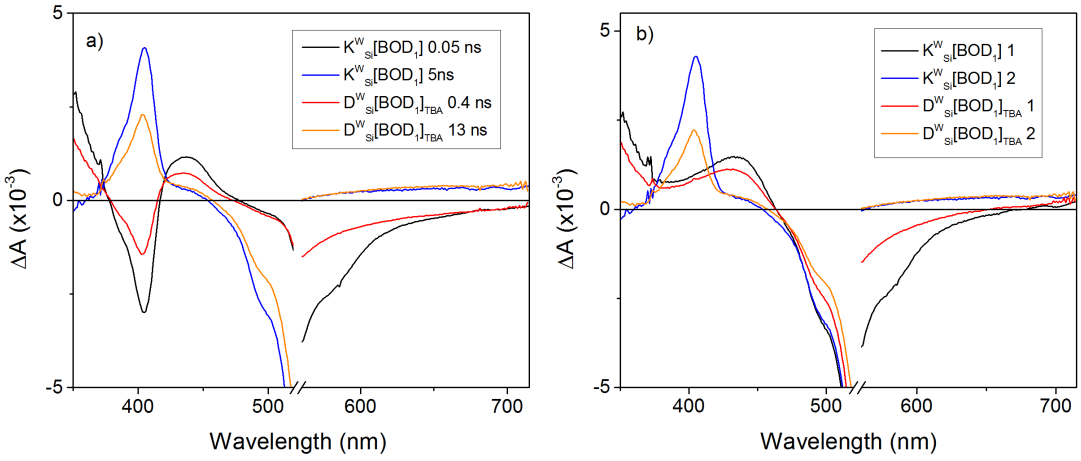

Figure 5.35: Results from global analysis of the transient absorption spectra of $D^{W}_{Si}[BOD_1]_{TBA}$ and $K^{W}_{Si}[BOD_1]$ in dichloromethane. a) Decay-associated difference spectra; b) evolution-associated difference spectra.

Charge-separation is about 8 times faster for $K^{W}_{Si}[BOD_1]$ than $D^{W}_{Si}[BOD_1]_{TBA}$. Charge-recombination is also slightly slower for the Dawson system, which is consistent with the study by Matt *et al.* for iridium-polyoxometalate systems.[28]

The effect of changing the Keggin polyoxotungstate to a Dawson polyoxotungstate on the dynamics of the bodipy-POM is shown by the energy level diagram in Figure 5.36. In both cases the charge-transfer excited state is formed and relaxation occurs directly to the ground state without forming a bodipy-centred triplet excited state. Charge-separation is much slower for the Dawson polyoxometalate than the Keggin but the timescales of charge-recombination are similar.

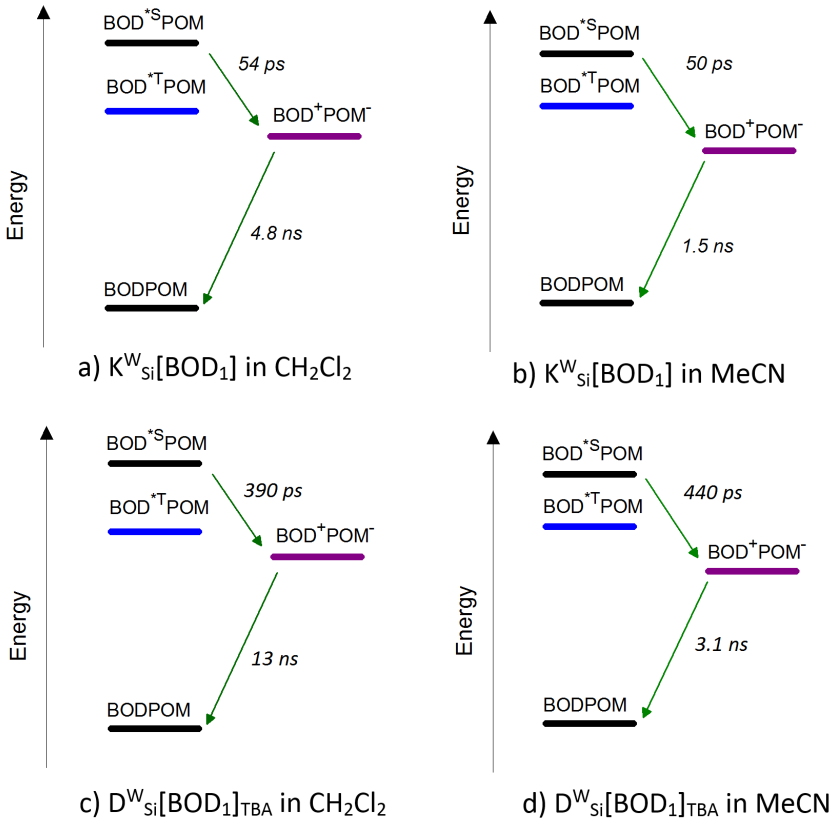

Figure 5.36: Energy level diagram representing the timescales of charge-separation and charge-recombination for $D^{W}_{Si}[BOD_1]_{TBA}$ and $K^{W}_{Si}[BOD_1]$.

5.7 Counter cation

The photoinduced dynamics of $D^{W}_{Si}[BOD_1]_{TBA}$, $D^{W}_{Si}[BOD_1]_{TEA}$ and $D^{W}_{Si}[BOD_1]_{TMA}$ are discussed in this section. The Dawson bodipy-polyoxotungstates contain an organosilicon

linker group and differ in the counter ion, a factor which has been reported to influence the solubility and electrochemical properties of polyoxometalates.[2,5]

5.7.1 Transient absorption spectroscopy

Transient absorption difference spectra of $D^{W}_{Si}[BOD_1]_{TEA}$ and $D^{W}_{Si}[BOD_1]_{TMA}$ in acetonitrile solution are similar to that of $D^{W}_{Si}[BOD_1]_{TBA}$, and are shown in Figure 5.37 with results from single-point analysis detailed in Table 5.9. Transient absorption spectroscopy of $D^{W}_{Si}[BOD_1]_{TMA}$ in dichloromethane solution was also performed, but $D^{W}_{Si}[BOD_1]_{TEA}$ was not soluble in this solvent.

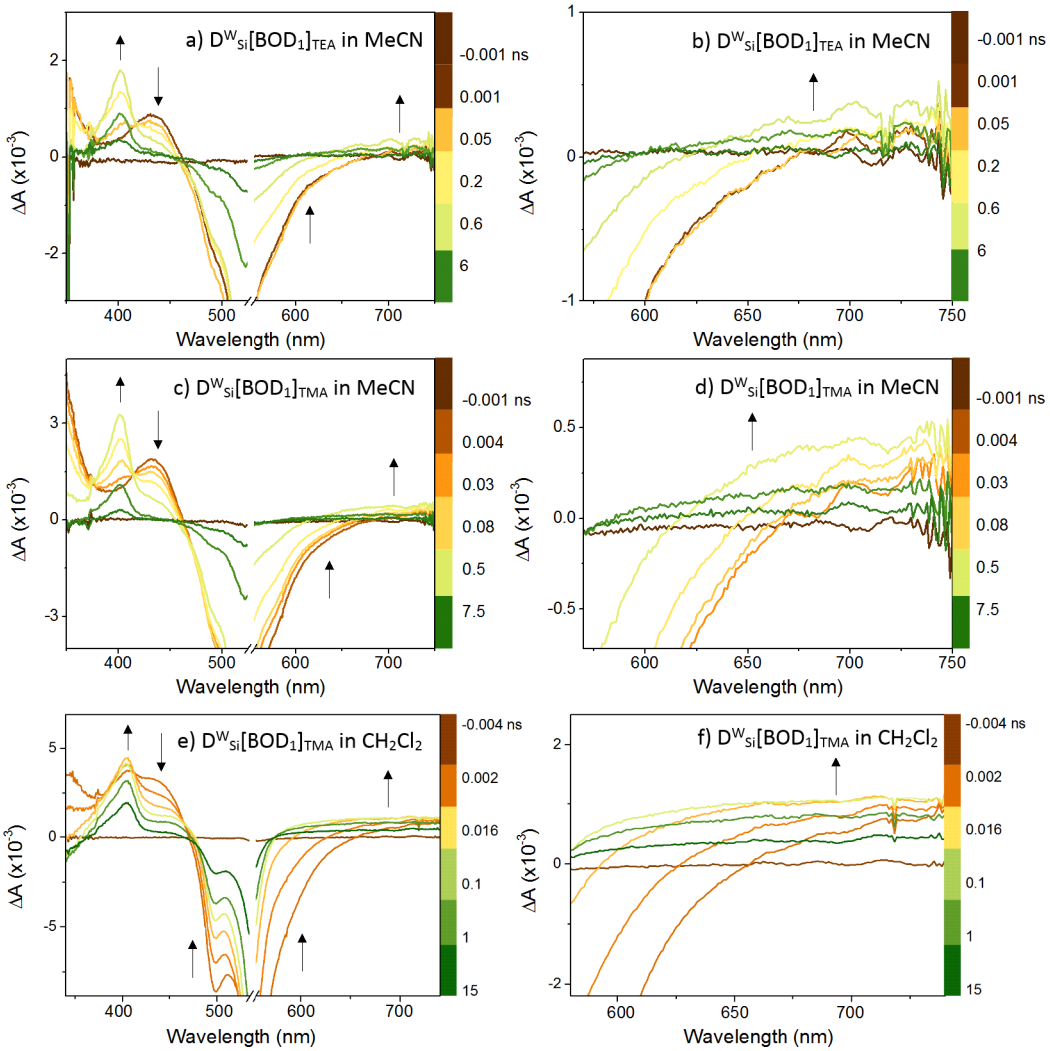

Figure 5.37: Transient absorption difference spectra of Dawson bodipy-polyoxometalate hybrids at selected time delays following excitation at 540 nm. a),c),d) Across the visible region; b),d),f) an expansion of the POM^{-} region.

	Lifetime, ns	
	Dichloromethane	Acetonitrile
$D^{W}_{Si}[BOD_1]_{TEA}$	τ_{405} (rise) = 0.005±0.001	τ_{401} (rise) = 0.18±0.01
	τ_{405} = 0.40±07 (40%), 23±3 (60%)	τ_{401} = 2.99±0.09
	τ_{440} = 0.008±0.001 (67%), 4.7±0.6 (33%)	τ_{435} = 0.48±0.02
	τ_{499} = 0.01±0.001 (52%), 14±2 (48%)	τ_{496} = 2.3±0.05
	τ_{596} = 0.003±0.0002	τ_{604} = 0.22±0.007
	τ_{711} (rise) = 0.002±0.001	τ_{707} (rise) = 0.18±0.03
	τ_{711} = 0.9±0.1 (40%), 31±5 (60%)	τ_{707} = 2.7±0.3

Table 5.9: Lifetimes derived from single-point analysis of transient absorption spectra of $D^{W}_{Si}[BOD_1]_{TEA}$. Where a bi-exponential fit is used, the amplitudes of each component are given in brackets. λ_{exc} = 540 nm.

	Lifetime, ns
$D^{W}_{Si}[BOD_1]_{TEA}$	τ_{401} (rise) = 0.13±0.004
	τ_{401} = 3.1±0.1
	τ_{435} = 0.52±0.04
	τ_{496} = 2.7±0.09
	τ_{601} = 0.3±0.02
	τ_{702} (rise) = 0.12±0.008
	τ_{702} = 4.9±0.5

Table 5.10: Lifetimes derived from single-point analysis of transient absorption spectra of $D^{W}_{Si}[BOD_1]_{TEA}$ in acetonitrile solution. λ_{exc} = 540 nm.

For both $D^{W}_{Si}[BOD_1]_{TEA}$ and $D^{W}_{Si}[BOD_1]_{TMA}$ in acetonitrile solution, excitation at 540 nm results in the formation of a bodipy singlet excited state similar to that formed for $D^{W}_{Si}[BOD_1]_{TBA}$. This transient decays with τ = *ca.* 300 ps for all three systems, and evolves into a charge-separated state which consists of a sharp peak at 405 nm and a broad absorption above 650 nm. Results from global analysis of $D^{W}_{Si}[BOD_1]_{TBA}$, $D^{W}_{Si}[BOD_1]_{TEA}$ and $D^{W}_{Si}[BOD_1]_{TMA}$ in acetonitrile are shown in Figure 5.38. The dynamics are similar for all Dawson bodipy-polyoxometalate systems in this solvent.

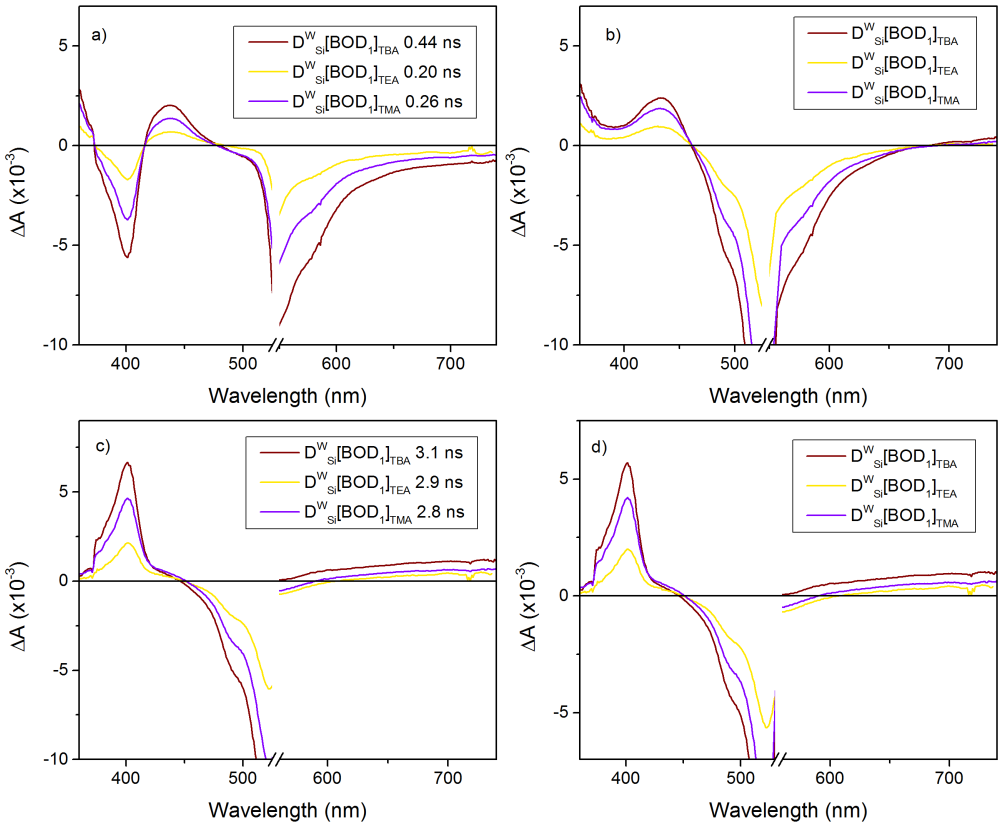

Figure 5.38: Results from global analysis of transient absorption spectra of Dawson bodipy-polyoxometalate hybrids in acetonitrile solution. Left) decay-associated difference spectra; right) evolution-associated difference spectta; a),b) the bodipy singlet excited state, species 1; c),d) the charge-separated state, species 2.

In dichloromethane solution the transient absorption spectra of $D^W_{Si}[BOD_1]_{TMA}$ are different to $D^W_{Si}[BOD_1]_{TBA}$, confirming that the counter ion has an effect on the photoinduced dynamics of the bodipy-polyoxometalate hybrid system. Following excitation of $D^W_{Si}[BOD_1]_{TMA}$, the bodipy-centred first excited singlet state is generated, together with the sharp signal of the charge-separated state at 405 nm and 711 nm, which rises with a lifetime of $\tau = 5$ ps. A bi-exponential function was used to fit the decay of the singlet excited state and gives a short component ($\tau = 8$ ps) and a longer component ($\tau = 5$ ns). Stimulated emission at 596 nm decayed with $\tau = 3$ ps, which suggests that the singlet excited state decays on a fast (ps) timescale to form the charge-separated state. Results from global analysis of $D^W_{Si}[BOD_1]_{TBA}$ and $D^W_{Si}[BOD_1]_{TMA}$ show the difference in dynamics in dichloromethane solution (Figure 5.39).

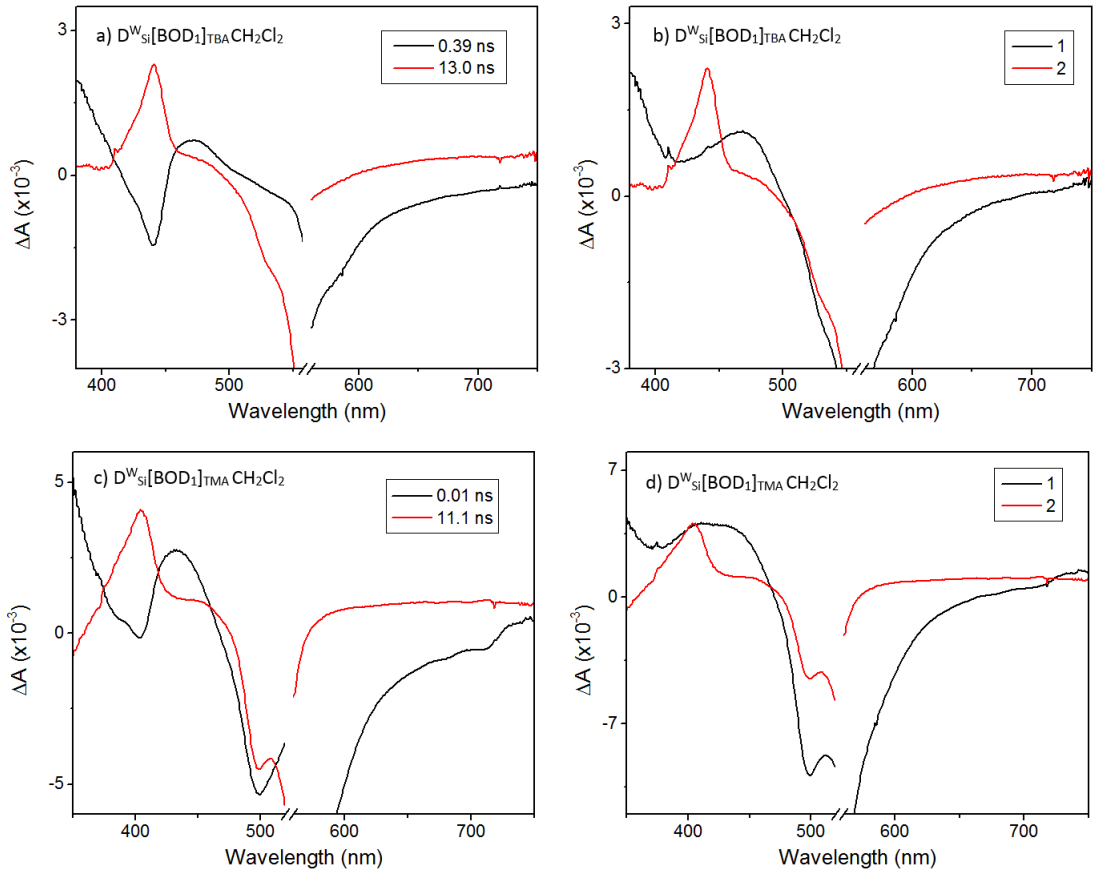

Figure 5.39: Results from global analysis of transient absorption data of Dawson hybrids in dichloromethane. Left) decay-associated difference spectra; right) evolution-associated difference spectra.

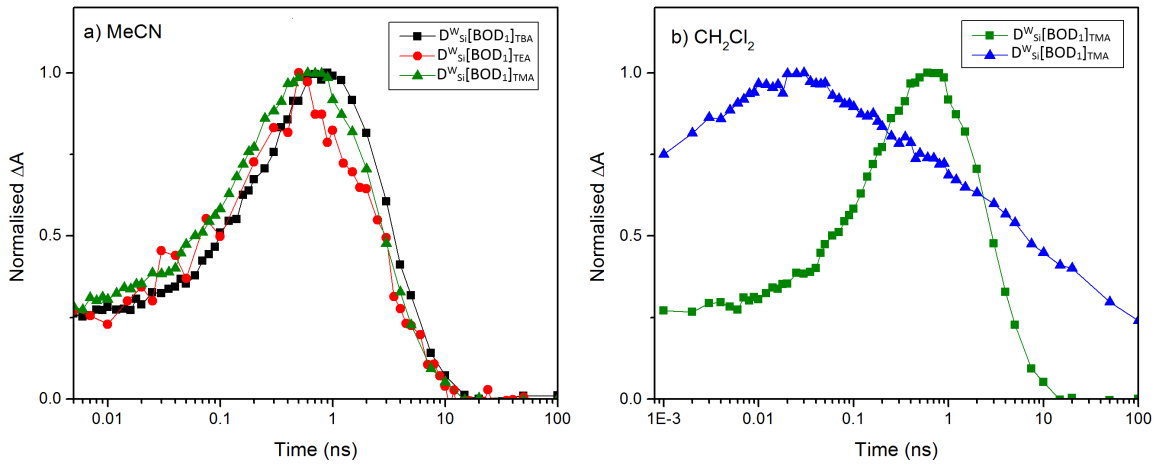

Figure 5.40: Single-point decay traces from transient absorption spectra of Dawson hybrids showing the decay of the charge-separated state at 400 nm. a) In acetonitrile; b) in dichloromethane.

The formation of the charge-separated state occurs on a considerably shorter timescale for $D^{W}_{Si}[BOD_1]_{TMA}$ in dichloromethane than $D^{W}_{Si}[BOD_1]_{TBA}$, as shown by the decay traces in Figure 5.40. The dynamics are summarised in the energy level diagram in Figure 5.41. $D^{W}_{Si}[BOD_1]_{TMA}$ has a larger driving force for charge-separation due to the more positive reduction potential of the system with the tetramethylammonium counter ions. This is consistent with charge-separation in the Marcus normal region, which was also observed for iridium-polyoxometalate hybrid systems reported by the group of Proust.[28]

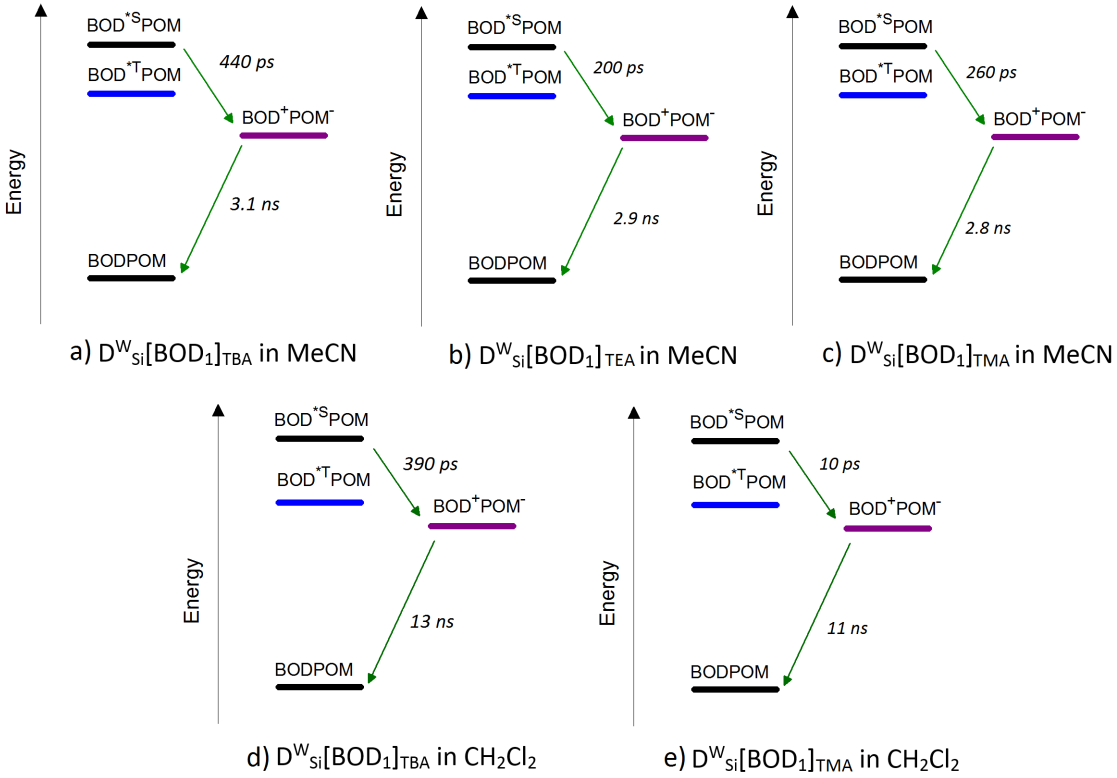

Figure 5.41: Energy level diagram describing the relaxation pathways and lifetimes of Dawson bodipy-polyoxotungstate hybrids which contain different counter ions.

5.8 Conclusions

In this study we have shown that the photoinduced dynamics of covalently-bound bodipy-polyoxometalate compounds are dependent on the structure of the polyoxometalate, the metal atom, the linker group, the bridge, the counter cation an the solvent. For all systems the absorption spectra in the visible region are dominated by the bodipy groups, and there is little electronic communication between the bodipy photosensitiser and the

polyoxometalate in the hybrid structures. A significant solvent dependence is observed in a number of these systems, which is attributed to then stabilisation of the charge-transfer excited state in a more polar solvent. However, it is noted that the difference in dielectric constant between the two solvents was not considered and in future this should be taken into account.

For Keggin polyoxotungstates $K^{W}{}_{Si}[BOD_1]$ and $K^{W}{}_{Sn}[BOD_2]$, changing the linker group from organosilicon to organotin shifts the first reduction of the polyoxometalate to a more negative potential than that of the bodipy group, which leads to thermodynamically unfavourable charge transfer for the organotin system and only the bodipy-centred singlet excited state is formed following excitation. However, for $K^{Mo}{}_{Sn}[BOD_2]$ which contains a polyoxomolybdate and an organotin linker group, the reduction potential of the POM is shifted to a more positive potential and charge transfer is thermodynamically favourable. Charge-separation is fast (τ = *ca.* 50 ps) for the polyoxotungstate $K^{W}{}_{Si}[BOD_1]$ and is slightly slower for the polyoxomolybdate $K^{Mo}{}_{Sn}[BOD_2]$ which shows a greater solvent dependence (τ = 180 ps in dichloromethane, τ = 98 ps in acetonitrile). The charge-transfer excited state is stabilised in dichloromethane and charge-recombination occurs via a long-lived triplet excited state (τ = 495 ns). This triplet excited state is not observed in acetonitrile and instead charge-recombination for $K^{Mo}{}_{Sn}[BOD_2]$ occurs on a similar timescale to $K^{W}{}_{Si}[BOD_1]$ in acetonitrile (*ca.* 1.5 ns). For the two Keggin systems which form the charge-transfer excited state in acetonitrile, charge-separation occurs in the Marcus normal region, which is consistent with reported iridium-polyoxometalate systems.

For bodipy-polyoxotungstate hybrids $K^{W}{}_{Si}[BOD_1]$, $D^{W}{}_{Si}[BOD_1]_{TBA}$, $D^{W}{}_{Si}[BOD_1]_{TEA}$ and $D^{W}{}_{Si}[BOD_1]_{TMA}$, the charge-separated state in the visible region is characterised as a sharp peak resembling BOD^{+} and a broad peak resembling POM^{-} at longer wavelengths. In the infrared region the charge-separated state is identified by a slight shift and broadening of the band around 1420 cm^{-1}. We also observe a significant counter ion effect, with the charge-separated state formed fastest for $D^{W}{}_{Si}[BOD_1]_{TMA}$ in dichloromethane, whilst charge-recombination remains similar for all systems. However, for the other Dawson systems, charge-separation is slower than for the Keggin analogue. For future optimisation of these bodipy-polyoxometalate systems it is suggested that changing the counter cation on the Keggin structures would be an interesting study.

The dynamics observed from transient absorption spectroscopy were largely determined using single-point analysis. However for $K^{Mo}{}_{Sn}[BOD_2]$ where the spectrum of the charge-transfer excited state overlapped with the spectrum of the singlet excited state, global analysis was used to successfully extract the separate components. Time-resolved infrared spectroscopy was used to identify subtle changes in the vibrational spectra upon excitation, but the transient spectra contain many bands in the fingerprint region and global analysis was particularly useful for representing these species. The characterisation of the triplet excited state together with density functional theory modelling would provide further information about the nature of these species.

The bodipy-polyoxometalate systems investigated in this work are promising candidates for photocatalysis or photo(electro)catalysis applications. The bodipy photosensitisers have high molar absorption coefficients and suitable redox properties for most of the polyoxometalate systems, and have sites for further functionalisation on the bodipy core. Charge-separation is fastest for the Dawson polyoxotungstate system which contains an organosilicon linker group and tetramethylammonium counter ion, τ = 10 ps in dichloromethane. The tetrabutylammonium analogue of this Dawson system showed the longest-lived charge-separated state, τ = 13 ns in dichloromethane.

References

(1) Long, D. L.; Burkholder, E.; Cronin, L. *Chem. Soc. Rev.* **2007**, *36*, 105–21.

(2) Ammam, M. *J. Mater. Chem. A* **2013**, *1*, 6291.

(3) Sadakane, M.; Steckhan, E. *Chem. Rev.* **1998**, *98*, 219–238.

(4) Song, Y. F.; Tsunashima, R. *Chem. Soc. Rev.* **2012**, *41*, 7384–402.

(5) Proust, A.; Matt, B.; Villanneau, R.; Guillemot, G.; Gouzerh, P.; Izzet, G. *Chem. Soc. Rev.* **2012**, *41*, 7605–22.

(6) Proust, A.; Thouvenot, R.; Gouzerh, P. *Chem. Commun.* **2008**, *16*, 1837–52.

(7) Walsh, J. J.; Bond, A. M.; Forster, R. J.; Keyes, T. E. *Coord. Chem. Rev.* **2016**, *306*, 217–234.

(8) Wang, S. S.; Yang, G. Y. *Chem. Rev.* **2015**, *115*, 4893–962.

(9) Sartorel, A.; Carraro, M.; Scorrano, G.; De Zorzi, R.; Geremia, S.; McDaniel, N. D.; Bernhard, S.; Bonchio, M. *J. Am. Chem. Soc.* **2008**, *130*, 5006–7.

(10) Han, X. B.; Zhang, Z. M.; Zhang, T.; Li, Y. G.; Lin, W.; You, W.; Su, Z. M.; Wang, E. B. *J. Am. Chem. Soc.* **2014**, *136*, 5359–66.

(11) Lv, H.; Geletii, Y. V.; Zhao, C.; Vickers, J. W.; Zhu, G.; Luo, Z.; Song, J.; Lian, T.; Musaev, D. G.; Hill, C. L. *Chem. Soc. Rev.* **2012**, *41*, 7572–89.

(12) Schonweiz, S.; Rommel, S. A.; Kubel, J.; Micheel, M.; Dietzek, B.; Rau, S.; Streb, C. *Chem. Eur. J* **2016**, *22*, 12002–5.

(13) Streb, C. *Dalton Trans.* **2012**, *41*, 1651–9.

(14) Papaconstantinou, E. *Chem. Soc. Rev.* **1989**, *18*, 1.

(15) Gómez-Romero, P.; Chojak, M.; Cuentas-Gallegos, K.; Asensio, J. A.; Kulesza, P. J.; Casañ-Pastor, N.; Lira-Cantú, M. *Electrochem. Commun.* **2003**, *5*, 149–153.

(16) Wang, H.; Hamanaka, S.; Nishimoto, Y.; Irle, S.; Yokoyama, T.; Yoshikawa, H.; Awaga, K. *J. Am. Chem. Soc.* **2012**, *134*, 4918–24.

(17) Herrmann, S.; Ritchie, C.; Streb, C. *Dalton Trans.* **2015**, *44*, 7092–104.

(18) Nishimoto, Y.; Yokogawa, D.; Yoshikawa, H.; Awaga, K.; Irle, S. *J. Am. Chem. Soc.* **2014**, *136*, 9042–52.

(19) Dolbecq, A.; Dumas, E.; Mayer, C. R.; Mialane, P. *Chem. Rev.* **2010**, *110*, 6009–48.

(20) Sazani, G.; Pope, M. T. *Dalton Trans.* **2004**, *13*, 1989–94.

(21) Parrot, A.; Izzet, G.; Chamoreau, L. M.; Proust, A.; Oms, O.; Dolbecq, A.; Hakouk, K.; El Bekkachi, H.; Deniard, P.; Dessapt, R.; Mialane, P. *Inorg. Chem.* **2013**, *52*, 11156–63.

(22) Harriman, A.; Elliott, K. J.; Alamiry, M. A. H.; Pleux, L. L.; Séverac, M.; Pellegrin, Y.; Blart, E.; Fosse, C.; Cannizzo, C.; Mayer, C. R.; Odobel, F. *J. Phys. Chem. C* **2009**, *113*, 5834–5842.

(23) Odobel, F.; Severac, M.; Pellegrin, Y.; Blart, E.; Fosse, C.; Cannizzo, C.; Mayer, C. R.; Elliott, K. J.; Harriman, A. *Chem. Eur. J* **2009**, *15*, 3130–8.

(24) Matt, B.; Coudret, C.; Viala, C.; Jouvenot, D.; Loiseau, F.; Izzet, G.; Proust, A. *Inorg. Chem* **2011**, *50*, 7761–8.

(25) Matt, B.; Renaudineau, S.; Chamoreau, L. M.; Afonso, C.; Izzet, G.; Proust, A. *J. Org. Chem.* **2011**, *76*, 3107–12.

(26) Matt, B.; Moussa, J.; Chamoreau, L.-M.; Afonso, C.; Proust, A.; Amouri, H.; Izzet, G. *Organometallics* **2012**, *31*, 35–38.

(27) Matt, B.; Xiang, X.; Kaledin, A. L.; Han, N.; Moussa, J.; Amouri, H.; Alves, S.; Hill, C. L.; Lian, T.; Musaev, D. G.; Izzet, G.; Proust, A. *Chem. Sci.* **2013**, *4*, 1737.

(28) Matt, B.; Xiang, X.; Kaledin, A. L.; Han, N.; Moussa, J.; Amouri, H.; Alves, S.; Hill, C. L.; Lian, T.; Musaev, D. G.; Izzet, G.; Proust, A. *Chem. Sci.* **2013**, *4*, 2041–6539.

(29) Izzet, G.; Volatron, F.; Proust, A. *Chem. Rec.* **2017**, *17*, 250–266.

(30) Saad, A.; Oms, O.; Dolbecq, A.; Menet, C.; Dessapt, R.; Serier-Brault, H.; Allard, E.; Baczko, K.; Mialane, P. *Chem. Commun.* **2015**, *51*, 16088–91.

(31) Black, F. A.; Jacquart, A.; Toupalas, G.; Alves, S.; Proust, A.; Clark, I. P.; Gibson, E. A.; Izzet, G. *Chem. Sci.* **2018**, *9*, 5578–5584.

(32) Lakowicz, J. R., *Principles of Fluorescence Spectroscopy*; Springer: 2006; Chapter 1: Introduction to Fluorescence.

(33) Summers, G. H.; Lefebvre, J. F.; Black, F. A.; Davies, E. S.; Gibson, E. A.; Pullerits, T.; Wood, C. J.; Zidek, K. *Phys. Chem. Chem. Phys.* **2015**, *18*, 1059–1070.

(34) Lefebvre, J. F.; Sun, X. Z.; Calladine, J. A.; George, M. W.; Gibson, E. A. *Chem. Commun.* **2014**, *50*, 5258–5260.

Chapter 6

Performance of Cyclometalated Ruthenium Complexes in Dye-Sensitised Solar Cells

6.1 Aims

This chapter focuses on the photovoltaic performance of a series of cyclometalated ruthenium sensitisers which differ in their ligand structures. The performances of titanium dioxide solar cells sensitised with these complexes are compared to determine the influence of various structural modifications to the ligands including the number of anchor groups, extending conjugation and the addition of heteroatoms. One dye is then further optimised to achieve its highest possible performance in an n-type dye-sensitised solar cell.

6.2 Introduction

Ruthenium (II) polypyridine complexes have been extensively investigated as sensitisers for titanium dioxide dye-sensitised solar cells, due to their favourable properties such as broad absorption and relatively long excited state lifetimes.[1] Structural modifications to the ligands surrounding the ruthenium can allow these properties to be tuned.[2–4] Early examples of these sensitisers include ruthenium *tris*-bipyridine complexes which have shown electron injection into the conduction band of titanium dioxide upon illumination.[5,6] The

bidentate 2,2'-bipyridyl ligands were modified with carboxylic acid groups (dicarboxy-bipyridyl ligands) to anchor them to the titanium dioxide surface. Work by the group of Grätzel in the 1990s, including the seminal paper in 1991, resulted in dye-sensitised solar cells with power conversion efficiencies of 5-7 % using trinuclear ruthenium complexes with bipyridine and phenanthroline ligands.[7,8] The bipyridine complex which gave the highest efficiency is shown in Figure 6.1 (complex 1). Following these results many ruthenium (II) polypyridine complexes with different ligand architectures have been synthesised and commonly give dye-sensitised solar cells with high efficiencies. A brief summary including some key structures is given here.

Following the success of their initial results, Grätzel's group developed a series of ruthenium (II) dicarboxy-bipyridyl complexes where one bipyridine ligand of the three was replaced with electron donating groups.[9] The most successful dye (named N3) contained thiocyanate groups and achieved a power-conversion efficiency of 10 %. The group then developed the doubly-protonated form, N719.[10] N3 and N719 are commercially available and are still popular reference compounds for dye-sensitised titanium dioxide systems.[11,12] Their high efficiencies have been attributed to broad absorption profiles and favourable energy levels, in addition to the direction and magnitude of the dipole which promotes electron transfer towards titanium dioxide.[13] This effect is determined by the position of the anchor groups relative to the thiocyanate groups and their geometry at the surface. The sulphur atoms of the thiocyanate groups are thought to interact with iodide in the electrolyte to encourage regeneration and this effect is most enhanced when the thiocyante groups are positioned away from the anchor groups.[14]

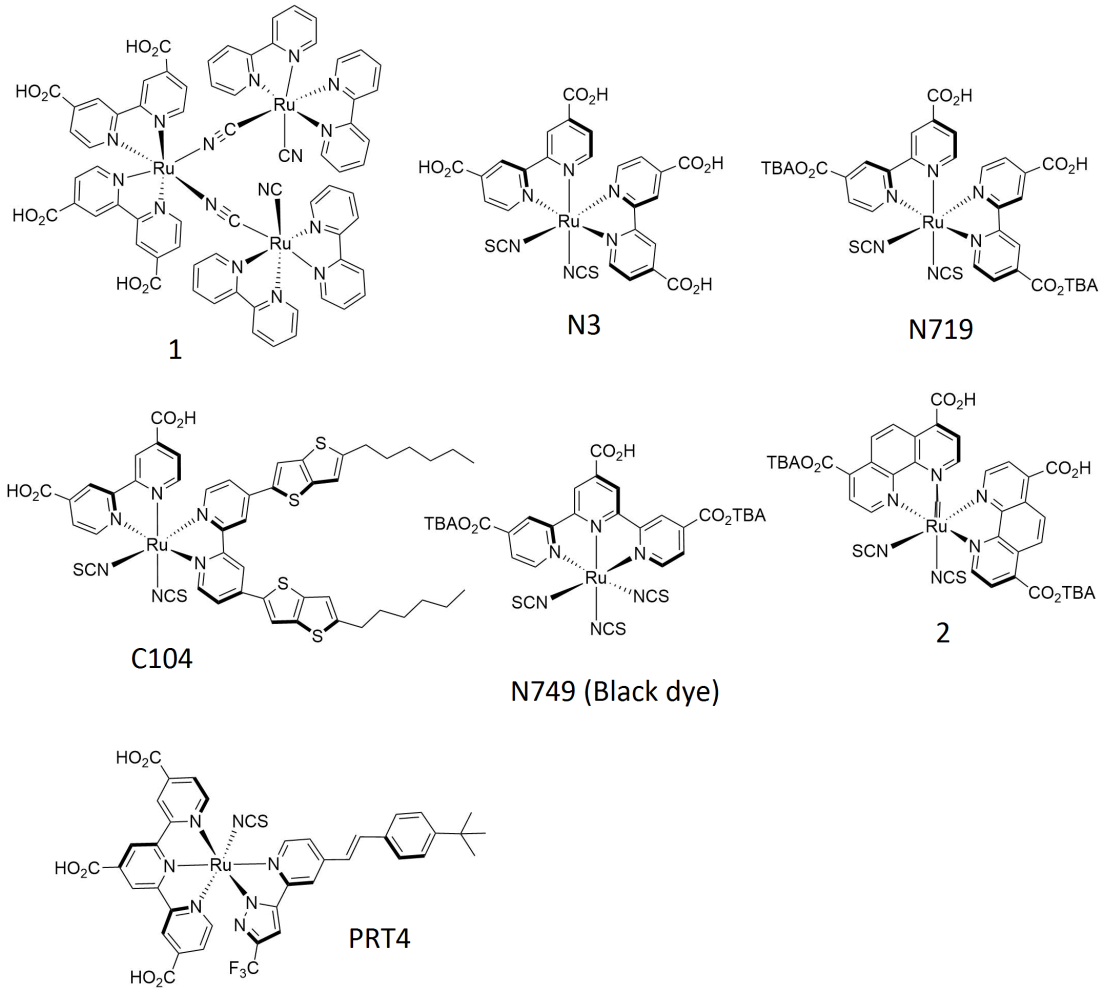

Figure 6.1: Structures of some high-performing ruthenium sensitisers used in titanium dioxide solar cells. 1, ref [7]; N3, ref [9]; N719, ref [10]; C104, ref [15]; N749, ref [16]; 2, ref [17]; PRT4, ref [18].

A strategy to improve the efficiency of systems sensitised with these ruthenium complexes includes extending the π system of the bipyridine ligands to broaden absorption, increase the molar absorption coefficient and prevent aggregation.[19–21] For example, the absorption coefficient of the metal-to-ligand charge transfer (MLCT) band can be increased by incorporating electron-rich thiophene groups onto the ligands.[22–24] C104 is an example of this and devices with this dye achieved efficiencies of 10.5 %.[15] Increasing the extent of conjugation on the bipyridine ligand can tune the photophysical properties but increases the size of the dye and lowers dye adsorption at the surface.[3] Therefore, efforts have been made to synthesise new ligand environments without extensively increasing the size of the complex, such as replacing bipyridyl-type ligands with tridentate terpyridine ligands which have been shown to extend absorption.[25–28] N749, commonly referred to as the

'black dye' was developed by the group of Grätzel and contains a tricarboxy terypyridyl ligand. This dye gives a high incident photon-to-current conversion efficiency of *ca.* 80% across the visible spectrum. Complexes containing terpyridine ligands absorb further into the red region than their corresponding bipyridine complexes,[29] which leads to an extended photocurrent response up to 920 nm.[16] Other ligand systems include phenanthroline ligands, which have extended conjugation and a rigid structure.[30–32] Studies on a series of ruthenium phenanthroline complexes in which the positions and number of anchor groups was modified suggested that two carbonyl groups were necessary for effective injection.[17,33,34] The phenanthroline analogue of N719 (complex 2 in Figure 6.1) gave a power conversion efficiency of 6.1 %.[17]

The absorption band can be extended to longer wavelengths using a strong donor ligand,[35] for example thiocyanate ligands which are common in bipyridine or terpyridine ruthenium dyes like N3, N719 and N749. However, the highest occupied molecular orbital (HOMO) level of these ruthenium dyes is partially delocalised over the thiocyanate ligands, so it would be beneficial to replace these ligands with an organic system which would allow the HOMO level to be tuned.[36,37] It has been shown that when two of the thiocyanate ligands of N479 were replaced with a bidentate pyridine-pyrazolate ligand (complex PRT4) there was an increase in the absorption coefficient and absorption to longer wavelengths.[18] Similarly, cyclometalating ligands have been used, and the ruthenium complexes discussed in this chapter are in this class of dye.

Cyclometalated complexes contain ligands which make ruthenium-carbon σ bonds, and there are now many examples of these as sensitisers for dye-sensitised solar cells.[36,38] The cyclometalating ligand is favourable as a replacement for thiocyanate ligands due to the strong σ donation of the ruthenium-carbon bond[39,40] and greater stability relative to the ruthenium-thiocyante bond. Generally these ruthenium complexes contain bipyridine or terpyridine ligands as well the cyclometalating ligand. The first example of a cyclometalated ruthenium complex used in dye-sensitised solar cells was by the group of van Koten in 2007.[41,42] The cyclometalating ligand was tridentate and was based on the dicarboxy-terpyridyl ligand in which a pyridine group had been replaced with a phenyl group (6-phenyl-2,2'-bipyridine-4,4'-dicarboxylic acid). The ligand therefore coordinated to ruthenium through two nitrogen atoms and a carbon atom, which will be given the

notation N∧N∧C-donating in this thesis, and similar terminology will be used where the donating atoms are substituted. The most successful complex from van Koten's series achieved an incident photon-to-current conversion efficiency (IPCE) of around 70 % and is shown in Figure 6.2 (complex 3).

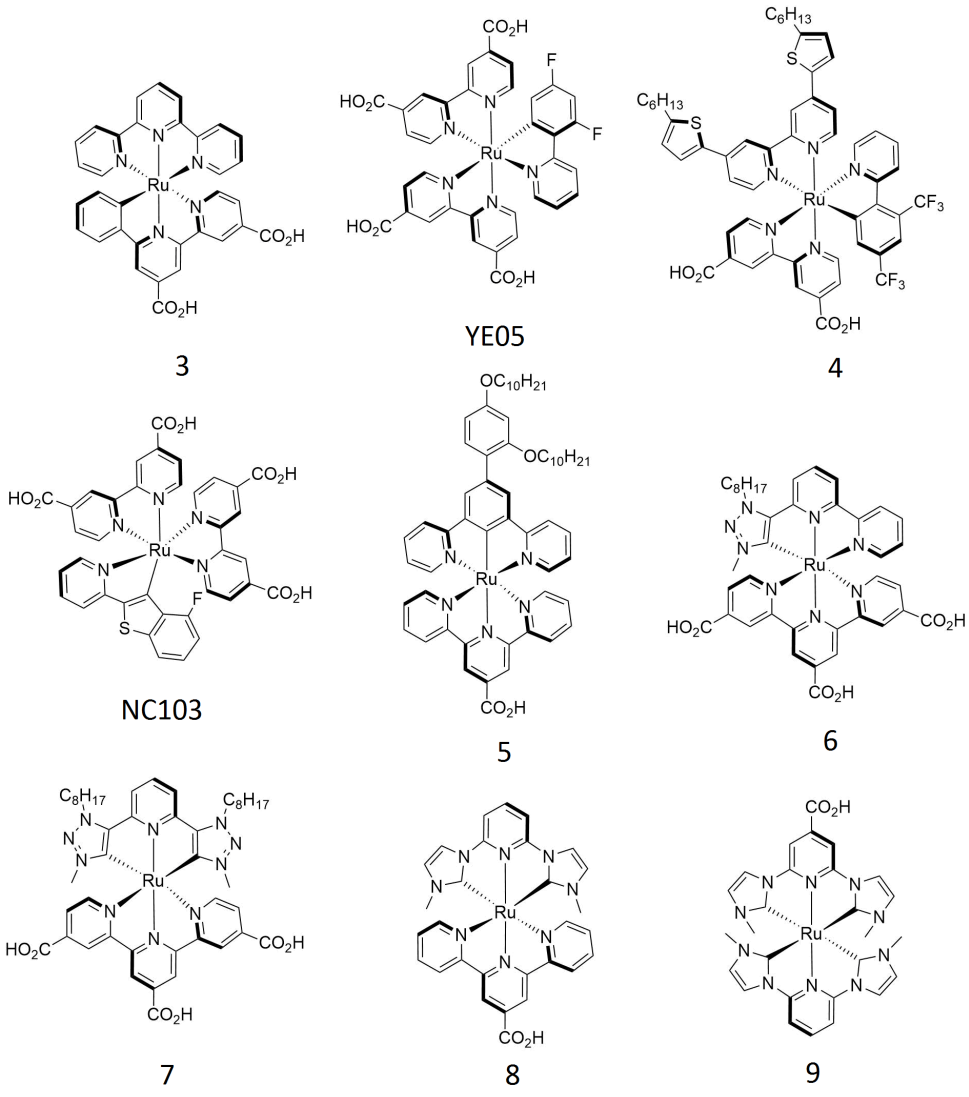

Figure 6.2: Structures of some cyclometalated ruthenium sensitisers used in titanium dioxide solar cells. 3, ref [41]; YE05, ref [43]; 4, ref [44]; NC103, ref [45]; 5, ref [46]; 6,7, ref [47]; 8,9, ref [48].

Following this Grätzel's group reported the ruthenium dicarboxy-bipyridyl complex YE05 which contained a 2-(2,4-difluorophenyl)pyridine (N∧C) cyclometalating ligand which gave 10.1 % power conversion efficiency.[43] There have been efforts by Berlinguette and others to modify the pyridine-phenyl ligand such as that shown in ruthenium complex 4.[44,49] Other ruthenium complexes containing N∧C ligands synthesised for this applica-

tion include pyridine-pyrazole[50] and pyridine-thiophene ligands,[45,51] such as NC103 which achieved a power conversion efficiency of 4.22 %. Examples of tridentate cyclometalating N∧C∧N ligands such as pyridine-phenyl-pyridine (complex 5) reached nearly 3 % efficiency.[46] Berlinguette reported a series of C∧N∧N and C∧N∧C triazole-containing ligands including complexes 6 and 7,[47] and there have been similar studies on pyrazole-containing complexes (complexes 8 and 9).[48]

In addition to titanium dioxide dye-sensitised solar cells, there are examples of cyclometalated ruthenium complexes as sensitisers for p-type nickel oxide systems. Their absorption in the red region is a favourable property for p-type systems which are used in tandem dye-sensitised solar cells. The lower energy photons are often collected by the photocathode and the higher energy photons are collected at the photoanode, so a red-absorbing dye minimises the spectral overlap.[52–54] In contrast to the cyclometalated systems discussed in the context of titanium dioxide n-type dye-sensitised solar cells, the anchor is instead placed on the cyclometalating ligand where the HOMO is localised. For example, Wu *et al.* synthesised a series of ruthenium complexes with a N∧C pyridine-phenyl cyclometalating ligand which was extended with a triphenylamine donor group.[55] The anchoring carboxylic acid ligand is attached to the triphenylamine group and the length of the ruthenium to triphenylamine bridge was changed.[56] Bipyridine, phenanthroline and bathophenanthroline ligands were used as the non-cyclometalating ligands. The bipyridine complex O3 generated the highest photocurrent of 3.04 mA cm^{-1}. O3 and the phenanthroline derivative O13 are shown in Figure 6.3. Further extending the light absorption of this complex to give O18 increased the efficiency to 0.1 %.[57]

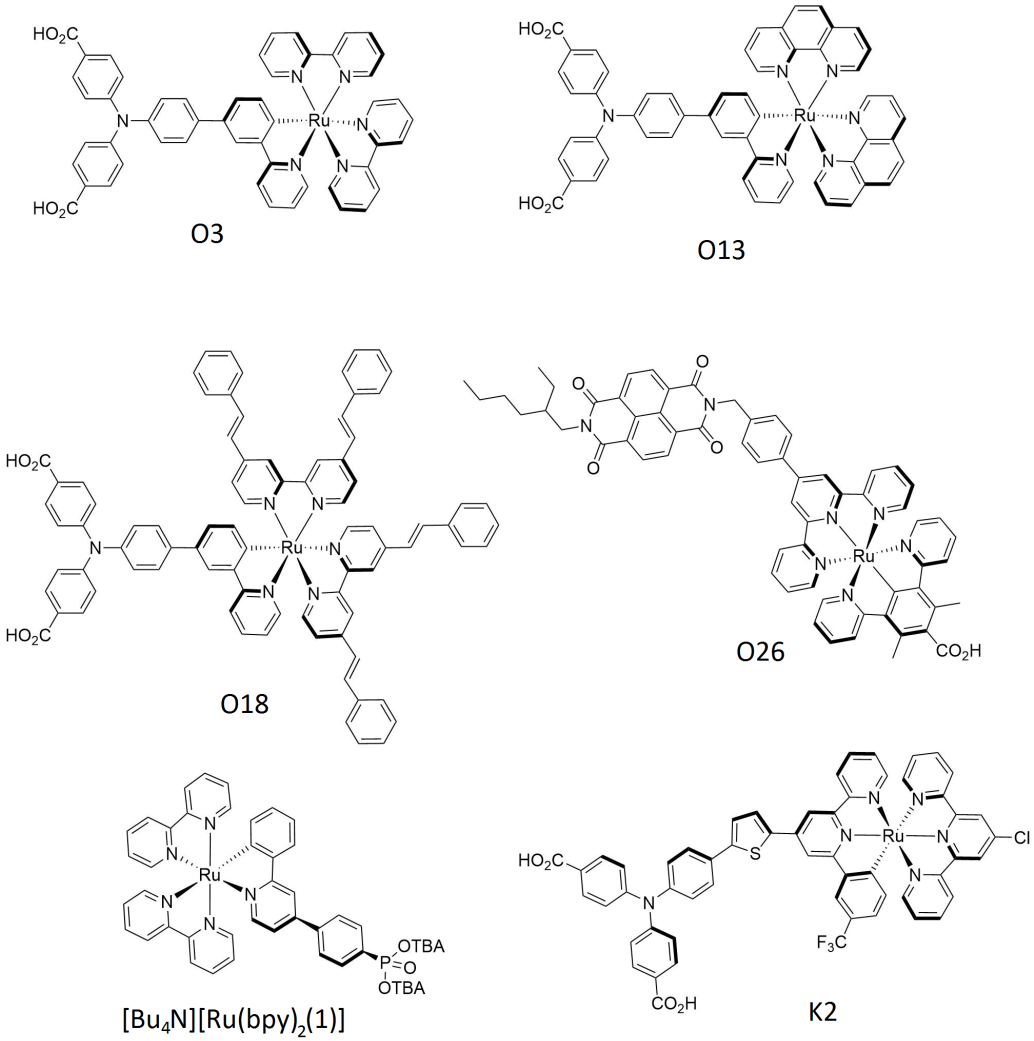

Figure 6.3: Structures of cyclometalated ruthenium dyes used as sensitisers in nickel oxide dye-sensitised solar cells. O3,O13, ref [55]; O18, ref [57]; O26, ref [58]; $[Bu_4N][Ru(bpy)_2(1)]$, ref [59]; K2, ref[60].

Wu's group then developed O26 which used a naphthalenediimide acceptor group to increase the charge-separated state lifetime by directing charge away from the surface.[58] Other p-type systems with the phenyl-pyridine N∧C ligand have been reported by the group of Housecroft, with a phosphonic acid anchor on the cyclometalating ligand which achieved 0.116 % ($[Bu_4N][Ru(bpy)_2(1)]$).[59,61,62] Our group has previously tested the performance of a ruthenium complex containing a tridentate N∧N∧C terpyridine derivative as the cyclometalating ligand, K2.[60]

6.3 Cyclometalated ruthenium dyes

Contributions for Chapter 6: The design and synthesis of the structures tested here were performed by the group of Dr. Kozhevnikov. Solar cell experiments and spectroscopic analysis was performed by the author of this thesis.

In collaboration with the research group of Dr. Kozhevnikov, a series of ruthenium complexes which contained cyclometalating ligands were designed and synthesised, and the structures are shown in Figure 6.4. Ru1-11 all contain a terpyridine ligand which has one, two or three carboxylic acid anchoring groups. The cyclometalating ligands are tridentate C∧N∧O (for Ru1 and Ru2) or C∧N∧N (Ru3-11). Ru12 does not contain a cyclometalated ruthenium-carbon bond but instead two 1,4,5,8-tetraazaphenanthrene ligands and a dipyridophenazine ligand through which the dye anchors via a carboxylic acid group. Examples of ruthenium compounds containing dipyridophenazine ligands have been reported,[63] including analogues of N3 and N719,[64] but ruthenium complexes containing 1,4,5,8-tetraazaphenanthrene have not been used as sensitisers for dye-sensitised solar cells to our knowledge. The presence of ligands which contain non-donating nitrogen atoms creates a π deficiency on the ligand,[65] which could make Ru12 useful for p-type dye-sensitised solar cells and therefore it is included in this study.

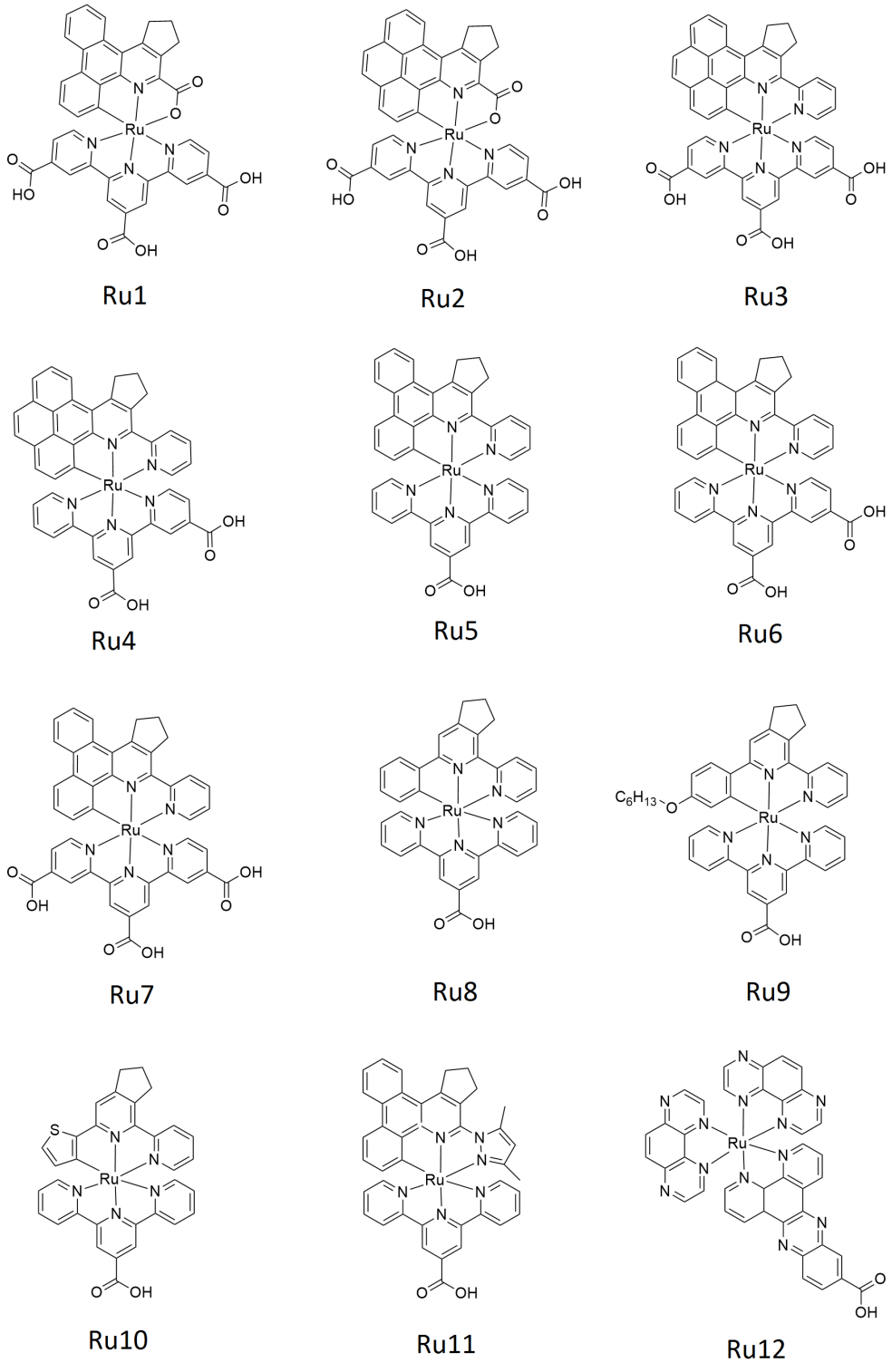

Figure 6.4: Structures of ruthenium dyes studied in this chapter.

The architectures of the cyclometalating ligands are all slightly different and the following discussions will group comparable structures for clarity. The structures of the cyclometalating ligands of each dye and their respective comparable analogues are shown in Table 6.1. Ru12 is not included in these comparisons but was still tested as a sensitiser in titanium dioxide and nickel oxide dye-sensitised solar cells.

Ligand		Comparison
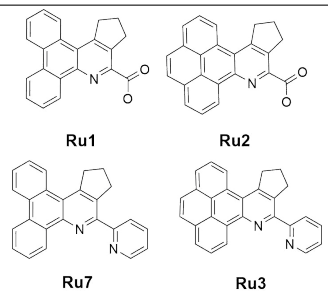	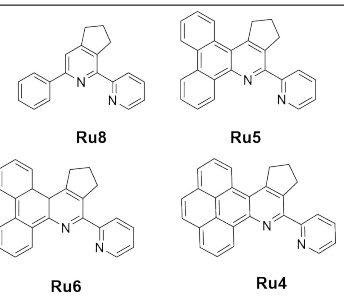	Increased conjugation
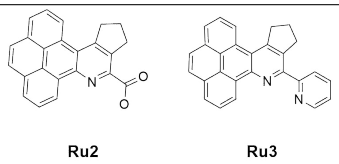	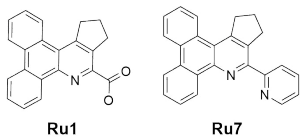	C∧N∧N to C∧N∧O
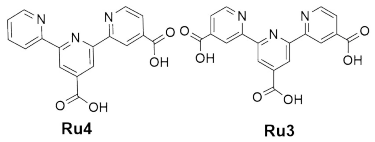	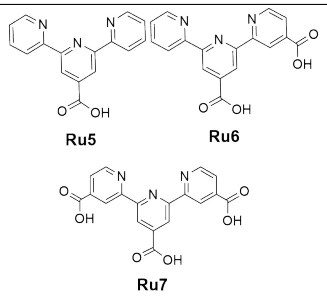	Number of anchor groups
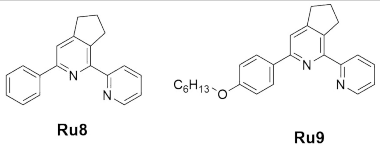		Addition of alkyl group
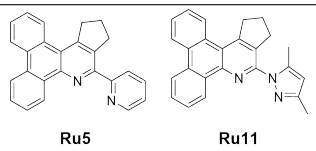		Pyridine to pyrazole
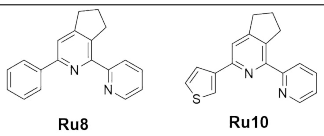		Phenyl to thiophene

Table 6.1: Comparison of ligand structures for Ru1-11.

6.3.1 Steady state film absorption

The ruthenium complexes Ru1-12 were adsorbed onto films of titanium dioxide on FTO coated glass substrates, which were prepared as described in the Experimental Section 3.2. Briefly, titanium dioxide films comprised of a compact titanium dioxide layer and two layers of doctor-bladed paste containing 20 nm anatase particles. The films were sintered in a muffle furnace at 500 °C for 30 minutes then immersed in solutions containing 0.3 mM of dye in 1:1 acetonitrile:*tert*-butanol overnight, as this experimental procedure has been reported for high-performing n-type dye-sensitised solar cells containing N719.[11] Figure 6.5 shows the steady state absorption profiles of Ru1-11 when adsorbed onto titanium dioxide films.

Panels a) and b) of Figure 6.5 compare the absorption spectra of dyes where the extent of conjugation on the cyclometalating ligand changes. Ru1 contains a tricarboxylic acid terpyridine ligand and a C∧N∧O dibenzo[f,h]quinoline cyclometalating ligand. Ru2 also contains a tricarboxylic acid terpyridine ligand but the structure of the cyclometalating ligand is pyreno[5,4-b]pyridine, in which the ligand π system is extended over an additional phenyl group. This increase in conjugation results in a higher absorbance around 550 nm in the absorption spectrum of Ru2 relative to Ru1. Ru7 and Ru3 have the same structures as Ru1 and Ru2, respectively, except that the cyclometalating ligand is C∧N∧N-donating through a pyridine group in place of the carboxylic group in Ru1 and Ru2. For Ru7 and Ru3 the effect of increasing conjugation on the absorption spectra is less pronounced, and the absorption profiles are very similar to that of Ru2, which shows that the carboxylic donating group and the pyridine donating group have a similar effect on the absorption properties, apart from a small blue-shift of the absorption maxima from 535 nm for Ru2 to 527 nm for Ru3.

Ru6 and Ru4 contain C∧N∧N-donating dibenzo[f,h]quinoline and pyreno[5,4-b]pyridine ligands, the same as Ru7 and Ru3, respectively. Consistent with Ru7 and Ru3, their absorption profiles in the visible region on titanium dioxide are not greatly affected by the increase in conjugation. However, the absorption profiles of Ru6 and Ru4 are sharper than that of Ru7 and Ru3, and also of Ru1 and Ru2, which is attributed to the contribution to the π systems of an additional anchoring group present in Ru4 and Ru6.

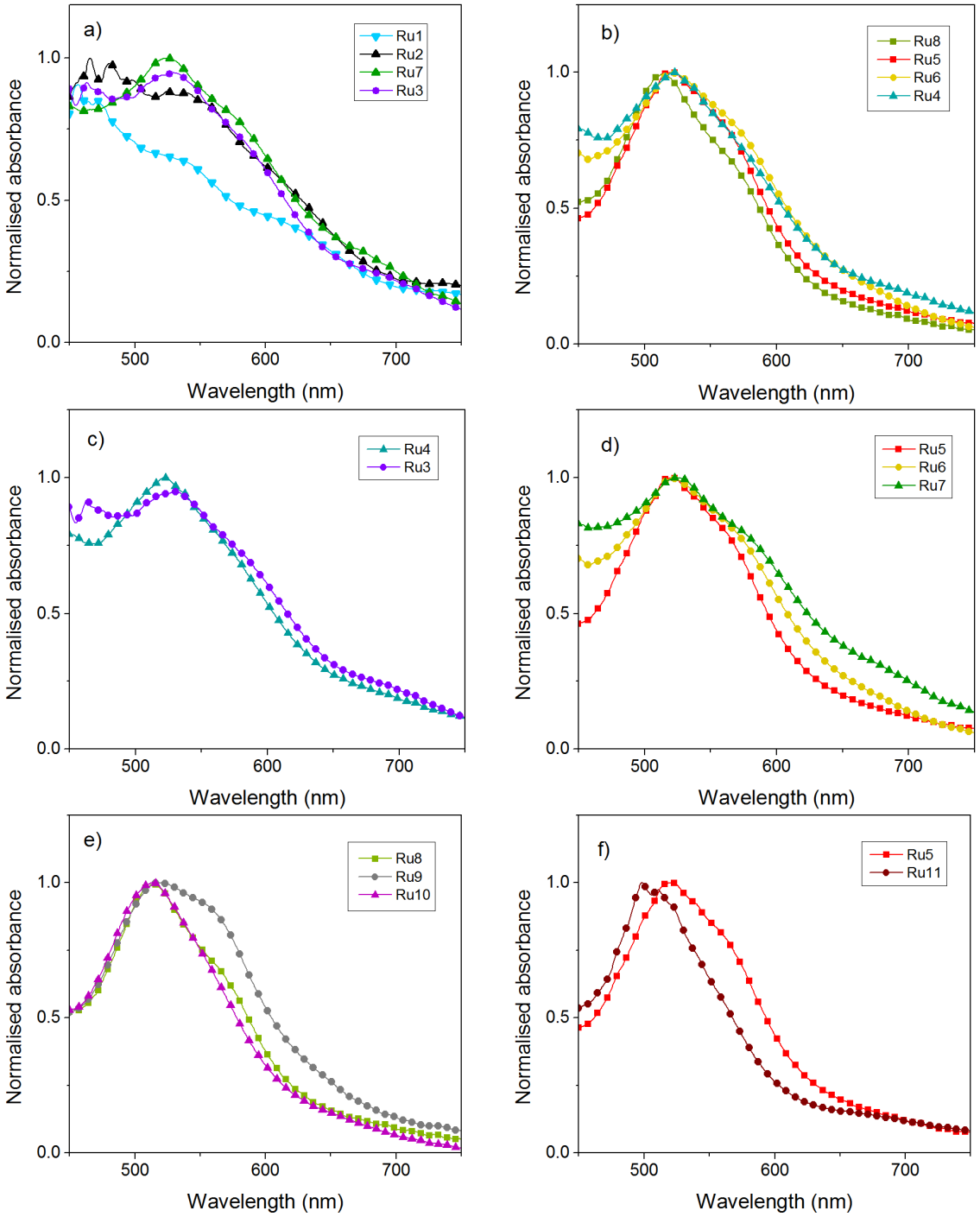

Figure 6.5: Absorption spectra of titanium dioxide films sensitised with ruthenium dyes Ru1-11.

This is also consistent with Ru5 and Ru8 which contain only one carboxylic anchoring group on the terpyridine ligand and have sharper absorption spectra relative to those containing three anchoring groups. Ru8 contains a 6-phenyl-2,2'-bipyridine cyclometalating ligand, and Ru5 contains the same dibenzo[f,h]quinoline ligand as Ru1 and Ru7. The π

system of Ru8 is less extensive than that of Ru5, and this is reflected in the electronic absorption spectra, as Ru5 has a higher absorption around 550 nm. Ru5, Ru6 and Ru7 contain one, two and three carboxylic anchoring groups respectively, and the broadening effect observed for Ru3 relative to Ru4 is also observed for these three dyes as the number of anchor groups increases (Figure 6.5 d)). For this series of ruthenium complexes, increasing the extent of conjugation on the cyclometalating ligand increases the molar absorption coefficient in the visible region for C∧N∧O-donating ligands, and increasing the number of carboxylic acid anchor groups from one to three broadens the absorption band.

The addition of a long-chain alkoxy group to the cyclometalating ligand broadens the absorption into the red region by *ca.* 60 nm (Figure 6.5 e)) for Ru9 relative to Ru8. In fact, the addition of this group has a similar effect on the absorption spectrum as increasing the π system on the cyclometalating ligand by another phenyl group, as the absorption profiles of Ru9 and Ru5 are similar. The alkoxy group may also have other benefits such as hindering aggregation at the surface. Ru10 has the same structure as Ru8 but contains a thiophene group on the cyclometalating ligand instead of a phenyl group, and the absorption spectra of these dyes on titanium dioxide are similar. However when the pyridine group on the other side of the cyclometalating ligand in Ru5 is replaced with an N-donating pyrazole group (Ru11), the absorption spectrum is blue-shifted by *ca.* 20 nm. These comparisons of the absorption spectra on titanium dioxide films shown that small modifications to the cyclometalating ligand, for example the addition of an alkoxy group, can be applied to tune the photophysical properties. Some modifications which were anticipated to have a similar effect, for example the addition of a phenyl group to the π system, do not consistently affect the absorption spectra.

Ru12 which contains 1,4,5,8-tetraazaphenanthrene ligands and a dipyridophenazine ligand, does not absorb as broadly as the other ruthenium dyes tested in this chapter. Its absorption profile on titanium dioxide (Figure 6.6) is consistent with other 1,4,5,8-tetraazaphenanthrene ruthenium complexes.[65]

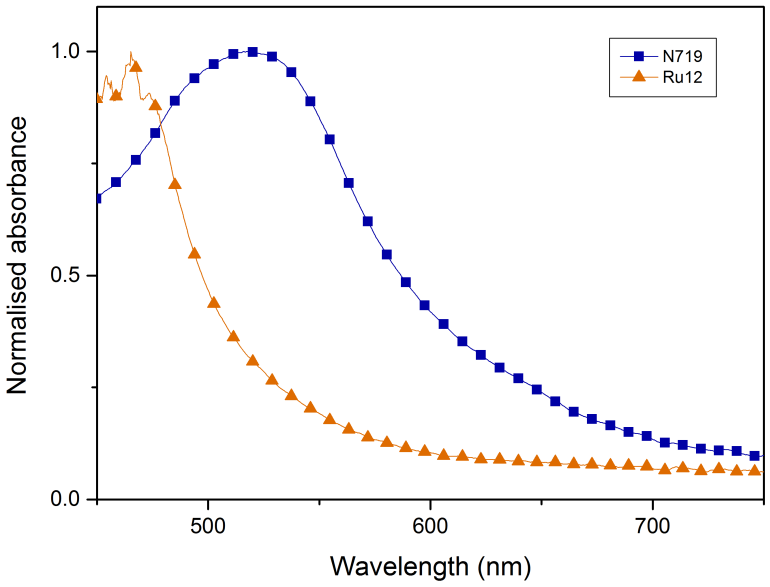

Figure 6.6: Absorption spectra of titanium dioxide films sensitised with Ru12 and N719 for reference.

6.3.2 Dye-sensitised solar cells

Titanium dioxide films sensitised with Ru1-12 were used to fabricate n-type dye-sensitised solar cells in order to evaluate the photovoltaic performances of the dyes. N719 was chosen as a suitable reference dye for these compounds to ensure that the general fabrication and testing methods were consistent with systems already reported.[11] For the following solar cell results, titanium dioxide films consisted of a compact titanium dioxide layer followed by two layers of transparent paste containing 20 nm anatase particles, an opaque layer of larger particles and a final compact layer of titanium dioxide. The sensitised films were assembled into dye-sensitised solar cells as described in the Experimental Section 3.2 with a platinised counter electrode.

Two solutions of iodide/triiodide electrolyte were used, containing different concentrations of iodine and additives. The first is referred to as electrolyte A in this section and consisted of 0.1 M iodine and 1.0 M lithium iodide in acetonitrile solution. The second, electrolyte B, consisted of 0.6 M tetrabutylammonium iodide, 0.015 M iodine, 0.5 M *tert*-butylpyridine and 0.1 M guanidinium thiocyanate in acetonitrile. N719 and many other sensitisers for titanium dioxide systems are known to achieve higher efficiencies with the additives in electrolyte B.

Tert-butylpyridine (and other nitrogen containing heterocycles) are commonly used to increase the open-circuit voltage,[9] and it has been suggested that this is due to either the reduction of charge-recombination between the electrolyte and electrons in the titanium dioxide film, or by a negative shift of the conduction band.[66–68] Positive ions, for example guanidinium ions, have been reported to positively shift the conduction band to increase electron injection and facilitate the assembly of a compact dye layer which reduces the dark current and increases the photovoltage.[69,70] The concentrations of these additives have been chosen based on a system which is reported to give a power conversion efficiency of 10 % for N719-sensitised titanium dioxide.[11]

The performance of dye-sensitised solar cells were evaluated by recording their current-voltage characteristics in the dark and under AM 1.5 1 sun illumination to determine the power conversion efficiency. Incident photon-to-current conversion efficiency (IPCE) plots were also recorded between 300 nm and 700 nm, and the value at the absorption maximum of the dyes is given. The relevant photovoltaic parameters for cells fabricated with electrolyte A are detailed in Table 6.2 and with electrolyte B in Table 6.3.

	V_{OC} (mV)	J_{SC} (mA cm^{-2})	FF (%)	η (%)	IPCE (%)
N719	450	12.8	44	2.55	75
Ru1	228	1.91	55	0.24	11
Ru2	108	0.39	31	0.01	2
Ru3	223	3.41	47	0.36	23
Ru4	222	4.35	54	0.52	33
Ru5	350	3.54	62	0.77	30
Ru6	325	4.8	60	0.93	17
Ru7	305	6.4	57	1.12	33
Ru8	335	3.91	63	0.83	37
Ru9	390	6.92	63	1.7	60
Ru10	346	3.89	59	0.79	35
Ru11	274	0.6	60	0.1	8
Ru12	246	0.31	43	0.03	7

Table 6.2: Photovoltaic properties of n-DSCs assembled with 0.1 M I_2 and 0.1 M LiI in acetonitrile. V_{OC} is the open-circuit voltage; J_{SC} is the short-circuit photocurrent density; FF is the fill factor; η is the power conversion efficiency.

	V_{OC} (mV)	J_{SC} (mA cm^{-2})	FF (%)	η (%)	IPCE (%)
N719	760	9.96	50	3.78	60
Ru1	429	0.12	56	0.03	1
Ru2	386	0.02	59	0.01	5
Ru3	423	0.29	63	0.29	2
Ru4	546	1.8	78	0.59	15
Ru5	626	0.18	57	0.06	2
Ru6	504	1.42	64	0.46	2
Ru7	565	0.32	65	0.12	1
Ru8	670	0.27	59	0.11	3
Ru9	624	0.2	60	0.08	3
Ru10	697	0.81	67	0.38	6
Ru11	466	0.09	49	0.02	1
Ru12	376	0.03	71	0.01	-

Table 6.3: Photovoltaic properties of n-DSCs assembled with 0.6 M tetrabutylammonium iodide, 0.015 M I_2, 0.5 M *tert*-butylpyridine and 0.1 M guanidium thiocyanate in acetonitrile. V_{OC} is the open-circuit voltage; J_{SC} is the short-circuit photocurrent density; FF is the fill factor; η is the power conversion efficiency.

In general, the dyes performed poorly on titanium dioxide with both electrolyte A and electrolyte B. The performance of N719 improved with the addition of additives in the electrolyte, achieving 2.55 % power conversion efficiency with electrolyte A, which increased to 3.78 % with electrolyte B. However, Ru1-12 generally performed better without these additives. The highest efficiency achieved was for Ru9, which contains a C∧N∧N cyclometalating ligand with an alkoxy substituent, and one carboxylic anchoring group. With electrolyte A, Ru9 generated a photocurrent density of 6.92 mA cm^{-2}, closely followed by Ru7 which has a very different structure containing three anchor groups and a more extended π system on the cyclometalating ligand. The photovoltages achieved when electrolyte B was used were higher for all systems than when electrolyte A was used, and the highest open-circuit voltage was achieved by Ru10 (697 mV). With electrolyte B, Ru12 did not generate a large enough photocurrent for an IPCE value to be determined. It should also be mentioned that dye-sensitised solar cells with p-type nickel oxide films dyed with Ru12 were fabricated but no appreciable photocurrent or voltage was achieved.

Despite their broad absorption on titanium dioxide, the dyes all gave low performances relative to N719. Hybrid functional density functional theory was performed by Dr. Martsinovich for a sample of the dyes, and the results are given in the Appendix, Table A.9 and Figure A.5. It was found that for Ru6, Ru7, Ru4 and Ru3, the HOMO-LUMO gap energies were similar apart from Ru3 for which the energy was slightly lower. The HOMO levels were all above the valence band edge of titanium dioxide, but the LUMO levels were all below the conduction band of titanium dioxide. This suggests that recombination will be efficient but the initial electron-injection will be inefficient. This is likely the reason for the low performance of the dyes in general. However, enough photocurrent was generated to make some sensible conclusions regarding structure and performance, and suggests that the estimate of the conduction band edge of titanium dioxide by density functional theory may not be accurate.

Increasing conjugation

For dyes which are comparable by their increasing conjugation on the π system of the cyclometalating ligand, there is an unexpected decrease in performance as the extent of conjugation is increased. The current-voltage curves for Ru1 vs Ru2, Ru7 vs Ru3, Ru6 vs Ru4 and Ru8 vs Ru5 are shown in Figure 6.7. With electrolyte A there is a consistent increase in both the photocurrent and photovoltage generated for dyes containing a dibenzo[f,h]quinoline ligand (Ru1, Ru7, Ru6) relative to the corresponding dyes containing a phenanthro[4,5-*fgh*]quinoline ligand (Ru2, Ru3 and Ru4). This is accompanied by an increase in dark current for systems with a more conjugated π system, which is indicative of greater recombination between the titanium dioxide and the electrolyte. This suggests that complexes containing ligands with bulkier π systems do not block recombination at the surface as effectively as the smaller dyes. This trend is consistent with electrolyte B, but the dark current is slightly reduced for Ru2 and Ru3.

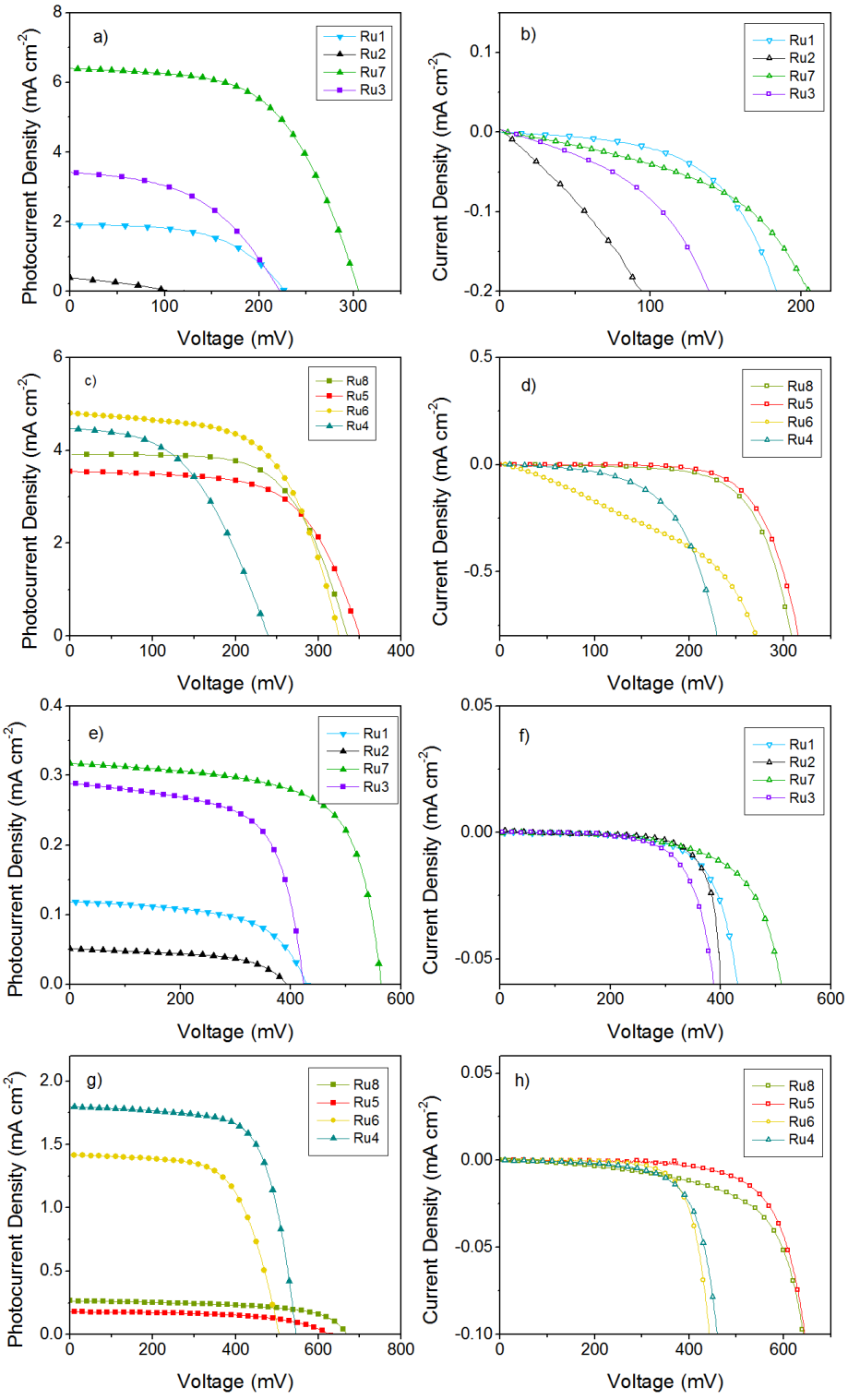

Figure 6.7: Current-voltage characteristics of n-type DSCs assembled with dyes which are comparable by the extent of conjugation on the cyclometalating ligand, (left) under 1 sun illumination and (right) in the dark. a-d) Electrolyte A; e-h) electrolyte B.

Ru5 and Ru8 generate lower photocurrents than the other dyes in this comparison, but generate a higher photovoltage which is attributed to the lower dark current, and this trend is observed in both electrolytes. This supports the observation that larger dyes have a higher dark current, as Ru5 and Ru5 both contain only one anchoring group and have less bulky cyclometalating ligands. Ru8 perfoms relatively well, and generates a similar photocurrent and photovoltage with electrolyte A to Ru5 and Ru3 which contain more extended π systems. The IPCE plots shown in Figure 6.8 are for the cells whose current-voltage curves are given in Figure 6.7. The IPCE spectra of Ru8 and Ru5 are sharper than those of Ru1, Ru2, Ru7, Ru3, Ru6 and Ru4, consistent with their absorption spectra on titanium dioxide. Despite generating a relatively high photocurrent with both electrolyte systems, the IPCE spectra of Ru6 are low, which may be due to the higher dark current observed for this dye.

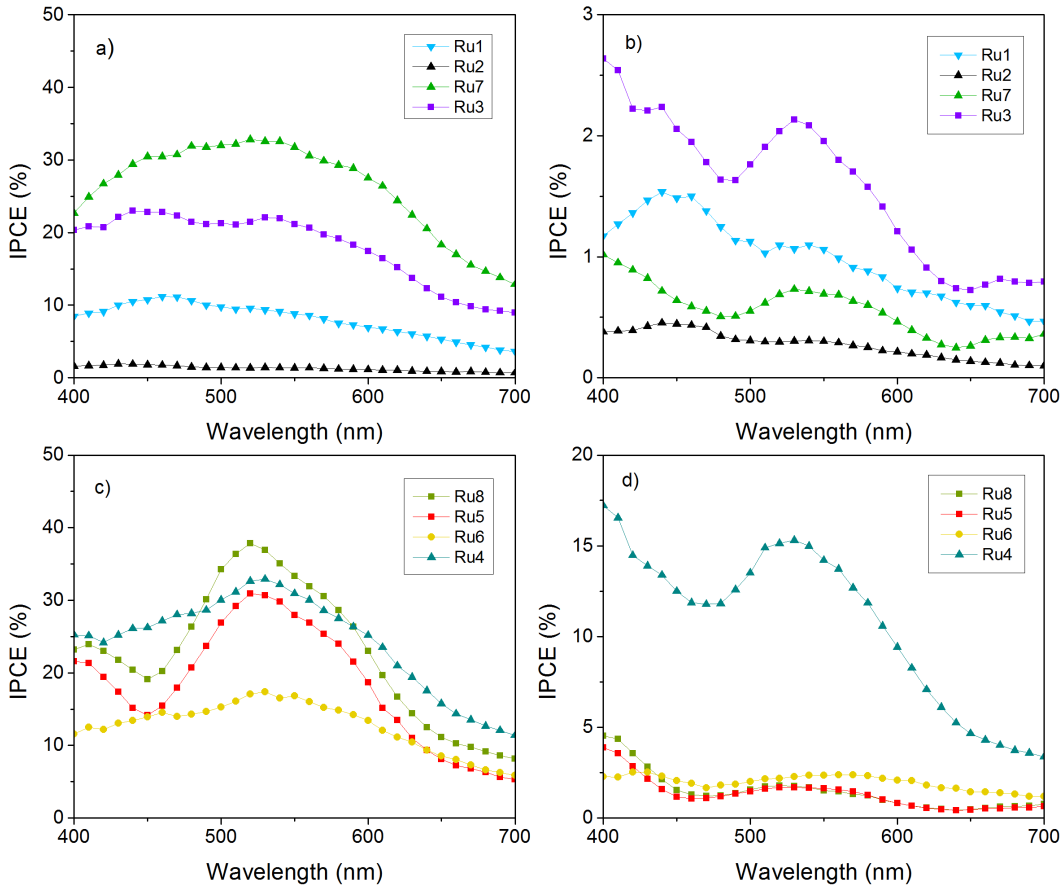

Figure 6.8: IPCE plots of dyes which are comparable by their extent of conjugation on the cyclometalating ligand. a),c) Electrolyte A; b),d) electrolyte B.

Changing the donor groups

Figure 6.7 shows the comparison of Ru2 vs Ru3 and Ru1 vs Ru7, in which the C∧N∧O cyclometalating ligand is changed to C∧N∧N. Their power conversion efficiencies in dye-sensitised solar cells with both electrolyte A and electrolyte B follow Ru3 > Ru2 and R7 > R1. There is nearly a five times increase in the power conversion efficiency generated by Ru7 relative to Ru1 in electrolyte A, four times with electrolyte B. Ru1 and Ru2 are generally low performing relative to the other dyes which suggests that the C∧N∧O ligand with a carboxylic acid donating group does not give high efficiencies under these conditions. This is likely due to a shift in the HOMO energy of the C∧N∧O cyclometalating ligand which influences the regeneration efficiency.

Increasing the number of anchor groups

It has been suggested for titanium dioxide dye-sensitised solar cells that dyes with two anchoring groups are required for efficient dye adsorption and charge-injection of electrons from the dye into the conduction band.[17,33,34] This series allows a comparison of systems which contain one to three carboxylic anchoring groups on the terpyridine ligand. The systems which are compared here are Ru4 vs Ru3 and Ru5 vs Ru6 vs Ru7. For the latter series, there is a clear trend in the increase in the number of anchoring groups and the performance for dye-sensitised solar cells fabricated with electrolyte A. This is shown in Figure 6.9 c). As the number of anchor groups increases from one to three, the photocurrent increases and the overall power conversion efficiency increases.

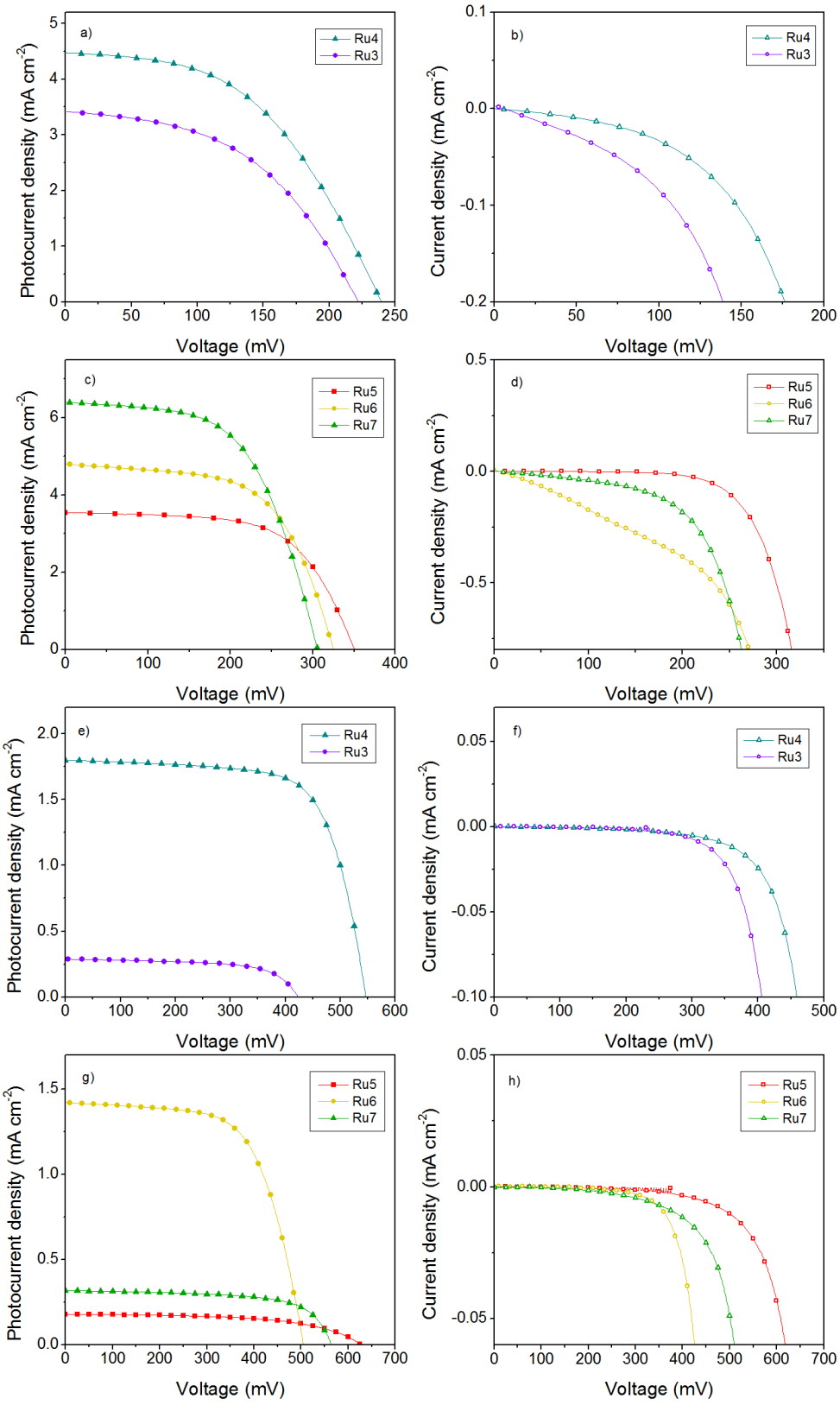

Figure 6.9: Current-voltage characteristics of n-type DSCs assembled with dyes which are comparable by their increasing numbers of anchoring groups (left) under 1 sun illumination and (right) in the dark. a-d) Electrolyte A; e-h) electrolyte B.

As discussed previously, Ru6 has particularly high dark current due to titanium dioxide/electrolyte recombination. When electrolyte B is used, Ru6 performs better than Ru5 and Ru7, which suggests that the additives in the electrolyte are hindering this recombination. Ru7 performs better than Ru5 with both electrolytes, which agrees with previous reports that an increased number of anchoring groups increases performance. However, Ru4 which contains two anchor groups generates a higher photocurrent than Ru3 which contains three. This suggests that when there is no significant charge-recombination between titanium dioxide and the electrolyte, two carboxylic anchor groups are optimum. The IPCE spectra of Ru5-7 (Figure 6.10) show that Ru4 and Ru6 which both contain two carboxylic anchor groups, perform better than the other dyes in this comparison in both electrolytes with the exception of Ru6 in electrolyte A which suffers from high dark current due to recombination between the titanium dioxide and electrolyte.

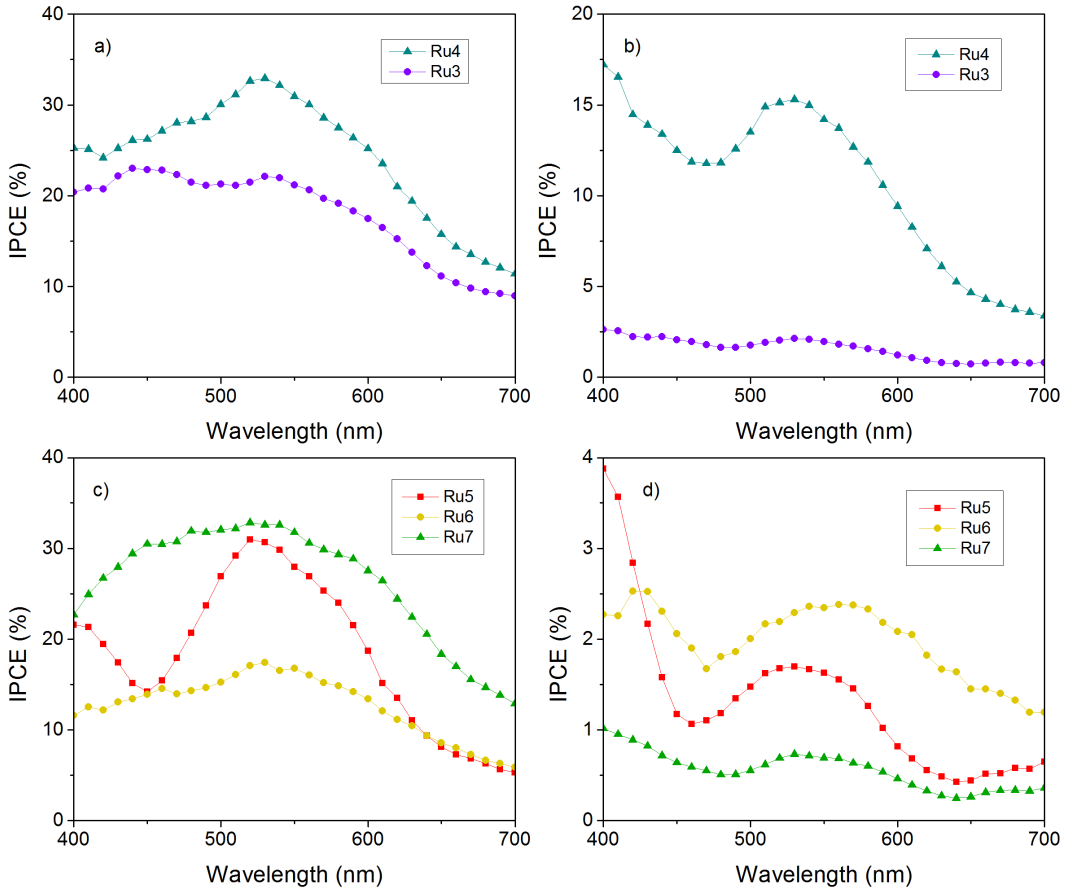

Figure 6.10: IPCE plots n-DSCs assembled with dyes which are comparable by the number of anchor groups. a),c) Electrolyte A; b),d) electrolyte B.

Modifying the C∧N∧N ligand

When the pyridine group on the C∧N∧N cyclometalating ligand of Ru5 is replaced with an N-donating pyrazole group (Ru11), the solar cell performance decreases with both electrolytes. This may be due the effect on the HOMO energy of the pyrazole ligand of Ru11 which contains non-donating nitrogen atoms. An increase in the HOMO level for Ru11 is consistent with the absorption spectra on titanium dioxide, as the absorption profile of Ru5 was red-shifted relative to Ru11. The series including Ru8, Ru9 and Ru10 allows comparison of a number of structural modifications to the C∧N∧N cyclometalating ligand. Ru8 vs Ru9 compares the addition of a long-chain alkoxy group to the phenyl group of the 6-phenyl-2,2'-bipyridine ligand. As shown in Figure 6.5, Ru9 with the alkoxy chain has a broader absorption spectrum than Ru8, and the solar cell performance of Ru9 is higher than that of Ru8 with electrolyte A, Figure 6.11.

With electrolyte B, both Ru8 and Ru9 have low performance and give similar power conversion efficiencies. When the phenyl group is replaced with a C-donating thiophene group, Ru10, the solar cell performance is very similar to that of Ru8 with a phenyl group. This is to be expected as the absorption spectra on titanium dioxide films were similar for Ru8 and Ru10. However, with electrolyte B the performance of Ru10 increases relative to Ru8, despite the higher dark current of Ru10 with this electrolyte. Dyes Ru8, Ru9 and Ru10 all perform surprisingly well with electrolyte A considering their small size and sharper absorption relative to other dyes in this series.

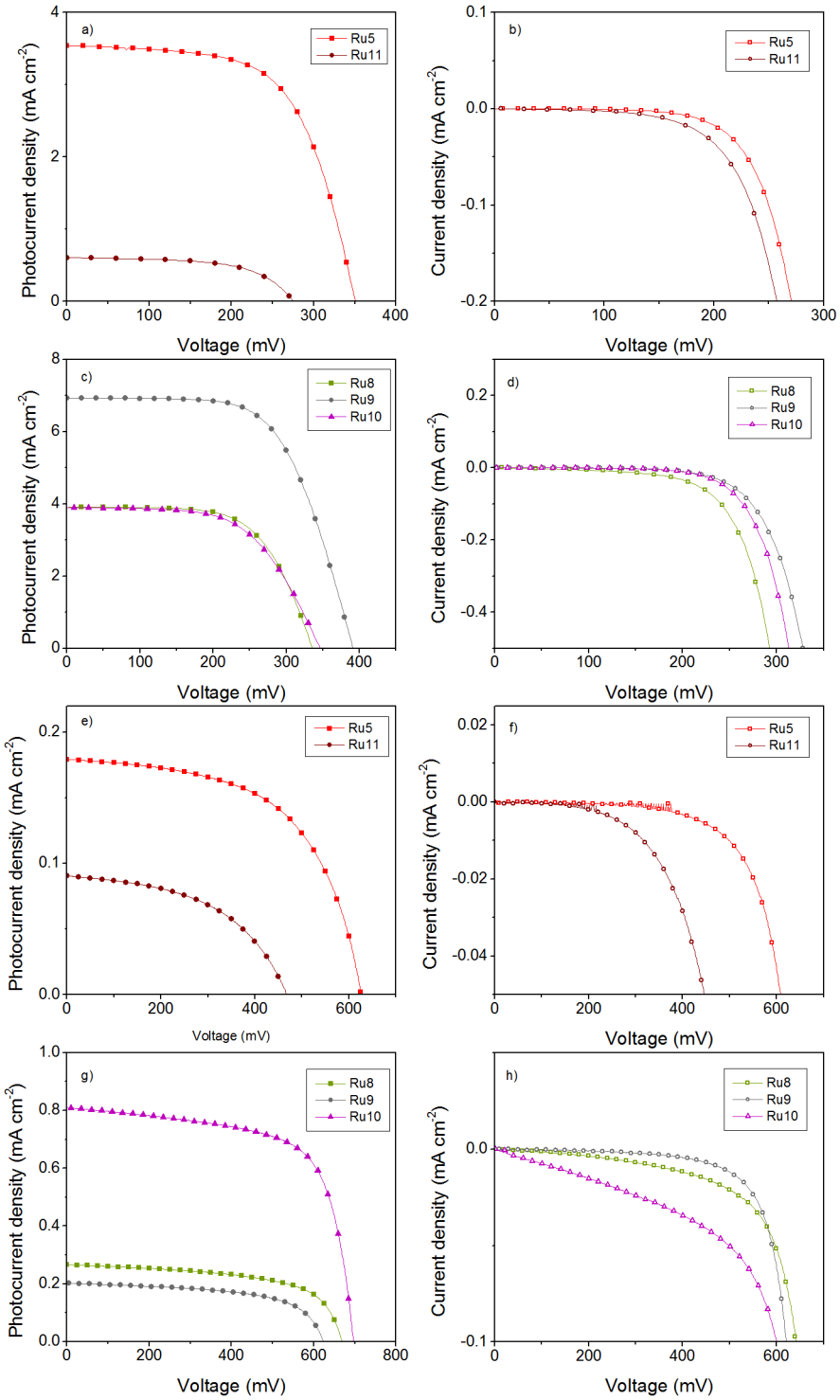

Figure 6.11: Current-voltage characteristics of n-DSCs assembled with dyes which are comparable by the structure of the cyclometalating ligand (left) under 1 sun illumination and (right) in the dark. a-d) Electrolyte A; e-h) electrolyte B.

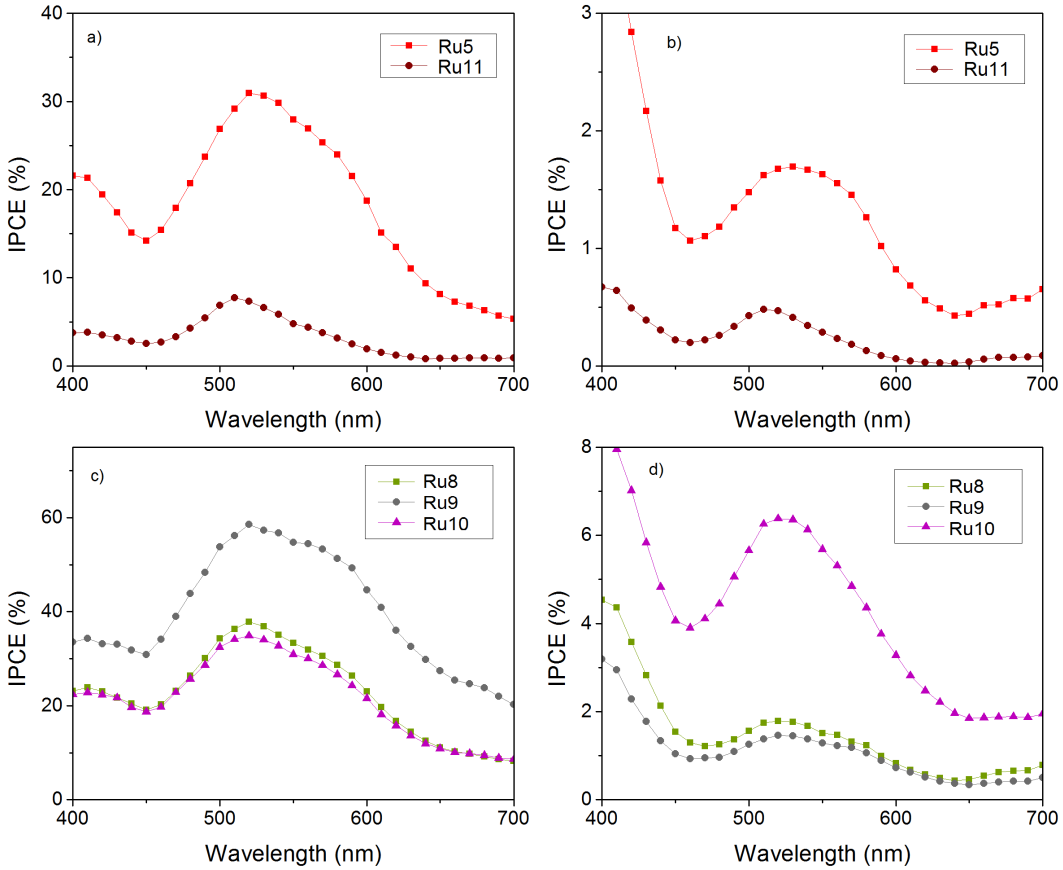

Figure 6.12: IPCE plots of n-DSCs assembled with dyes which are comparable by the structure of the C∧N∧N ligand. a),c) Electrolyte A; b),d) electrolyte B.

The current-voltage characteristics of n-type dye-sensitised solar cells assembled with these ruthenium complexes has allowed some initial conclusions to be drawn regarding ligand structure and performance. Specifically, smaller dyes with two or three carboxylic anchoring groups and C∧N∧N cyclometalating ligands performed well. The following sections outline the optimisation of Ru3 which contains a ligand of synthetic interest.

6.4 Optimisation

Ru3 contains a pyreno[5,4-b]pyridine cyclometalating ligand which is novel in dye-sensitised solar cells so the success of this new ligand system was investigated further. Further spectroscopic analysis and optimisation of dye-sensitised solar cells was performed. The HOMO energy of Ru3 was calculated to be 1.5 eV above the valence band minimum of titanium dioxide from density functional theory (Appendix Table A.9). This positions the HOMO level of Ru3 lower than the valence band edge of nickel oxide which is *ca.* 1.7

eV lower than the valence band edge of titanium dioxide.[71,72] As there is a driving force for charge-injection, ΔG_{inj}, from nickel oxide to Ru3, p-type nickel oxide dye-sensitised solar cells were also fabricated.

6.4.1 Steady state absorption

The absorption profile of Ru3 in acetonitrile solution is shown in Figure 6.13. The absorption profile extends over a broad region of the visible spectrum between 350 nm and 700 nm. The bands between 350 nm and 450 nm are attributed to ligand-centered π-π^* transitions, and the bands at longer wavelength are attributed to metal-to-ligand charge transfer transitions. The molar absorption coefficient at 427 nm is 8851 dm^3 mol^{-1} cm^{-1}. This is lower than some of the organic dyes shown in previous chapters of this thesis, for example BOD1-5 and the CAD dyes, but is similar to other ruthenium dyes (N719 *ca.* 10 000 dm^3 mol^{-1} cm^{-1})[51] and ruthenium dyes with cyclometalating ligands.[38,39]

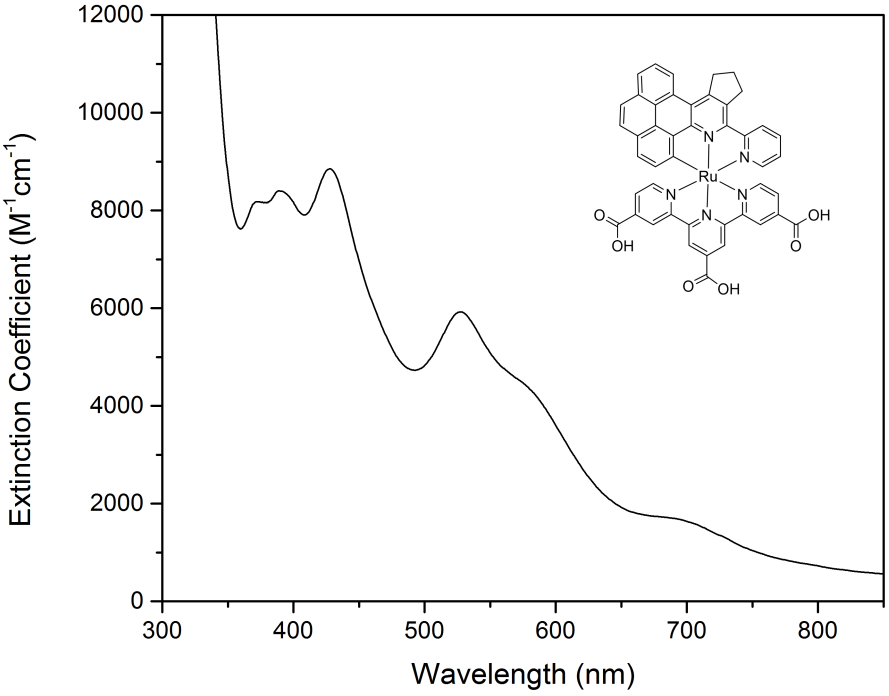

Figure 6.13: Absorption spectrum of Ru3 in acetonitrile solution.

For absorption experiments of Ru3-sensitised films, nickel oxide films consisting of a *ca.* 1 μm thick layer of nickel oxide were immersed in a 0.3 mM solution of Ru3 in 1:1 acetonitrile:*tert*-butanol for at least 18 hours, which is the same procedure used to sensitise titanium dioxide films. The films were prepared by applying subsequent layers of nickel chloride solution, as described in the Experimental Section 3.2. Between layers the films were heated to 450 °C in a muffle furnace for 30 minutes. Titanium dioxide and nickel oxide films were immersed in separate dye baths and 10 mM chenodeoxycholic acid was added to each bath, as it has been reported to prevent aggregation of the dye at the surface during absorption.[73–77] The visible absorption spectra of Ru3-sensitised titanium dioxide and nickel oxide films are shown in Figure 6.14 and the absorption maxima are given in Table 6.4. The absorption spectra of at least two films from each bath was taken and a representative spectrum is shown.

	ε (dm^3 mol^{-1} cm^{-1})	λ_{max}(nm)			
	MeCN	TiO_2	Cheno|TiO_2	NiO	Cheno|NiO
Ru3	8851 (428), 5920 (528)	530	527	525	529

Table 6.4: Absorption maxima of Ru3 in acetonitrile solution and when adsorbed onto titanium dioxide and nickel oxide films. The molar absorption coefficient was recorded in acetonitrile solution.

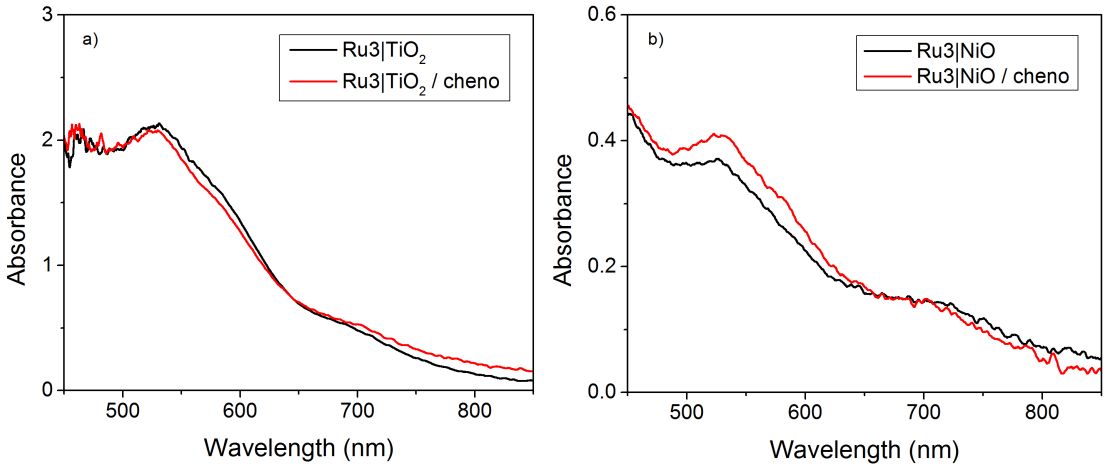

Figure 6.14: Absorption profile of Ru3 adsorbed onto nickel oxide and titanium dioxide films, in the presence and absence of 10 mM chenodeoxycholic acid in the dye bath during sensitisation.[76]

The absorption maximum of Ru3 on titanium dioxide is slightly red-shifted by *ca.* 5 nm relative to on nickel oxide, and is not largely affected by the presence of chenodeoxycholic acid in the dye bath, apart from a slight blue-shift on titanium dioxide and a slight red-shift on nickel oxide. The film absorbance on nickel oxide is much lower relative to the dye on titanium dioxide, which indicates lower dye loading on nickel oxide, although the absorbance of the dye is slightly increased with chenodeoxycholic acid.

6.4.2 Dye-sensitised solar cells

Dye-sensitised solar cells were fabricated from nickel oxide and titanium dioxide films sensitised with Ru3. Titanium dioxide dye-sensitised solar cells assembled with N719 were also prepared for reference. For n-type cells, the films were prepared as in Section 6.3.2 with a compact titanium dioxide layer, two transparent layers, an opaque scattering layer and a final compact layer. Two electrolytes, A and B were used and contained the same components and concentrations as described in the previous section. The photovoltaic parameters of Ru3 and N719 titanium dioxide solar cells prepared with and without chenodeoxycholic acid are shown in Table 6.5. The results of p-type dye-sensitised solar cells made with Ru3-sensitised nickel oxide are also detailed. Ru3 p-type dye-sensitised solar cells achieved a reasonable photovoltage of 77 mV with electrolyte A when chenodeoxycholic acid was present in the dye bath, but the photocurrent generated was too low to determine an IPCE.

The results for n-type dye-sensitised solar cells were much more encouraging. The power conversion efficiency of N719 dye-sensitised solar cells is increased by *ca.* 0.5 % when chenodeoxycholic acid is present during the sensitisation process. This trend is also observed for Ru3 with both electrolytes, and with electrolyte B the photocurrent is doubled when chenodeoxycholic acid is present. For both Ru3 and N719 n-type cells, the photocurrent decreases when electrolyte B is used relative to electrolyte A, but the photovoltage is higher. This is likely due to the presence of guanidinium ions which create a compact layer at the surface, increasing the photovoltage.[69,70]

Dye|semiconductor	Electrolyte	V_{OC} (mV)	J_{SC} (mA cm^{-2})	FF (%)	η (%)	IPCE (%)
N719|TiO_2	A	405	9.52	67	2.59	68
N719/cheno|TiO_2	A	395	12.78	58	2.93	75
N719|TiO_2	B	780	9.44	63	4.64	60
N719/cheno|TiO_2	B	806	9.91	65	5.22	78
Ru3|TiO_2	A	314	9.67	48	1.47	56
Ru3/cheno|TiO_2	A	301	7.67	53	1.23	38
Ru3|TiO_2	B	583	1.45	68	0.58	9
Ru3/cheno|TiO_2	B	644	3.3	71	1.52	24
Ru3|NiO	A	16	0.3	22	0.001	-
Ru3/cheno|NiO	A	77	0.24	36	0.007	-

Table 6.5: Photovoltaic properties of p-type and n-type dye-sensitised solar cells. Electrolyte A: 0.1 M I_2, 1 M LiI, MeCN. Electrolyte B: 0.6 M tetrabutylammonium iodide, 0.0 15 M I_2, 0.5 M *tert*-butylpyridine and 0.1 M guanidine thiocyanate in acetonitrile. Cheno = chenodeoxycholic acid. V_{OC} = open-circuit voltage. J_{SC} = short-circuit photocurrent. FF = fill factor. η = power conversion efficiency.

With electrolyte A Ru3 achieves high photocurrent densities, *ca.* 8 mA cm^{-2}, but the most efficient cell was fabricated with electrolyte B and achieved a power conversion efficiency of 1.52 % (IPCE = 24 %). The current-voltage characteristics of the most efficient Ru3 and N719 dye-sensitised solar cells are shown in 6.15, which for both dyes was for cells assembled with electrolyte B and with chenodeoxycholic acid in the dye bath. The absorption profiles of Ru3 and N719 adsorbed onto titanium dioxide films are also shown together with the IPCE spectra. Both dyes have similar absorption spectra on titanium dioxide and have high dye-loading on the film, but the IPCE of N719 is four times that of Ru3. The difference in performance is likely due to inefficient charge-injection for Ru3, as density functional theory calculations revealed that the LUMO energy of Ru3 is *ca.* 1.0 V below that of the conduction band of titanium dioxide (Appendix Table A.9). In general Ru3 performs well in a titanium dioxide dye-sensitised solar cell, which is a promising result for this new ligand structure.

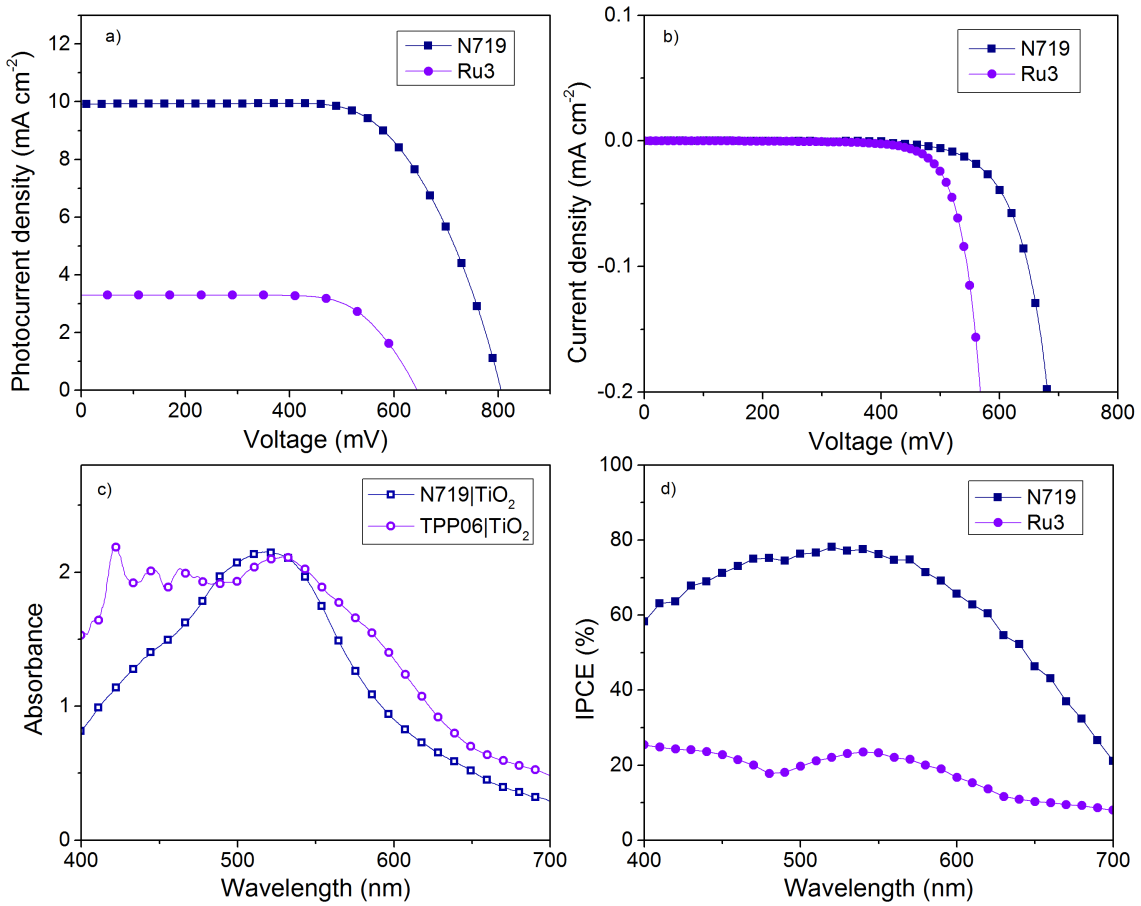

Figure 6.15: Photovoltaic properties of titanium dioxide dye-sensitied solar cells assembled with N719 and Ru3. The films were sensitised with 10 mM chenodeoxycholic acid in the dye bath and solar cells were fabricated with electrolyte B. a) Current-voltage curves under AM 1.5 1 sun illumination; b) current-voltage curves in the dark; c) film absorbance; d) IPCE plots of cells which gave the current-voltage curves shown in a).

6.5 Conclusions

This chapter presented a series of ruthenium dyes which contain C∧N∧N or C∧N∧O cyclometalating ligands with slightly different ligand structures. Their performances in n-type dye-sensitised solar cells were screened and compared, allowing some initial conclusions to be drawn regarding structure and performance. Density functional theory calculations of a selection of the dyes adsorbed on titanium dioxide suggested that charge-injection would be inefficient as the LUMO energy level lies below the conduction band of titanium dioxide. Despite this, reasonable photocurrents were generated by some of the dyes in this series.

Dyes which were comparable by their increasing extent of conjugation on the cyclometalating ligand showed that the more extended pyreno[5,4-b]pyridine ligand gave lower performances than those containing a dibenzo[f,h]quinoline ligand. This was attributed to higher dark current for the more extended systems, which is likely related to the stacking of the π system at the surface. It is also concluded that two carboxylic acid anchoring groups give an optimum performance. The highest performance was achieved by Ru9 which contains an alkoxy chain on the cyclometalating ligand. This feature may hinder aggregation and charge-recombination between the electrolyte and titanium dioxide.

Ru3 contains a pyreno[5,4-b]pyridine group on the cyclometalating ligand which is of synthetic interest and this dye was further optimised. When the fabrication and testing of dye-sensitised solar cells containing Ru3 were repeated, and films were sensitised in the presence of chenodeoxycholic acid, photocurrents of *ca.* 8 mA cm^{-2} were achieved. The dye achieved a reasonable power conversion efficiency but was lower than that of N719, and this difference was attributed to an insufficient driving force for injection. These initial results indicate the potential success of this new ligand.

References

(1) Hagfeldt, A.; Boschloo, G.; Sun, L.; Kloo, L.; Pettersson, H. *Chem. Rev.* **2010**, *110*, 6595–663.

(2) Qin, Y.; Peng, Q. *Int. J. Photoenergy* **2012**, *2012*, 1–21.

(3) Pashaei, B.; Shahroosvand, H.; Graetzel, M.; Nazeeruddin, M. K. *Chem. Rev.* **2016**, *116*, 9485–564.

(4) Aghazada, S.; Gao, P.; Yella, A.; Marotta, G.; Moehl, T.; Teuscher, J.; Moser, J. E.; De Angelis, F.; Gratzel, M.; Nazeeruddin, M. K. *Inorg. Chem.* **2016**, *55*, 6653–9.

(5) Anderson, S.; Constable, E. C.; Dare-Edwards, M. P.; Goodenough, J. B.; Hamnett, A.; Seddon, K. R.; Wright, R. D. *Nature* **1979**, *280*, 571–573.

(6) Desilvestro, J.; Graetzel, M.; Kavan, L.; Moser, J.; Augustynski, J. *J. Am. Chem. Soc.* **1985**, *107*, 2988–2990.

(7) O'Regan, B.; Grätzel, M. *Nature* **1991**, *353*, 737–740.

(8) Nazeeruddin, M. K.; Liska, P.; Moser, J.; Vlachopoulos, N.; Gratzel, M. *Helv. Chimi. Acta* **1990**, *73*, 1788–1803.

(9) Nazeeruddin, M. K.; Kay, A.; Rodicio, I.; Humphry-Baker, R.; Mueller, E.; Liska, P.; Vlachopoulos, N.; Graetzel, M. *J. Am. Chem. Soc.* **1993**, *115*, 6382–6390.

(10) Nazeeruddin, M. K.; Zakeeruddin, S. M.; Humphry-Baker, R.; Jirousek, M.; Liska, P.; Vlachopoulos, N.; Shklover, V.; Fischer, C.-. H.; Grätzel, M. *Inorg. Chem.* **1999**, *38*, 6298–6305.

(11) Ito, S.; Murakami, T. N.; Comte, P.; Liska, P.; Grätzel, C.; Nazeeruddin, M. K.; Grätzel, M. *Thin Solid Films* **2008**, *516*, 4613–4619.

(12) Chiba, Y.; Islam, A.; Watanabe, Y.; Komiya, R.; Koide, N.; Han, L. *Jpn. J. Appl. Phys.* **2006**, *45*, L638–L640.

(13) De Angelis, F.; Fantacci, S.; Selloni, A.; Gratzel, M.; Nazeeruddin, M. K. *Nano. Lett.* **2007**, *7*, 3189–95.

(14) Privalov, T.; Boschloo, G.; Hagfeldt, A.; Svensson, P. H.; Kloo, L. *J. Phys. Chem. C* **2008**, *113*, 783–790.

(15) Gao, F.; Wang, Y.; Zhang, J.; Shi, D.; Wang, M.; Humphry-Baker, R.; Wang, P.; Zakeeruddin, S. M.; Gratzel, M. *Chem. Commun.* **2008**, *23*, 2635–7.

(16) Nazeeruddin, M. K.; Péchy, P.; Grätzel, M. *Chem. Commun.* **1997**, *18*, 2988–2990.

(17) Hara, K.; Sugihara, H.; Singh, L. P.; Islam, A.; Katoh, R.; Yanagida, M.; Sayama, K.; Murata, S.; Arakawa, H. *J. Photochem. Photobiol. A* **2001**, *145*, 117–122.

(18) Chen, B. S.; Chen, K.; Hong, Y. H.; Liu, W. H.; Li, T. H.; Lai, C. H.; Chou, P. T.; Chi, Y.; Lee, G. H. *Chem. Commun.* **2009**, *39*, 5844–6.

(19) Wang, P.; Zakeeruddin, S. M.; Moser, J. E.; Humphry-Baker, R.; Comte, P.; Aranyos, V.; Hagfeldt, A.; Nazeeruddin, M. K.; Grätzel, M. *Adv. Mater.* **2004**, *16*, 1806–1811.

(20) Chen, C. Y.; Chen, J. G.; Wu, S. J.; Li, J. Y.; Wu, C. G.; Ho, K. C. *Angew. Chem. Int. Ed.* **2008**, *47*, 7342–5.

(21) Chen, C. Y.; Wu, S. J.; Li, J. Y.; Wu, C. G.; Chen, J. G.; Ho, K. C. *Adv. Mater.* **2007**, *19*, 3888–3891.

(22) Chen, C. Y.; Wu, S. J.; Wu, C. G.; Chen, J. G.; Ho, K. C. *Angew. Chem. Int. Ed.* **2006**, *45*, 5822–5.

(23) Chen, C. Y.; Wang, M.; Li, J. Y.; Pootrakulchote, N.; Alibabaei, L.; Ngoc-le, C. H.; Decoppet, J. D.; Tsai, J. H.; Gratzel, C.; Wu, C. G.; Zakeeruddin, S. M.; Gratzel, M. *ACS Nano.* **2009**, *3*, 3103–9.

(24) Yu, Q.; Wang, Y.; Yi, Z.; Zu, N.; Zhang, J.; Zhang, M.; Wang, P. *ACS Nano.* **2010**, *4*, 6032–8.

(25) Koyyada, G.; Kumar Ch, P.; Salvatori, P.; Marotta, G.; Lobello, M. G.; Bizzarri, O.; De Angelis, F.; Malapaka, C. *Inorganica Chim. Acta* **2016**, *442*, 158–166.

(26) Ozawa, H.; Sugiura, T.; Kuroda, T.; Nozawa, K.; Arakawa, H. *J. Mater. Chem. A* **2016**, *4*, 1762–1770.

(27) Ozawa, H.; Fukushima, K.; Urayama, A.; Arakawa, H. *Inorg. Chem.* **2015**, *54*, 8887–9.

(28) Mongal, B. N.; Bhattacharya, S.; Sengupta, S.; Mandal, T. K.; Datta, J.; Naskar, S. *Sol. Energy* **2016**, *134*, 107–118.

(29) Nazeeruddin, M. K.; Péchy, P.; Renouard, T.; Zakeeruddin, S. M.; Humphry-Baker, R.; Comte, P.; Liska, P.; Cevey, L.; Costa, E.; Shklover, V.; Spiccia, L.; Deacon, G. B.; Bignozzi, C. A.; Grätzel, M. *J. Am. Chem. Soc.* **2001**, *123*, 1613–1624.

(30) Reynal, A.; Forneli, A.; Martinez-Ferrero, E.; Sanchez-Diaz, A.; Vidal-Ferran, A.; Palomares, E. *Eur. J. Inorg. Chem.* **2008**, *2008*, 1955–1958.

(31) Fan, S.-H.; Wang, K.-Z.; Yang, W.-C. *Eur. J. Inorg. Chem.* **2009**, *2009*, 508–518.

(32) Chen, C. Y.; Lu, H. C.; Wu, C. G.; Chen, J. G.; Ho, K. C. *Adv. Funct. Mater.* **2007**, *17*, 29–36.

(33) Yanagida, M.; Singh, L. P.; Sayama, K.; Hara, K.; Katoh, R.; Islam, A.; Sugihara, H.; Arakawa, H.; Nazeeruddin, M. K.; Grätzel, M. *Dalton Trans.* **2000**, 2817–2822.

(34) Hara, K.; Sugihara, H.; Tachibana, Y.; Islam, A.; Yanagida, M.; Sayama, K.; Arakawa, H.; Fujihashi, G.; Horiguchi, T.; Kinoshita, T. *Langmuir* **2001**, *17*, 5992–5999.

(35) Funaki, T.; Yanagida, M.; Onozawa-Komatsuzaki, N.; Kasuga, K.; Kawanishi, Y.; Kurashige, M.; Sayama, K.; Sugihara, H. *Inorga. Chem. Commun.* **2009**, *12*, 842–845.

(36) Bomben, P. G.; Robson, K. C. D.; Koivisto, B. D.; Berlinguette, C. P. *Coord. Chem. Rev.* **2012**, *256*, 1438–1450.

(37) Constable, E. C.; Housecroft, C. E. *Polyhedron* **1990**, *9*, 1939–1947.

(38) Djukic, J.-P.; Sortais, J.-B.; Barloy, L.; Pfeffer, M. *Eur. J. Inorg. Chem.* **2009**, *2009*, 817–853.

(39) Bomben, P. G.; Robson, K. C.; Sedach, P. A.; Berlinguette, C. P. *Inorg. Chem.* **2009**, *48*, 9631–43.

(40) Albrecht, M. *Chem. Rev.* **2010**, *110*, 576–623.

(41) Wadman, S. H.; Kroon, J. M.; Bakker, K.; Lutz, M.; Spek, A. L.; van Klink, G. P. M.; van Koten, G. *Chem. Commun.* **2007**, *19*, 1907.

(42) Wadman, S. H.; Kroon, J. M.; Bakker, K.; Havenith, R. W. A.; van Klink, G. P. M.; van Koten, G. *Organometallics* **2010**, *29*, 1569–1579.

(43) Bessho, T.; Yoneda, E.; Yum, J. H.; Guglielmi, M.; Tavernelli, I.; Imai, H.; Rothlisberger, U.; Nazeeruddin, M. K.; Gratzel, M. *J. Am. Chem. Soc.* **2009**, *131*, 5930–4.

(44) Bomben, P. G.; Gordon, T. J.; Schott, E.; Berlinguette, C. P. *Angew. Chem. Int. Ed.* **2011**, *50*, 10682–5.

(45) Li, C.-Y.; Su, C.; Wang, H.-H.; Kumaresan, P.; Hsu, C.-H.; Lee, I. T.; Chang, W.-C.; Tingare, Y. S.; Li, T.-Y.; Lin, C.-F.; Li, W.-R. *Dyes Pigm.* **2014**, *100*, 57–65.

(46) Aghazada, S.; Zimmermann, I.; Ren, Y.; Wang, P.; Nazeeruddin, M. K. *ChemistrySelect* **2018**, *3*, 1585–1592.

(47) Sinn, S.; Schulze, B.; Friebe, C.; Brown, D. G.; Jager, M.; Altuntas, E.; Kubel, J.; Guntner, O.; Berlinguette, C. P.; Dietzek, B.; Schubert, U. S. *Inorg. Chem.* **2014**, *53*, 2083–95.

(48) Park, H. J.; Kim, K. H.; Choi, S. Y.; Kim, H. M.; Lee, W. I.; Kang, Y. K.; Chung, Y. K. *Inorg. Chem.* **2010**, *49*, 7340–52.

(49) Bomben, P. G.; Koivisto, B. D.; Berlinguette, C. P. *Inorg. Chem.* **2010**, *49*, 4960–71.

(50) Aghazada, S.; Zimmermann, I.; Scutelnic, V.; Nazeeruddin, M. K. *Organometallics* **2017**, *36*, 2397–2403.

(51) Nguyen, T. D.; Lan, Y. P.; Wu, C. G. *Inorg. Chem.* **2018**, *57*, 1527–1534.

(52) Wood, C. J.; Cheng, M.; Clark, C. A.; Horvath, R.; Clark, I. P.; Hamilton, M. L.; Towrie, M.; George, M. W.; Sun, L.; Yang, X.; Gibson, E. A. *J. Phys. Chem. C* **2014**, *118*, 16536–16546.

(53) Nattestad, A.; Mozer, A. J.; Fischer, M. K.; Cheng, Y. B.; Mishra, A.; Bauerle, P.; Bach, U. *Nat. Mater.* **2010**, *9*, 31–5.

(54) Wood, C. J.; Summers, G. H.; Gibson, E. A. *Chem. Commun.* **2015**, *51*, 3915–3918.

(55) Ji, Z.; Natu, G.; Wu, Y. *ACS Appl. Mater. Interfaces* **2013**, *5*, 8641–8.

(56) Ji, Z.; Natu, G.; Huang, Z.; Kokhan, O.; Zhang, X.; Wu, Y. *J. Phys. Chem. C* **2012**, *116*, 16854–16863.

(57) He, M.; Ji, Z.; Huang, Z.; Wu, Y. *J. Phys. Chem. C* **2014**, *118*, 16518–16525.

(58) Ji, Z.; Wu, Y. *J. Phys. Chem. C* **2013**, *117*, 18315–18324.

(59) Brunner, F.; Marinakis, N.; Wobill, C.; Willgert, M.; Ertl, C. D.; Kosmalski, T.; Neuburger, M.; Bozic-Weber, B.; Glatzel, T.; Constable, E. C.; Housecroft, C. E. *J. Mater. Chem. C* **2016**, *4*, 9823–9833.

(60) Wood, C. J.; Robson, K. C. D.; Elliott, P. I. P.; Berlinguette, C. P.; Gibson, E. A. *RSC Adv.* **2014**, *4*, 5782.

(61) Ertl, C. D.; Ris, D. P.; Meier, S. C.; Constable, E. C.; Housecroft, C. E.; Neuburger, M.; Zampese, J. A. *Dalton Trans.* **2015**, *44*, 1557–70.

(62) Marinakis, N.; Wobill, C.; Constable, E. C.; Housecroft, C. E. *Polyhedron* **2018**, *140*, 122–128.

(63) Murali, M. G.; Wang, X.; Wang, Q.; Valiyaveettil, S. *RSC Adv.* **2016**, *6*, 57872–57879.

(64) Thathong, Y.; Traipop, K.; Sudyoadsuk, T.; Jitchati, R. *Adv. Mater. Res.* **2013**, *770*, 145–148.

(65) Kajouj, S.; Marcelis, L.; Lemaur, V.; Beljonne, D.; Moucheron, C. *Dalton Trans.* **2017**, *46*, 6623–6633.

(66) Huang, S. Y.; Schlichthörl, G.; Nozik, A. J.; Grätzel, M.; Frank, A. J. *J. Phys. Chem. B* **1997**, *101*, 2576–2582.

(67) Schlichthörl, G.; Huang, S. Y.; Sprague, J.; Frank, A. J. *J. Phys. Chem. B* **1997**, *101*, 8141–8155.

(68) Boschloo, G.; Haggman, L.; Hagfeldt, A. *J. Phys. Chem. B* **2006**, *110*, 13144–50.

(69) Grätzel, M. *J. Photochem. Photobiol. A* **2004**, *164*, 3–14.

(70) Kopidakis, N.; Neale, N. R.; Frank, A. J. *J. Phys. Chem. B* **2006**, *110*, 12485–9.

(71) Ho, P.; Thogiti, S.; Lee, Y. H.; Kim, J. H. *Sci. Rep.* **2017**, *7*, 2272.

(72) He, J.; Lindström, H.; Hagfeldt, A.; Lindquist, S. E. *Sol. Energy Mater. Sol. Cells* **2000**, *62*, 265–273.

(73) Hara, K.; Dan-oh, Y.; Kasada, C.; Ohga, Y.; Shinpo, A.; Suga, S.; Sayama, K.; Arakawa, H. *Langmuir* **2004**, *20*, 4205–4210.

(74) Yum, J. H.; Jang, S. R.; Humphry-Baker, R.; Gratzel, M.; Cid, J. J.; Torres, T.; Nazeeruddin, M. K. *Langmuir* **2008**, *24*, 5636–40.

(75) Lu, H.-P.; Tsai, C.-Y.; Yen, W.-N.; Hsieh, C.-P.; Lee, C.-W.; Yeh, C.-Y.; Diau, E. W.-G. *J. Phys. Chem. C* **2009**, *113*, 20990–20997.

(76) Yum, J. H.; Moon, S. J.; Humphry-Baker, R.; Walter, P.; Geiger, T.; Nuesch, F.; Gratzel, M.; Nazeeruddin, M. D. *Nanotechnology* **2008**, *19*, 424005.

(77) Lee, K.-M.; Suryanarayanan, V.; Ho, K.-C.; Justin Thomas, K. R.; Lin, J. T. *Sol. Energy Mater. Sol. Cells* **2007**, *91*, 1426–1431.

Chapter 7

Design and Synthesis of a Benchmark Dye for p-Type Materials

7.1 Aims

This chapter presents the synthesis and photophysical properties of a small organic dye which has been designed as a reference for screening new p-type materials. The structure and properties of the dye are influenced by results from previous chapters of this thesis, incorporating strong absorption in the visible region, a suitable anchoring group to adsorb to nickel oxide and spectroscopic handles in the infrared region for analysis.

7.2 Introduction

Contributions for Chapter 7: All synthesis and experiments were performed by the author except for density functional theory calculations which were carried out by Gareth Summers.

Despite the progress that has been made towards improving the efficiency of p-type nickel oxide dye-sensitised solar cells, with the highest power conversion efficiency recorded at 2.51 %,[1] the performances of these systems are still considerably lower than that of n-type titanium dioxide systems which have reached 14 % efficiency.[2] Some of the biggest challenges that are limiting the progress of nickel oxide dye-sensitised systems are the properties of the material itself. For example, nickel oxide has poor conductivity and slow

hole diffusion which results in fast recombination of the charge-separated state, as the holes generated in nickel oxide recombine with the dye or species in the electrolyte rather than being collected at the contact.[3–5] Also, nickel atoms in the film are responsible for an electrochromic effect which results in competition for light between the films and the sensitiser.[6] Whilst many groups have tried to overcome these limitations by changing the dye and the redox couple,[7–10] there is substantial research into alternative p-type materials to replace nickel oxide. Examples of other p-type transparent conducting oxides tested for the application of dye-sensitised solar cells include copper (II) oxide (CuO),[11–13] delafossite compounds ($CuMO_2$, M = Ga, Al, Cr, Fe, B),[14–22] and copper (I) thiocyanate (CuSCN).[23]

Similar to nickel oxide, there are a variety of dyes which have been used to sensitise alternative p-type materials, and their structures and properties are shown in Figure 7.1 and Table 7.1. Amongst the numerous dye-sensitised p-type systems, there are a few dyes which are more commonly used and can be thought of as reference dyes. For example, Coumarin 343 has been used to sensitise nickel oxide, copper chromium oxide ($CuCrO_2$) and copper iron oxide ($CuFeO_2$). The small dye has well-understood mechanisms of photoinduced charge transfer on nickel oxide,[24–26] however, it gives low photovoltaic performance (η = 0.02-0.05 %).[3,27,28] This is attributed to fast $dye^-|NiO^+$ charge-recombination and low absorption in the visible region. When Coumarin 343 was used to sensitise copper iron oxide, a high photovoltage was achieved (365 mV) but a low overall efficiency (0.01 %). Other small dyes which have been used to test the performance of alternative p-type materials include Fast Green (η = 0.011 % on copper oxide), phthalocyanines (η = 0.07-0.19 % on copper oxide) and Crystal Violet (IPCE = 25 % on copper thiocyanate).[12,13,23]

A commonly used benchmark dye is P1, discussed in Chapter 4, which generally gives high photocurrent densities on nickel oxide,[10,29–31] and has also been used to sensitise new p-type transparent conducting oxides, for example copper oxide and copper gallium oxide.[11,15] However, the performance of P1 is not consistent (J_{SC} = *ca.* 1.5 to 5.5 mA cm^{-2} on nickel oxide with an iodide/triiodide redox couple). Also, the synthesis of P1 is challenging with multiple steps involving coupling reactions, and the absorption spectrum is broad which makes interpretation of the transient absorption spectra difficult.

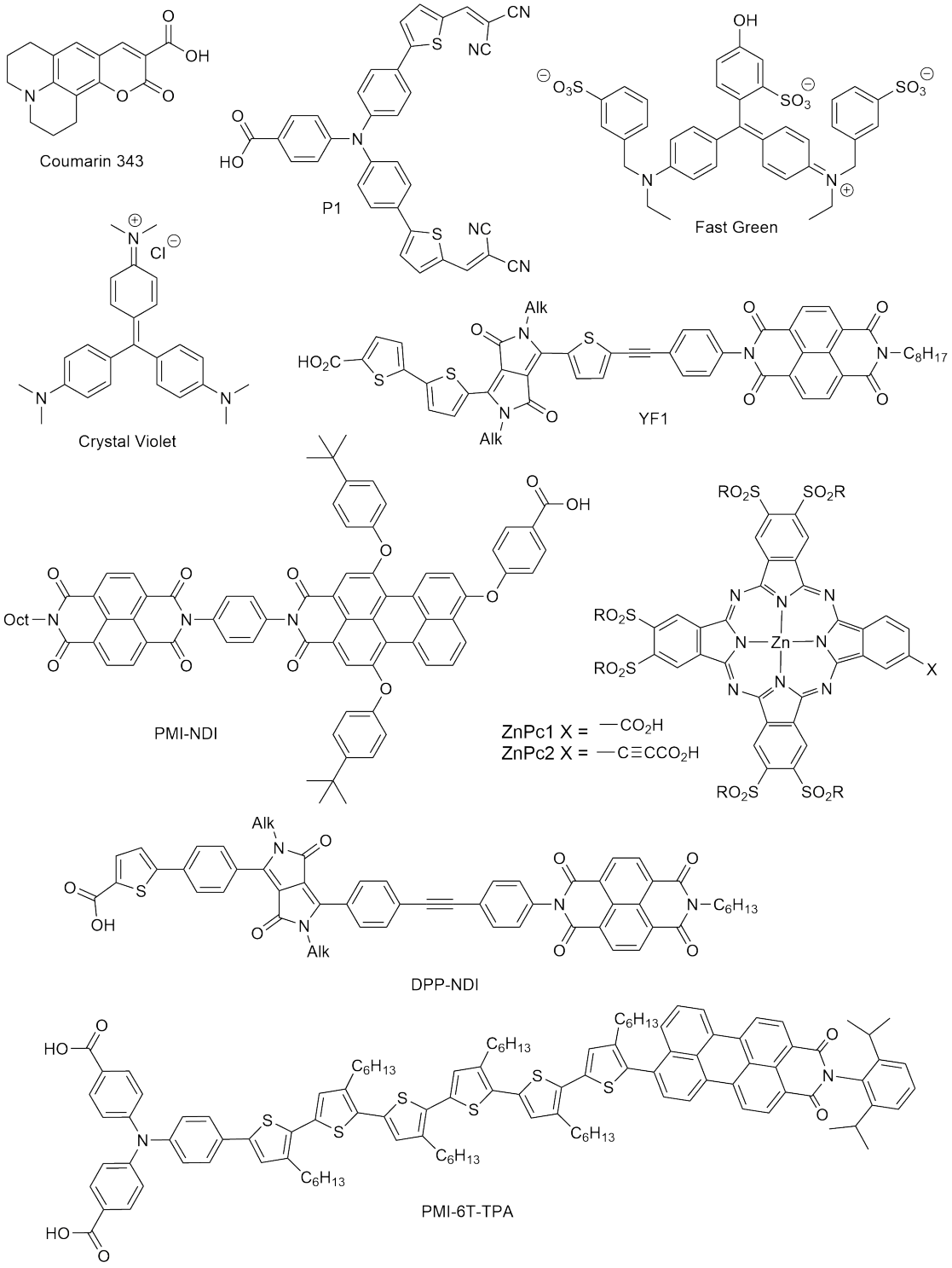

Figure 7.1: Structures of dyes used to sensitise p-type materials for dye-sensitised solar cells.

Dye	Material	Electrolyte	J_{SC} (mA cm^{-2})	V_{OC} (mV)	η (%)	IPCE (%)	Ref
Coumarin 343	NiO	I^-/I_3^-	0.55	98	0.016		[27]
	NiO	I^-/I_3^-	0.86	101	0.031		[3]
	NiO	I^-/I_3^-	1.89	71	0.05		[28]
	NiO	I^-/I_3^-	0.58	90	0.016		[20]
	$CuCrO_2$	I^-/I_3^-	0.44	82	0.014		[20]
	$CuFeO_2$	I^-/I_3^-	0.07	365	0.010		[19]
P1	NiO	I^-/I_3^-	1.52	110	0.05	18	[32]
	NiO	I^-/I_3^-	2.51	110	0.08	35	[33]
	NiO	I^-/I_3^-	5.48	84	0.15	64	[28]
	NiO	I^-/I_3^-	2.31	132	0.101	23	[34]
	NiO	I^-/I_3^-	2.88	140	0.075	36	[31]
	NiO	I^-/I_3^-	4.67	93	0.143	30	[35]
	NiO	$Co^{2+/3+}$	1.65	441	0.4	35	[36]
	CuO	I^-/I_3^-	0.77	88	0.03	4	[11]
	$CuGaO_2$	I^-/I_3^-	0.384	180	0.026		[15]
	$CuGaO_2$	$Co^{2+/3+}$	0.165	357	0.018		[15]
YF1	CuO	$Co^{2+/3+}$	0.72	316	0.97	5	[11]
Crystal Violet	CuSCN					25	[23]
ZnPc1	CuO	I^-/I_3^-	1.93	93	0.067	15	[13]
ZnPc2	CuO	$Co^{2+/3+}$	1.99	224	0.141	15	
	CuO	I^-/I_3^-	2.78	102	0.103	27	
	CuO	$Co^{2+/3+}$	2.35	251	0.191	21	
Fast Green	CuO	I^-/I_3^-	0.3	115	0.011	3	[12]
DPP-NDI	NiO	I^-/I_3^-	1.38	155	0.09	25	[37]
	NiO	$Co^{2+/3+}$	1.62	365	0.18	20	[37]
	CuO	$Co^{2+/3+}$	0.2	332	0.029	2	[11]
PMI-NDI	NiO	I^-/I_3^-	1.64	130	0.074		[16]
	NiO	$Co^{2+/3+}$	1.2	285	0.141		
	$CuGaO_2$	I^-/I_3^-	0.29	41	0.023		
	$CuGaO_2$	$Co^{2+/3+}$	0.12	375	0.0149		
PMI-6T-TPA	NiO	I^-/I_3^-	5.4	226	0.45	60	[18]
	NiO	$Co^{2+/3+}$	3.72	640	1	40	
	$CuCrO_2$	I^-/I_3^-	1.98	268	0.23	15	
	$CuCrO_2$	$Co^{2+/3+}$	1.23	734	0.48	5	

Table 7.1: Properties of benchmark dyes used to sensitise different p-type materials for dye-sensitised solar cells.

High photocurrents have been generated for p-type dye-sensitised systems with larger, more elaborate structures. Perylenemonoimide (PMI) dyes[16,18,22] and other push-pull organic dyes[15,17,38] give high efficiencies on nickel oxide, and promising performances on new p-type materials. For example PMI-6T-TPA shown in Figure 7.1 gives a power conversion efficiency of $\eta = 0.48$ % on copper chromium oxide.[18] However, these compounds are synthetically demanding and are only used by a few research groups. In general there is a need for a synthetically simple benchmark dye which is suitable for testing new p-type materials with a variety of redox couples.

In this chapter the synthesis and properties of a new benchmark dye are proposed. The dye FAB4, whose structure is shown in Figure 7.2 combines simple synthesis with favourable spectroscopic properties and push-pull character to promote charge transfer away from the surface of a p-type material.

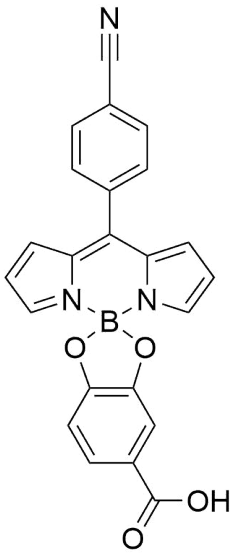

Figure 7.2: Structure of proposed benchmark dye FAB4.

FAB4 consists of a boron dipyrromethene core, which is unsubstituted at the α and β positions, similar to BOD3 and BOD5 which were discussed in Section 4.3 of Chapter 4. A phenyl group with a nitrile substituent is used as an acceptor group at the *meso* position. Different to BOD1-5, the carboxylic acid anchoring group is attached at the bodipy core via a catechol, rather than appended through the *meso* position. Bodipy sensitisers with unsubstituted α and β positions are less common for dye-sensitised solar cells, and there are only a few examples for this application which contain groups other

than fluorine atoms coordinated at the boron.[39,40] To our knowledge FAB4 is the first example of a bodipy molecule for dye-sensitised solar cells which positions the anchor group at the boron atom. The following sections outline the logic behind the design, synthesis and resulting properties of FAB4.

7.2.1 Synthesis

Benchmark dyes need to be made in large quantities with high purity. Most dyes used are based on extended structures for example P1, BOD3, BOD5 and CAD3 which were described in Chapter 4. Synthetic routes to these compounds often involve multiple steps containing coupling reactions which are generally low-yielding and give products with impurities which are difficult to remove.[30,37,41,42] However, the simple BOD1 was produced using a 'one-pot' method and gave surprisingly high performance when used as a sensitiser for nickel oxide dye-sensitised solar cells. The signal of the reduced $BOD1^-$ was weak in the transient absorption spectra, and the structure does not include any spectroscopic markers in the infrared region. We therefore chose a simple bodipy compound as the base for our benchmark dye, and included infrared handles in the structure and donor and acceptor groups to improve the solar cell performance. Boron dipyrromethene compounds can be synthesised in one or two steps and there are many reports of easy modifications at all positions of the core, including substituting the fluorine atoms.[43,44] Another advantage of small dyes like BOD1 is that they potentially give higher dye-loading on the surface, which improves the photocurrent generated by increasing light absorption and increases the photovoltage by protecting the surface. We observed an increase in the dye-loading for the small, linear dye CAD4 in Section 4.4 relative to the larger dye CAD3.[45]

Most of the bodipy dyes which have been discussed in this thesis, including BOD1, BOD2 and BOD4 from Section 4.3 and BOD_1 and BOD_2 from Chapter 5 all contain a 2,8-diethyl-1,3,7,9-tetramethyl bodipy core. The substituents around the 3-ethyl-2,4-dimethylpyrrole (kryptopyrrole) starting material prevent side reactions occurring during the bodipy synthesis as there is only one accessible reaction site. Kryptopyrrole is also less prone to polymerisation than pyrrole which leads to easier purification of the reaction products.[43,46] However, it was observed from density functional theory calculations of BOD1-5 that the dyes which contained a 2,8-diethyl-1,3,7,9-tetramethyl bodipy core had *meso* substituents

which were in a different plane to the core. For such systems there was a lower extent of electronic coupling between the triphenylamine donor and bodipy acceptor groups and as a result these dyes had a sharper, more blue-shifted absorption band. Similarly, for the bodipy-polyoxometalate hybrids $K^{W}{}_{Sn}[BOD_2]$ and $K^{Mo}{}_{Sn}[BOD_2]$, where the bodipy photosensitiser contained an alkynyl group at the *meso* position, the absorption was red-shifted relative to $K^{W}{}_{Si}[BOD_1]$, where the *meso* substituent was a phenyl group. For our benchmark dye, reported synthetic routes to bodipy compounds which include a nitrile group directly at the *meso* position involved multiple steps,[47] so a more facile synthesis was chosen in which a benzonitrile *meso* substituent was incorporated during the formation of the bodipy core. A bodipy core with unsubstituted α and β positions was chosen to promote electronic coupling between the bodipy core and the substituent at the *meso* position. The synthetic route to FAB4 consisted of three steps using commercially available starting materials, and is shown in Figure 7.3.

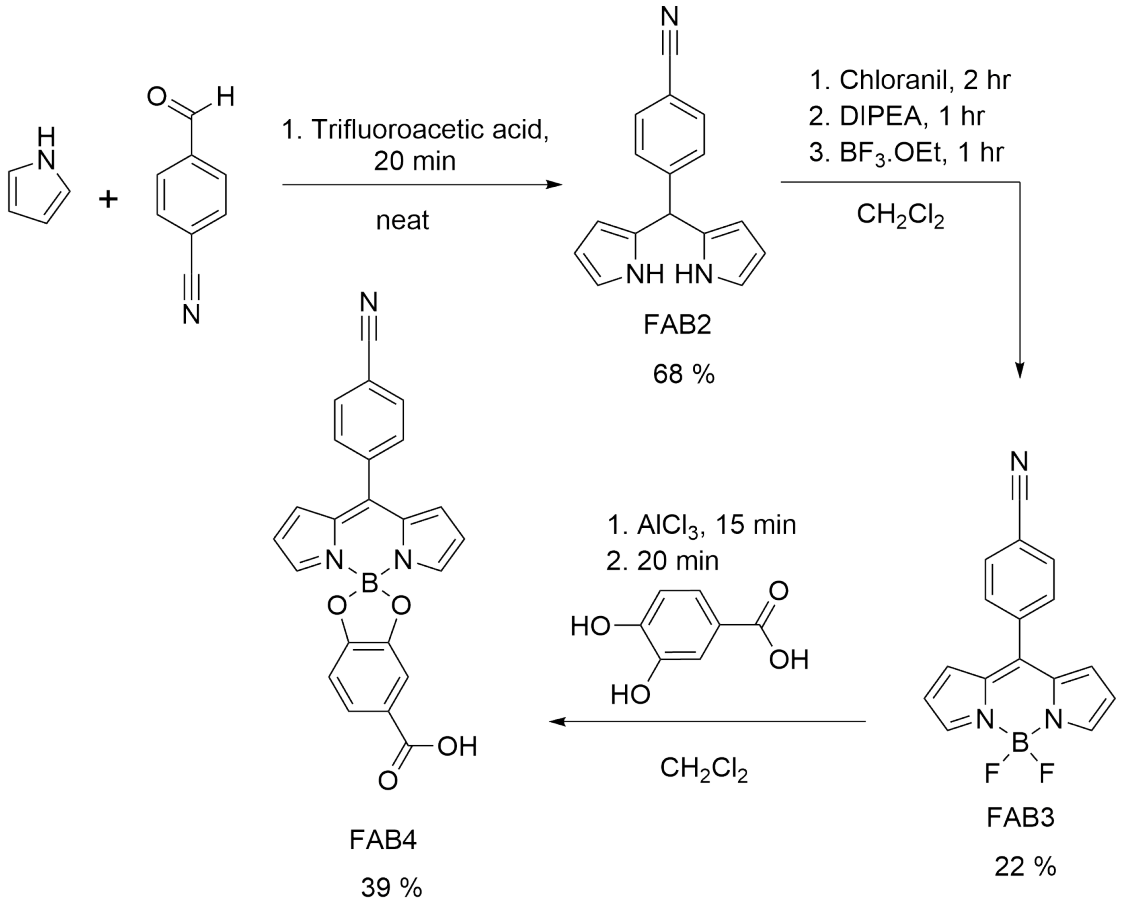

Figure 7.3: Synthetic route to FAB4, including experimental yields of each reaction step.

The coordination group (catechol) at the boron atom is likely to be the least stable part of the molecule, so this group was added in the last step of the synthesis. Zhang *et al.* reported a one-step synthesis of the bodipy FAB3,[48] however, when this synthesis method was repeated by the author, the product was difficult to purify due to a large amount of compounds in the reaction mixture. Here, a stepwise approach was used to firstly form the dipyrromethane FAB2, which was then oxidised and used to form the bodipy FAB3. The fluorine atoms were then substituted with 3,4-dihydroxybenzoic acid to form the novel compound FAB4, following a modified literature procedure.[49] Details of the synthesis are given in the Experimental chapter, Section 3.3. Briefly, FAB2 was formed in the reaction between pyrrole and 4-cyanobenzaldehye with an excess of trifluoroacetic acid at room temperature in 20 minutes. The dipyrromethane was isolated in 68 % yield, and the reaction was successful on a relatively large scale (*ca.* 1 g). The product was characterised by ^{1}H NMR and ^{13}C NMR spectroscopy, and the spectra are given in the Appendix, Figures A.6 and A.7. Small amounts of pyrrole (*ca.* 9 % from ^{1}H NMR) are present in the product, however no further purification methods were used at this stage due to the instability of the dipyrromethane in solution.

In the second step FAB2 was oxidised using tetrachloro-1,4-benzoquinone (chloranil) and coordinated using boron trifluoride diethyletherate to form the bodipy FAB3 in 22 % yield. This was the lowest-yielding step of the synthesis but the product is of high purity and easily forms crystals when the filtrate is concentrated. The ^{1}H shifts are in good agreement with those reported for this molecule in ref [48] and the full ^{1}H NMR spectrum is given in the Appendix in Figure A.8. The crystal structure of FAB3 is shown in Figure 7.4. The phenyl group is slightly out of plane from the bodipy core, but this effect is reduced relative to density functional theory calculations of BOD1, BOD2 and BOD4, where the bodipy core was generally perpendicular to the *meso* substituent.[50] This should allow good electronic communication between the bodipy core and the benzonitrile group.

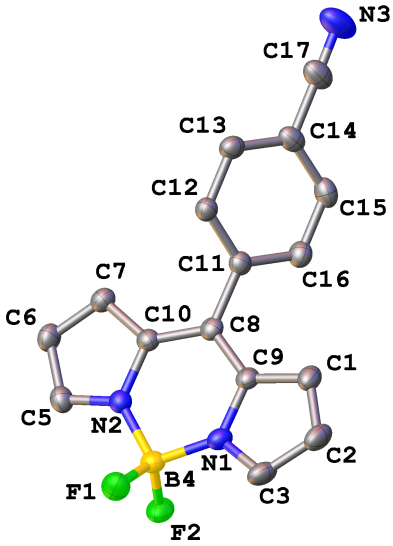

Figure 7.4: Crystal structure of FAB3. Boron, fluorine, nitrogen and carbon atoms are labelled.

FAB4 was synthesised from FAB3 using 3,4-dihydroxybenzoic acid in presence of an excess of aluminium chloride. The substitution of fluorine atoms at the boron of a bodipy by a catechol has been reported previously and a general procedure was used here.[49,51] The product was formed in 39 % yield, though the ^{1}H and ^{13}C NMR spectra, which are given in the Appendix (Figures A.11 and A.12), show that the product contains catechol impurities. The aromatic region of the ^{1}H NMR spectrum is expanded in Figure 7.5 and the colours of labelled protons relate to the correlation spectrum (COSY) in Figure 7.6. Further purification of the product was attempted but the catechol impurity was difficult to remove. It is assumed that the catechol impurities may bind to the surface of nickel oxide without contributing to light absorption, and may therefore decrease the dye loading. However, as the catechol only absorbs in the ultraviolet region, it is unlikely to compete for light absorption with FAB4. Nonetheless it would be beneficial to investigate a suitable way of purifying FAB4 to avoid unwanted effects from the catechol impurity.

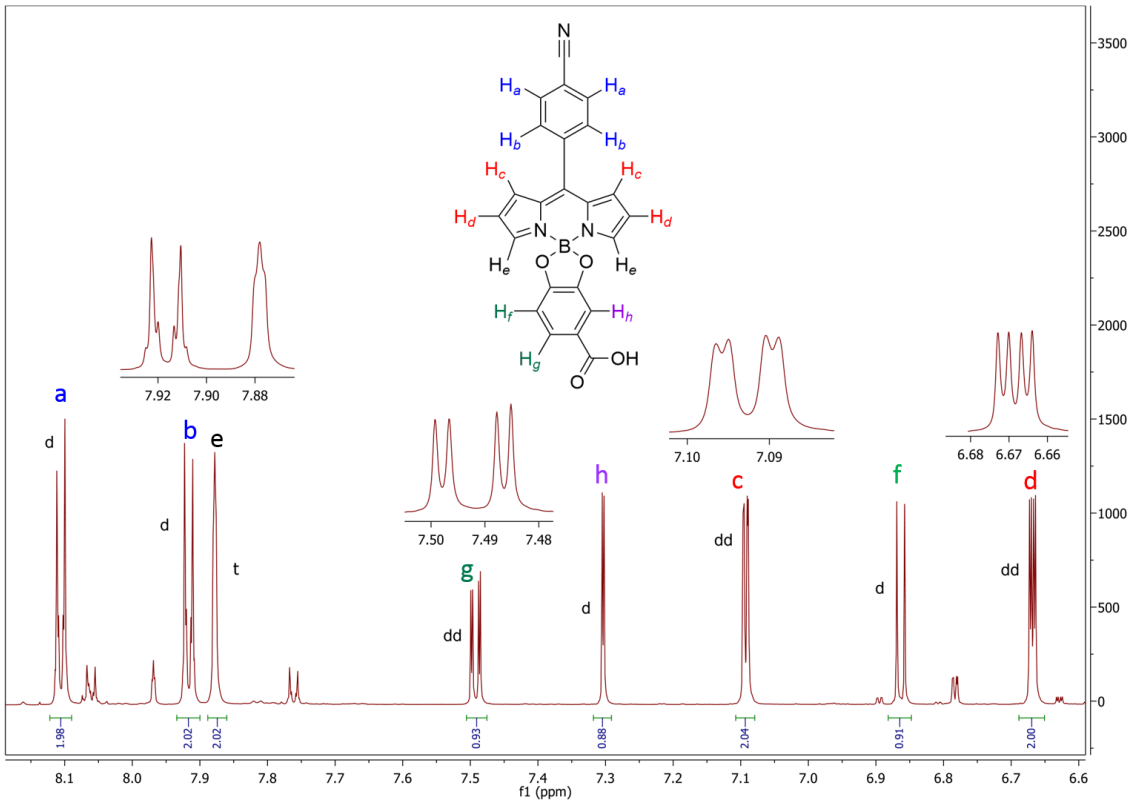

Figure 7.5: Expansion of the aromatic region of the ^{1}H NMR of FAB4.

In general, the synthesis of the new bodipy compound FAB4 was successful, with the product formed in an overall yield of 6 %. The formation of the bodipy FAB3 was the lowest-yielding step of the synthesis and future work should optimise this reaction. The synthesis contains only three steps and does not required any coupling reactions or high temperatures. Variations of FAB4 could be easily produced by using a phenyl-aldehyde with different substituents to incorporate at the *meso* position. Also, catechol compounds with various functional groups are commercially available so the anchoring unit could also be tuned. The photophysical properties and initial photovoltaic performance of FAB4 will be described in the following sections.

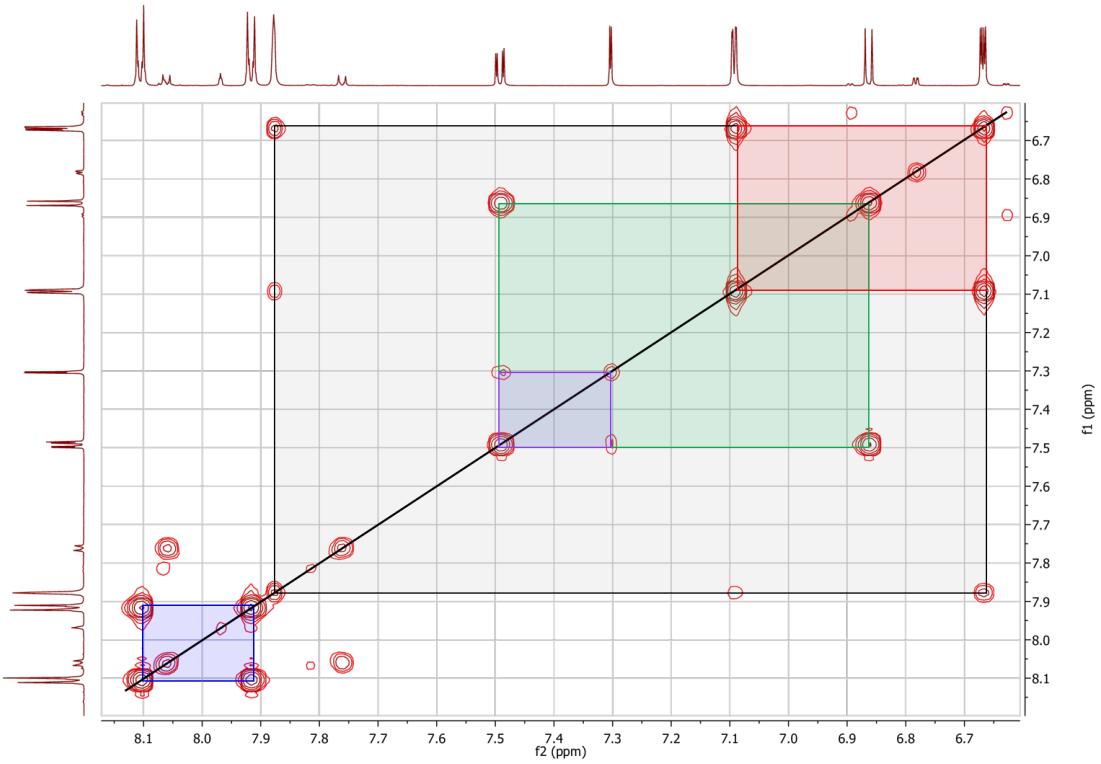

Figure 7.6: COSY spectrum of FAB4. Coloured boxes relate to coupling protons which are labelled in Figure 7.5.

7.2.2 Steady state electronic absorption

The absorption spectrum of FAB4 was recorded in dichloromethane solution together with that of FAB3 to determine the effect of the catechol group on the electronic structure. The absorption and emission spectra are shown in Figure 7.7 and the photophysical properties are detailed in Table 7.2. The shape of the absorption spectra of FAB3 and FAB4 are similar, consisting of a sharp peak with a shoulder at higher energies, which is characteristic of a bodipy S_0-S_1 absorption. A broad absorption between 300 nm and 400 nm is weaker than the main absorption band which absorbs between 450 nm and 550 nm. The absorption maximum of FAB4 is red-shifted by *ca.* 7 nm relative to FAB3, due to a small contribution from the catechol group to the π system.

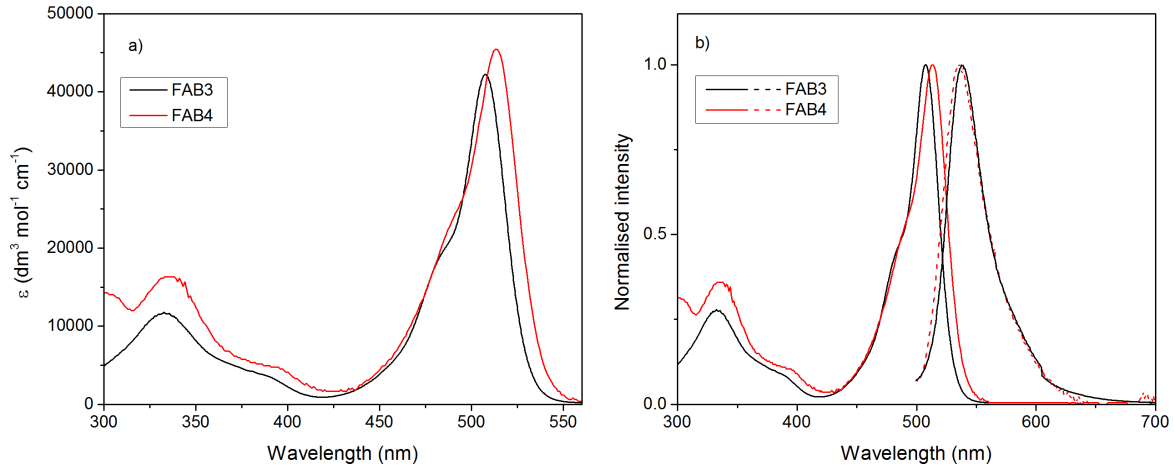

Figure 7.7: Normalised absorption (solid lines) and emission (dashed lines) of FAB3 and FAB4 in dichloromethane solution. Excitation wavelength of emission spectra = 480 nm.

	λ_{max} (nm)	λ_{em} (nm)	ε (dm^3 mol^{-1} cm^{-1})	$E_{0\text{-}0}$ (eV)	Φ_{FL}
FAB3	507	536	42 196	2.38	0.0054
FAB4	514	538	45 204	2.36	0.011

Table 7.2: Photophysical properties of FAB3 and FAB4. The wavelengths of maximum absorption (λ_{max}) and emission (λ_{em}), the absorption coefficient (ε) and fluorescence quantum yield (ϕ_L) were all determined in dichloromethane solution. $E_{0\text{-}0}$ is calculated from the wavelength of intersection between absorption and emission spectra (λ_{int}): $E_{0\text{-}0} = 1240/\lambda_{int}$.

The unsubstituted bodipy core of FAB4 was designed to maximise the contribution of the *meso* susbstituent to the π system of the bodipy, however the absorption maxima of FAB4 in dichloromethane is blue-shifted by *ca.* 14 nm relative to that of BOD1 which contains a 2,8-diethyl-1,3,7,9-tetramethyl bodipy core. This difference is attributed to the contribution of the electron-donating methyl and ethyl groups to the π system of BOD1. Red-shifting the absorption profile is an important factor for p-type dyes designed for tandem dye-sensitised solar cell applications where competition for higher-energy photons which are generally absorbed at the photonanode should be minimised. Red-absorbing p-type dyes are generally large structures, for example diketopyrrolopyrrole or the perylenemonoimide-oligothiophene-triphenylamine compound PMI-6T-TPA shown in Figure 7.1,[41,42] though our group has reported smaller dyes with red-shifted absorption profiles that generate high photocurrent densities on nickel oxide such as CAD3 and CAD4 which were discussed in Section 4.4.[45,52] The absorption maximum of FAB4

in dichloromethane is red-shifted relative to that of benchmark dyes Coumarin 343 and P1, and synthesis is considerably less complex than the red-absorbing dyes mentioned above. The molar absorption coefficient of FAB4 is similar to that of BOD1 (ε BOD1 = 52 000 dm^3 mol^{-1} cm^{-1}). The HOMO-LUMO energies of FAB4 could be further tuned by functionalisation at the α and β positions of the core.

FAB4 is significantly less emissive in acetonitrile and the molar absorption coefficients of FAB3 and FAB4 is reduced relative to in dichloromethane, shown in Figure 7.8. This suggests that the charge-transfer excited state is stabilised in the more polar solvent, which is consistent with the slight blue-shift observed in acetonitrile.

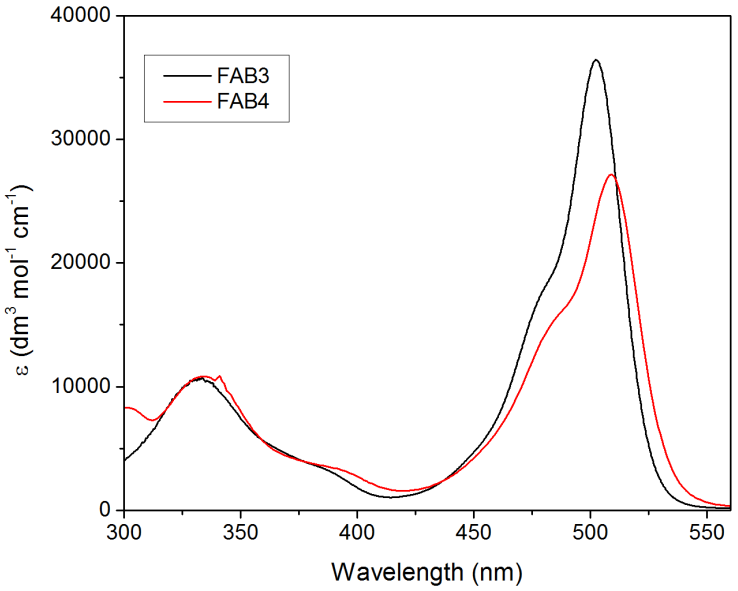

Figure 7.8: Absorption spectra of FAB3 and FAB4 in acetonitrile solution.

In the previously-reported transient absorption spectra of BOD2, a sharp signal corresponding to a bodipy-centered triplet excited state was observed,[53] and in Chapter 5 a distinctive signal was observed for an oxidised BOD^+ in the bodipy-polyoxometalate hybrid molecules. The sharp absorption of FAB4 should therefore be a suitable spectroscopic marker in the visible region.

7.2.3 Steady state vibrational absorption

The majority of the structures that have been investigated in this thesis are aromatic systems and contain many vibrational bands in the fingerprint region.

However we were able to characterise the vibrational spectrum of a bodipy-localised triplet excited state using time-resolved infrared spectroscopy in Section 4.5, and this was also observed for bodipy-polyoxometalate hybrid molecules in Chapter 5. The time-resolved infrared spectra of P1 contained a transient signal corresponding to the ν(CN) of the malononitrile acceptor groups, but multiple bands were present in this region due to different conformers. For our benchmark dye FAB4 we have incorporated a nitrile acceptor group as a spectroscopic handle in the infrared region, in a simple structure which should produce less complex spectra. The ground state infrared spectra of FAB3 and FAB4 are shown in Figure 7.9 and frequencies of major bands are listed in Table 7.3.

The ground state infrared spectra of FAB3 and FAB4 contain similar bands in the fingerprint region. Two bands at 1566 cm^{-1} to 1540 cm^{-1} and 1413 cm^{-1} to 1388 cm^{-1} are similar to those observed in the infrared spectra of P1, BOD2, $K^{W}{}_{Si}[BOD_1]$, $K^{W}{}_{Sn}[BOD_2]$ and $K^{Mo}{}_{Sn}[BOD_2]$ which were attributed to the ν(C=C) of phenyl vibrations. For FAB3 and FAB4 these bands are due to ν(C=C) on the benzonitrile substituent at the *meso* position of the bodipy. For both dyes a band in the nitrile region is present, at 2233 cm^{-1} for FAB3 and 2231 cm^{-1} for FAB4. The ν(CN) band is similar in shape to that observed in the ground state infrared spectrum of P1 at a similar frequency. The infrared spectrum of FAB4 contains a sharp vibration at 1673 cm^{-1} which is attributed to the ν(C=O) of the carbonyl group on the catechol acceptor. In general, FAB4 contains infrared markers on the anchor (ν(C=O)), the bodipy core (ν(C=C)) and the acceptor (ν(CN)) which can be monitored using time-resolved infrared spectroscopy.

	Wavenumber, cm^{-1}
FAB3	2233, 1566, 1540, 1413, 1388
FAB4	2231, 1673, 1568, 1541, 1413, 1386

Table 7.3: Major bands in the ground state infrared spectra of FAB3 and FAB4, relating to the spectra shown in Figure 7.9.

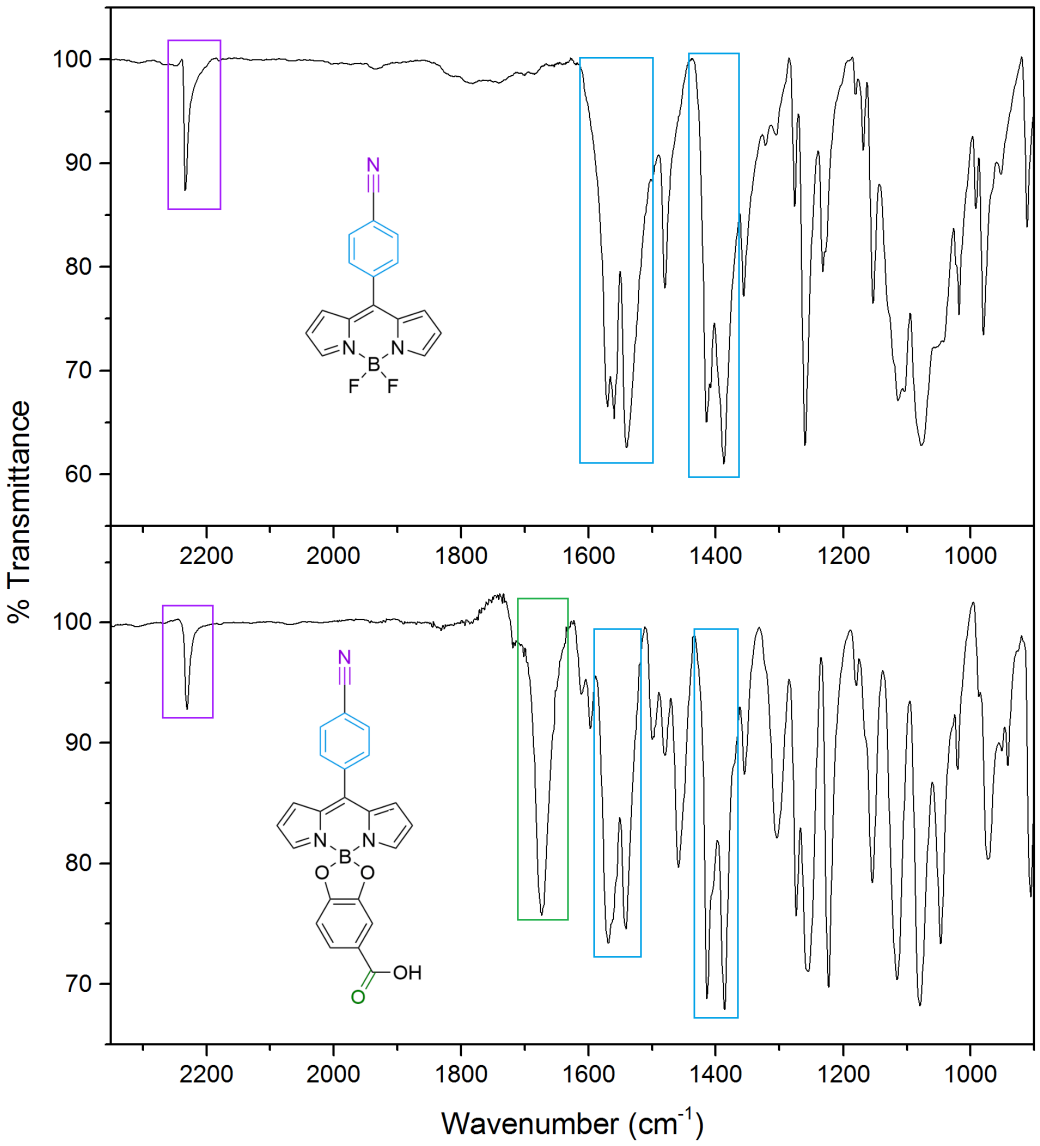

Figure 7.9: Ground state infrared spectra of FAB3 (top) and FAB4 (bottom). Coloured boxes highlight bands relating to nitrile (purple), carbonyl (green) and phenyl (blue) vibrations. Infrared spectra were taken of powders crushed and pressed into potassium bromide disks.

7.2.4 Donor-acceptor character

Reducing the rate of dye$^-$|p-SC$^+$ charge-recombination and increasing the lifetime of the charge-separated state can be achieved by using dyes with long bridges between donor and acceptor groups, giving charge-separated state lifetimes up to hundreds of microseconds on nickel oxide.[54] The longest-lived dye$^-$|NiO$^+$ system in the work presented in this thesis is for the push-pull dye BOD2 which was discussed in Section 4.5, τ = *ca.* 180 ns.[53,55] For efficient donor-acceptor character in push-pull dyes such as BOD2, the LUMO of the

dye should be localised at the acceptor group and the HOMO should be localised at the donor. However, it has been reported for bodipy systems that the HOMO level of the bodipy core is localised on the bodipy pyrroles, and the LUMO is localised at the *meso* position,[56–61] which is towards the donor group in the case of BOD1-5.

For our benchmark dye FAB4, the anchor group is situated at the bodipy core and the nitrile acceptor group is positioned at the *meso* position, which was anticipated to efficiently direct charge away from the surface when FAB4 is anchored to a p-type semiconductor. When a catechol group is coordinated to the boron atom this does not greatly affect the position of the HOMO and LUMO orbitals on the bodipy core, as shown in a study by Richards *et al.*[62] The HOMO-LUMO orbitals of FAB4 were calculated by Gareth Summers using density functional theory, together with BOD1 for comparison, and are shown in Figure 7.10. For BOD1 the HOMO level is localised on the bodipy pyrroles, which is consistent with the studies mentioned above. For FAB4 the HOMO is localised at the catechol anchor unit and the LUMO is at the nitrile acceptor group.

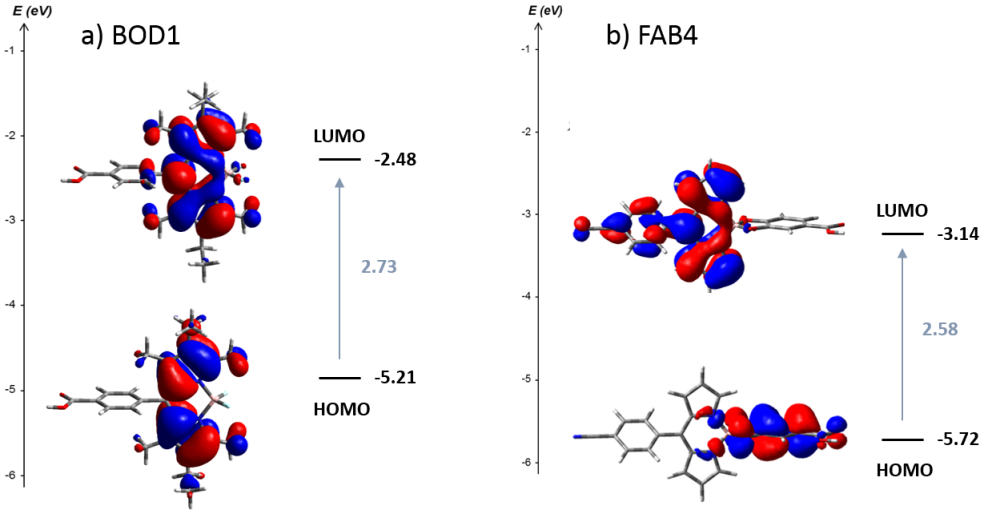

Figure 7.10: Calculated energy level diagrams of BOD1 and FAB4 using B3LYP/6-31G(d).

Figure 7.11 shows the HOMO-1 and HOMO-2 levels calculated by time-dependent density functional theory. The HOMO-2 level is localised on the catechol, but the HOMO-1 level is localised on the bodipy pyrroles, similar to BOD1. This suggests that the charge in FAB4 should be successfully directed from the bodipy core towards the nitrile acceptor group upon excitation. A summary of the main electronic transitions is given in the Appendix in Table A.10. The calculated $E_{0\text{-}0}$ of FAB4 is 2.89 eV (430 nm) which is lower

than that recorded experimentally in solution (2.41 eV, 514 nm).

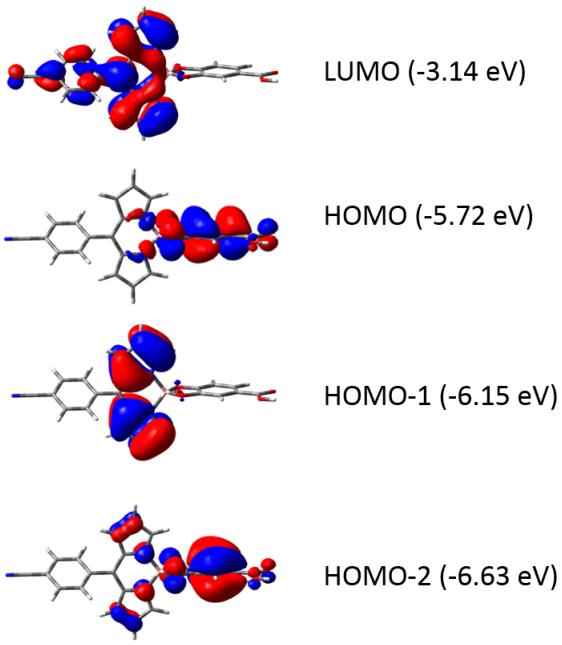

Figure 7.11: Calculated energy levels FAB4 using B3LYP/6-31G(d). Performed by Gareth Summers.

7.2.5 Electrochemistry

The electrochemical properties of FAB4 were measured in dichloromethane to determine the driving forces for charge-injection and dye-regeneration, ΔG_{inj} and ΔG_{reg} respectively. A three electrode setup was used with a glassy carbon working electrode, a platinum wire counter electrode and a silver/silver^{+} reference electrode which consisted of a silver wire immersed in a solution of supporting electrolyte containing silver nitrate, which was separated from the sample in solution by a Vycor glass frit. The supporting electrolyte was 0.2 M tetrabutylammonium hexafluorophosphate. To calibrate the electrodes ferrocene was added to the solution and the potential of ferrocene/ferrocinium was determined using cyclic voltammetry. Cyclic voltammograms and differential pulse voltammograms of FAB4 are shown in Figure 7.12.

The first reduction of FAB4 is a quasi-reversible process, ΔE_p = 0.08 V, and occurs at -1.03 V vs ferrocene/ferrocenium. The electrochemical data is tabulated in Table 7.4 along with that of BOD1 for comparison. The values of ΔG_{inj} and ΔG_{reg} for BOD1 were calculated by methods discussed in Section 4.3.

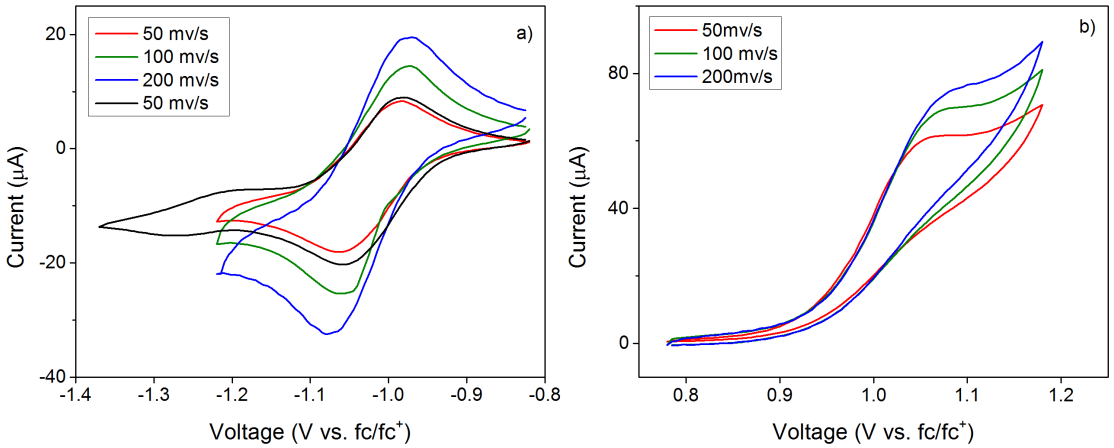

Figure 7.12: Cyclic voltammograms of 1 mM FAB4 dichloromethane, with 0.2 M $TBAPF_6$. A glassy carbon working electrode, platinum wire counter electrode and Ag/Ag^+ reference electrode were used. a) Reduction; b) oxidation.

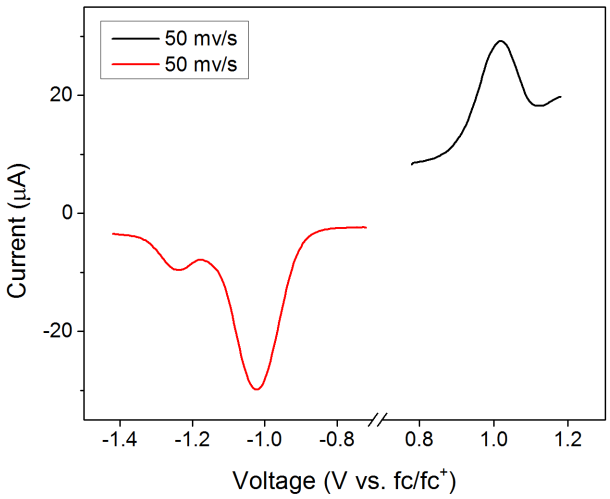

Figure 7.13: Differential pulse voltammograms showing the electrochemical reduction and oxidation of 1 mM FAB4 in dichloromethane, with 0.2 M $TBAPF_6$. A glassy carbon working electrode, platinum wire counter electrode and Ag/Ag^+ reference electrode were used.

The first reduction and first oxidation processes of FAB4 occur at a more positive potential than BOD1 by *ca* 0.5 V. As a result, ΔG_{inj} is very large for FAB4 and ΔG_{reg} is smaller than BOD1 for regeneration with an iodide/triiodide redox couple. These results show that there is sufficient driving force for charge-injection by nickel oxide and dye-regeneration by an iodide/triiodide redox couple for FAB4.

	D^+/D	D/D^-	D^*/D^-	ΔG_{inj}	ΔG_{reg}
	(V vs fc/fc^+)			(eV)	(eV)
FAB4	1.02	- 1.03	1.33	-1.45	-0.21
BOD1[a]	0.64	-1.63	0.68	-0.80	-0.81

Table 7.4: Electrochemical properties of FAB4 and BOD1 in dichloromethane solution. [a]Values taken from ref [50]. D^+/D and D/D^- were determined from differential pulse voltammograms. $D^*/D^- = (D/D^-) + E_{0\text{-}0}$. $\Delta G_{inj} = E(NiO_{VB})$ - D^*/D^-; $\Delta G_{reg} = D/D^-$ - $E(I_3^-/I_2^{-\cdot})$, where $E(NiO_{VB})$ = -0.12 V vs fc/fc^+ and $E(I_3^-/I_2^{-\cdot})$ = -0.82 V vs fc/fc^+.

7.3 Spectroelectrochemistry

Spectroelectrochemical analysis of FAB4 was performed in both visible and infrared regions, to determine the spectra of the oxidised and reduced forms of the dye. A solution of FAB4 with tetrabutylammonium perchlorate supporting electrolyte was added to an OTTLE cell positioned in the path of spectrometer, using methods described in the Experimental Section 3.5. The cell was connected to a potentiostat and the difference spectra were recorded as an oxidising or reducing potential was held. The spectra of $FAB4^-$ and $FAB4^+$ in dichloromethane in the visible region are shown in Figure 7.14.

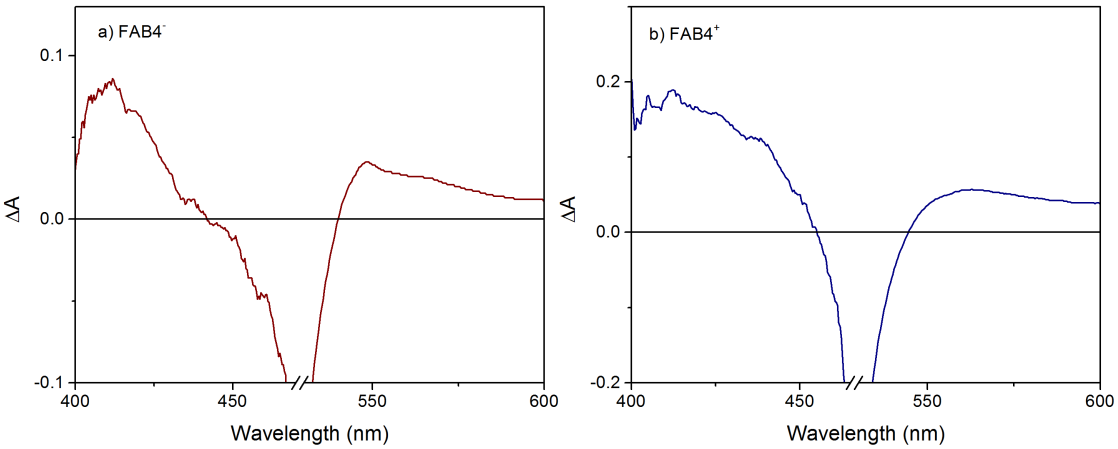

Figure 7.14: Absorbance difference spectra in the visible region of 1 mM FAB4 in dichloromethane with 0.1 M $TBAClO_4$, as a reducing or oxidising potential was applied electrochemically. a) -1.1 V vs Ag/Ag^+; b) 1.2 V vs Ag/Ag^+.

The spectrum of FAB4$^-$ contains sharper peaks than FAB4$^+$, and in general the spectra resemble that of BOD5$^-$ and BOD5$^+$ which can be found in ref [50]. Compared to spectroelectrochemical analysis of BOD_1 and BOD_2, Figure 5.13, the spectra of FAB4 are broader.

For spectroelectrochemical analysis in the infrared region, deuterated chloroform was used as this gave the fewest bands in the measured region (2500 cm^{-1} to 1000 cm^{-1}). The experimental setup was the same as for spectroelectrochemistry in the visible region, except the OTTLE cell was placed in the path of an infrared spectrometer and a higher concentration of FAB4 was used to increase the signal size. The infrared bands for FAB4$^+$ are weaker than FAB4$^-$. When FAB4 is electrochemically reduced, a band at 2200 cm^{-1} grows and is attributed to the ν(CN) of the acceptor group. A sharp negative band at 1600 cm^{-1} also grows and resembles the ground state infrared spectrum of the ν(C=O) of the anchoring group. Upon oxidation of FAB4, the negative signal of the carbonyl group is not present, but a broad vibration at 1800 cm^{-1} to 1700 $^{-1}$ grows. The band at 2200 cm^{-1} is also absent and instead a band at 2000 cm^{-1} grows. These results show that FAB4 has distinctive spectra in both the reduced and oxidised form in the visible and infrared regions, which makes it suitable for time-resolved spectroscopy and spectroscopic analysis when adsorbed on a semiconductor film.

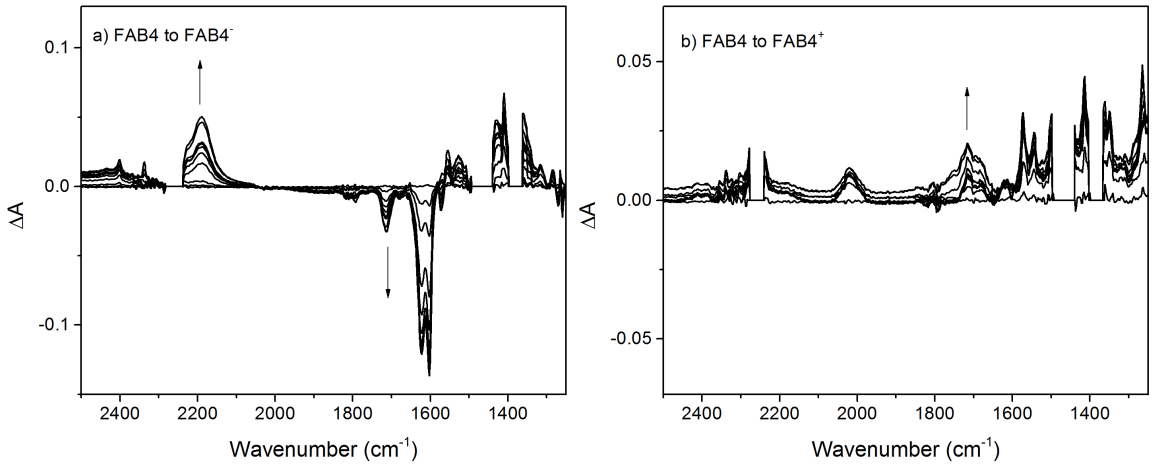

Figure 7.15: Absorbance difference spectra in the infrared region of 5 mM FAB4 in deuterated chloroform with 0.1 M TBAClO_4, as a reducing or oxidising potential was applied electrochemically. a) -1.1 V vs Ag/Ag$^+$; b) 1.2 V vs Ag/Ag$^+$. Signals due to the solvent have been set to zero.

7.4 Dye-sensitised solar cells

Nickel oxide dye-sensitised solar cells were fabricated with FAB4 to assess the photovoltaic performance of our benchmark dye. Nickel oxide films on conductive FTO glass were prepared and sensitised as described in the Experimental Section 3.2. The films were sensitised in dye baths containing 0.3 mM FAB4 in either dichloromethane or acetonitrile solution. Sensitised films were sandwiched to a platinised counter electrode and the cells were filled with an iodide/triiodide redox couple consisting of 0.1 M iodine and 1.0 M lithium iodide in acetonitrile. Current-voltage curves were used to determine the short-circuit photocurrent density (J_{SC}), open-circuit voltage (V_{OC}) and overall power conversion efficiency (η) of the devices. Incident photon-to-current conversion efficiency (IPCE) plots were recorded for wavelengths between 300 nm and 700 nm to determine the internal quantum efficiency of the device. The photovoltaic properties are detailed in Table 7.5 and the current-voltage curves and IPCE plots are shown in Figure 7.16. Dye-sensitised solar cells fabricated with P1 were also fabricated to check the consistency of the fabrication testing methods, and the photovoltaic properties of BOD1 are included in Table 7.5 for comparison.

	Dye bath	Voc (mV)	Jsc (mA cm^{-2})	FF (%)	η (%)	IPCE (%)	APCE (%)
P1	MeCN	106	3.15	35.3	0.115	43	45
FAB4	MeCN	68	0.28	33.2	0.006	8	13
	CH_2Cl_2	98	0.42	33.2	0.014	13	19
[a]BOD1	MeCN	95	1.48	36.0	0.05	20	27

Table 7.5: Photovoltaic performance of FAB4, P1 and BOD1 nickel oxide dye-sensitised solar cells, with an electrolyte containing 0.1 M I_2 and 1.0 M LiI in acetonitrile. APCE = IPCE/LHE; LHE = 1 - 10^{-A}. [a]Taken from ref [50]. On average three cells were fabricated for each condition, and a representative cell is given here.

The absorbance spectra of FAB4 and P1 adsorbed onto nickel oxide films are shown in Figure 7.16. On nickel oxide, P1 absorbs broadly from 400 nm to 600 nm. FAB4 absorbs more sharply between 450 nm and 550 nm, which is consistent with the absorption profiles in solution.[29] The absorbance of P1|NiO films is also higher than that of FAB4|NiO.

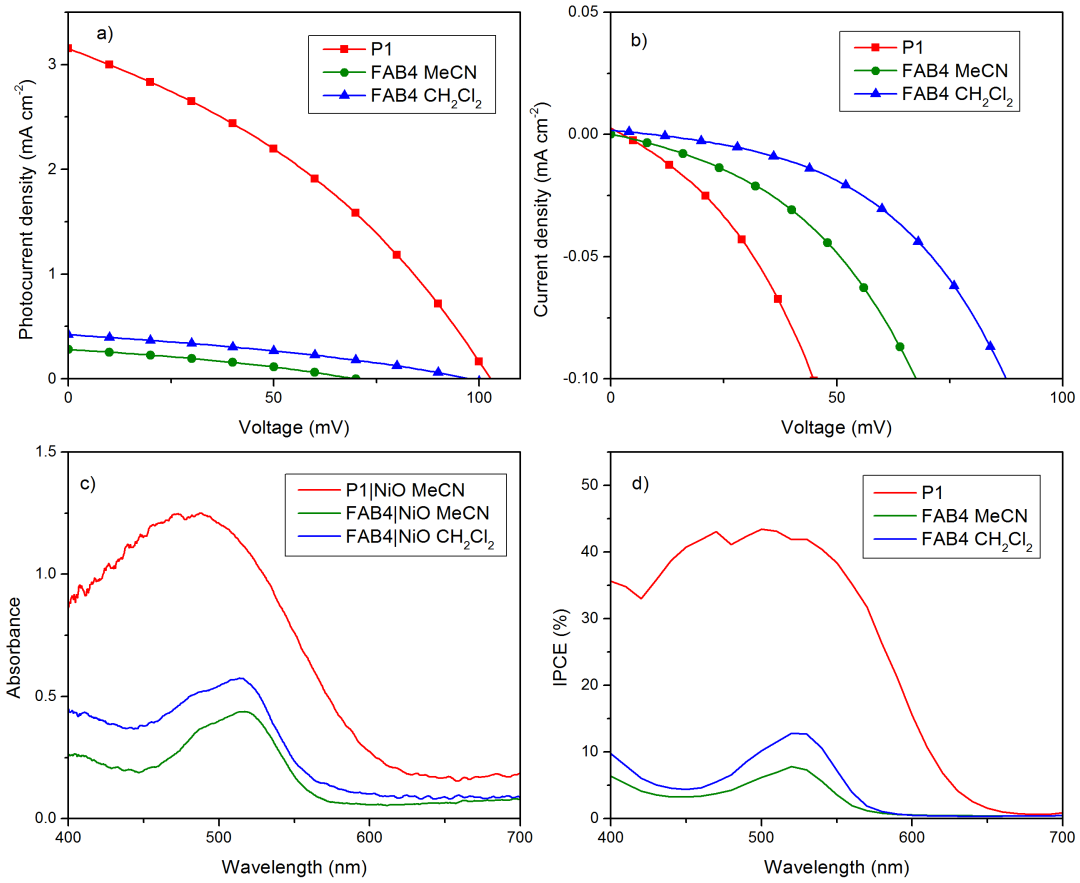

Figure 7.16: Photovoltaic properties of FAB4 and P1. a) Current-voltage curves under AM 1.5 1 sun illumination; b) current-voltage curves in the dark; c) absorbance spectra on NiO; d) incident photon-to-current conversion spectra.

For FAB4, films which were sensitised in dichloromethane dye baths performed better than those in acetonitrile dye baths. The best performing FAB4 cell achieved an open-circuit voltage of 98 mV, which is typical of a nickel oxide solar cell and is similar to the photovoltage values achieved for bodipy dyes BOD1-5 in Section 4.3 (95 mV to 109 mV). The photocurrent density values achieved by FAB4 were low, despite a promising IPCE value of 13 %, which is likely due to the narrow absorption of FAB4 and low absorbance of FAB4 on nickel oxide. The photocurrent generated was surprisingly lower than BOD1. We attribute the low performance of FAB4 to the position of the HOMO orbital in the principle energy transition, which does not include the catechol anchor group. Therefore the anchor is decoupled from the nickel oxide surface, which may hinder charge-injection. However, FAB4 does generate measureable photocurrent between 450 nm and 550 nm, so is still potentially useful as an easy-to-produce dye for testing new p-type materials.

7.5 Conclusions

This chapter examined the desirable properties of benchmark dyes for p-type materials, and presented the synthesis of the small push-pull dye FAB4 which is the first example of a bodipy for dye-sensitised solar cells to include an anchoring group coordinated at the boron atom. Preliminary photophysical, electrochemical and photovoltaic properties of FAB4 revealed that this new dye has infrared markers on the anchor and acceptor groups, strong absorption in the visible region and sufficient driving force for charge-injection to nickel oxide. Density functional theory calculations of this dye showed effective donor-acceptor character as the primary electronic transition involves the direction of charge away from the anchoring group. However, the anchor group is not involved in this transition. Although the photocurrent density values of FAB4-sensitised solar cells were low in these initial studies, a promising IPCE of 13 % was achieved with an iodide/triiodide electrolyte and dichloromethane dye bath.

The structure of the dye allows further tuning, for example the conjugation could be extended at the α and β positions without affecting the rotation of the benzonitrile acceptor group at the *meso* position and alternative anchoring units could be coordinated by using catechols with different functional groups in the final step of the synthesis. Transient absorption and time-resolved infrared studies should be performed on this dye to determine the excited state dynamics.

References

(1) Perera, I. R.; Daeneke, T.; Makuta, S.; Yu, Z.; Tachibana, Y.; Mishra, A.; Bauerle, P.; Ohlin, C. A.; Bach, U.; Spiccia, L. *Angew. Chem. Int. Ed.* **2015**, *54*, 3758–62.

(2) Kakiage, K.; Aoyama, Y.; Yano, T.; Oya, K.; Fujisawa, J.; Hanaya, M. *Chem. Commun.* **2015**, *51*, 15894–7.

(3) Mori, S.; Fukuda, S.; Sumikura, S.; Takeda, Y.; Tamaki, Y.; Suzuki, E.; Abe, T. *J. Phys. Chem. C* **2008**, *112*, 16134–16139.

(4) Zhu, H.; Hagfeldt, A.; Boschloo, G. *J. Phys. Chem. C* **2007**, *111*, 17455–17458.

(5) D'Amario, L.; Jiang, R.; Cappel, U. B.; Gibson, E. A.; Boschloo, G.; Rensmo, H.; Sun, L.; Hammarstrom, L.; Tian, H. *ACS Appl. Mater. Interfaces* **2017**, *9*, 33470–33477.

(6) Boschloo, G.; Hagfeldt, A. *J. Phys. Chem. B* **2001**, *105*, 3039–3044.

(7) Gibson, E. A. *Chem. Soc. Rev.* **2017**, *46*, 6194–6209.

(8) Nikolaou, V.; Charisiadis, A.; Charalambidis, G.; Coutsolelos, A. G.; Odobel, F. *J. Mater. Chem. A* **2017**, *5*, 21077–21113.

(9) Nattestad, A.; Perera, I.; Spiccia, L. *J. Photochem. Photobiol. C* **2016**, *28*, 44–71.

(10) Odobel, F.; Pellegrin, Y.; Gibson, E. A.; Hagfeldt, A.; Smeigh, A. L.; Hammarström, L. *Coord. Chem. Rev.* **2012**, *256*, 414–2423.

(11) Jiang, T.; Bujoli-Doeuff, M.; Farré, Y.; Pellegrin, Y.; Gautron, E.; Boujtita, M.; Cario, L.; Jobic, S.; Odobel, F. *RSC Adv.* **2016**, *6*, 112765–112770.

(12) Sumikura, S.; Mori, S.; Shimizu, S.; Usami, H.; Suzuki, E. *J. Photochem. Photobiol. A* **2008**, *194*, 143–147.

(13) Langmar, O.; Ganivet, C. R.; Lennert, A.; Costa, R. D.; de la Torre, G.; Torres, T.; Guldi, D. M. *Angew. Chem. Int. Ed.* **2015**, *54*, 7688–92.

(14) Yu, M.; Draskovic, T. I.; Wu, Y. *Phys. Chem. Chem. Phys.* **2014**, *16*, 5026–33.

(15) Yu, M.; Natu, G.; Ji, Z.; Wu, Y. *J. Phys. Chem. Lett.* **2012**, *3*, 1074–1078.

(16) Renaud, A.; Chavillon, B.; Le Pleux, L.; Pellegrin, Y.; Blart, E.; Boujtita, M.; Pauporté, T.; Cario, L.; Jobic, S.; Odobel, F. *J. Mater. Chem.* **2012**, *22*, 14353.

(17) Ahmed, J.; Blakely, C. K.; Prakash, J.; Bruno, S. R.; Yu, M.; Wu, Y.; Poltavets, V. V. *J. Alloys Compd.* **2014**, *591*, 275–279.

(18) Powar, S.; Xiong, D.; Daeneke, T.; Ma, M. T.; Gupta, A.; Lee, G.; Makuta, S.; Tachibana, Y.; Chen, W.; Spiccia, L.; Cheng, Y.-B.; Götz, G.; Bäuerle, P.; Bach, U. *J. Phys. Chem. C* **2014**, *118*, 16375–16379.

(19) Zhu, T.; Deng, Z.; Fang, X.; Huo, Z.; Wang, S.; Dong, W.; Shao, J.; Tao, R.; Song, C.; Wang, L. *J. Alloys Compd.* **2016**, *685*, 836–840.

(20) Xiong, D.; Xu, Z.; Zeng, X.; Zhang, W.; Chen, W.; Xu, X.; Wang, M.; Cheng, Y.-B. *J. Mater. Chem.* **2012**, *22*, 24760.

(21) Nattestad, A.; Zhang, X.; Bach, U.; Cheng, Y. *J. Photon. Energy* **2011**, *1*, 011103–1.

(22) Jiang, T.; Bujoli-Doeuff, M.; Farré, Y.; Blart, E.; Pellegrin, Y.; Gautron, E.; Boujtita, M.; Cario, L.; Odobel, F.; Jobic, S. *RSC Adv.* **2016**, *6*, 1549–1553.

(23) Fernando, C. A. N.; Kumarawadu, I.; Takahashi, K.; Kitagawa, A.; Suzuki, M. *Sol. Energy Mater. Sol. Cells* **1999**, *58*, 337–347.

(24) Mizoguchi, Y.; Fujihara, S. *Electrochem. Solid State Lett.* **2008**, *11*, K78–K80.

(25) Morandeira, A.; Boschloo, G.; Hagfeldt, A.; Hammarstrom, L. *J. Phys. Chem. B* **2005**, *109*, 19403–10.

(26) Morandeira, A.; Boschloo, G.; Hagfeldt, A.; Hammarström, L. *J. Phys. Chem. C* **2008**, *112*, 9530–9537.

(27) Nattestad, A.; Ferguson, M.; Kerr, R.; Cheng, Y. B.; Bach, U. *Nanotechnology* **2008**, *19*, 295304.

(28) Li, L.; Gibson, E. A.; Qin, P.; Boschloo, G.; Gorlov, M.; Hagfeldt, A.; Sun, L. *Adv. Mater.* **2010**, *22*, 1759–62.

(29) Qin, P.; Wiberg, J.; Gibson, E. A.; Linder, M.; Li, L.; Brinck, T.; Hagfeldt, A.; Albinsson, B.; Sun, L. *J. Phys. Chem. C* **2010**, *114*, 4738–4748.

(30) Wood, C. J.; Summers, G. H.; Gibson, E. A. *Chem. Commun.* **2015**, *51*, 3915–3918.

(31) Chang, C. H.; Chen, Y. C.; Hsu, C. Y.; Chou, H. H.; Lin, J. T. *Org. Lett.* **2012**, *14*, 4726–9.

(32) Qin, P.; Zhu, H.; Edvinsson, T.; Boschloo, G.; Hagfeldt, A.; Sun, L. *J. Am. Chem. Soc.* **2008**, *130*, 8570–1.

(33) Qin, P.; Linder, M.; Brinck, T.; Boschloo, G.; Hagfeldt, A.; Sun, L. *Adv. Mater.* **2009**, *21*, 2993–2996.

(34) Yen, Y. S.; Chen, W. T.; Hsu, C. Y.; Chou, H. H.; Lin, J. T.; Yeh, M. C. *Org. Lett.* **2011**, *13*, 4930–3.

(35) Jin, B.; Wu, W.; Zhang, X.; Guo, F.; Zhang, Q.; Hua, J. *Chem. Lett.* **2013**, *42*, 1271–1272.

(36) Liu, H.; Xiang, W.; Tao, H. *J. Photochem. Photobiol. A* **2017**, *344*, 199–205.

(37) Favereau, L.; Warnan, J.; Pellegrin, Y.; Blart, E.; Boujtita, M.; Jacquemin, D.; Odobel, F. *Chem. Commun.* **2013**, *49*, 8018–20.

(38) Xu, Z.; Xiong, D.; Wang, H.; Zhang, W.; Zeng, X.; Ming, L.; Chen, W.; Xu, X.; Cui, J.; Wang, M.; Powar, S.; Bach, U.; Cheng, Y.-B. *J. Mater. Chem. A* **2014**, *2*, 2968.

(39) Kumaresan, D.; Thummel, R. P.; Bura, T.; Ulrich, G.; Ziessel, R. *Chem. Eur. J.* **2009**, *15*, 6335–6339.

(40) Singh S. P.; Gayathri, T. *Eur. J. Org. Chem.* **2014**, *22*, 4689–4707.

(41) Farre, Y.; Raissi, M.; Fihey, A.; Pellegrin, Y.; Blart, E.; Jacquemin, D.; Odobel, F. *ChemSusChem* **2017**, *10*, 2618–2625.

(42) Nattestad, A.; Mozer, A. J.; Fischer, M. K.; Cheng, Y. B.; Mishra, A.; Bauerle, P.; Bach, U. *Nat. Mater.* **2010**, *9*, 31–5.

(43) Loudet, A.; Burgess, K. *Chem. Rev.* **2007**.

(44) Bessette, A.; Hanan, G. S. *Chem. Soc. Rev.* **2014**, *43*, 3342–405.

(45) Black, F. A.; Wood, C. J.; Ngwerume, S.; Summers, G. H.; Clark, I. P.; Towrie, M.; Camp, J. E.; Gibson, E. *Faraday Discuss.* **2017**, *198*, 449–461.

(46) Rao, P. D.; Dhanalekshmi, S.; Littler, B. J.; Lindsey, J. S. *J. Org. Chem.* **2000**, *65*, 7323–7344.

(47) Kim, S.; Bouffard, J.; Kim, Y. *Chem. Eur. J.* **2015**, *21*, 17459–65.

(48) Zhang, X.; Xu, Y.; Guo, P.; Qian, X. *New J. Chem.* **2012**, *36*, 1621.

(49) Tahtaoui, C.; Thomas, C.; Rohmer, F.; Klotz, P.; Duportail, G.; Mely, Y.; Bonnet, D.; Hibert, M. *J. Org. Chem.* **2007**, *72*, 269–72.

(50) Summers, G. H.; Lefebvre, J. F.; Black, F. A.; Davies, E. S.; Gibson, E. A.; Pullerits, T.; Wood, C. J.; Zidek, K. *Phys. Chem. Chem. Phys.* **2015**, *18*, 1059–1070.

(51) Wijesinghe, C. A.; El-Khouly, M. E.; Blakemore, J. D.; Zandler, M. E.; Fukuzumi, S.; D'Souza, F. *Chem. Commun.* **2010**, *46*, 3301–3.

(52) Wood, C. J.; Cheng, M.; Clark, C. A.; Horvath, R.; Clark, I. P.; Hamilton, M. L.; Towrie, M.; George, M. W.; Sun, L.; Yang, X.; Gibson, E. A. *J. Phys. Chem. C* **2014**, *118*, 16536–16546.

(53) Lefebvre, J. F.; Sun, X. Z.; Calladine, J. A.; George, M. W.; Gibson, E. A. *Chem. Commun.* **2014**, *50*, 5258–5260.

(54) Zhang, L.; Favereau, L.; Farre, Y.; Mijangos, E.; Pellegrin, Y.; Blart, E.; Odobel, F.; Hammarstrom, L. *Phys. Chem. Chem. Phys.* **2016**, *18*, 18515–27.

(55) Black, F. A.; Clark, C. A.; Summers, G. H.; Clark, I. P.; Towrie, M.; Penfold, T.; George, M. W.; Gibson, E. A. *Phys. Chem. Chem. Phys.* **2017**, *19*, 7877–7885.

(56) Karlsson, J. K.; Harriman, A. *J. Phys. Chem. A* **2016**, *120*, 2537–46.

(57) Popere, B. C.; Della Pelle, A. M.; Poe, A.; Balaji, G.; Thayumanavan, S. *Chem. Sci.* **2012**, *3*, 3093.

(58) Misra, R.; Dhokale, B.; Jadhav, T.; Mobin, S. M. *Dalton Trans.* **2014**, *43*, 4854–61.

(59) Lu, H.; Mack, J.; Yang, Y.; Shen, Z. *Chem. Soc. Rev.* **2014**, *43*, 4778–823.

(60) Lincoln, R.; Greene, L. E.; Krumova, K.; Ding, Z.; Cosa, G. *J. Phys. Chem. A* **2014**, *118*, 10622–30.

(61) Erten-Ela, S.; Yilmaz, M. D.; Icli, B.; Dede, Y.; Icli, S.; Akkaya, E. U. *Org. Lett.* **2008**, *10*, 3299–302.

(62) Richards, V. J.; Gower, A. L.; Smith, J. E.; Davies, E. S.; Lahaye, D.; Slater nee Phillips, A. G.; Lewis, W.; Blake, A. J.; Champness, N. R.; Kays, D. L. *Chem. Commun.* **2012**, *48*, 1751–3.

Chapter 8

Conclusions and Perspectives

This thesis has focused on determining charge transfer mechanisms for a variety of dye structures in the excited state, for sytems in solution or adsorbed onto a nickel oxide film. The primary aim was to investigate systems useful for the application of p-type dye-sensitised solar cells and to gain further understanding of the charge-recombination process. This was achieved using time-resolved spectroscopy where dyes adsorbed onto a nickel oxide film and in some cases in the presence of a redox couple in solution, are excited with a laser pulse and their dynamics after excitation are followed spectroscopically. Some common themes were relevant throughout and are summarised here with key results of this work.

Charge-recombination

Fast charge-recombination has been identified as a major limiting factor of nickel oxide p-type dye-sensitised solar cells, though the charge-separated state lifetime does not consistently correlate with performance. This work has investigated the formation and decay of charge-separated states for a number of push-pull dyes on nickel oxide. Efficient charge-injection and charge-separated state lifetimes on a picosecond timescale were recorded for all BOD1, BOD3, BOD4 and BOD5, despite large differences in solar cell performance. Charge-separated state lifetimes were slightly faster for the smaller dyes BOD1 and BOD4 (τ = *ca.* 5 ps) relative to the synthetically more complex systems BOD3 and BOD5 which had a greater extent of donor-acceptor character (τ = *ca.* 600 ps). The charge-separated

state lifetimes of BOD3 and BOD5 were on a similar timescale to that of P1 (*ca.* 200 ps) which also generates high photocurrents in a p-type dye-sensitised solar cell. The charge-separated state lifetime of BOD2 was the longest of the dyes in this thesis (*ca.* 180 ns) but the dye doesn't perform as well as BOD3, BOD5, P1 or CAD3 (τ = *ca.* 1.2 ns), and time-resolved spectroscopy experiments suggested that the inefficient formation of the charge-separated state was likely to limit the performance of this dye. The small dye CAD4 showed particularly fast charge-recombination (τ = *ca.* 10 ps) and did not perform as well as CAD3 in a p-type dye-sensistised solar cells, which may be due to the new binding moiety.

Characterisation

One key result presented in this thesis is the characterisation of the infrared spectrum of a triplet bodipy excited state. This was observed in the time-resolved infrared spectra of BOD2 and $K^{Mo}{}_{Sn}$[BOD2] in dichloromethane solutions as a sharp band at *ca.* 1523 cm^{-1} to 1525 cm^{-1}. This band is distinctive from the ν(C=C) of other bands in the fingerprint region relating to the bodipy. The identification of this species provides a reference for other systems containing bodipy groups where a triplet excited state is formed upon excitation, and particularly where the absorption bands in the visible region are broad and difficult to assign.

For bodipy-polyoxometalate hybrid compounds, the charge-transfer excited state was characterised in the transient absorption spectrum resembling the broad absorption of POM^- and the sharp absorption of $bodipy^+$. This was observed in the transient absorption spectra of $K^{W}{}_{Si}[BOD_1]$, $^{W}{}_{Si}[BOD_1]_{TBA}$, $D^{W}{}_{Si}[BOD_1]_{TEA}$ and $D^{W}{}_{Si}[BOD_1]_{TMA}$. The vibrational spectrum of the $POM^-bodipy^+$ charge-transfer excited state was also characterised in the time-resolved infrared spectra as a broad band at *ca.* 1425 cm^{-1}. The distinctive features of the charge-transfer excited state allow the photoinduced dynamics of these systems to be easily followed.

Versatile bodipys

This work presented many examples of bodipy chromophores with very different properties. Bodipy photosensitisers were used as acceptor groups in push-pull dyes BOD1-BOD5

which all had high molar absorption coefficients over a range of absorption maxima from 528 nm to 565 nm. Small structural modifications to the bodipy core resulted in red-shifted and broadened absorption for BOD3 and BOD5 which were particularly successful as photosensitisers for p-type dye-sensitised solar cells. Similarly, a bodipy group was used as an acceptor in FAB4, with a more blue-shifted absorption at 514 nm. A modification to the fluorine atoms allowed an anchor group to be appended to the bodipy at the opposite position to the anchors in BOD1-5. The bodipy-polyoxometalate hybrids demonstrate the use of bodipy chromophores as donating groups, and a charge-transfer excited state with an oxidised bodipy^{+} is observed for $K^{W}{}_{Si}[BOD_1]$, $K^{Mo}{}_{Sn}[BOD_2]$, $D^{W}{}_{Si}[BOD_1]_{TBA}$, $D^{W}{}_{Si}[BOD_1]_{TEA}$ and $D^{W}{}_{Si}[BOD_1]_{TMA}$. By replacing the phenyl group at the *meso* position of BOD_1 with an alkynyl substituent in BOD_2, the absorption maximum is shifted from 527 nm to 574 nm. In general, a variety of bodipy structures are presented in this thesis, and the different substituents around the bodipy core allow tuning of the photophysical properties. In the final results chapter an easy synthesis of a bodipy was designed to include spectroscopic handles, and anchor group and favourable energy levels, further demonstrating the versatility and tunability of these compounds.

Experimental conditions

Commonly, the charge-separated state lifetime of dye|semiconductor systems is reported for a dye adsorbed on a dry film, as for BOD1-5. The photoinduced dynamics are therefore determined under conditions which are considerably different to those inside a dye-sensitised solar cell, where an electrolyte and counter electrode are present, and there is an applied bias. The laser power used for time-resolved spectroscopy experiments is also considerably higher than the 1 sun illumination of a standard solar cell test. The differences between experimental and realistic conditions are generally limited by experimental restrictions. For time-resolved spectroscopy these include the required optical density of the sample, which for transient absorption experiments should be less than 0.3 at the excitation wavelength, whereas a film prepared for dye-sensitised cells would typically have an absorbance of *ca.* 2. The thicknesses of nickel oxide films are also lower for time-resolved spectroscopy experiments to minimise the absorbance of the film.

To ensure that the experimental conditions were as realistic as possible, time-resolved

spectroscopy experiments of CAD3 and CAD4 were performed in the presence and absence of an electrolyte containing iodine and lithium iodide similar to that used to fill p-type dye-sensitised solar cells. The concentration of iodine and lithium iodide in electrolytes used for time-resolved spectroscopy was lower than that used in dye-sensitised solar cells to reduced the contribution from iodine to the absorption spectrum in the visible region, but this still gives a more realistic representation of the system. In the presence of the electrolyte the rate of charge-recombination decreased which indicated interactions between species in the electrolyte and the dyes. This is a unique feature of the charged acceptor group and may contribute to the high performance of CAD3 and the relatively high photocurrent generated by the small dye CAD4.

For the application of dye-sensitised solar cells, dyes commonly have high molar absorption coefficients and broad absorption profiles which can saturate the detectors of spectrometers and mask other signals in transient absorption experiments. Future work in this area could investigate techniques and methods which further bridge the gap between experimental and real conditions.

Analysis of kinetics

As discussed above, many of the dyes in this thesis have broad absorption profiles and the spectra of their corresponding excited state species can overlap. In this thesis global analysis was used to separate the spectra of overlapping transient species, together with time-resolved infrared spectroscopy which was used to investigate changes in the vibrational spectra upon excitation. Global analysis of the transient absorption spectra of BOD3|NiO and BOD5|NiO distinguished the spectra and corresponding lifetimes associated with the excited state, charge-transfer excited state and charge-separated state. For BOD3|NiO the transient peak of the charge-separated state was small in amplitude and single-point analysis suggested much faster charge-recombination. Similarly, global analysis of both transient absorption and time-resolved infrared spectra of $K^{Mo}{}_{Sn}[BOD_2]$ confirmed the presence of the charge-transfer excited state, which confirmed that the bodipy-localised triplet excited state was formed following the decay of the charge-transfer excited state.

Previous transient absorption experiments of BOD2 reported a long-lived charge-separated state lifetime on nickel oxide, despite a low solar cell performance relative to P1. In this

work time-resolved infrared spectroscopy of BOD2|NiO revealed that both the charge-transfer excited and charge-separated state were present following excitation and this likely contributed to the lower IPCE of BOD2 relative to P1. The charge-transfer excited state and charge-separated state on nickel oxide were determined using a global analysis method of the time-resolved infrared spectra, as single-point analysis was less successful due to multiple overlapping bands. For future work on conjugated organic dyes which have many infrared vibrations, it is suggested that global analysis of time-resolved infrared spectra is the most appropriate analysis technique.

Appendix A

Appendix

	[a] λ_{max} (nm)	[b] ε ($dm^3\ mol^{-1}\ cm^{-1}$)	[c] D/D^+ (V vs fc/fc^+)	[d] D/D^- (V vs fc/fc^+)	[e] $E_{0\text{-}0}$ (eV)	[f] D^*/D^- (V vs fc/fc^+)
BOD1	528	52 000	0.64	-1.63	2.31	0.68
BOD2	540	112 000	0.65	-1.48	2.27	0.79
BOD3	565	65 700	0.63	-1.29	2.11	0.82
BOD4	526	81 700	0.62	-1.66	2.33	0.67
BOD5	561	65 824	0.74	-1.27	2.14	0.87

Table A.1: Electrochemical and photophysical data for BOD1-5. Values determined from ref [1]. [a,b]Absorption maxima and molar absorption coefficient values in dichloromethane solution. [c,d]The first reduction and oxidation potentials determined from electrochemical analysis. [e]Determined from the point of intersection between absorption and emission spectra. [f] $D^*/D^- = D/D^- + E_{0\text{-}0}$.

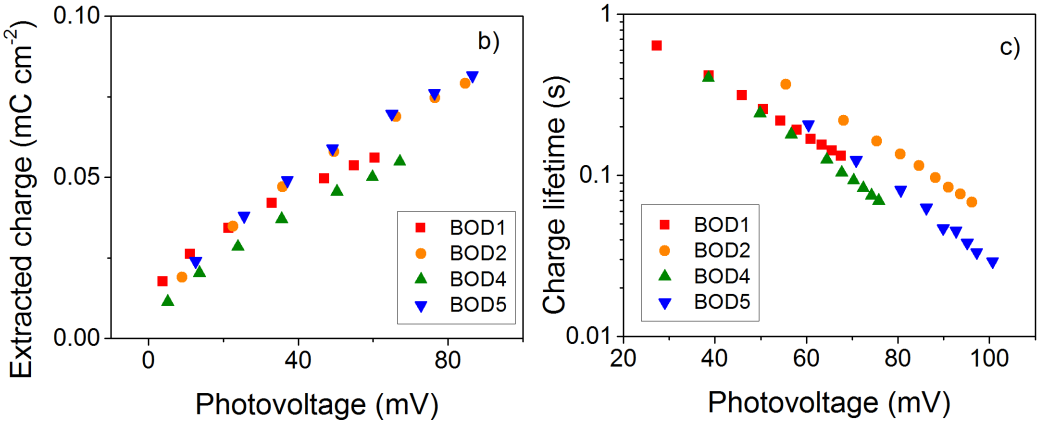

Figure A.1: Charge transient measurements of p-DSCs sensitised with BOD1, BOD2, BOD4 and BOD5.

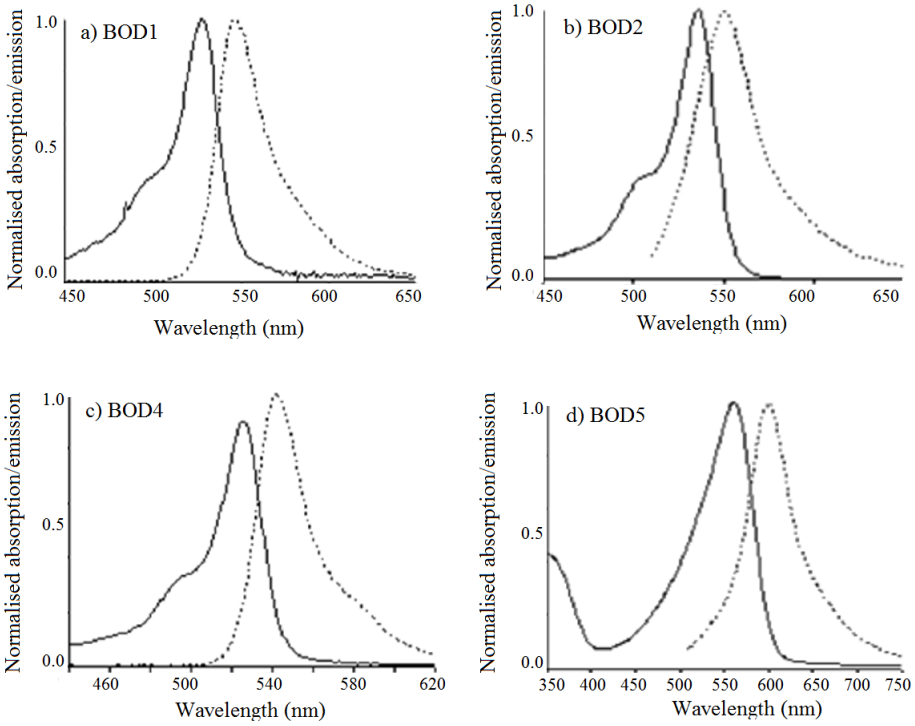

Figure A.2: Emission spectra of BOD1, BOD2, BOD4 and BOD5 in dichloromethane solution. Taken and adapted from ref [1]. BOD3 was not sufficiently emissive to obtain a spectrum.

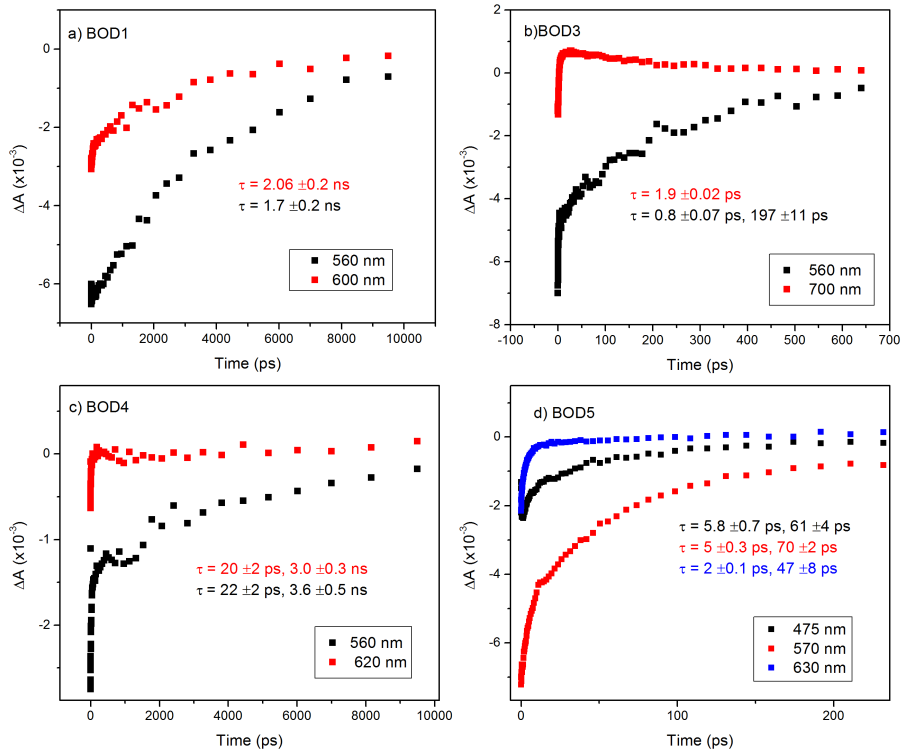

Figure A.3: Kinetic traces from single point analysis of transient absorption spectra of BOD1 and BOD3-5 in dichloromethane solution. $\lambda_{exc} = 532$ nm.

	D/D^+ (V vs fc/fc^+)	D/D^- (V vs fc/fc^+)	$E_{0\text{-}0}$ (eV)	D^*/D^- (V vs fc/fc^+)	ΔG_{inj} (eV)	ΔG_{reg} (eV)
CAD1	0.44	-1.05	1.72	0.67	-0.79	-0.23
CAD2	0.49	-0.97	1.66	0.69	-0.81	-0.15
CAD3	0.59	-0.99	1.78	0.79	-0.91	-0.17
CAD4	0.89	-0.98	1.88	0.90	-1.02	-0.16

Table A.2: Selected electrochemical and photophysical properties for the CAD dyes, from refs [2–4].

	Voc (mV)	Jsc (mA cm^{-2})	FF (%)	η (%)	IPCE (%)	Dye loading (mol cm^{-2})
[a]CAD3	101	8.21	31	0.25	50	7.36 x10^{-6}
CAD4	84	3.96	32	0.11	35	17.2 x10^{-6}

Table A.3: Photovoltaic performance of CAD3 and CAD4. [a]Taken from ref [3]. Electrolyte: 0.1 M I_2, 1.0 M LiI in acetonitrile.

	Lifetime, ps
CAD3	τ_{428} = 3485
	τ_{485} = 3242
	τ_{610} = 2861

Table A.4: Average lifetimes obtained from single-point analysis of transient absorption spectra of CAD3|NiO in the presence of 0.1 M $LiClO_4$ in acetonitrile. λ_{exc} = 532 nm.

	D/D^+ (V vs fc/fc^+)	D/D^- (V vs fc/fc^+)	$E_{0\text{-}0}$ (eV)	D^*/D^- (V vs fc/fc^+)
P1	0.69	-1.46	2.25	0.79
BOD2	0.65	-1.48	2.27	0.79

Table A.5: Selected electrochemical and photophysical properties of P1 and BOD2, from ref [5] and ref[1].

Assignment	Lifetime, ps			
	CH_2Cl_2	CD_3CN	NiO	NiO|I^-/I_3^-
CN	τ_{2234} = 836 ±127		τ_{2228} = 14 ±2 (79%), 283 ±115 (15%)	τ_{2228} = 13 ±2 (82%), 1101 ±343 (12%)
	τ_{2223} = 1094 ±139		τ_{2217} = 14±4 (71%), 108 ±65 (19%)	τ_{2211} = 17 ±2 (82%), 427 ±129 (17%)
	τ_{2178} = 892 ±91		τ_{2173} = 13 ±4	τ_{2173} = 19 ±2 (72 %), 650 ±107 (22%)
	τ_{2146} = 968 ±104		τ_{2130} = 9 ±4 (67%), 146 ±72 (29%)	τ_{2130} = 19 ±3 (73%), 895 ±160 (25%)
C=O	τ_{1742} = 1091 ±192			
	τ_{1719} = 978 ±172			
C=C (Phenyl)	τ_{1583} = 1139 ±28	τ_{1589} = 37 ±3	τ_{1598} = 16 ±1 (81%), 563 ±138 (15%)	τ_{1595} = 12 ±1 (72%), 749 ±111 (24%)
	τ_{1561} = 1163 ±28	τ_{1564} = 39 ±3	τ_{1572} = 16 ±1 (77%), 496 ±64 (18%)	τ_{1575} = 13 ±2 (70%), 770 ±108 (25%)
	τ_{1498} = 1103 ±27	τ_{1450} = 34 ±6	τ_{1553} = 13 ±3 (76%), 191 ±58 (21%)	τ_{1555} = 10 ±1 (77%), 128 ±21 (20 %)
	τ_{1447} = 1148 ±64	τ_{1329} = 24 ±4	τ_{1509} = 2 ±0.2 (87%), 375 ±39 (12%)	τ_{1510} = 12 ±1 (65%), 901 ±93 (32 %)
	τ_{1333} = 1153 ±76	τ_{1310} = 36 ±3	τ_{1326} = 18 ±1 (75%), 528 ±84 (16%)	τ_{1325} = 13 ±1 (73%), 803 ±105 (22%)
	τ_{1324} = 1100 ±67		τ_{1314} = 12 ±1 (80%), 298 ±57 (14%)	τ_{1314} = 13 ±2 (72%), 510 ±88 (22%)
	τ_{1310} = 1127 ±65			
C=C (Thiophene)	τ_{1434} = 1184 ±45	τ_{1436} = 42 ±4	τ_{1434} = 13 ±1 (79%), 424 ±60 (18%)	τ_{1436} = 13±1 (73%), 707 ±92 (23%)
	τ_{1407} = 1073 ±29	τ_{1407} = 35 ±3	τ_{1382} = 220 ±47	τ_{1396} = 14 ±3 (67%), 819 ±148 (31%)

Table A.6: Lifetimes obtained from single-point analysis of the time-resolved infrared spectra of P1 following excitation at 532 nm. Where a multi-exponential function is used, the amplitudes of each component are given in brackets.

Assignment	Lifetime, ps			
	CH_2Cl_2	CD_3CN	NiO	NiO|I^-/I_3^-
C=O	τ_{1738} rise = 21 ±8 τ_{1738} = 509 ±72 τ_{1715} rise = 30 ±10 τ_{1715} = 368 ±70			
C=C (Phenyl)	τ_{1598} rise = 20 ±8 τ_{1598} = 492 ±102 τ_{1573} rise = 23 ±6 τ_{1573} = 499 ±89	τ_{1497} rise = 8 ±3 τ_{1497} = 43 ±10 τ_{1597} rise = 6 ±2 τ_{1597} = 69 ±11 τ_{1570} rise = 7 ±3 τ_{1570} = 41 ±3	τ_{1573} = 3 ±0.2 (81%), 27 ±5 (15%), 540 ±190 (4%)	τ_{1570} = 3 ±1 (76%), 143 ±20 (18%), 5700 ±1900 (6%)
C=C (Bodipy)	τ_{1543} = 109±30 (50%), 807 ±200 (50%) τ_{1525} rise = 405 ±66 τ_{1525} = 616 000±131 000 τ_{1507} = 44 ±6 τ_{1339} = 28 ±3 τ_{1324} = 458 ±70 (68%), 728 000 ±189 000 (32%)	τ_{1543} = 60 ±5 τ_{1507} = 7 ±1 τ_{1340} = 18 ±2 τ_{1324} = 59 ±9	τ_{1543} = 2 ±0.7 (85%), 38 ±6 (8%), 35 000 ±6 000 (6%) τ_{1530} = 2355 000 ±525 000 τ_{1522} = 2 ±0.2 τ_{1507} = 4 ±0.6 (63%), 51 ±10 (24%), 19 000 ± 4 000 (12%)	τ_{1550} = 10 ±1 (62%), 511 ±59 (24%), 102 000 ±13 000 (14%) τ_{1520} = 29 000 ±9000 τ_{1505} = 17 ±4 (67%), 749 ±264 (14%), 38 000 ±7000 (23%) τ_{1480} = 43 ±24 (26%), 868 ± 211 (45%), 443 000 ±156 000 (25%)
C=C (Thiophene)	τ_{1409} rise = 22 ±4 τ^{1409} = 495 ±49	τ_{1416} rise = 5 ±2 τ_{1416} = 61 ±6	τ_{1484} = 1 ±0.1 (83%), 75 ±9 (11%), 163 000 ±43 000 (4%)	τ_{1405} = 18 ±1 (74%), 275 ±44 (25%), 37 000 ±12 000 (8%)

Table A.7: Lifetimes obtained from single-point analysis of the time-resolved infrared spectra of BOD2 following excitation at 532 nm. Where a multi-exponential function is used, the amplitudes of each component are given in brackets.

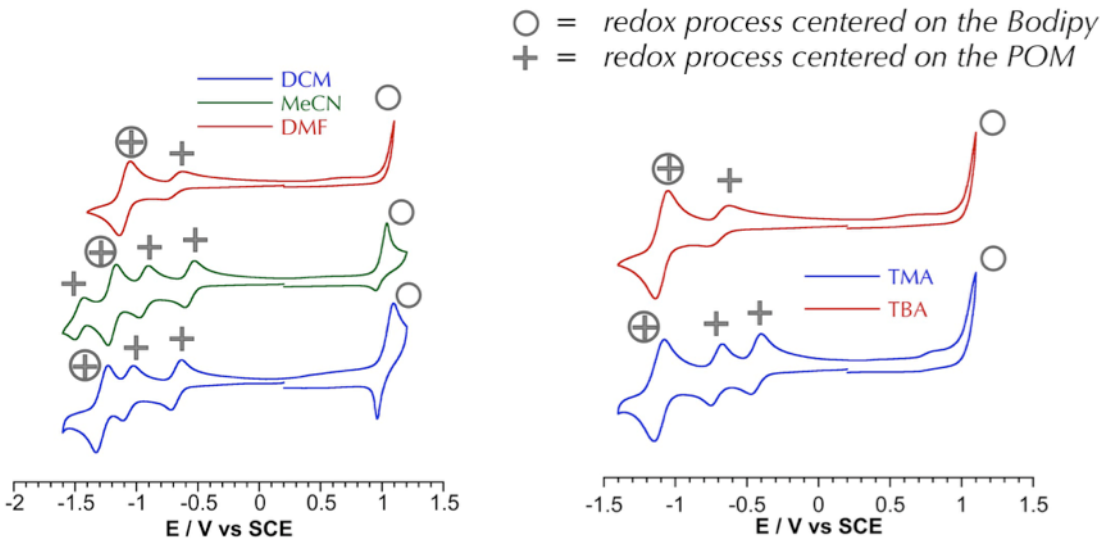

Figure A.4: Electrochemistry of POM4, which contains tetrabutylammonium cations, in different solvents (left), and POM4 and POM6 in DMF. POM6 contains tetramethylammonium cations.

	Voc (mV)	Jsc (mA cm^{-2})	FF (%)	η (%)	IPCE (%)
[a]P1	84	5.48	33	0.15	63
[b]BOD2	95	1.58	35	0.05	23

Table A.8: Photovoltaic performance of P1 and BOD2. [a]Values taken from ref [6]. [b]Solar cells were fabricated and characterised by the author. The electrolyte contained 0.1 M I_2 and 1.0 M LiI in acetonitrile.

Dye	Eg (eV)	ΔE (eV) (HOMO above TiO_2 VBM)	ΔE (eV) (LUMO below TiO_2 CBM)	LUMOs below TiO_2 CBM
Ru6	2.76	1.5	0.5	LUMO-LUMO+2
Ru7	2.60	0.5	1.4	LUMO-LUMO+6
Ru4	2.62	2.0	0.5	LUMO-LUMO+2
Ru3	2.41	1.5	1.0	LUMO-LUMO+3

Table A.9: Calculated electronic properties of a selection of cyclometalated ruthenium dyes adsorbed on titanium dioxide films, calculated using density functional theory (PBEO functional). This was performed by Dr. Martsinovich. VBM = valence band minimum. CBM = conduction band minimum.

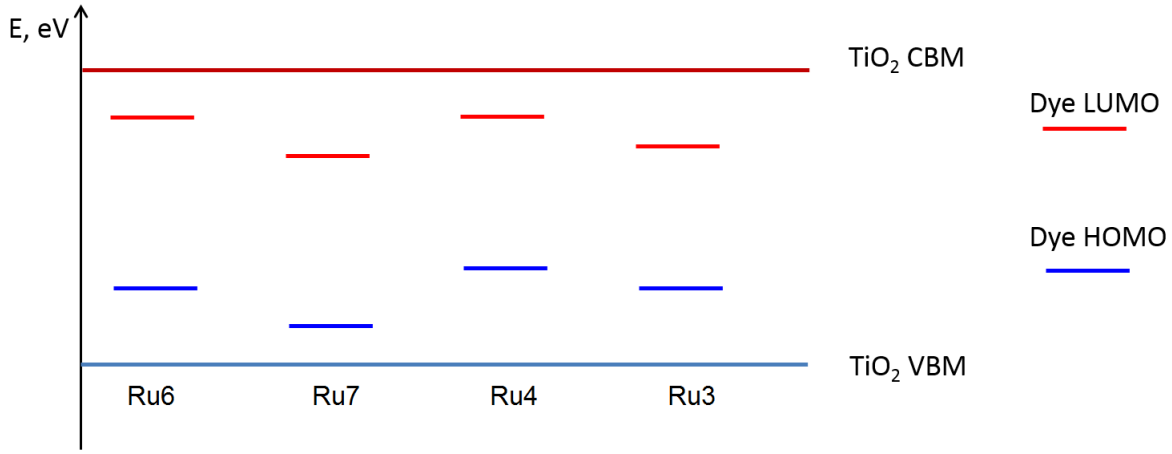

Figure A.5: Schematic of dye|TiO_2 energy levels calculated by density functional theory for a selection of cyclometalated ruthenium sensitisers, from the data shown in Table A.9.

#	λ (nm)	E (eV)	f[a]	Orbitals	Transition
1	430	2.89	0.249	HOMO-1 to LUMO (100 %)	Bodipy π to π^*
2	416	2.98	0.131	HOMO-2 to LUMO (69 %)	Catechol to bodipy charge transfer
				HOMO-1 to LUMO (31 %)	

Table A.10: Transitions calculated using density functional theory of FAB4. [a] Oscillator strength.

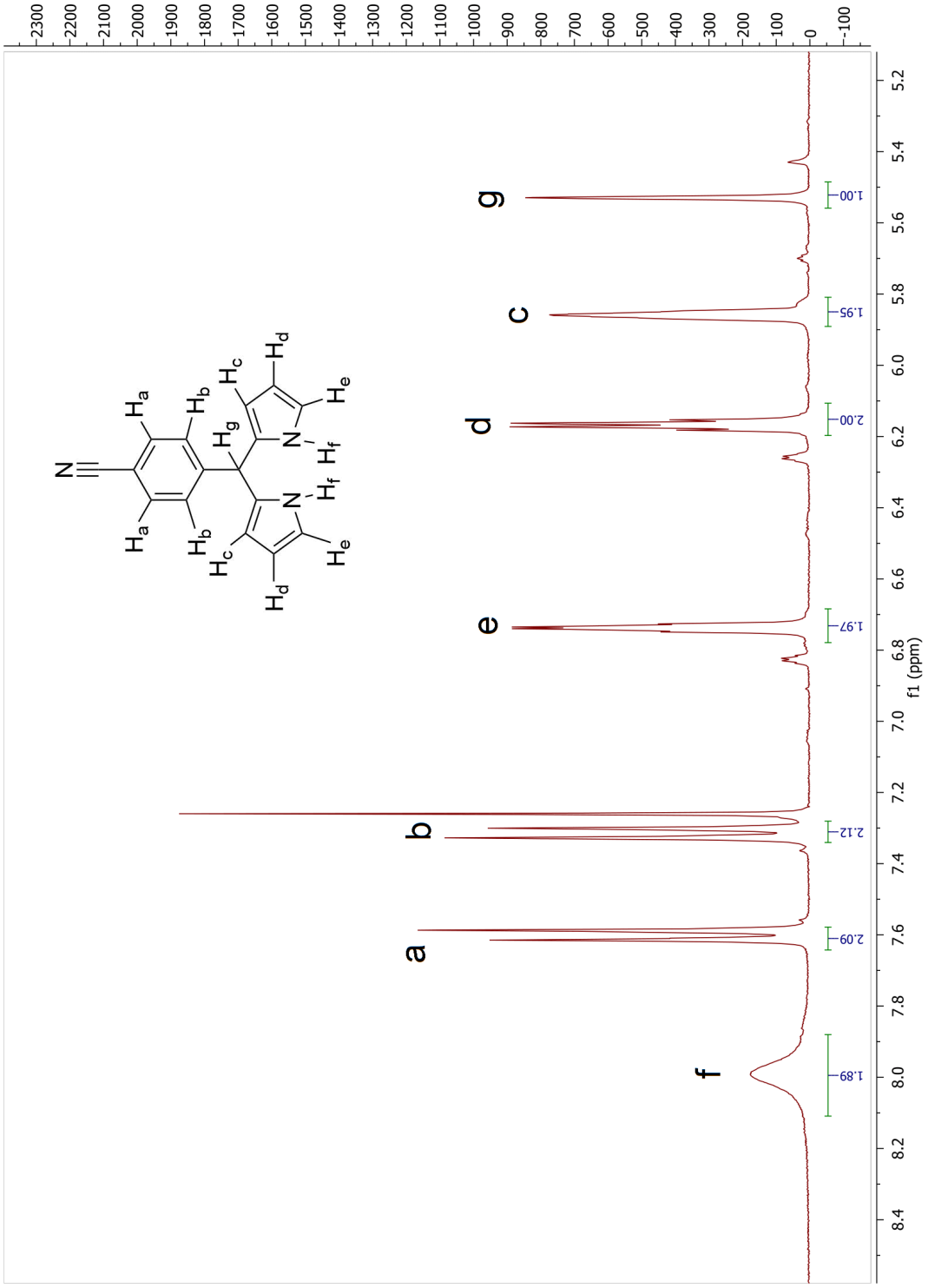

Figure A.6: ^{1}H NMR spectrum of FAB2 in deuterated chloroform. 300 MHz.

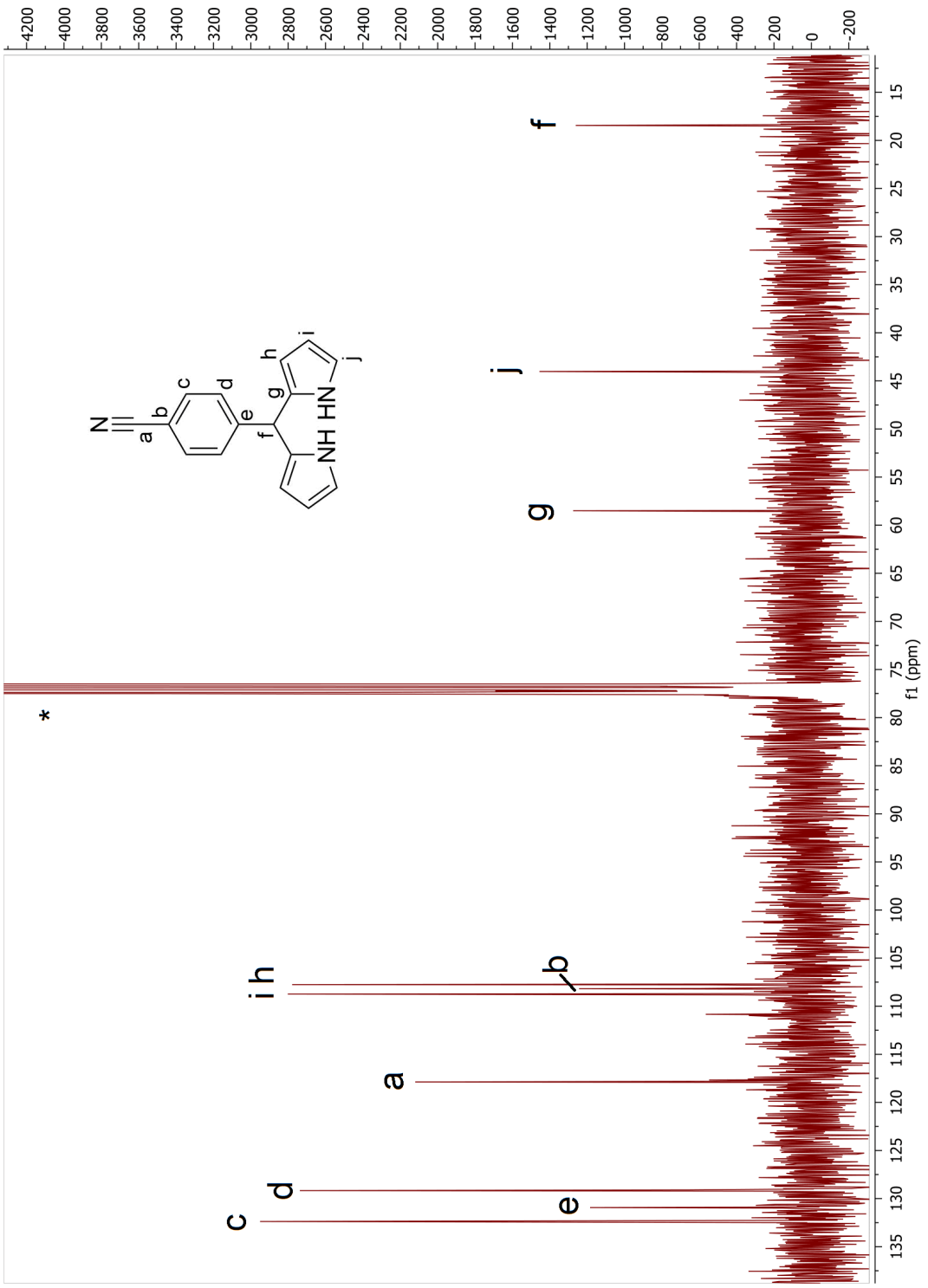

Figure A.7: ^{13}C NMR spectrum of FAB2 in deuterated chloroform. 75 MHz.

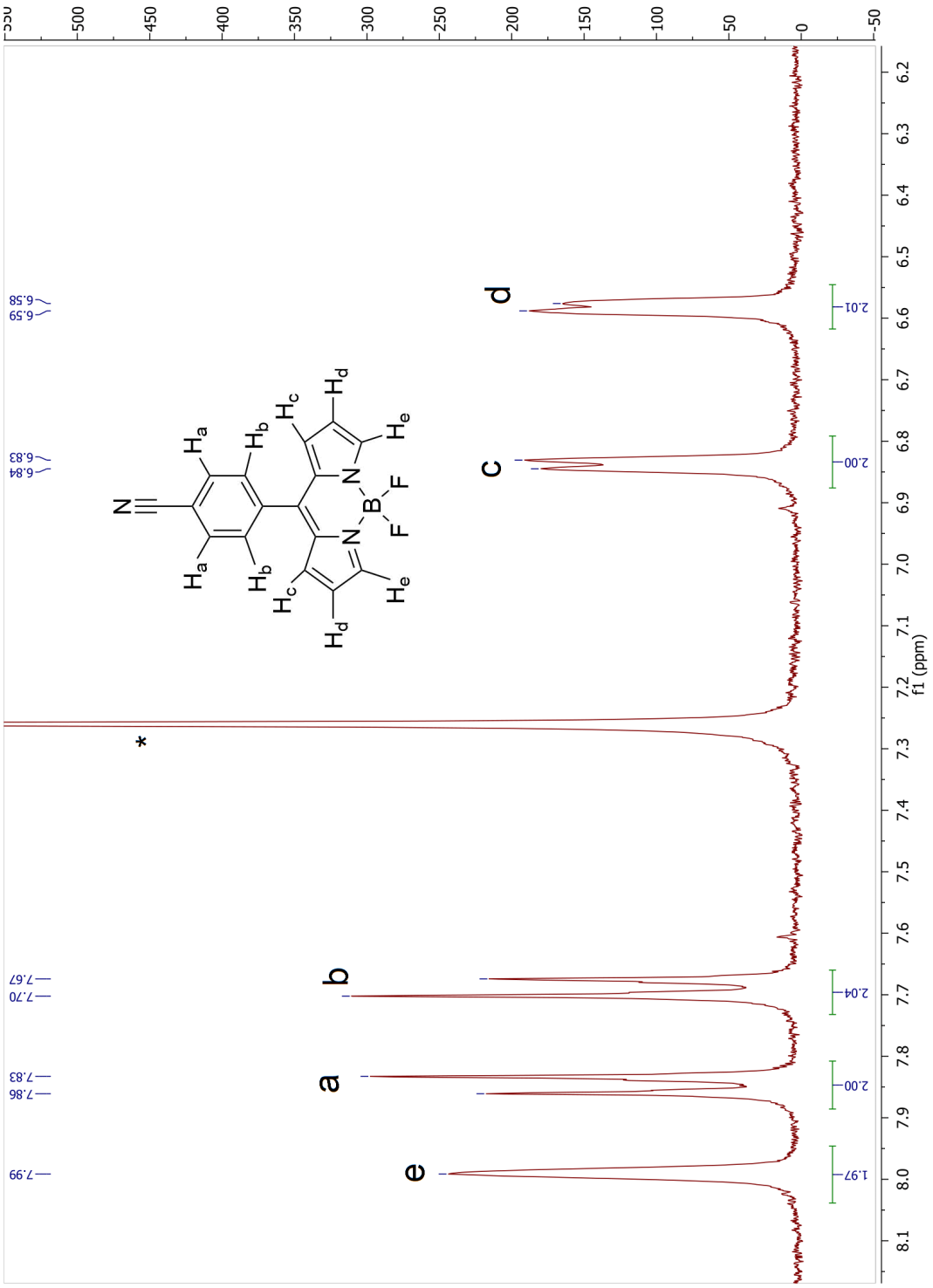

Figure A.8: ^{1}H NMR spectrum of FAB3 in deuterated chloroform. 300 MHz. * = solvent peak.

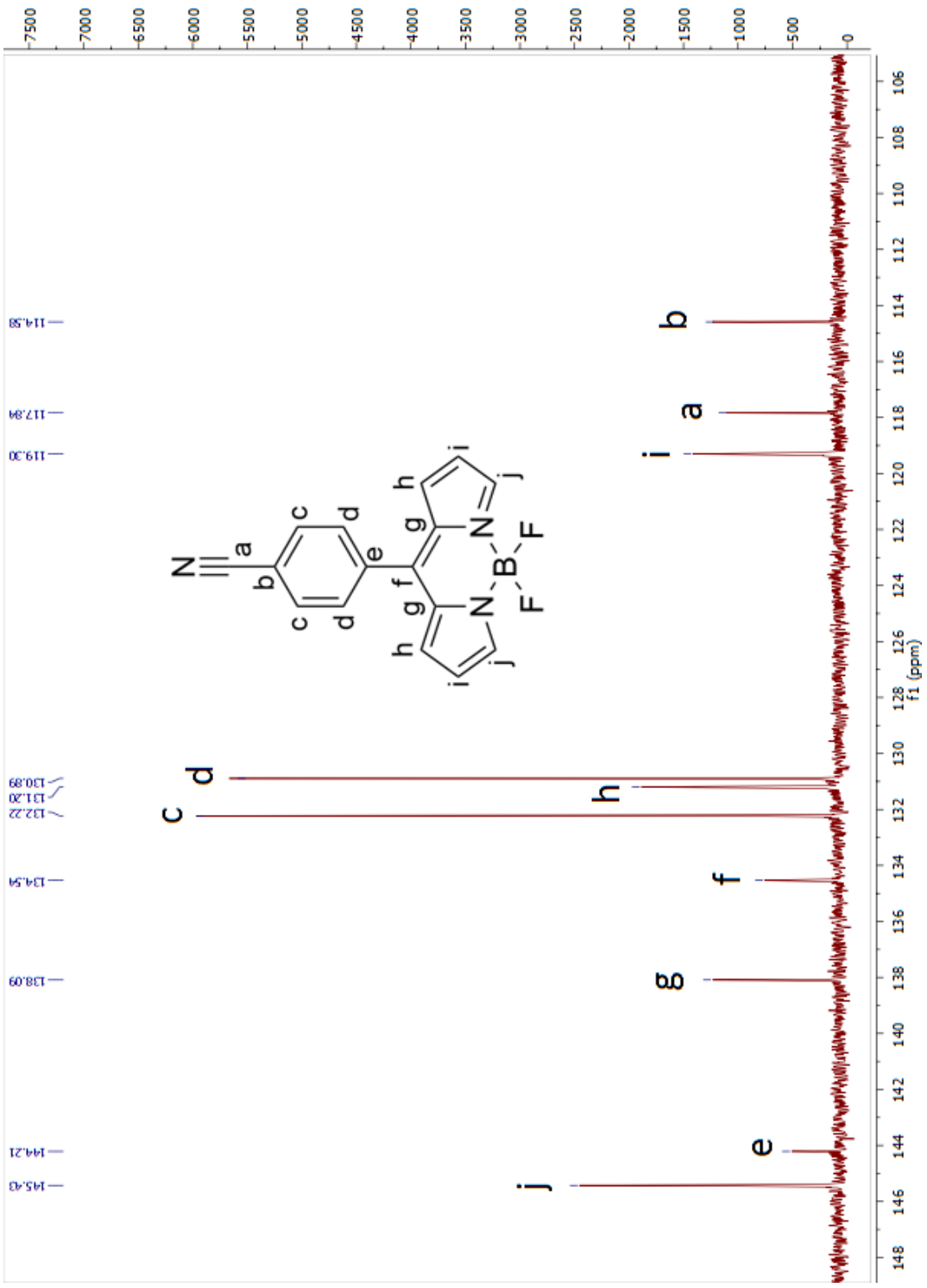

Figure A.9: ^{13}C NMR spectrum of FAB3 in deuterated chloroform. 126 MHz.

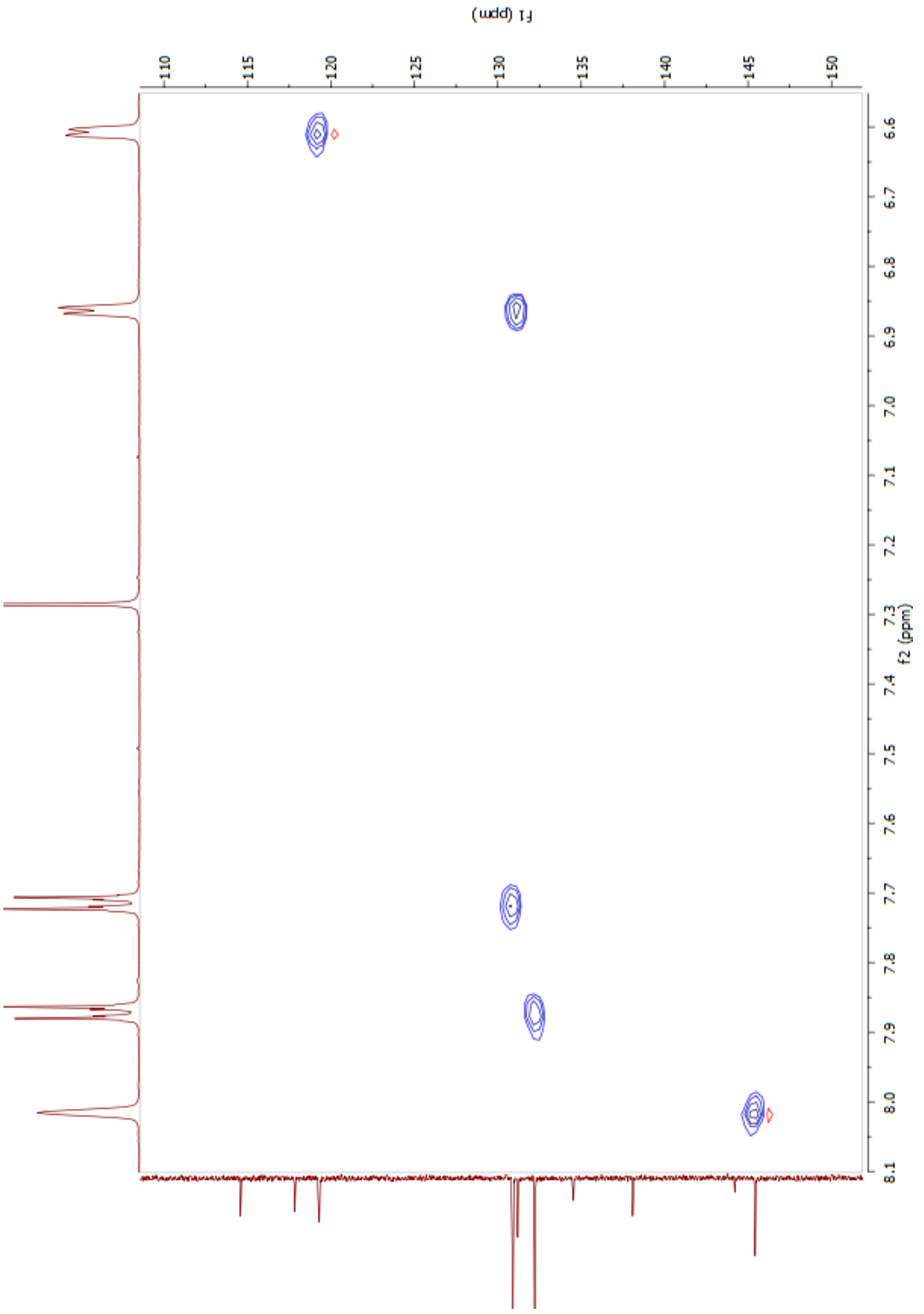

Figure A.10: HSQC spectrum of FAB3 in deuterated chloroform.

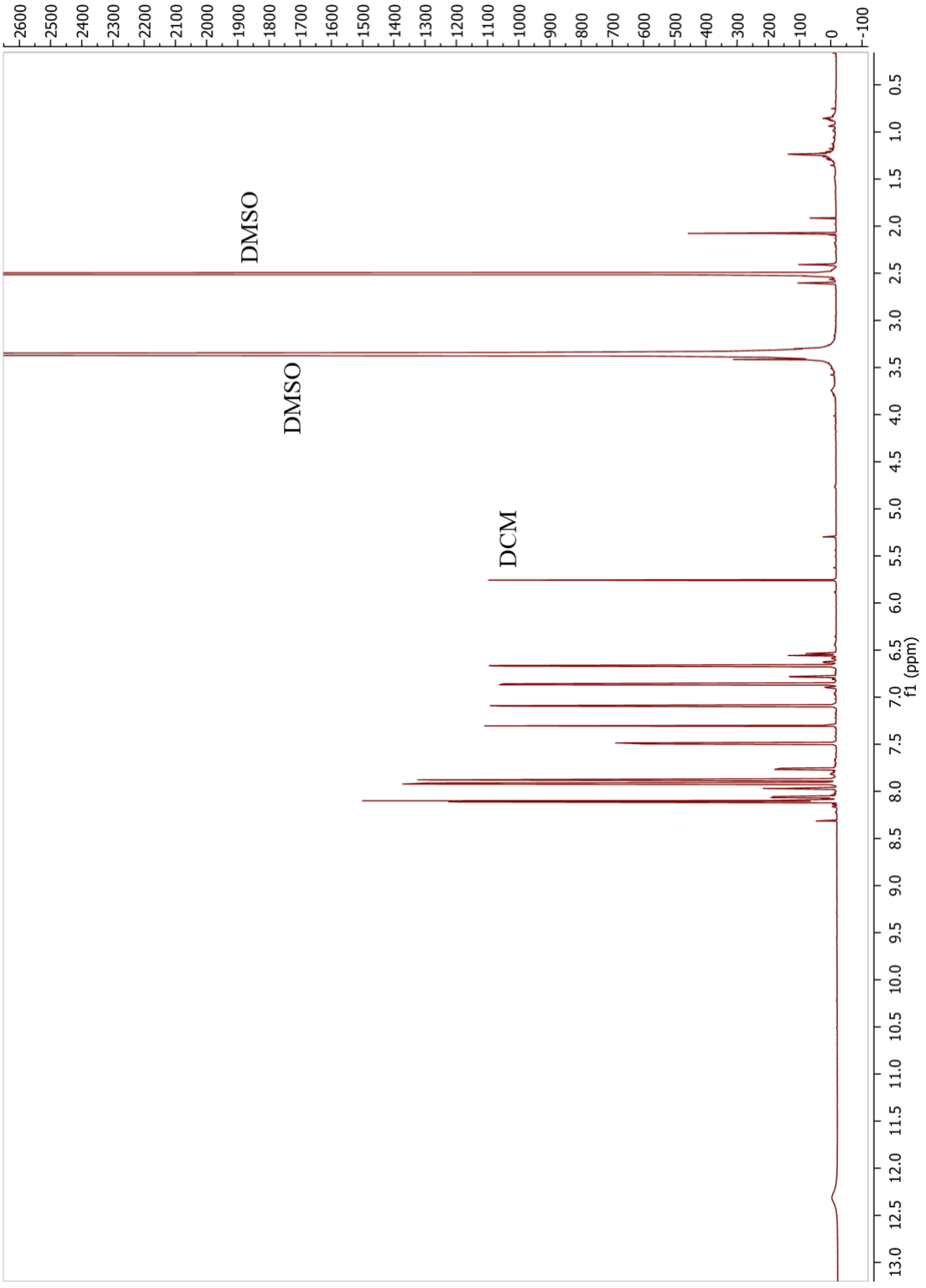

Figure A.11: Full spectrum of ^{1}H NMR of FAB4 in deuterated dimethyl sulfoxide. 700 MHz.

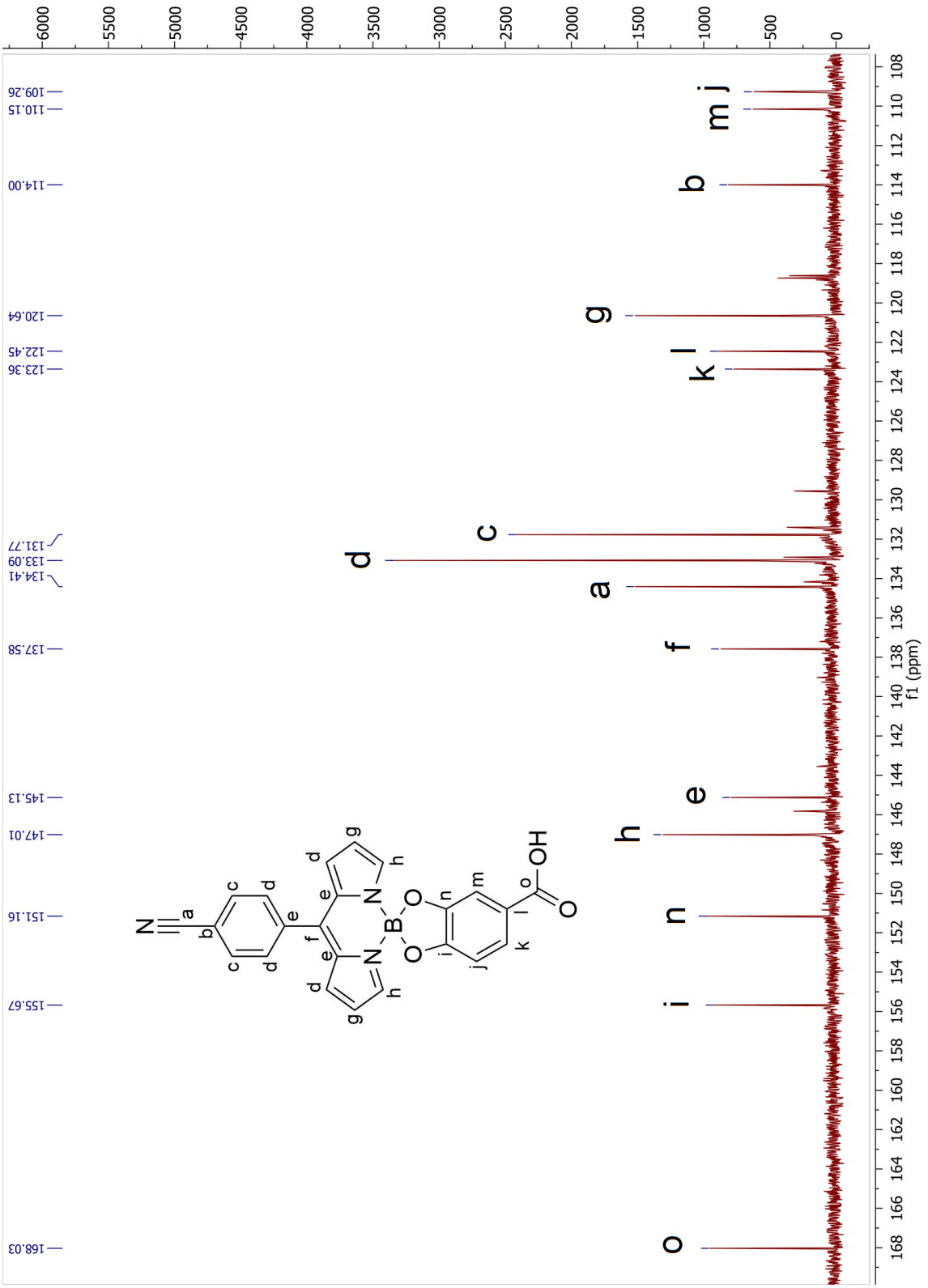

Figure A.12: ^{13}C NMR spectrum of FAB4 in deuterated dimethyl sulfoxide. 176 MHz.

References

(1) Summers, G. H.; Lefebvre, J. F.; Black, F. A.; Davies, E. S.; Gibson, E. A.; Pullerits, T.; Wood, C. J.; Zidek, K. *Phys. Chem. Chem. Phys.* **2015**, *18*, 1059–1070.

(2) Wood, C. J.; Cheng, M.; Clark, C. A.; Horvath, R.; Clark, I. P.; Hamilton, M. L.; Towrie, M.; George, M. W.; Sun, L.; Yang, X.; Gibson, E. A. *J. Phys. Chem. C* **2014**, *118*, 16536–16546.

(3) Wood, C. J.; Summers, G. H.; Gibson, E. A. *Chem. Commun.* **2015**, *51*, 3915–3918.

(4) Black, F. A.; Wood, C. J.; Ngwerume, S.; Summers, G. H.; Clark, I. P.; Towrie, M.; Camp, J. E.; Gibson, E. *Faraday Discuss.* **2017**, *198*, 449–461.

(5) Lefebvre, J. F.; Sun, X. Z.; Calladine, J. A.; George, M. W.; Gibson, E. A. *Chem. Commun.* **2014**, *50*, 5258–5260.

(6) Qin, P.; Wiberg, J.; Gibson, E. A.; Linder, M.; Li, L.; Brinck, T.; Hagfeldt, A.; Albinsson, B.; Sun, L. *J. Phys. Chem. C* **2010**, *114*, 4738–4748.